Comenius University in Bratislava
Faculty of Mathematics, Physics and Informatics

Nuclear β and $\beta\beta$ decay studies for neutrino physics

Dissertation thesis

2025 Mgr. Niţescu Ovidiu-Vasile

Comenius University in Bratislava
Faculty of Mathematics, Physics and Informatics

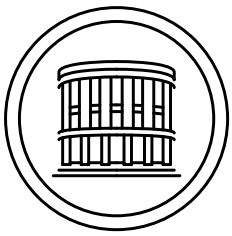

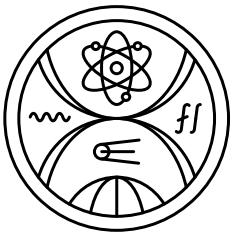

Nuclear β and $\beta\beta$ decay studies for neutrino physics

Dissertation thesis

Mgr. Niţescu Ovidiu-Vasile

Study program: Nuclear and Subnuclear Physics

Department: Department of Nuclear Physics and Biophysics

Supervisor: Prof. RNDr. Fedor Šimkovic, CSc.,
Faculty of Mathematics, Physics and Informatics,
Comenius University in Bratislava, 842 48 Bratislava, Slovakia

Consultant: Prof. Dr. Sabin Stoica,
International Centre for Advanced Training and Research in Physics, 077125 Măgurele, Romania

Bratislava, 2025

Comenius University Bratislava
Faculty of Mathematics, Physics and Informatics

THESIS ASSIGNMENT

Name and Surname:	Ovidiu-Vasile Nițescu
Study programme:	Nuclear and Subnuclear Physics (Single degree study, Ph.D. III. deg., full time form)
Field of Study:	Physics
Type of Thesis:	Dissertation thesis
Language of Thesis:	English
Secondary language:	Slovak

Title: Nuclear β and ββ decay studies for neutrino physics

Annotation: Neutrinos hold the key to many unanswered questions about the universe. They can help us understand how the universe was created, what dark matter is, why matter is more prevalent than antimatter, and what occurs during the collisions of neutron stars or black holes. Neutrinos were produced within the first second of the Big Bang and continue to be generated everywhere in the universe. They are one of its fundamental components. It is fascinating that, despite their significance, we still do not fully understand their basic physical properties, such as their fermionic nature, mass, CP properties, or even how many different types exist. Neutrino physics research benefits from using atomic nuclei as probes to explore fundamental properties and interactions of neutrinos. Combining theoretical and experimental studies of beta decay, double beta decay, and other nuclear processes may resolve many neutrino physics problems. These processes will be theoretically explored using modern field theory tools and advanced many-body methods. This Ph.D. study has the following main objectives:

• Studying the β-spectrum shape is vital for understanding physics beyond the standard model and neutrino physics. With improved experimental capabilities and increased statistics in the low-energy region, electron exchange corrections play a crucial role. It is planned to investigate the role of the orthogonality continuum and bound states in the final atom on the energy distribution of emitted electrons. There is a chance that it might resolve the mismatch between previous predictions and experimental measurements in the low-energy region.
• Measuring neutrino mass from β-decay involves analyzing the electron spectrum, particularly near its endpoint, where detectable effects occur. The low Q value enhances the number of events in this critical interval. The most sensitive measurements come from tritium's superallowed β transition, with the KATRIN experiment recently reporting an upper limit of $m_\beta = 0.45$ eV. Rhenium-187 is a strong candidate for neutrino mass measurement because of its low Q value of 2.4709 keV. Its unique forbidden β ground state to ground state transition will be theoretically investigated, including atomic electron exchange, finite nuclear size, and screening effect corrections.
• Research into new physics beyond the Standard Model through $2\nu\beta\beta$ decay is becoming increasingly promising. Key areas of focus include neutrino self-interactions, right-handed neutrinos, the existence of bosonic neutrinos, and sterile neutrinos with masses up to the process's Q-value. Additionally,

studies are investigating violations of Lorentz invariance and 0νββ decays with Majoron emission. In this context, the improved formalism of the 2νββ decay and 2ν double electron capture to ground and excited states of the final nucleus will be presented. The Taylor expansion will consider the lepton energies in energy denominators, leading to a set of kinematic factors and related nuclear matrix elements.
• Research is planned to explore the effects of electron state phase shifts on Molybdenium-100 2νββ decay, specifically the angular correlation of emitted electrons. The findings will underscore the significance of investigating how electron phase shifts influence the distinct features of β and ββ decay.
• A novel semi-empirical framework will be introduced to describe the 2νββ NMEs deduced from measured half-lives. This framework will consider the number of protons and neutrons, pairing effects, isospin, and nuclear deformation degrees of freedom. A comparison with the systematic calculation of 2νββ NME within the most advanced nuclear models will be presented. Predictions for observing additional 2νββ decay transitions will be given.

Addressing these tasks is essential to advancing experiments on double beta decay in underground labs, neutrino mass measurements, and our understanding of neutrino physics and nuclear structure.

Aim: This PhD thesis intends to improve the theoretical description of β and ββ decays, enabling more accurate investigations of neutrino properties and interactions.

Literature:
[1] F. Šimkovic: Neutrino masses and interactions and neutrino experiments in the laboratory (review article). Physics-Uspekhi 64 (12), 1238-1260 (2021).
[2] S.M. Bilenky: Introduction to the Physics of Massive and Mixed Neutrinos. Lecture Notes in Physics 817. Springer-Verlag Berlin Heidelberg 2010.
[3] Carlo Giunti and Chung W. Kim: Neutrino Physics and Astrophysics, Oxford University Press 2007, ISBN 978–0–19–850871–7.
[4]Peter Ring and Peter Schuck: The Nuclear Many-Body Problem, Springer-Verlag Berlin Heidelberg 1980.
Textbooks on nuclear and particle physics, as well as articles from academic journals and arXiv.

Keywords: Neutrino mass and mixing of neutrinos, nuclear β and ββ decays, electron and double electron capture in nuclei, relativistic electron wave function, electron exchange effect, nuclear matrix element, Dirac-Hartree-Fock-Slater many-body method.

Tutor: prof. RNDr. Fedor Šimkovic, CSc.
Consultant: prof. Sabin Stoica
Department: FMFI.KJFB - Department of Nuclear Physics and Biophysics
Head of department: prof. RNDr. Jozef Masarik, DrSc.

41391294

Comenius University Bratislava
Faculty of Mathematics, Physics and Informatics

Assigned: 09.01.2020

Approved: 13.01.2020 prof. RNDr. Jozef Masarik, DrSc.
Guarantor of Study Programme

.....
Student

.....
Tutor

Univerzita Komenského v Bratislave
Fakulta matematiky, fyziky a informatiky

ZADANIE ZÁVEREČNEJ PRÁCE

Meno a priezvisko študenta: Ovidiu-Vasile Nițescu
Študijný program: jadrová a subjadrová fyzika (Jednoodborové štúdium, doktorandské III. st., denná forma)
Študijný odbor: fyzika
Typ záverečnej práce: dizertačná
Jazyk záverečnej práce: anglický
Sekundárny jazyk: slovenský

Názov: Nuclear β and ββ decay studies for neutrino physics
Štúdium β a ββ rozpadov jadier zamerané na fyziku neutrín

Anotácia: Neutrína skrývajú odpovede na množstvo dôležitých nezodpovedaných otázok. Môžu nám poodhaliť ako vznikol vesmír, čo je jeho tmavá hmota, prečo vo vesmíre dominuje hmota nad antihmotou, a čo sa deje pri zrážkach neutrónových hviezd či čiernych dier. Neutrína vznikli v prvej sekunde Veľkého tresku a odvtedy vznikajú všade vo vesmíre dodnes. Sú jeho hlavnou komponentnou. Fascinujúce je, že napriek tomu doposiaľ nepoznáme ich základné fyzikálne vlastnosti - fermiónovú podstatu (dirakovská alebo majoranovská), hmotnosti, CP vlastnosti a ani to, koľko majú identít. Atómové jadrá sú sondami pre štúdium základných vlastností a interakcií neutrín. Experimentálnym a teoretickým štúdiom beta rozpadu, dvojitého beta rozpadu a iných jadrových procesov možno vyriešiť tieto problémy. Tento projekt má za cieľ teoreticky preskúmať uvedené procesy s využitím nástrojov modernej teórie poľa a moderných mnoho-nukleónových metód. Hlavné ciele dizertačnej práce sú nasledovné:

• Presne určenie energetického spektra elektrónov emitovaných v beta premene jadier umožňuje študovať javy súvisiace s fyzikou za Štandardným modelom fyziky častíc o ktorej existencii máme dôkaz v podobe malých hmotností neutrín určených pozorovaniami neutrínových oscilácií. Zdokonalené experimentálne techniky a zariadenia umožňujú meranie spektra elektrónov v oblasti nízkych energií, kde dôležitú úlohu majú korekcie vyplývajúce z atómového elektrónového výmenného efektu. Formalizmus tohto fenoménu, ktorý zahŕňa opis viazaných elektrónov dcérskeho atómu a emitovaných elektrónov, bude zdokonalený zabezpečením orthogonality týchto dvoch kategórií stavov elektrónov. Ďalej, vlnové funkcie viazaných elektrónov budú určené mnohočasticovou Dirac-Hartree-Fock-Slater metódou. Predpokladá sa, že uvedeným spôsobom nesúlad medzi teoretickými predpoveďami a experimentálnymi meraniami v uvedenej oblasti energií môže byť vyriešený.

• Laboratórne merania hmotností neutrín sa realizujú štúdiom konca energetického spektra beta rozpadu jadier, kde sa prejavujú efekty hmotnosti neutrín. Preferované na štúdium sú beta premeny s malou Q hodnotou, ktorej zodpovedá väčší počet eventov v študovanom energetickom intervale energií elektrónov. V súčasnosti najsilnejšie horné ohraničenie na efektívnu hmotnosť neutrín 0.45 eV bolo určené experimentom KATRIN registrujúceho beta rozpad trícia. Zakázaný beta rozpad rénia-187 s ešte nižšou Q hodnotou (2,4709 keV) je taktiež preferovaným kandidátom na meranie hmotnosti neutrín.

Bude realizovaný presnejší výpočet beta spektra rénia-187 do základného stavu konečného jadra zahrňujúci atómový elektrónový výmenný efekt, efekty konečného rozmeru jadra a vplyvu atómových elektrónov na určenie vlnovej funkcie emitovaného elektrónu.

• Výskum zameraný na hľadanie novej fyziky za Štandardným modelom fyziky častíc pomocou dvojneutrínového dvojitého beta rozpadu ($2\nu\beta\beta$) jadier sa úspešne rozvíja a napreduje. Zahŕňa možnosť existencie vlastných interakcií neutrín, interakcie neutrín cez pravé prúdy, možnú existenciu čiastočne bozónových neutrín a sterilných neutrín, narušenie Lorentzovej invariancie atď. V tejto súvislosti bude prezentovaný dokonalejší formalizmus $2\nu\beta\beta$ rozpadu a dvojneurínového dvojitého záchutu elektrónov do základného a vzbudených stavov konečného jadra. Využitím taylorovskej expanzie budú brané do úvahy energie leptónov v energetických menovateľoch jadrových maticových elementov. Ako dôsledok, rozpadová šírka procesu bude daná sumou kinematických faktorov váhovaných súčinom maticových elementov.

• Predmetom záujmu bude vplyv fázových posunov elektrónových stavov v coulombickom potenciáli atómového jadra na charakteristiky dvojitého beta rozpadu jadier. Výpočty budú zamerané na určenie uhlového rozdelenia vyletujúcich elektrónov v prípade $2\nu\beta\beta$ rozpadu molybdénu-100. Získané výsledky umožnia určiť potrebu výskumu vplyvu fázových posunov elektrónových stavov na charakteristiky β aj $\beta\beta$ jadrových prechodov vo všeobecnosti.

• $2\nu\beta\beta$ rozpad jadier je najzriedkavejší pozorovaný proces s polčasom rozpadu približne 100 miliónkrát a viacej väčším v porovnaní dobou existencie vesmíru. Bol pozorovaný v prípade jedenástich párno-párnych izotopov. Hodnoty maticových elementov $2\nu\beta\beta$-rozpadu jadier, odvodené z nameraných polčasov rozpadu, vykazujú značné rozdiely jednotlivých hodnôt a sú predmetom záujmu vedeckej komunity. Bude navrhnutý semi-empirický vzťah na reprodukciu uvedených maticových elementov, ktorého stupňami voľnosti budú rôzne kombinácie pomeru protónového a neutrónového čísla, hodnoty izospinu párno-párneho jadra v základnom stave, charakteristiky spárovania nukleónov a deformácie počiatočného a konečného jadra. Dosiahnuté výsledky budú porovnané s výsledkami teoretických modelov atómového jadra a iných fenomenologických modelov. Budú predpovedané $2\nu\beta\beta$ polčasy rozpadov ďalších jadier, ktoré sú predmetom experimentálneho záujmu.

Vyriešenie vyššie stanovených úloh je dôležité pre súčasné a budúce experimenty v dvojitého beta rozpadu jadier v podzemných laboratóriách, laboratórne merania hmotnosti neutrín a vo všeobecnosti pre fyziku neutrín a porozumenie štruktúry atómových jadier.

Cieľ: Cieľom tejto dizertačnej práce je zdokonaliť teoretický popis β a $\beta\beta$ rozpadov jadier, čo umožní presnejšie určenie základných vlastností neutrín a ich interakcií.

Literatúra:
[1] F. Šimkovic: Neutrino masses and interactions and neutrino experiments in the laboratory (review article). Physics-Uspekhi 64 (12), 1238-1260 (2021).
[2] S.M. Bilenky: Introduction to the Physics of Massive and Mixed Neutrinos. Lecture Notes in Physics 817. Springer-Verlag Berlin Heidelberg 2010.

[3] Carlo Giunti and Chung W. Kim: Neutrino Physics and Astrophysics, Oxford University Press 2007, ISBN 978–0–19–850871–7.
[4]Peter Ring and Peter Schuck: The Nuclear Many-Body Problem, Springer-Verlag Berlin Heidelberg 1980.
Knižné publikácie týkajúce sa slabých interakcií a neutrín ako aj štruktúry atómových jadier, publikácie v recenzovaných časopisoch a arXiv báze na internete.

Kľúčové slová: Hmotnosti a zmiešavanie neutrín, β a ββ rozpady atómových jadier, elektrónový a dvojitý elektrónový záchyt jadrom, relativistická vlnová funkcia elektrónov, atómový elektrónový výmenný efekt, jadrový maticový element, mnohočasticová metóda Dirac-Hartree-Fock-Slater.

Školiteľ: prof. RNDr. Fedor Šimkovic, CSc.
Konzultant: prof. Sabin Stoica
Katedra: FMFI.KJFB - Katedra jadrovej fyziky a biofyziky
Vedúci katedry: prof. RNDr. Jozef Masarik, DrSc.

Spôsob sprístupnenia elektronickej verzie práce:
bez obmedzenia

Dátum zadania: 09.01.2020

Dátum schválenia: 13.01.2020 prof. RNDr. Jozef Masarik, DrSc.
garant študijného programu

.....
študent

.....
školiteľ

I hereby declare that I have written this thesis independently, under the guidance of my supervisor, with the assistance of the consultant, and using the cited literature.

Bratislava

29.01.2025

.....
Mgr. Niţescu Ovidiu-Vasile

Abstract

Neutrinos remain the most mysterious fundamental particles despite significant advancements in neutrino physics over the last two decades. Several fundamental questions remain unanswered concerning the nature of neutrinos, their absolute mass scale, hierarchy, CP violation properties, and the potential existence of additional sterile neutrinos. Atomic nuclei serve as valuable probes for studying neutrinos' fundamental properties and interactions, revealing insights in complex ways. These questions can be answered through experimental and theoretical studies of nuclear β and $\beta\beta$ decays and other nuclear processes. This dissertation uses field theory and advanced many-body methods to explore and improve the theoretical description of these processes.

The atomic exchange effect involving the final atom's bound electrons and those emitted in the β-decay and two-neutrino double beta ($2\nu\beta\beta$)-decay is re-examined. The Dirac-Hartree-Fock-Slater self-consistent calculations provide the electron wave functions. In contrast to prior research, the orthogonality of the final atom's continuum and bound electron states is guaranteed. This approach demonstrably resolves the discrepancy between previous theoretical predictions and experimental measurements in the low-energy region of the β spectrum. The significance of exchange corrections is also examined in the context of a leading candidate for establishing the neutrino mass scale: the unique first forbidden β-decay of ^{187}Re. A significant change in the energy distribution of emitted electrons is found.

The Taylor expansion formalism for describing the $2\nu\beta\beta$-decay rate to 0^+ states is extended to 2^+ excited states and the two-neutrino double electron capture (2νECEC). In addition, the presented study differs from previous ones by incorporating radiative and atomic exchange corrections in the predictions of $2\nu\beta\beta$-decay observables. The impact of the electron phase shift on the angular correlation between the emitted electrons is investigated. Additionally, the contribution of all bound s-wave electrons available for capture in the 2νECEC processes is evaluated, unlike in prior studies in which only the K and L_1 orbitals were considered. A systematic study is conducted for all nuclei undergoing the 2νECEC transition, and a more detailed calculation leading to significant improvement is presented for the recently measured 2νECEC of ^{124}Xe.

Finally, another subject of interest is the large spread of the effective nuclear matrix elements (NMEs) of $2\nu\beta\beta$-decay, deduced from measured half-lives. A novel semi-empirical formula (SEF) for calculating $2\nu\beta\beta$-decay NMEs is proposed. The degrees of freedom are the ratio of proton and neutron numbers, isospin, like nucleon pairing, and the deformation properties of the initial and final nuclei. Compared with the previous phenomenological and nuclear models, the SEF yields the best agreement with the experimental NMEs. Its stability and predictive power are cross-validated, and predictions are provided for nuclear systems of experimental interest.

Abstrakt

Napriek intenzívnemu výskumu a výraznému pokroku dosiahnutému vo fyzike neutrín za posledné dve desaťročia, neutrína zostávajú najzáhadnejšími elementárnymi časticami. Nezodpovedané sú otázky týkajúce sa podstaty neutrín (dirakovská alebo majoranovská), absolútnej škály a hierarchii hmotností neutrín, možného narušenie nábojovo-priestorovej symetrie a potenciálnej existencie sterilných neutrín. Atómové jadrá predstavujú laboratórium na štúdium základných vlastností a interakcií neutrín, ktoré poskytuje dôležité poznatky o týchto najrozšírenejších časticiach vo vesmíre. Odpovede na uvedené otázky je možné nájsť experimentálnym a teoretickým štúdiom β a $\beta\beta$ rozpadov jadier a ďalších jadrových procesov. Predkladaná dizertácia prezentuje presnejší teoretický popis uvedených procesov s využitím aparátu teórie poľa a moderných mnohočasticových metód.

Predmetom záujmu bol vplyv atómového výmenného efektu, ktorý zahŕňa opis viazaných elektrónov dcérskeho atómu a emitovaných elektrónov, na energetické rozdelenie elektrónov v β a $\beta\beta$ rozpade jadier. Vlnové funkcie viazaných elektrónov boli určené mnohočasticovou Dirac-Hartree-Fock-Slater metódou. Na rozdiel od predošlých výpočtov, bola zabezpečená orthogonalita stavov viazaných elektrónov s tými v kontinuu, čo sa ukázalo ako veľmi podstatné. Preukázateľne to vyriešilo problém nesúhlasu teoretických výpočtov s experimentálnymi meraniami v nízkoenergetickej oblasti β spektra. Výpočty zahrňujúce atómový výmenný efekt boli realizované aj v prípade zakázaného β-rozpadu jadra ^{187}Re, ktorý umožňuje laboratórne meranie hmotnosti neutrín. Zistilo sa, že zahrnutie daného efektu do výpočtov vedie na podstatnú modifikáciu energetického rozdelenia emitovaných elektrónov.

Ďalej, formalizmus taylorovskej expanzie polčasu rozpadu dvojneutrínového dvojitého beta ($2\nu\beta\beta$) rozpadu jadier do 0^+ stavov konečného jadra bol zovšeobecnený aj na prípad prechodov do 2^+ vzbudených stavov a proces dvojneutrínového dvojitého záchytu elektrónov jadrom (2νECEC). Zodpovedajúce výpočty polčasov rozpadov týchto procesov zahrnuli aj radiačné korekcie a korekcie majúce pôvod v atómovom výmennom efekte. Novým elementom bola aj analýza vplyvu fáz vlnových funkcií emitovaných elektrónov v $\beta\beta$ rozpade jadier na ich uhlové rozdelenie. Na rozdiel od predošlých štúdií týkajúcich sa 2νECEC procesu, keď bol uvažovaný len záchyt elektrónov z K a L_1 orbít, boli brané do úvahy príspevky do rozpadovej šírky tohto procesu od záchytu všetkých viazaných elektrónov v s-stave. Bol prezentovaný systematický výpočet polčasu rozpadu 2νECEC prechodov a detailný výpočet pre 2νECEC rozpad jadra ^{124}Xe vedúci k lepšiemu súhlasu s výsledkami nedávno realizovaného experimentu.

Napokon, predmetom štúdií boli aj hodnoty maticových elementov $2\nu\beta\beta$-rozpadu jadier, odvodené z nameraných polčasov rozpadu, ktoré vykazujú značné rozdiely jednotlivých hodnôt. Bola navrhnutá semi-empirická formula na výpočet týchto maticových elementov, ktorej vstupmi sú pomer protónového a neutrónového čísla jadra, hodnota izospinu zodpovedajúceho párno-párneho jadra v základnom stave, charakteristiky spárovania nukleónov a deformácie počiatočného a konečného jadra. Bolo demonštrované, že v porovnaní s výsledkami teoretických modelov atómového jadra a iných fenomenologických modelov, prezentovaný formalizmus vykazuje najlepšiu zhodu s experimentálnymi hodnotami $2\nu\beta\beta$ maticových elementov. S využitím prezentovanej metódy boli určené $2\nu\beta\beta$ polčasy rozpadov jadier, ktoré sú predmetom experimentálneho záujmu.

Acknowledgments

I would like to express my deepest gratitude and appreciation to the following individuals, whose unwavering support, guidance, and encouragement have been invaluable throughout my doctoral journey.

First and foremost, I would like to extend my heartfelt gratitude to my Ph.D. supervisor, Prof. RNDr. Fedor Šimkovic, CSc. Your expertise, patience, and commitment to my academic and personal growth have been instrumental in shaping the success of this thesis. Beyond physics, I have learned from you the importance of enjoying and valuing each project. Moreover, I have come to understand that there is no shame in admitting when I do not know something, as it opens the door to learning and growth. I am truly grateful for the knowledge, wisdom, and encouragement you have shared.

I am also grateful to my colleagues and research collaborators who have contributed to my academic development, Prof. Dr. Sabin Stoica, Prof. Dr. Mihai Horoi, Dr. Stefan Ghinescu, Mgr. Rastislav Dvornický, PhD., Mgr. Zuzana Bardačová and Mgr. Eliška Eckerová. The collaborative environment we shared fostered intellectual discussions, which played a significant role in refining my ideas and enhancing the quality of my research.

Finally, I want to express my heartfelt thanks to my loving wife, Dr. Anca Niţescu. Your unwavering support, patience, and understanding during this challenging journey gave me the strength to persevere. I am forever grateful for your unwavering belief in me and for being my pillar of support (T.B.).

Contents

1 Introduction

1.1 Nuclear β-decay

Over the past century, the weak interaction has been one of the most intensely debated topics in physics. Together with electromagnetism, the strong interaction, and gravitation, it is one of the four known fundamental forces of the Standard Model (SM) of particle physics. Today, we understand several unique characteristics of the weak interaction: it is the only force that violates parity symmetry, the only one capable of changing the flavor of quarks and leptons, and it involves mediators with remarkably large masses. Beyond these distinct characteristics, what truly sets the weak interaction apart is its ability to provide tangible ways to test our current understanding of physics through processes such as nuclear β-decay and $\beta\beta$-decay.

Nuclear β-decay is one of the most common types of radioactive decay found in nature as can be seen from Fig. 1.1 which displays the main decay modes of the observed nuclei. It was first theoretically described by Fermi in his seminal 1934 paper on the theory of β-decay [1]. Fermi was trying to describe the following experimentally observed process,

$$(A, Z) \rightarrow (A, Z+1) + e^- + \bar{\nu}_e, \tag{1.1}$$

in which an atomic nucleus with mass number A and atomic number Z undergoes a charge change by one unit, emitting an electron and an antineutrino. Nowadays, nuclear β-decay includes three distinct modes, where one nucleon in the initial nucleus, (A, Z), is transformed as follows

$$\begin{aligned} (A, Z) &\rightarrow (A, Z+1) + e^- + \bar{\nu_e} \quad (\beta^-\text{-decay}), \\ (A, Z) &\rightarrow (A, Z-1) + e^+ + \nu_e \quad (\beta^+\text{-decay}), \\ e^- + (A, Z) &\rightarrow (A, Z-1) + \nu_e \quad (\text{electron capture}). \end{aligned} \tag{1.2}$$

In the electron capture process the capture take place from an atomic bound orbital. The Q-value of each of the process from Eq. (1.2) is defined as the total kinetic energy of the final-state leptons.

These nuclear transitions can be described in the first order perturbation theory by considering the weak interaction β-decay Hamiltonian density,

$$\mathcal{H}_\beta(x) = \frac{G_F \cos\theta_C}{\sqrt{2}} \overline{e}(x)\gamma_\mu(1-\gamma_5)\nu_e(x)j^\mu(x), \tag{1.3}$$

where $e(x)$ and $\nu_e(x)$ are the field operators for the electron and neutrino, respectively, entering the left-handed leptonic current and $j_\mu(x)$ is the hadronic current. Here, G_F is the Fermi coupling constant, $G_F = 1.16637{\times}10^{-5}$ GeV^{-2} and θ_C is the mixing angle of Cabibbo-Kobayashi-Maskawa (CKM) matrix for mixing quark flavors with $\cos\theta_C = 0.97373{\pm}0.00031$ [2]. A detailed derivation from hadronic and leptonic weak-interaction currents is beyond the scope of this thesis. For an in-depth discussion, readers are encouraged to consult the seminal works of Shopper [3] and of Behrens and Bühring [4].

The β-decay nuclear transitions are classified in accordance with the final-state leptons orbital angular momenta. By definition, the $\beta^\pm$-decay is called *allowed* if the final-state leptons are emitted with $l = 0$ (or in a s-state) relative to the nucleus. In the allowed

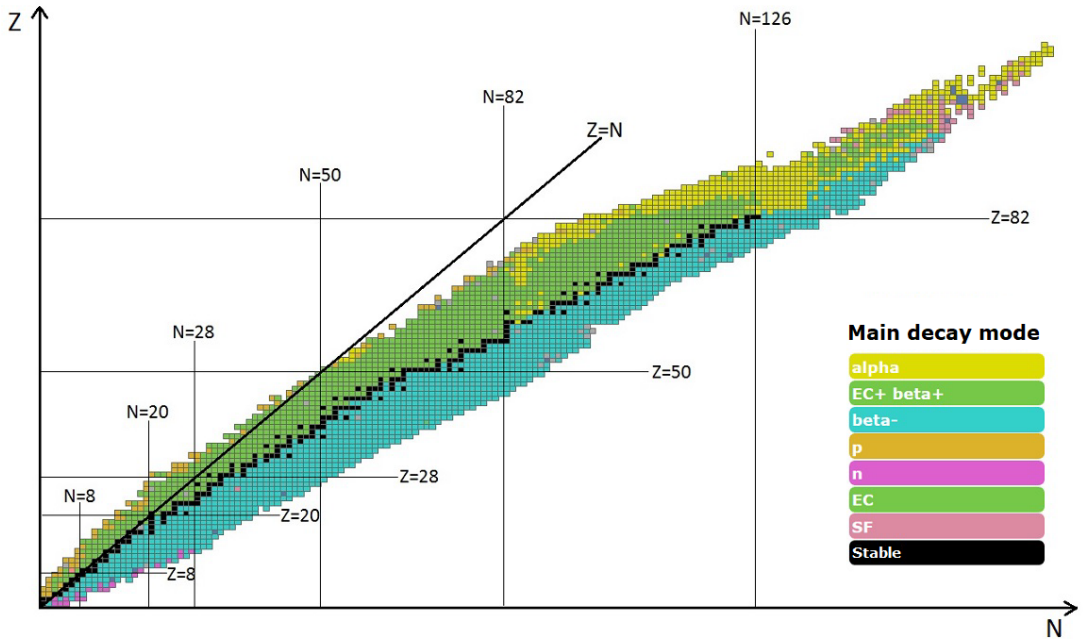

Figure 1.1: The main decay modes for the nuclei observed in nature. The figure was constructed using [5].

electron capture, the atomic electron is captured from a bound s-state of the initial atom. If the final-state particle carries away a non-zero orbital angular momentum, the decays are called *forbidden* transitions, although this terminology can be misleading [3]. If L is the total final state lepton orbital angular momentum and $L > 0$, the transition is called L^{th}*-forbidden* β-decay. In addition, if the change in the total nuclear angular momentum is maximal, the forbidden transition is called *unique-forbidden*, while the others are called *non-unique forbidden* transition.

In addition to the orbital angular momentum, the leptons involved in the decay has spin $s = 1/2$. Thus the final-state particles form $\beta^{\pm}$-decay can couple to total spin $S = 0$ or $S = 1$. In the allowed electron capture, the initial proton and the captured electron can couple to $j \pm 1/2$ and the final neutron and the emitted neutrino can couple to $j \pm 1/2$ or $j \mp 1/2$. The selection rules for allowed β-decay are presented in Table 1.1, where (J_i, π_i) and (J_f, π_f) are the initial and final nuclear total angular momenta and parities. The difference in the total nuclear angular momentum is denoted as $\Delta J = |J_f - J_i|$. The allowed β-decay with $S = 0$ are called *Fermi transitions*, while the ones with $S = 1$ are called *Gamow-Teller transitions*.

In this work, we focus on addressing corrections to the electron spectra for allowed and first unique forbidden transitions. While the separation of the nuclear matrix element and the phase-space factor is not straightforward for non-unique forbidden β-decays [4, 6], this separation can be more easily achieved for allowed and unique forbidden transitions. For

Table 1.1: Classification of allowed β-decay.

Transition	ΔJ	$\pi_f \pi_i$
Fermi	0	+1
Gamow-Teller	1 ($J_i = 0$ or $J_f = 0$)	+1
Gamow-Teller	0,1 ($J_i > 0$,$J_f > 0$)	+1

allowed β-decays, the electron spectrum is proportional to the following product [4]:

$$\frac{d\Gamma}{dE_e} \propto p_e E_e (E_0 - E_e)^2 F_0(Z, E_e), \tag{1.4}$$

where $F_0(Z, E_e)$ is the so-called Fermi function and the term $p_e E_e (E_0 - E_e)^2$ is the statistical phase space factor that reflects the momentum distribution between the neutrino and the electron. Here, E_e is the total energy of the electron, $p_e = \sqrt{E_e^2 - m_e^2}$ is the electron momentum, and $E_0 = Q + m_e$ is the maximum energy of the electron. The Fermi function, which encodes the electrostatic interaction between the electron and the final atom, can be expressed in terms of the large- and small-component radial functions, $\tilde{g}_\kappa(E_e, r)$ and $\tilde{f}_\kappa(E_e, r)$, respectively, of the emitted electron,

$$F_0(Z, E_e) = \frac{\tilde{g}^2_{-1}(E_e, R) + \tilde{f}^2_1(E_e, R)}{j_0(p_e R)\ j_0(p_e R)}, \tag{1.5}$$

evaluated on the nuclear surface of the final nucleus R. The radial functions are discussed in detail in Section A.3. Here, $j_0(p_e r)$ are the spherical Bessel functions.

For unique first forbidden transitions the spectrum is a sum of two contributions associated with emission of electrons in s-state or $p_{3/2}$-state,

$$\begin{aligned} \frac{d\Gamma}{dE_e} &= \frac{d\Gamma^{p_{3/2}}}{dE_e} + \frac{d\Gamma^{s_{1/2}}}{dE_e} \\ &\propto p_e E_e (E_0 - E_e)^2 \left[F_1(Z, E_e) p_e^2 + F_0(Z, E_e)(E_0 - E_e)^2 \right], \end{aligned} \tag{1.6}$$

where the corresponding Fermi function for the $p_{3/2}$-state electrons is

$$F_1(Z, E_e) = \frac{\tilde{g}^2_{-2}(E_e, R) + \tilde{f}^2_2(E_e, R)}{j_1(p_e R)\ j_1(p_e R)}. \tag{1.7}$$

This dissertation investigates specific nuclear β-decay transitions, but it is essential to recognize that nuclear β-decays have played a foundational role in the development of the SM [7] and remain a critical focus of modern physics research [8]. Advancements in experimental techniques have enabled detailed explorations of both SM and beyond Standard Model (BSM) phenomena through nuclear β-decay studies.

Nuclear β-decay provides a rich platform for testing the limits of the SM. It serves as a testing ground for deviations from the pure $V - A$ theory [9], including the potential existence of right-handed currents associated with new heavy particles. Additionally, nuclear β-decay offers a framework for examining Lorentz invariance through sidereal variations in experimental measurements [10]. High-precision measurements of the β spectrum are especially valuable for probing exotic currents beyond the SM's electroweak framework or identifying form factors arising from quantum chromodynamics (QCD) effects [11, 12, 13]. These investigations, by closely analyzing the spectrum's shape and features, can reveal deviations from theoretical predictions, offering insights into the dynamics of weak interactions and the possibility of new physics.

One area of contemporary focus is the study of Fermi allowed transitions, often referred to as super-allowed transitions. These are particularly significant because they provide a highly sensitive means of testing the conserved vector current (CVC) hypothesis and the unitarity of the CKM matrix, which governs quark mixing in the weak interaction. Any deviation observed in super-allowed β-decay measurements could indicate new physics beyond the SM, potentially involving hypothetical particles or interactions absent in the current theoretical framework. Recent comprehensive reviews of these studies are available in [14, 15, 16]. The electron capture (EC) process also holds a critical position in both

fundamental and applied research. It plays a pivotal role in various studies such as neutrino mass scale determination [17, 18, 19], nuclear astrophysics [20], radionuclide metrology [21], and nuclear medicine [22, 23, 24, 25].

Furthermore, nuclear β-decay experiments are important for studying the fundamental properties of neutrinos, including their masses, mixing angles, and potential sterile neutrino components [26, 27, 28]. Such measurements contribute significantly to understanding neutrino oscillations and addressing unresolved questions in neutrino physics, advancing our knowledge of these elusive particles and their role in the universe.

1.2 Nuclear $\beta\beta$-decay

In 1935, about a year after the Fermi weak interaction theory was introduced [1], Goeppert-Mayer considered, at the suggestion of Wigner, the two-neutrino double-beta decay ($2\nu\beta\beta$-decay) [29]:

$$(A, Z) \rightarrow (A, Z+2) + e^- + e^- + \overline{\nu}_e + \overline{\nu}_e. \tag{1.8}$$

In this process, two neutrons in the initial even-even nucleus are converted into two protons while emitting two electrons and two electron antineutrinos. The half-life of $2\nu\beta\beta$-decay was estimated to be 10^{17} years, assuming a Q-value of about 10 MeV [29]. In 1939, after the theory of Majorana neutrinos was introduced [30], Furry proposed the concept of neutrinoless double-beta decay ($0\nu\beta\beta$-decay) [31],

$$(A, Z) \rightarrow (A, Z+2) + e^- + e^-, \tag{1.9}$$

involving two subsequent β-decays of neutrons connected via the exchange of virtual neutrinos [32]. This process is forbidden within the SM as it violates lepton number conservation. Its detection would provide direct evidence of total lepton number violation (LNV) by two units ($\Delta L = 2$), signaling physics beyond the SM. Moreover, such an observation would indicate that neutrinos are Majorana fermions, meaning they are their own antiparticles, as initially proposed by Majorana [30].

For proton-rich nuclei other modes of double-beta decay (DBD) transforming the even-even (A, Z) nucleus into the even-even $(A, Z-2)$ nucleus [33, 34]: the double-positron emitting ($2\nu/0\nu\beta^+\beta^+$) mode, the atomic electron capture with coincident positron emission ($2\nu/0\nu\mathrm{EC}\beta^+$) mode, and the double electron capture ($2\nu/0\nu$ECEC) mode. Each channel has two variants: neutrinoless (0ν) and two-neutrino (2ν) mode, depending on whether the neutrinos are emitted:

$$\begin{aligned}
(A, Z) &\rightarrow (A, Z-2) + e^+ + e^+ + (\nu_e + \nu_e)\,, \\
e_b^- + (A, Z) &\rightarrow (A, Z-2) + e^+ + (\nu_e + \nu_e)\,, \\
e_b^- + e_b^- + (A, Z) &\rightarrow (A, Z-2) + e^+ + e^+ + (\nu_e + \nu_e)\,.
\end{aligned} \tag{1.10}$$

The transitions of proton-rich nuclei are less favored due to smaller Q-value, small overlap of the bound electron wave function with the nucleus, and Coulomb repulsion on positrons. However, compared to $\beta\beta$-decay, $\beta^+\beta^+$ or ECβ^+ modes have clear experimental signatures– at least four or at least two 511 keV γ-rays, respectively, from positrons annihilation with atomic electrons– and coincidence trigger logic might be employed in their detection [35, 36].

The DBD transitions occur whenever the β-decay of the initial nucleus to the intermediate odd-odd nucleus is energetically forbidden or significantly suppressed by angular

momentum selection rules. This suppression is attributed to the enhanced stability of even-even nuclei compared to odd-odd nuclei, resulting from the pairing interaction between nucleons, as illustrated in Figure 1.2.

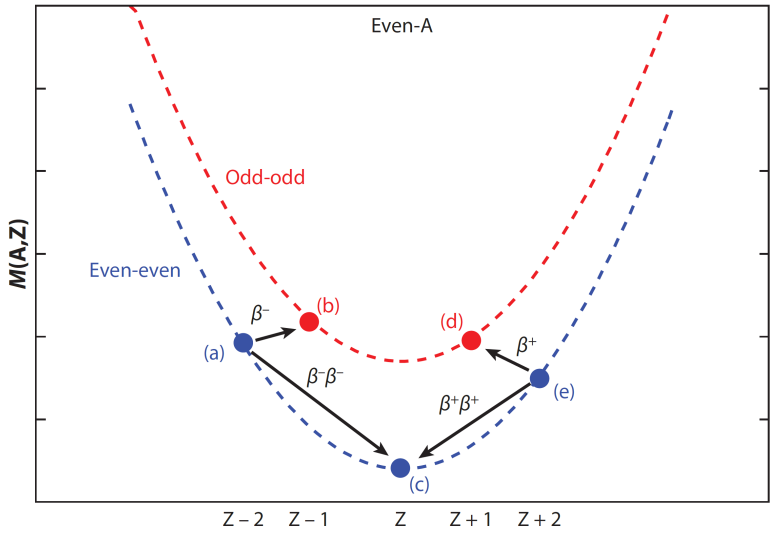

Figure 1.2: The mass parabola of even-even (blue) and odd-odd (red) nuclei. The even-even nuclei are more stable then odd-odd ones. The $\beta\beta$-decay, (a)→(c), is energetically allowed, while β-decay, (a)→(b), is forbidden. Figure is taken from [37].

The first direct observation of $2\nu\beta\beta$-decay, allowed by the SM, was achieved for ^{82}Se in 1987 [38, 39]. Nowadays, the $2\nu\beta\beta$-decay has been detected in direct counter experiments in nine different nuclei, including decays into two excited states. In addition to laboratory experiments, geochemical and radiochemical observations of $2\nu\beta\beta$-decay transitions have been recorded [40] (and references therein). There are also positive indications of the 2νECEC mode for ^{130}Ba and ^{132}Ba from geochemical measurements [41, 42, 43], as well as for ^{78}Kr [44, 45]. Recently, the first direct observation of the 2νECEC process in ^{124}Xe was reported [46, 47, 48, 49]. In Table 1.2 and Table 1.3 we present the most precise experimental half-lives for $2\nu\beta\beta$-decay and for 2νECEC processes, respectively.

From the theoretical point of view, the $2\nu\beta\beta$-decay can be described within the SM as a second-order weak interaction process. Schematically, DBD can be depicted as two consecutive virtual single β-decays. The first virtual β-decay transition occurs from the ground state of the parent nucleus to excited states of an intermediate odd-odd nucleus, while the second transition takes place from the excited states of the intermediate nucleus to either the ground state or excited states of the daughter nucleus. Figure 1.3 illustrates an example of this process specifically for the DBD of ^{100}Mo.

The inverse half-life of the $2\nu\beta\beta$-decay is usually expressed as a product,

$$\left[T^{2\nu}_{1/2}\right]^{-1} = G^{2\nu} g_A^4 \left| M^{2\nu}_{GT} - \left(\frac{g_V}{g_A}\right)^2 M^{2\nu}_{F} \right|^2 , \tag{1.11}$$

between the phase-space factor (PSF), $G^{2\nu}$, and the nuclear matrix element (NME) which contains the double Gamow-Teller (GT) component, $M^{2\nu}_{\mathrm{GT}}$, and Fermi (F) component, $M^{2\nu}_{\mathrm{F}}$. $g_V\,(g_A)$ is the vector (axial-vector) coupling constant. The NMEs for $2\nu\beta\beta$-decay NMEs are given by [63, 64, 65, 66]

Table 1.2: The measured half-lives, in years (yr), for different $2\nu\beta\beta$-decay transition from 0^+ ground state to 0^+ ground state. For the transitions to excited states we consider the recommended values from [40] and the final excited state is indicated in parenthesis near the final nucleus. For ^{128}Te, the experimental half-life is obtained using the ratio $T^{2\nu-\text{exp}}_{1/2}(^{130}\text{Te})/T^{2\nu-\text{exp}}_{1/2}(^{128}\text{Te}) = (3.52 \pm 0.11) \times 10^{-4}$ [50].

$2\nu\beta\beta$-decay	$T^{2\nu}_{1/2}$[yr]
^{48}Ca$\rightarrow^{48}$Ti	$6.4^{+1.3}_{-1.1} \times 10^{19}$[51]
^{76}Ge$\rightarrow^{76}$Se	$2.022^{+0.042}_{-0.042} \times 10^{21}$[52]
^{82}Se$\rightarrow^{82}$Kr	$8.69^{+0.10}_{-0.07} \times 10^{19}$[53]
^{96}Zr$\rightarrow^{96}$Mo	$2.35^{+0.21}_{-0.21} \times 10^{19}$[54]
^{100}Mo$\rightarrow^{100}$Ru	$7.07^{+0.11}_{-0.11} \times 10^{18}$[55]
^{100}Mo$\rightarrow^{100}$Ru (0^+_2)	$6.7^{+0.5}_{-0.4} \times 10^{20}$ [40]
^{116}Cd$\rightarrow^{116}$Sn	$2.63^{+0.11}_{-0.12} \times 10^{19}$[56]
^{128}Te$\rightarrow^{128}$Xe	$2.49^{+0.09}_{-0.09} \times 10^{24}$
^{130}Te$\rightarrow^{130}$Xe	$8.76^{+0.17}_{-0.18} \times 10^{20}$[57, 58]
^{136}Xe$\rightarrow^{136}$Ba	$2.17^{+0.06}_{-0.06} \times 10^{21}$[59]
^{150}Nd$\rightarrow^{150}$Sm	$9.3^{+0.7}_{-0.6} \times 10^{18}$[60]
^{150}Nd$\rightarrow^{150}$Sm (0^+_2)	$1.2^{+0.3}_{-0.2} \times 10^{20}$[40]
^{238}U$\rightarrow^{238}$Pu	$2.0^{+0.6}_{-0.6} \times 10^{21}$[61]

Table 1.3: The measured half-lives, in years (yr), for different 2νECEC transitions. 2νKK means that only the capture from K-orbital have been observed. For ^{130}Ba we consider the recommended value from [40] as the current measurements are geochemical.

2νECEC transition	$T^{2\nu\text{ECEC}}_{1/2}$[yr]
^{78}Kr$\rightarrow^{78}$Se	
2νKK	$1.9^{+1.3}_{-0.8} \times 10^{22}$[45]
^{124}Xe$\rightarrow^{124}$Te	
2νKK	$(1.8 \pm 0.5) \times 10^{22}$ [46]
^{124}Xe$\rightarrow^{124}$Te	
2νECEC	$(1.1 \pm 0.2) \times 10^{22}$ [47]
	$(1.09 \pm 0.15) \times 10^{22}$ [48]
	$(1.03 \pm 0.16) \times 10^{22}$ [49]
^{130}Ba$\rightarrow^{130}$Xe	
2νECEC	$(2.2 \pm 0.5) \times 10^{21}$ [40]

$$M^{2\nu}_{GT,F} = \sum_n \frac{\langle f \| \mathcal{O}_{GT,F} \| J^+_n \rangle \langle J^+_n \| \mathcal{O}_{GT,F} \| i \rangle}{E_n - (E_i + E_f)/2} \tag{1.12}$$

where the operators,

$$\mathcal{O}_{GT} = \sum_{k=1}^{A} \tau^+_k \sigma_k, \quad \mathcal{O}_F = \sum_{k=1}^{A} \tau^+_k, \tag{1.13}$$

are connecting the initial $|i\rangle$ and final $|f\rangle$ states, with energies E_i and E_f, respectively, with the states of the intermediate nucleus $|J^+_n\rangle$ with energies E_n. The summation goes over all possible states of the intermediate odd-odd nucleus, 1^+ states for GT component and 0^+ states for F component. Here τ^+_k is the isospin-raising operator transforming a neutron into a proton, and σ_k is the nucleon spin operator. Due to the reliable approximation of a conservation of isospin in nuclei, the F contribution is typically disregarded in the calculation of NMEs for $2\nu\beta\beta$-decay, and the GT contribution is considered to be dominant.

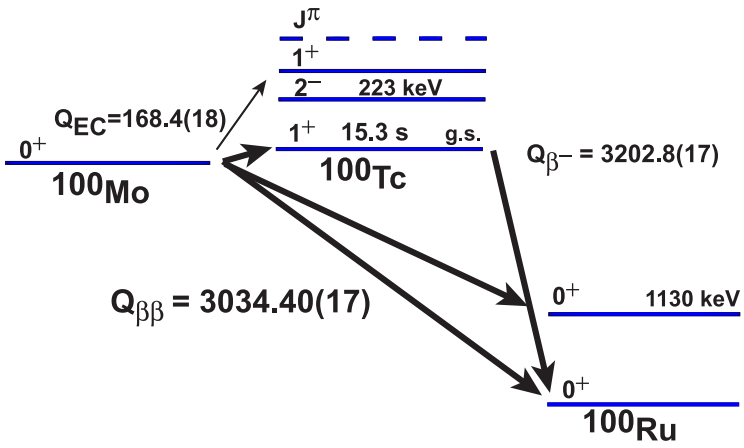

Figure 1.3: The nuclear levels involved in DBD of ^{100}Mo. For the intermediate nucleus, ^{100}Tc, only a few excited states are shown. Figure is reproduced from [62].

For the $0\nu\beta\beta$-decay, if the light neutrino exchange produced by left-handed currents is assumed as the underlying mechanism triggering the decay, the inverse half-life is commonly written as [67],

$$\left[T^{0\nu}_{1/2}\right]^{-1} = G^{0\nu} g_A^4 \left|M^{0\nu}\right|^2 \left(\frac{m_{\beta\beta}}{m_e}\right)^2, \tag{1.14}$$

where $m_{\beta\beta}$ is the effective Majorana neutrino mass. Assuming the exchange of a Majorana neutrino in the standard light-neutrino mechanism of $0\nu\beta\beta$-decay provides a direct link between the effective neutrino mass and the decay rate. Thus, a measurement of the half-life of $0\nu\beta\beta$-decay could provide crucial information about the absolute neutrino mass scale and its ordering. This will be discussed in the following Section.

Beyond the simplest light-neutrino exchange mechanism, various alternative theoretical models predict different exchange mechanisms for $0\nu\beta\beta$-decay [67, 68, 69, 28]. Assuming multiple mechanisms, the inverse half-live of the $0\nu\beta\beta$-decay can be written as [67],

$$\left[T^{0\nu}_{1/2}\right]^{-1} = \sum_i G^{0\nu}_i g_A^4 \left|M^{0\nu}_i\right|^2 \left(\frac{\eta_i}{m_e}\right), \tag{1.15}$$

where the PSFs, $G^{0\nu}_i$, and the NMEs, $M^{0\nu}_i$, are distinct for each mechanism. The lepton number violating parameters (LNVP) η_i serve to differentiate between various mechanisms and in the case of light-neutrino exchange mechanism $\eta \equiv m_{\beta\beta}$. One of the most prominent new physics model that incorporates the LNV is the minimal left-right symmetric model (LRSM) [70], which extends the SM gauge symmetry to the group $\mathrm{SU}(2)_L \otimes \mathrm{SU}(2)_R \otimes \mathrm{U}(1)_{B-L}$. In addition to the left-handed $V-A$ weak currents, the LRSM also includes the leptonic and hadronic right-handed $V+A$ weak currents. This extension allows for multiple $0\nu\beta\beta$-decay mechanisms, including light and heavy Majorana neutrino exchange, both with and without right-handed currents. Beyond these, additional exchange mechanisms may involve sterile neutrinos, neutralinos, and contributions from short-range interactions arising from higher-dimensional operators within effective field theory descriptions of physics beyond the SM. For an overview of various mechanisms that can trigger $0\nu\beta\beta$-decay, see [71, 72, 73, 74].

One of the theoretical challenges in $2\nu\beta\beta$-decay and $0\nu\beta\beta$-decay is the calculation of the NMEs, a long-standing problem in this field. The difficulty arises because the nuclei involved in $\beta\beta$-decay are typically open-shell medium and heavy nuclei with complex structures. Moreover, for the two-neutrino mode, a complete set of 1^+ intermediate nucleus states must

be described, while for the neutrinoless mode, contributions from all multipolarities are required. An overview of the NMEs calculations and predictions is provided in Chapter 8

In addition to NMEs, the precision of observables such as the single and summed energy distributions and angular correlation between the emitted electrons is crucial for understanding various hypothesis in $2\nu\beta\beta$-decay [75, 76] and for unraveling the underlying mechanism driving $0\nu\beta\beta$-decay [77, 73, 78, 79, 80]. Additionally, the SM predictions for the $2\nu\beta\beta$-decay also play an important role in the experimental searches for weakly interacting massive particles (WIMPs) and coherent elastic neutrino-nucleus scattering (CEνNS). In particular, in liquid Xenon experiments, the $2\nu\beta\beta$-decay of ^{136}Xe represents an inevitable source of background. Therefore, precise theoretical predictions for $2\nu\beta\beta$-decay are necessary for several upcoming experiments aiming to detect WIMPs and CEνNS [81, 82, 83, 84].

The eager search for the hypothetical $0\nu\beta\beta$-decay [85] translates into rich statistics for $2\nu\beta\beta$ events. This is primarily due to the role played by the $2\nu\beta\beta$-decay spectrum as a background for the expected $0\nu\beta\beta$-decay signal. The growing statistics for the $2\nu\beta\beta$-decay make the exploration of new physics BSM possible. Three fundamental concepts have been employed in the BSM models that extend the $2\nu\beta\beta$-decay [86]: (i) non-standard interactions, (ii) violation of fundamental symmetries, and (iii) emission of new bosons or fermions emitted in the decay. Today, these models include the exploration of right-handed neutrino interactions [87], neutrino self-interaction [88], violation of the Pauli exclusion principle [89], violation of Lorentz invariance [90, 91, 92, 93], sterile neutrinos with masses up to the Q-value of the process [94, 95], $0\nu\beta\beta$ decays with Majoron(s) emission [96, 97, 98, 99, 100, 101, 102, 103, 104, 105, 106], and quadruple-β-decay [107].

The current experimental constraints on various strength parameters associated with the BSM models are obtained by analyzing the shape of the summed electron energy distribution of $2\nu\beta\beta$-decay [86]. However, the most striking signatures in many BSM scenarios are expected in the angular correlation distributions between the emitted electrons [87, 88, 94, 89, 92, 93, 105, 104]. A notable example is the direction flip in the emission of electrons when right-handed currents are included in $2\nu\beta\beta$-decay [87]. Fortunately, the concept of tracking individual electrons [108] is also actively pursued in next-generation experiments such as SuperNEMO [109] and NEXT-100 [110]. The tracking capability will provide valuable insights into the underlying mechanism of $0\nu\beta\beta$-decay [77, 73, 72, 79, 80], if observed, and will strongly enhance the sensitivity to BSM scenarios in $2\nu\beta\beta$-decay.

1.3 Neutrino mass measurements

Early measurements of neutrinos produced in the sun, atmosphere, and accelerators hinted at the possibility of neutrino oscillations, where neutrinos transition between different "flavors" (electron, muon, and tau). Such oscillations imply non-zero neutrino masses. Starting in 1998, compelling evidence for neutrino oscillations emerged through observations from Super-Kamiokande [111, 112, 113, 114], SNO [115, 116, 117, 118, 119, 120, 121], KamLAND [122], and several other experiments. Nowadays, these oscillations are analyzed within the minimal three-neutrino framework. This model considers that the known flavors states $(\nu_e, \nu_\mu, \nu_\tau)$ are quantum superpositions of three massive states ν_k with masses m_k $(k = 1, 2, 3)$, i.e.,

$$\nu_\alpha = \sum_{k=1}^{3} U^*_{\alpha k} \nu_k, \quad \text{with} \quad \alpha = e, \mu, \tau. \tag{1.16}$$

For Dirac neutrinos, the unitary Pontecorvo-Maki-Nakagawa-Sakata (PMNS) neutrino mixing matrix can be written as,

$$U = R_{23}\tilde{R}_{13}R_{12}, \tag{1.17}$$

where

$$\begin{aligned} R_{23} &= \begin{pmatrix} 1 & 0 & 0 \\ 0 & c_{23} & s_{23} \\ 0 & -s_{23} & c_{23} \end{pmatrix}, \qquad R_{12} = \begin{pmatrix} c_{12} & s_{12} & 0 \\ -s_{12} & c_{12} & 0 \\ 0 & 0 & 1 \end{pmatrix}, \\ \tilde{R}_{13} &= \begin{pmatrix} c_{13} & 0 & s_{13}\exp(-i\delta) \\ 0 & 1 & 0 \\ -s_{13}\exp(i\delta) & 0 & c_{13} \end{pmatrix}. \end{aligned} \tag{1.18}$$

Here, $s_{ij} = \sin(\theta_{ij})$ and $c_{ij} = \cos(\theta_{ij})$ for the mixing angles θ_{ij} and δ is the charge-parity (CP) phase. For Majorana neutrinos the PMNS neutrino mixing matrix from Eq. (1.17) must be multiplied the the diagonal P matrix defined as,

$$P = \begin{pmatrix} \exp(i\alpha_1) & 0 & 0 \\ 0 & \exp(i\alpha_2) & 0 \\ 0 & 0 & 1 \end{pmatrix} \tag{1.19}$$

where additional phases, α_1 and α_2, are the so-called Majorana phases.

If only three neutrino masses are assumed, the data from neutrino oscillation experiments constrain three mixing angles, i.e., θ_{12}, θ_{23}, and θ_{13}, the CP-violating phase, and two independent mass-squared differences [123],

$$\delta m^2 = m_2^2 - m_1^2, \qquad \Delta m^2 = m_3^2 - (m_1^2 + m_2^2)/2. \tag{1.20}$$

Under these conditions, two types of mass spectra (or mass ordering) are possible:

- Normal Ordering (NO): In this scenario, the mass eigenstates are arranged such that $m_1 < m_2 < m_3$ and $\Delta m^2 > 0$. In this case,

$$m_2 = \sqrt{\delta m^2 + m_{\text{lightest}}^2}, \qquad m_3 = \sqrt{\Delta m^2 + \frac{\delta m^2}{2} + m_{\text{lightest}}^2}, \tag{1.21}$$

  where $m_{\text{lightest}} = m_1$.

- Inverted Ordering (IO): In this scenario, the mass eigenstates are arranged such that $m_3 < m_1 < m_2$ and $\Delta m^2 < 0$. In this case,

$$m_1 = \sqrt{-\Delta m^2 - \frac{\delta m^2}{2} + m_{\text{lightest}}^2}, \qquad m_2 = \sqrt{-\Delta m^2 + \frac{\delta m^2}{2} + m_{\text{lightest}}^2}, \tag{1.22}$$

  where $m_{\text{lightest}} = m_3$.

Additional information about neutrino masses is needed to fully determine the three light neutrino masses, which would provide the absolute neutrino mass scale. This information might be obtained through direct measurements of neutrino mass in tritium β-decay, the observation of $0\nu\beta\beta$-decay, or cosmological measurements. However, none of these experiments currently possess the necessary sensitivity to achieve the required results.

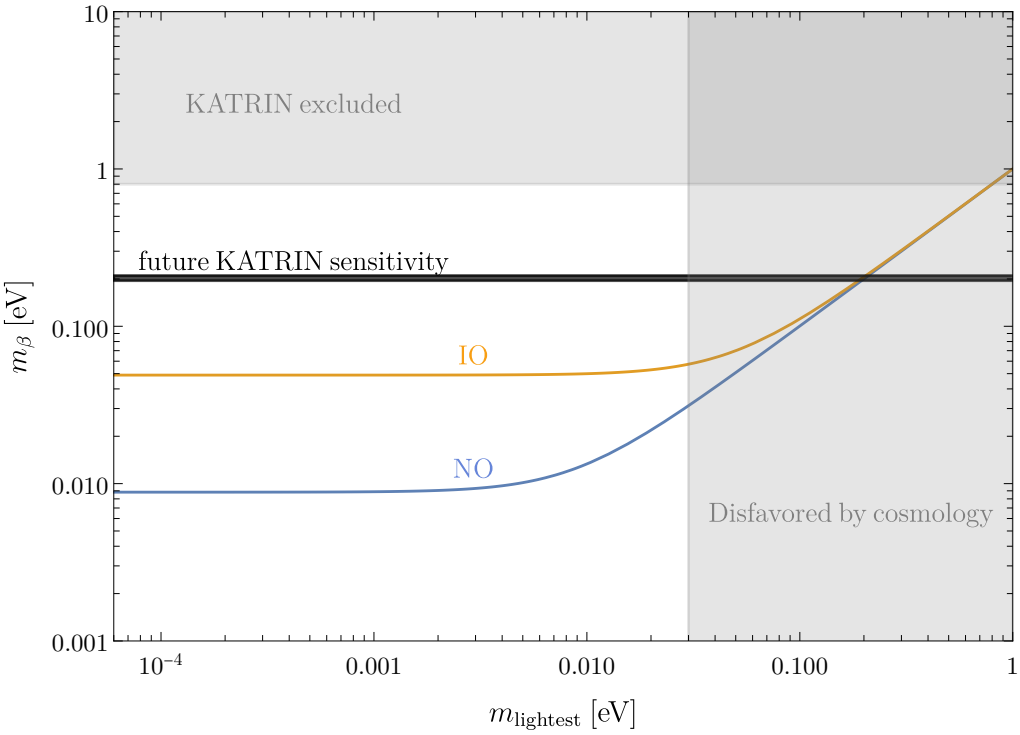

Figure 1.4: The effective neutrino mass, m_β measured from the β-decay as a function of the lightest neutrino mass, m_{lightest}. The function is presented for normal ordering (blue) and inverted ordering (orange). The best fit values for the neutrino oscillation parameters are adopted from [123]. The lowest limit from KATRIN [124] ($m_\beta < 0.8$ eV) and the exclusion from cosmology [125, 126] ($m_{\text{lightest}} < 30$ meV for NO scenario from $\sum_k m_k < 0.12$ eV) are displayed in the gray boxes. The future KATRIN sensitivity ($m_\beta < 0.2$ eV) is shown in black.

The distortion in the endpoint measurements of the spectrum of electrons emitted in a β-decay offers a direct means of determining the absolute neutrino mass scale. However, the number of events emitted near the endpoint, within an interval ΔT_e, is proportional to $(\Delta T_e/Q)^3$ [127, 128]. Therefore, a low Q-value β transition is desirable to enhance sensitivity. Consequently, some experiments are based on the ground-state to ground-state β-decays of tritium (^{3}H) and rhenium (^{187}Re) with Q-values of 18592.01(7) eV [129] and 2470.9(13) eV [130], respectively. Other experiments, such as HOLMES [17], NuMECs [18], and ECHo [19], aim to use the lowest energy electron capture of ^{163}Ho, which has a ground-state to ground-state Q-value of 2.833 keV [131]. Recently, there has also been a growing interest in ultra-low Q-value (under 1 keV) ground-state-to-excited-state β transitions [132, 133, 134], which represent potential candidates for future neutrino mass scale determination experiments.

The current best upper limit on effective neutrino mass from β-decay,

$$m_\beta = \sqrt{\sum_{k=1}^{3} |U_{ek}|^2 \, m_k^2} \tag{1.23}$$

was recently fixed from the tritium β-decay, measured by the KATRIN experiment [124], $m_\beta \leqslant 0.8$ eV. This limit far exceeds the previous investigations by Troitsk experiment, $m_\beta \leqslant 2.2$ eV [135], and Mainz experiment, $m_\beta \leqslant 2.3$ eV [136], also based on tritium β-decay. Even more recently, Project 8 has demonstrated that cyclotron radiation emission

spectroscopy (CRES) can constrain $m_\beta \leq 155$ eV from the tritium β spectrum using only a cm^3-scale physical detection medium [137]. This suggests that CRES is an attractive technique for next-generation direct neutrino mass experiments and for measuring the β spectra in general. In Fig. 1.4, m_β is displayed as a function of the lightest neutrino eigenstate. The current best upper limit and the future sensitivity of KATRIN experiment is also shown. We note that on the region disfavored by cosmology measurements, m_β is quite different depending on the ordering. It should be noted that the cosmological limit from Fig. 1.4 assumes the normal hierarchy of neutrino masses.

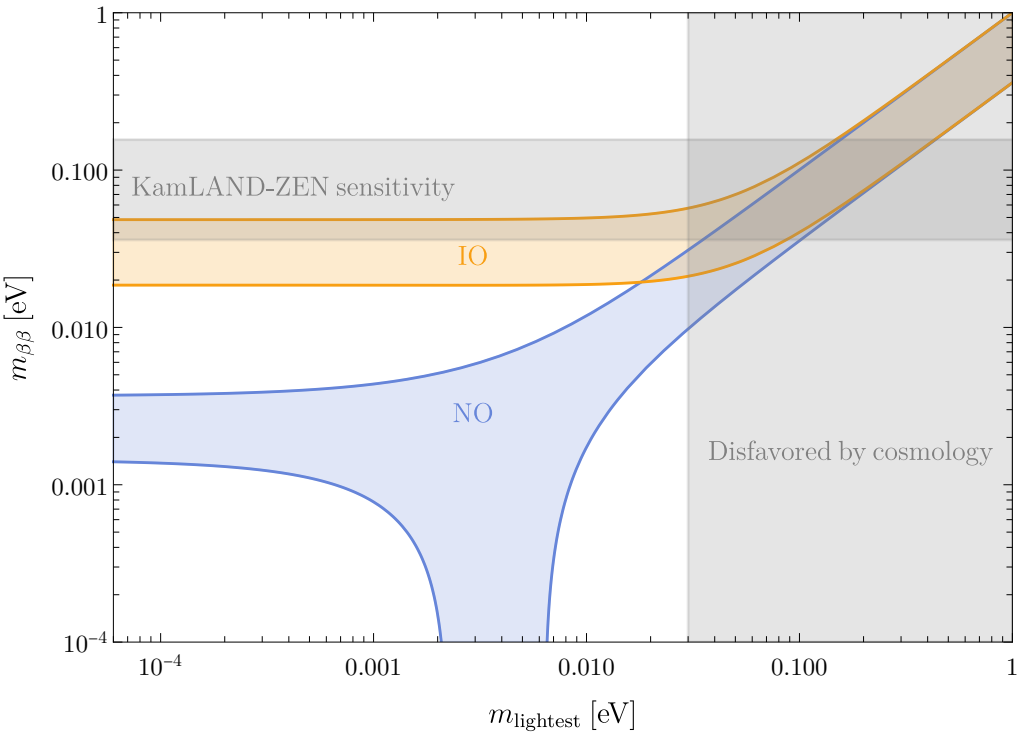

Figure 1.5: The effective Majorana mass $m_{\beta\beta}$ as a function of the lightest neutrino mass, m_{lightest}. The function is presented for normal ordering (blue) and inverted ordering (orange). The best fit values for the neutrino oscillation parameters are adopted from [123]. The domains are obtained with the variation of the Majorana phases. The most stringent limit achieved by KamLAND-ZEN collaboration [138] ($m_{\beta\beta} < 36 - 156$ meV) and the exclusion from cosmology [125, 126] ($m_{\text{lightest}} < 30$ meV for NO scenario from $\sum_k m_k < 0.12$ eV) are displayed in the gray.

Although the most direct method for assessing neutrino mass involves the kinematics of single β transitions and electron capture processes, valuable insights can also be derived from cosmological observations and $0\nu\beta\beta$ decay. Recent cosmological studies have provided an upper limit for the sum of neutrino masses, which is approximately 0.12 eV, i.e., $\sum_k m_k < 0.12$ eV [125, 126]. However, it is important to note that these limits rely on the specific cosmological assumptions employed [139, 140]. The lower limit of the half-life for $0\nu\beta\beta$ can also be used to establish an upper limit of the effective neutrino mass from $0\nu\beta\beta$-decay,

$$m_{\beta\beta} = \left| \sum_{k=1}^{3} U_{ek}^2 m_k \right|. \tag{1.24}$$

also known as the effective Majorana mass. Its behavior is more complicated as a function

Table 1.4: The best limits on $T^{0\nu}_{1/2}$ at 90% confidence level for different isotopes and the limits obtained for the effective Majorana mass. We adopt data from [85].

$0\nu\beta\beta$-decay	$T^{0\nu}_{1/2}$[yr]	$m_{\beta\beta}$ [eV]
^{48}Ca$\rightarrow^{48}$Ti	$> 5.8 \times 10^{22}$	$< 3.5 - 22$
^{76}Ge$\rightarrow^{76}$Se	$> 1.8 \times 10^{26}$	$< 0.079 - 0.180$
^{82}Se$\rightarrow^{82}$Kr	$> 4.6 \times 10^{24}$	$< 0.263 - 0.545$
^{96}Zr$\rightarrow^{96}$Mo	$> 9.2 \times 10^{21}$	$< 3.9 - 19.5$
^{100}Mo$\rightarrow^{100}$Ru	$> 1.8 \times 10^{24}$	$< 0.28 - 0.49$
^{116}Cd$\rightarrow^{116}$Sn	$> 2.2 \times 10^{23}$	$< 1.0 - 1.7$
^{128}Te$\rightarrow^{128}$Xe	$> 3.6 \times 10^{24}$	$< 1.5 - 4.0$
^{130}Te$\rightarrow^{130}$Xe	$> 2.2 \times 10^{25}$	$< 0.090 - 0.305$
^{136}Xe$\rightarrow^{136}$Ba	$> 2.3 \times 10^{26}$	$< 0.036 - 0.156$
^{150}Nd$\rightarrow^{150}$Sm	$> 2 \times 10^{22}$	$< 1.6 - 5.3$

of the lightest neutrino eigenstate as can be seen in Fig. 1.5. For inverted ordering $m_{\beta\beta}$ is in the range of tens of meV or larger. For normal ordering $m_{\beta\beta}$ is smaller, in the range of a few meV, but it can also be strongly suppressed when 2 meV $< m_{\text{lightest}} <$ 6 meV. As in Fig. 1.4, the cosmological limit presented in Fig. 1.5 is obtained assuming the normal hierarchy of neutrino masses.

The latest lower limits on $T^{0\nu}_{1/2}$ for various isotopes, along with the corresponding $m_{\beta\beta}$ upper limits, are presented in Table 1.4. The data are taken from [85]. The most stringent current limits are $m_{\beta\beta} < 79 - 180$ meV [141] (^{76}Ge), $m_{\beta\beta} < 90 - 305$ meV [142] (^{130}Te) and $m_{\beta\beta} < 36 - 156$ meV [138] (^{136}Xe). The provided intervals are associated with the ranges of model-dependent nuclear matrix element calculations. It is important to mention that these limits are applicable under the assumptions that neutrinos are Majorana particles (meaning they are their own antiparticles) and that the light-neutrino mechanism is responsible for driving $0\nu\beta\beta$-decay.

2 Main aims of the thesis

The main goal of the Ph.D. thesis is to revisit and further progress in the understanding of different nuclear and atomic corrections for nuclear β and $2\nu\beta\beta$-decay. The implications of those corrections in neutrino physics are of crucial importance. The main tasks of the dissertation thesis are presented below.

1. **Re-examining the atomic exchange correction in β-decay**

   Recently, the exchange correction was calculated for the nuclear β-decay of ^{45}Ca, ^{63}Ni, ^{85}Kr, ^{212}Pb, ^{214}Pb and ^{241}Pu [143, 144, 8, 145]. Although there is an increasing interest in the field, emerged from the new experimental measurements of the low energy β-decay, it seems that the exchange correction function has a completely different behavior than the recent measurements. We aim to re-examine the exchange correction for those β transitions and bring light to this ambiguity. On this part we focus on allowed β-decays transitions, but the results are extended to unique forbidden transitions in a subsequent part of the thesis. We will also investigate if the β-decay spectra including the reexamined exchange correction is in agreement with the experimental data for ^{67}Ni, ^{151}Sm and ^{210}Pb.

   Dealing with the exchange correction for nuclear β-decay requires precise knowledge of the wave functions of the bound electrons for the initial and final atom and the continuum wave function of the emitted electron from β-decay. We aim to develop the electrostatic potential for the initial and final atom with the Dirac-Hartree-Fock-Slater self-consistent method, which provides through the most reliable binding energies compared to the experimental values. For the continuum wave function of the β electron, the Dirac equation will be solved in the Dirac-Hartree-Fock-Slater potential for the final atom but modified to fulfill the asymptotic requirement for a scattering process.

   The exchange correction is expressed in terms of the overlaps between the initial atom's bound states and the final atom's continuum states. In the computation of the exchange correction, special care will be addressed to the integration procedure for the overlaps, which are fast oscillating functions. Furthermore, the orthogonalization of bound and continuum states of the final system will be investigated.

2. **Accurate energy distributions in the β-decay of ^{187}Re for neutrino mass measurement**

   Experimental efforts to achieve sub-eV sensitivity to the neutrino mass through the β spectrum of rhenium culminated in the collaboration between the MANU and MIBETA groups, forming the Microcalorimeter Arrays for a Rhenium Experiment (MARE) [146]. However, the MARE project eventually transitioned to holmium-based experiments like ECHo and HOLMES [147]. One possible reason for this shift is the limited theoretical understanding of the rhenium β spectrum, especially when compared to the comprehensive theoretical corrections available for tritium β-decay. Tritium decay benefits from a detailed theoretical framework, including corrections for screening, atomic exchange, finite nuclear size, radiative effects, and recoil [148, 149].

   This work aims to advance the theoretical description of ^{187}Re β-decay by incorporating all relevant corrections to its spectrum. The study begins by employing the same relativistic wave functions for emitted electrons as in our previous work

[128]. Building on this foundation, the theoretical precision of the rhenium decay spectrum will be enhanced by including corrections for finite nuclear size, diffuse nuclear surface, and screening effects. Screening will be calculated using the self-consistent Dirac-Hartree-Fock-Slater method, which accurately describes the atomic bound electrons surrounding the emitted electron during the decay process.

Additionally, this study aims to include the atomic exchange correction in the β-decay spectrum of ^{187}Re. The potential implications of these corrections on neutrino mass measurements using ^{187}Re will also be discussed, providing insights that could address the gaps in theoretical knowledge and potentially revitalize interest in rhenium-based neutrino mass experiments.

3. **Improved formalism for $2\nu\beta\beta$-decay and 2νECEC process**

   With the increasing data availability for the $2\nu\beta\beta$-decay mode, it is becoming feasible to place constraints on various BSM parameters by analyzing the experimental electron spectrum. Traditionally, the theoretical description of this process excluded the dependence of lepton energies in the energy denominators of NMEs. However, significant advancements in the theoretical framework for $2\nu\beta\beta$-decay observables have been achieved by incorporating this dependence [78].

   The aim of this work is to further extend the Taylor expansion formalism for $2\nu\beta\beta$-decay by including the often-neglected Fermi component of the NMEs. Additionally, the formalism will be expanded to describe $2\nu\beta\beta$-decay transitions from 0^+ to 2^+ states and the 2νECEC process. Predicted half-lives for transitions to excited states will be compared against recent experimental results.

   To enhance the precision of $2\nu\beta\beta$-decay observables, this study will apply the DHFS model, initially developed for β-decay, to describe the emitted electrons. Atomic exchange and radiative corrections will also be incorporated. For radiative corrections, contributions from both virtual photon exchange and real photon emission during $2\nu\beta\beta$-decay will be accounted for. These corrections will be integrated into the Taylor expansion formalism for transitions to both ground and excited states.

   For 2νECEC, the thesis aims to consider all s-wave electrons available for capture, extending beyond the K and L_1 orbitals typically included in earlier studies. The DHFS self-consistent method will be employed to describe the bound states of the captured electrons, offering a more realistic treatment of atomic screening and more accurate binding energies compared to prior investigations. Moreover, special attention will be given to the 2νECEC process in ^{124}Xe, the only isotope for which a half-life has been experimentally measured.

4. **The angular correlation between the electrons emitted in $2\nu\beta\beta$-decay and $0\nu\beta\beta$-decay**

   The current experimental constraints on various strength parameters associated with the BSM models are obtained by analyzing the shape of the summed electron energy distribution of $2\nu\beta\beta$-decay. However, the most striking signatures in many BSM scenarios are expected in the angular correlation distributions between the emitted electrons. A notable example is the direction flip in the emission of electrons when right-handed currents are included in $2\nu\beta\beta$-decay. Fortunately, the concept of tracking individual electrons [108] is also actively pursued in next-generation experiments such as SuperNEMO [109] and NEXT-100 [110].

   We aim to investigate if the phase shifts of the wave functions for the emitted electrons in $2\nu\beta\beta$-decay and $0\nu\beta\beta$-decay have any influence in the calculation of

the angular correlation factors or angular correlation distributions. Additionally, for $2\nu\beta\beta$-decay, we aim to develop the angular correlations expressions in the Taylor expansion formalism.

5. **A semi-empirical formula for two-neutrino DBD**

   A novel semi-empirical framework will be introduced to describe the $2\nu\beta\beta$ NMEs derived from experimental half-lives. This framework will incorporate key nuclear properties, including the number of protons and neutrons, pairing effects, isospin, and nuclear deformation degrees of freedom. A detailed comparison will be conducted with systematic $2\nu\beta\beta$ NME calculations performed using nuclear models. Additionally, the framework will provide predictions for the observation of new $2\nu\beta\beta$-decay transitions, offering valuable guidance for future experimental investigations.

3 Re-examining the atomic exchange correction in β-decay

In this Chapter, we revisit the calculation of the atomic exchange correction for β^--decay. Recently, this correction has been computed for the nuclear β-decay of ^{45}Ca, ^{63}Ni, ^{85}Kr, ^{212}Pb, ^{214}Pb, and ^{241}Pu [143, 144, 8, 145]. Despite the growing interest in this field, it appears that the recent exchange correction calculations exhibits a markedly different behavior compared to the earlier calculations [150, 151] and can not explain the recent experimental measurements in the low-energy region of the β-decay spectrum.

We demonstrate that the discrepancy in recent calculations arises from the omission of orthogonality between continuum and bound electron states within the potential of the final atom. By imposing this orthogonality condition using a modified DHFS self-consistent method, we observed significant differences in both the magnitude and energy dependence of the correction compared to previous results. Our findings suggest that this approach can resolve the mismatch between theoretical predictions and experimental measurements in the low-energy region of the electron spectrum. Furthermore, we provide an analytical expression for the atomic exchange correction applicable to a wide range of β emitters, spanning Z values from 1 to 102. The results for the β-decay of ^{151}Sm are discussed in detail, along with recent experimental validations of our model.

3.1 Introduction

The main atomic effects influencing the β spectrum stem from the screening of the β particle's wave function by the atomic electron cloud, the exchange between emitted and bound electrons, and the sudden change in nuclear charge. The latter effect can result in internal ionization (shake-off) or atomic excitations (shake-up), though its overall impact is typically limited to less than 0.1%. In contrast, the screening and exchange corrections can have a pronounced effect on the β spectrum shape and decay rate, particularly for low-energy transitions, such as those with low Q-values. The exchange correction arises when a β electron is created in a bound orbital of the final atom, corresponding to one that was occupied in the initial atom, while an atomic electron transitions from a bound orbital to a continuum orbital in the final atom.

The study of the exchange correction began in 1962 with Bahcall's seminal work [152], which focused exclusively on the exchange of emitted electrons from an allowed β-decay with bound electrons in the $1s$ orbital. This approximation resulted in a reduced emission probability at low energies. Two decades later, Haxton demonstrated that the exchange correction for tritium β-decay instead enhances the emission probability at low energies [153], a conclusion consistent with experimental observations. This enhancement at low energy was further corroborated by Harston and Pyper [150, 151] in their studies of various nuclear β-decays, including the allowed β transitions of ^{14}C, ^{35}S, and ^{106}Ru, as well as the non-unique first forbidden β transition of ^{241}Pu. It is noteworthy that certain non-unique first forbidden β-decays, such as that of ^{241}Pu, can be approximated as allowed transitions when $2\xi = \alpha Z/2R \gg E_0$ [154]. Here, ξ is a parameter defined by the final nucleus's radius R, nuclear charge Z, the fine structure constant α, and the transition's maximum energy E_0.

The exchange correction has recently been revisited for the non-unique first forbidden β-decay of ^{241}Pu [143]. While the wave functions for the emitted and bound electrons were

derived as analytical solutions of the Dirac equation under the hydrogenic approximation, as provided by Rose [155], it became evident that incorporating the exchange correction yielded an electron spectrum in better agreement with experimental data. These results for ^{241}Pu were later refined using more sophisticated wave functions in [144], which also included a study of the allowed β transition of ^{63}Ni. Further investigations into exchange corrections for β-decays, including those of ^{45}Ca and ^{241}Pu, are detailed in a comprehensive review of analytical corrections for allowed β-decays [8]. Beyond improving agreement with experimental spectra, the exchange effect plays a crucial role in excluding background β events in sensitive experimental setups such as LUX-ZEPLIN [82], XENONnT [81], and XENON1T [156]. In this context, atomic exchange corrections have been examined for the unique first forbidden transition of ^{85}Kr and the non-unique first forbidden transitions of ^{212}Pb and ^{214}Pb [145]. Despite growing interest in theoretical advancements, a mismatch with the experimental electron spectrum in the low-energy region persists.

Given the growing interest in the field and the enhanced experimental capabilities for measuring the low-energy region of β spectra, such as those enabled by metallic magnetic calorimeters (MMCs) [157, 158, 159], we revisit the calculation of the exchange effect. For the electron wave functions, we adopt a modified Dirac-Hartree-Fock-Slater self-consistent method, ensuring orthogonality between the continuum and bound electron states in the potential of the final atom. We found that the lack of orthogonality between these states in the final atom introduces errors in the overlaps with the initial atom's bound states, resulting in an underestimation of the total exchange correction.

We provide detailed calculations for the β-decays of ^{14}C, ^{45}Ca, ^{63}Ni, and ^{241}Pu, as well as for a broad range of β emitters with atomic numbers $Z = 1$ to 102. Except in the low-energy region, the total exchange correction increases progressively with the nuclear charge. However, even for $Z = 100$, the total exchange effect remains below 1% at a kinetic energy of 200 keV, rendering the correction negligible beyond this point depending on the desired accuracy. Additionally, we examine the partial contributions from orbitals beyond the $2s_{1/2}$ orbital and their impact on the total exchange correction. These contributions are especially significant for heavier atoms but diminish with increasing electron energy. Lastly, we provide an analytical expression for the total exchange correction as a function of the atomic number, facilitating straightforward implementation in experimental analyses.

3.2 Formalism for allowed β-decay

The electron spectrum for a nuclear β-decay is proportional with [4]

$$\frac{d\Gamma}{dE_e} \propto p_e E_e (E_0 - E_e)^2 F_0(Z', E_e) C(E_e), \tag{3.1}$$

where the term $p_e E_e (E_0 - E_e)^2$ is related to the statistical phase space factor that reflects the momentum distribution between the neutrino and the electron, $F_0(Z', E_e)$ is the so-called Fermi function and the shape factor, $C(E_e)$, contains the nuclear matrix elements and all the possible remaining terms dependent on lepton energy. Here E_e is the total energy of the electron, $p_e = \sqrt{E_e^2 - m_e^2}$ is the momentum of the electron, $E_0 = Q + m_e$ is its maximum energy and Z' is the atomic number of the final nucleus.

The Fermi function, which encodes the electrostatic interaction between the electron and the final atom, can be expressed in terms of the large- and small-component radial functions, $g'_\kappa(E_e, r)$ and $f'_\kappa(E_e, r)$ of the emitted electron,

$$F_0(Z', E_e) = g'^2_{-1}(E_e, R) + f'^2_{+1}(E_e, R), \tag{3.2}$$

evaluated on the nuclear surface of the final nucleus. The radial components of the continuum states and their normalization are discussed in Section A.3. A widely used approximation for the Fermi function is obtained by keeping the lowest power of the expansion in r of the radial wave functions corresponding to a uniformly charged sphere potential [63]

$$F_{k-1}(Z', E_e) = \left[\frac{\Gamma(2k+1)}{\Gamma(k)\Gamma(2\gamma_k+1)}\right]^2 (2pR)^{2(\gamma_k-k)} e^{\pi\eta} \left|\Gamma(\gamma_k + i\eta)\right|^2, \tag{3.3}$$

with $k = 1$ for allowed β transitions. The remaining quantities are detailed in in Section A.3. It is important to note that the phase shifts of the electron wave functions do not influence the calculation of the exchange correction. Therefore, we can write the expressions only with the real parts of the radial components.

For allowed transitions, the shape factor is not energy dependent, so their spectra are proportional with

$$\frac{d\Gamma}{dE_e} \propto p_e E_e (E_0 - E_e)^2 F_0(Z', E_e). \tag{3.4}$$

The modification of the allowed spectrum due to the exchange correction is given by the following transformation [150, 151]

$$\frac{d\Gamma}{dE_e} \Rightarrow \frac{d\Gamma}{dE_e} \times \left[1 + \eta^T(E_e)\right] \tag{3.5}$$

where

$$\begin{aligned} \eta^T(E_e) &= f_s(2T_s + T_s^2) + (1 - f_s)(2T_{\bar{p}} + T_{\bar{p}}^2) \\ &= \eta_s(E_e) + \eta_{\bar{p}}(E_e) \end{aligned} \tag{3.6}$$

Here,

$$f_s = \frac{g'^2_{-1}(E_e, R)}{g'^2_{-1}(E_e, R) + f'^2_{+1}(E_e, R)}, \tag{3.7}$$

and the quantities T_s and $T_{\bar{p}}$ depend respectively on the overlaps between the bound $s_{1/2}$ ($\kappa = -1$) and $\bar{p} \equiv p_{1/2}$ ($\kappa = 1$) orbitals wave functions in the initial state atom and the continuum states wave functions in the final state atom,

$$T_s = \sum_{(ns)'} T_{ns} = -\sum_{(ns)'} \frac{\langle \psi'_{E_e s} | \psi_{ns} \rangle}{\langle \psi'_{ns} | \psi_{ns} \rangle} \frac{g'_{n,-1}(R)}{g'_{-1}(E_e, R)} \tag{3.8}$$

and

$$T_{\bar{p}} = \sum_{(n\bar{p})'} T_{n\bar{p}} = -\sum_{(n\bar{p})'} \frac{\left\langle \psi'_{E_e \bar{p}} \middle| \psi_{n\bar{p}} \right\rangle}{\left\langle \psi'_{n\bar{p}} \middle| \psi_{n\bar{p}} \right\rangle} \frac{f'_{n,+1}(R)}{f'_{+1}(E_e, R)}. \tag{3.9}$$

The summations extend over all occupied orbitals of the final atom, which correspond to the parent electronic configuration under the sudden approximation. The radial components of the bound states, $g_{n,\kappa}(r)$ and $f_{n,\kappa}(r)$, are detailed in Section A.2. All primed wave functions pertain to the final atom.

According to the definition of the quantities T_s and $T_{\bar{p}}$, we can write

$$\eta_s(E_e) = \sum_n \eta_{ns} + f_s \sum_{\substack{n,m \\ n\neq m}} T_{ns} T_{ms} \tag{3.10}$$

and

$$\eta_{\bar{p}}(E_e) = \sum_n \eta_{n\bar{p}} + (1 - f_s) \sum_{\substack{n,m \\ n\neq m}} T_{n\bar{p}} T_{m\bar{p}} \tag{3.11}$$

Here we defined the partial exchange correction of nth s orbital and nth $\bar{p}$ orbital as,

$$\eta_{ns} = f_s(2T_{ns} + T_{ns}^2) \tag{3.12}$$

and

$$\eta_{n\bar{p}} = (1 - f_s)(2T_{n\bar{p}} + T_{n\bar{p}}^2), \tag{3.13}$$

respectively.

While the contribution from the exchange with $p_{1/2}$ orbitals, $\eta_{\bar{p}}(E_e)$, is relatively small, it should not be overlooked when striving for high precision [8]. Depending on the specific context, the $p_{1/2}$ contribution has either been excluded [150, 143, 144] or included [8, 145]. Additionally, the mixed sum in Eq. (3.10) was disregarded in [150] on the grounds that its impact on $\eta_s(E_e)$ is minimal. While this approximation is justified for high energies, the mixed sum can contribute approximately $1 - 3\%$ for kinetic energies below 1 keV [143].

The critical elements in calculating the exchange correction are the overlaps between the bound orbital electron wave functions in the initial atom and the continuum state electron wave function, with energy E_e, in the final atom, $\langle \psi'_{E_e s} | \psi_{ns} \rangle$. Numerical calculations face three key challenges. The first two stem from the oscillatory nature of the continuum state wave function: accurate knowledge of the wave function over a wide spatial range is essential, and careful attention must be given to the integration method. The third and most significant challenge is ensuring that the final-state electron continuum wave function is orthogonal to the bound orbital wave functions of the final state, i.e., $\langle \psi'_{E_e s} | \psi'_{ns} \rangle = 0$. This orthogonality condition must hold because these wave functions are eigenfunctions of the same Hamiltonian [150].

If the overlap integral $\langle \psi'_{E_e s} | \psi'_{ns} \rangle$ is not zero, or at least much smaller than $\langle \psi'_{E_e s} | \psi_{ns} \rangle$, then the calculation of $\langle \psi'_{E_e s} | \psi_{ns} \rangle$ may contain significant errors [150]. This issue has also been investigated in nucleon removal reactions such as (γ, p) and $(e, e'p)$, where substantial effects on the polarization of outgoing protons and photon asymmetry were observed for the (γ, p) reaction [160]. Additionally, orthogonalization has been applied to shake-off contributions during electron capture in ^{163}Ho using the Gram-Schmidt procedure [161].

To verify the orthogonality, we define the following dimensionless quantities,

$$T_{ns}^{\mathrm{ref}} = -\frac{\langle \psi'_{E_e s} | \psi'_{ns} \rangle}{\langle \psi'_{ns} | \psi_{ns} \rangle} \frac{g'_{n,-1}(R)}{g'_{-1}(E_e, R)}, \tag{3.14}$$

and

$$T_{n\bar{p}}^{\mathrm{ref}} = -\frac{\left\langle \psi'_{E_e \bar{p}} \middle| \psi'_{n\bar{p}} \right\rangle}{\langle \psi'_{n\bar{p}} | \psi_{n\bar{p}} \rangle} \frac{f'_{n,+1}(R)}{f'_{+1}(E_e, R)}, \tag{3.15}$$

which should be zero for any energy of the emitted electron.

Table 3.1: The relevant nuclear data for the isotopes considered in this work. For each ground state to ground state β transition we present the endpoint (second column) and the initial and final spin-parity states, J_i^π and J_f^π (third column). The Q-values of each β-decay are from [162]

Isotope	Q-value (keV)	J_i^π, J_f^π
^{10}C	156.476(4)	$0^+, 1^+$
^{45}Ca	259.7(7)	$7/2^-, 7/2^-$
^{63}Ni	66.977(15)	$1/2^-, 3/2^-$
^{241}Pu	20.78 (17)	$5/2^+, 5/2^-$

3.3 Exchange effect for the β-decay of ^{14}C, ^{45}Ca, ^{63}Ni and ^{241}Pu

To investigate the steps involved in the exchange correction calculation, we focus on four low Q-value β transitions that were recently studied—namely, ^{14}C [163, 164], ^{45}Ca [8], ^{63}Ni [144], and ^{241}Pu [143, 144]. The relevant nuclear data for these isotopes are summarized in Table 3.1. Based on the differences in the nuclear spin-parity states, the first three β transitions are classified as allowed transitions, while the last one is categorized as a non-unique first forbidden transition. However, the latter can be approximated as allowed using the ξ approximation [154]. We compute the exchange correction over an energy range starting from 200 eV up to the Q-value kinetic energy of the continuum electron for each transition (see the second column of Table 3.1).

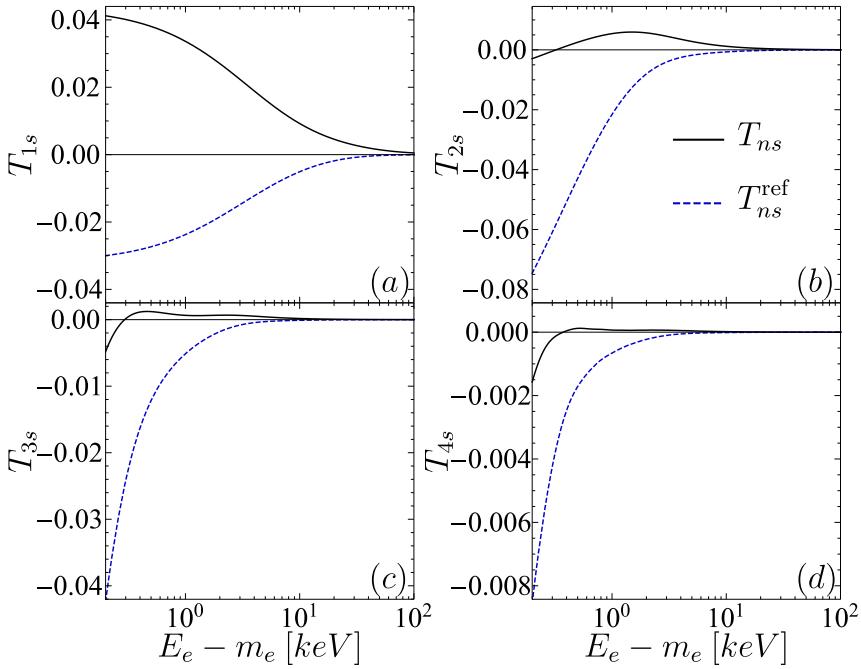

Figure 3.1: The dimensionless quantities T_{ns} (solid black) and $T_{ns}^{\rm ref}$ (dashed blue) defined in Eqs. (3.8) and (3.14), respectively, necessary to perform the exchange correction calculation for the β-decay of ^{45}Ca. The results are presented for $s_{1/2}$ orbitals with $n = 1$ (a), $n = 2$ (b), $n = 3$ (c), and $n = 4$ (d). The bound electron wave functions for both initial and final atoms are computed with the true DHFS method, and the continuum states of the final nucleus just with the electric and nuclear components of the potential. The figure is taken from [165].

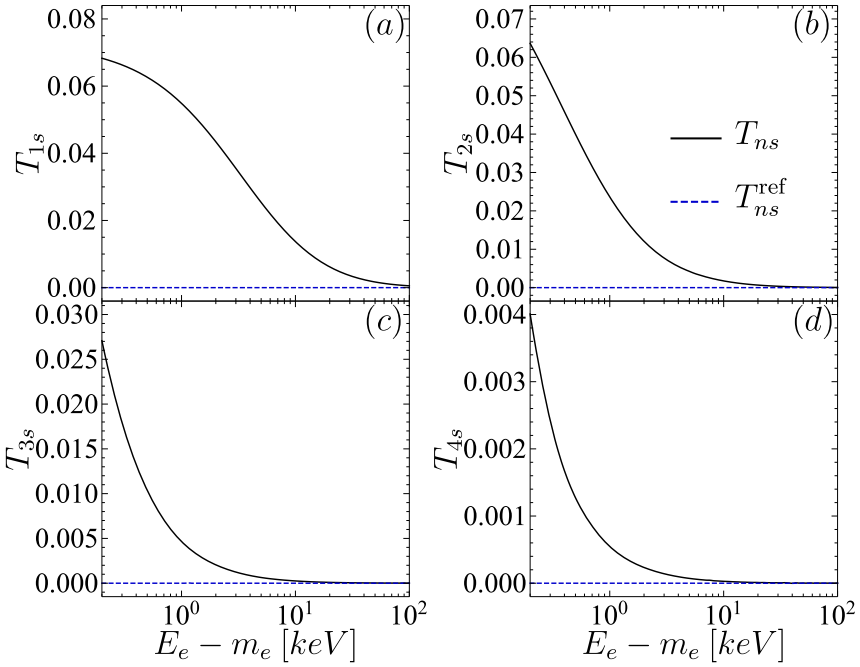

Figure 3.2: The dimensionless quantities T_{ns} (solid black) and $T_{ns}^{\rm ref}$ (dashed blue) defined in Eq. 3.8 and 3.14, respectively, necessary to perform the exchange correction calculation for the β-decay of ^{45}Ca. The results are presented for $s_{1/2}$ orbitals with $n = 1$ (a), $n = 2$ (b), $n = 3$ (c), and $n = 4$ (d). The bound and continuum electron wave functions are computed with the modified DHFS self-consistent method. The zero value of the quantity $T_{ns}^{\rm ref}$ indicates a perfect orthogonality between the continuum states of the emitted electron and the bound states of the atomic electrons of the final nucleus. The figure is taken from [165].

To examine the impact of orthogonality on the exchange correction, we adopt two different approaches for computing the electron wave functions. In the first approach, the bound wave functions for both the initial neutral atom and the final positive ion are derived using a standard DHFS self-consistent method. The continuum states for the emitted electron are then obtained by solving Eq. (A.54) with the nuclear and electronic potential of the final positive ion, i.e., $V(r) = V_{\rm nuc}(r) + V_{\rm el}(r)$. In the second approach, we employ the modified DHFS self-consistent method described in Section A.3.5. Here, the bound and continuum electron states of the final positive ion are calculated using the same potential defined in Eq. (A.73), as illustrated in the lower panel of Fig. A.1.

The non-orthogonal bound and continuum states from the first approach lead to non-zero values of the dimensionless quantities $T_{ns}^{\rm ref}$, as can be seen in Fig. 3.1, where we present all the contributions from the occupied $s_{1/2}$ orbitals in the case of ^{45}Ca β-decay. In the second approach, where the orthogonality is imposed as descried above, one can see in Fig. 3.2, that $T_{ns}^{\rm ref}$ are constant and zero for any energy of the continuum state. Thus, the dimensionless quantities T_{ns}, entering the total exchange effect calculation, are strongly influenced by whether the orthogonality is imposed or not. We can say that as long as the overlaps $\langle \psi'_{E_e s} | \psi'_{ns} \rangle$ are not zero then the overlaps $\langle \psi'_{E_e s} | \psi_{ns} \rangle$, and implicitly the quantities T_{ns}, are in error.

The non-orthogonal bound and continuum states derived from the first approach result in non-zero values of the dimensionless quantities $T_{ns}^{\rm ref}$. This is illustrated in Fig. 3.1, where we display the contributions from all occupied $s_{1/2}$ orbitals for the β-decay of ^{45}Ca. In contrast, the second approach, where orthogonality is enforced as described earlier, yields

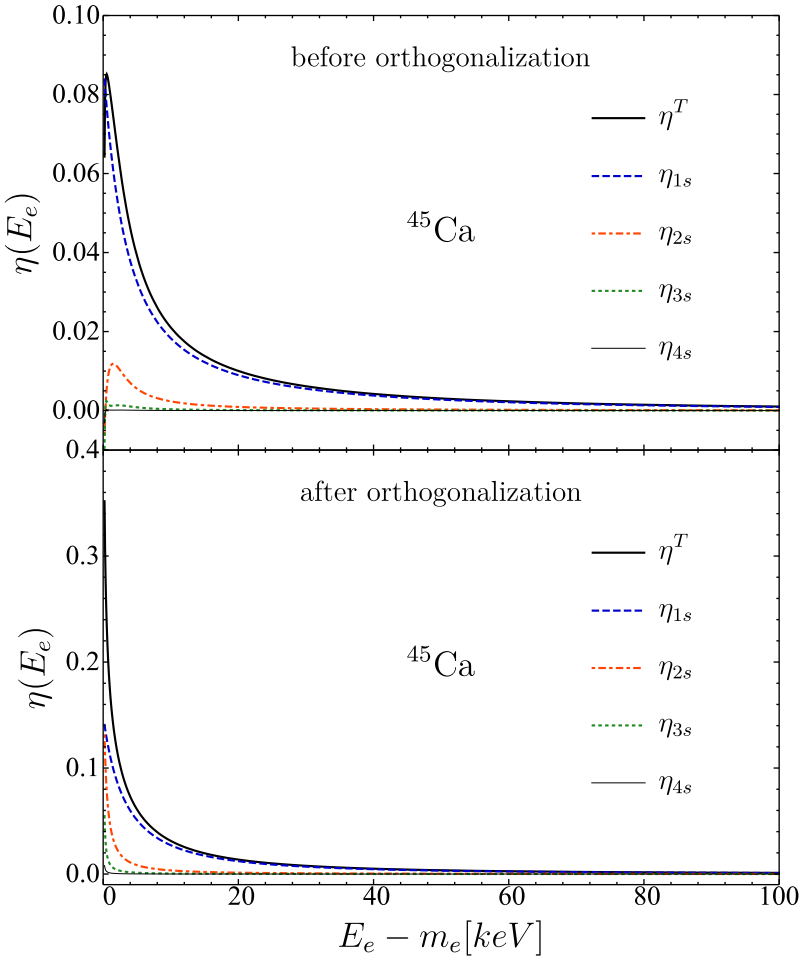

Figure 3.3: The total exchange correction and the partial contributions from all occupied $s_{1/2}$ orbitals as functions of the kinetic energy of the electron emitted in the β-decay of ^{45}Ca. The top figure is obtained with non-orthogonal continuum and bound states of the final atom (see text). In the bottom part the orthogonality is ensured by the modified DHFS self-consistent method. The figure is taken from [165].

constant and zero values for T_{ns}^{ref} at any continuum state energy, as shown in Fig. 3.2. These findings highlight that the dimensionless quantities T_{ns}, which are integral to calculating the total exchange effect, are highly sensitive to whether orthogonality is properly imposed. We conclude that when the overlaps $\langle\psi'_{Ees}|\psi'_{ns}\rangle$ are non-zero, the overlaps $\langle\psi'_{Ees}|\psi_{ns}\rangle$, and consequently the quantities T_{ns}, are significantly impacted and potentially erroneous.

For the β-decay of ^{45}Ca, Fig. 3.3 illustrates the total exchange effect, η^T, along with the partial contributions, η_{ns}. The results obtained using non-orthogonal states are displayed in the top panel, while those using orthogonal states are shown in the bottom panel.

The comparison reveals not only a completely different energy dependence of the exchange effect but also a strong influence of wave function orthogonality on its magnitude. Similar discrepancies in magnitude and energy dependence were noted in [166], though no concrete explanation was provided.

In the first approach, the exchange effect peaks at approximately 8% around 1 keV and then rapidly decreases for lower continuum state energies. A comparable exchange correction was reported in [8] (see Fig. 6, pg. 30) for the β-decay of ^{45}Ca. Conversely, when orthogonal states are employed, the exchange effect rises sharply with decreasing continuum state energy, reaching approximately 35% at 200 eV.

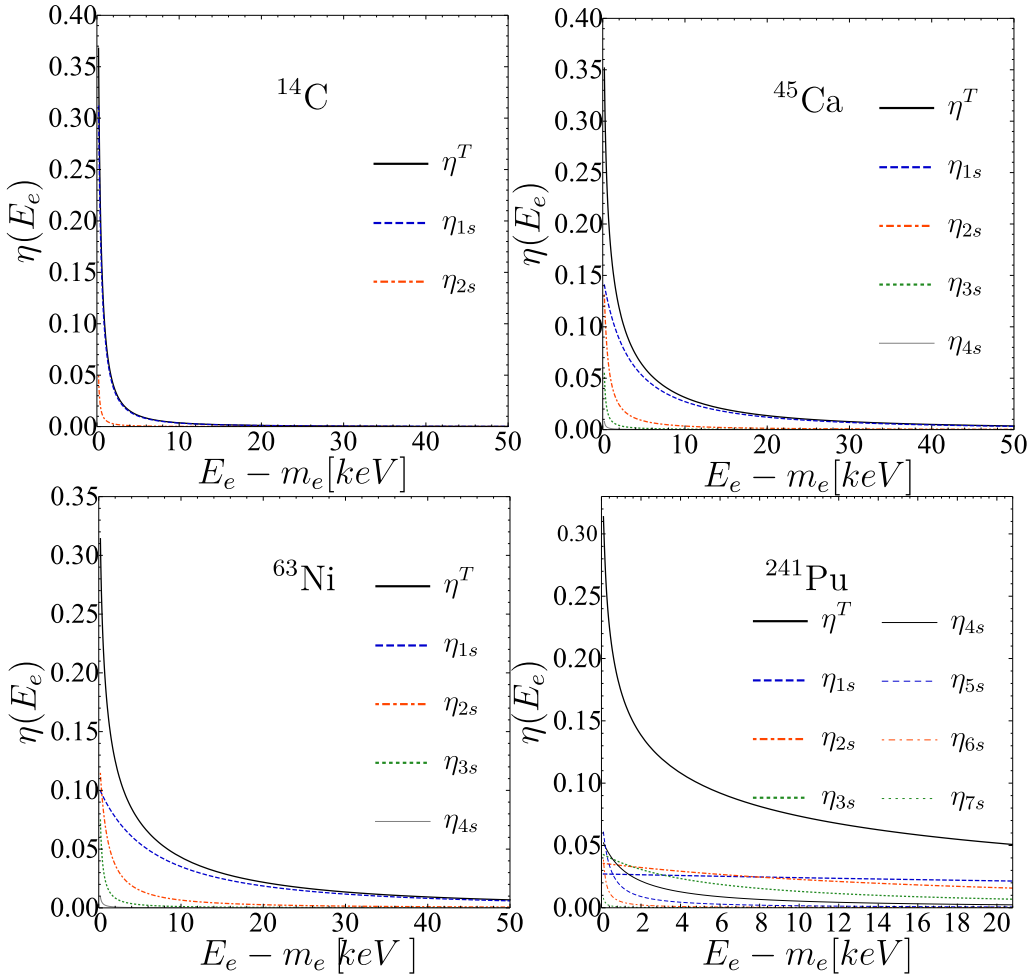

Figure 3.4: The total exchange correction, η^T, and each partial contributions, η_{ns}, coming from the exchange with $s_{1/2}$ occupied orbitals as functions of the kinetic energy of the emitted electron, $E_e - m_e$. The results are presented for the β-decay of ^{14}C, ^{45}Ca, ^{63}Ni and ^{241}Pu. The total exchange correction also includes the partial contributions coming from the exchange with the $p_{1/2}$ occupied orbitals, which are too small to be included in the plot. The figure is taken from [165].

The downturn observed in the non-orthogonal case is directly linked to the erroneous behavior of the T_{ns} quantities. Our investigation suggests that this downturn can even reverse the sign of the exchange effect at very low continuum state energies, resulting in a suppression of events in the low-energy region of the β spectrum. Therefore, any calculation of the exchange correction for ultra-low Q-value β transitions must rigorously enforce orthogonality between the continuum and bound wave functions in the final atom.

We also included contributions from exchanges with $p_{1/2}$ orbitals in the total exchange effect calculation for ^{45}Ca. However, these contributions are three orders of magnitude smaller than those from $s_{1/2}$ orbitals and are thus not visible in Fig. 3.3. In the non-orthogonal case, the $p_{1/2}$ contributions similarly exhibit a downturn, further contributing to the total exchange effect's suppression at low energies.

In the following, we present results for the ground-state-to-ground-state β transitions of ^{14}C, ^{45}Ca, ^{63}Ni, and ^{241}Pu, employing the modified DHFS self-consistent method and enforcing orthogonality between the continuum and bound states. Figure 3.4 illustrates the total exchange correction for each transition, along with the contributions from exchanges

with all occupied $s_{1/2}$ orbitals. The $p_{1/2}$ contributions are also included in the calculations. These contributions exhibit a behavior similar to that of the $s_{1/2}$ contributions but are approximately three orders of magnitude smaller. At the lowest energy considered for the continuum state, i.e., 200 eV, the exchange corrections are approximately 37%, 35%, 32%, and 27% for the β-decays of ^{14}C, ^{45}Ca, ^{63}Ni, and ^{241}Pu, respectively.

At first glance, the magnitude of the exchange effect appears to decrease with increasing nuclear charge, at least at 200 eV. However, as will be discussed in the following subsection, the dependence of the exchange correction on the atomic number is more intricate. This complexity arises from a combined effect involving the spatial extent of the atomic potential, the spatial distribution of the bound wave functions for different n values, and the closure of $s_{1/2}$ and $p_{1/2}$ orbitals.

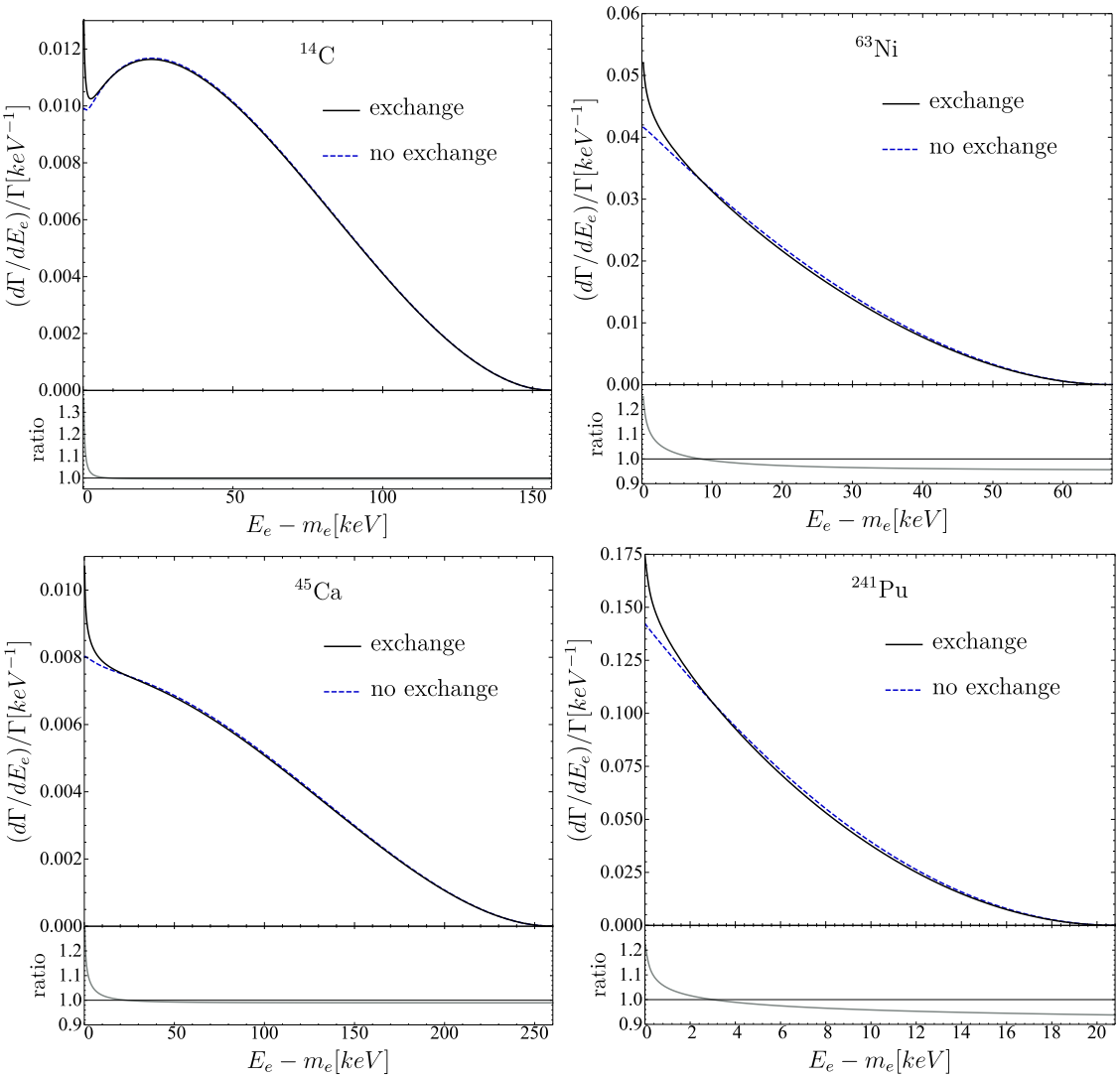

Figure 3.5: The normalized electron spectra for the β transitions of ^{14}C, ^{45}Ca, ^{63}Ni and ^{241}Pu, with the exchange effect included (solid black line) and without the exchange correction (dashed blue line). All spectra are normalized to unity over the full energy range. In the bottom panel of each β emitter, we present the ratio between normalized spectrum with exchange correction and the normalized spectrum without the exchange correction. The figure is taken from [165].

From this investigation, covering one light nucleus, two light-medium nuclei, and one

heavy nucleus, we also observe that heavier nuclei exhibit exchange corrections that persist at higher energies. This trend and its implications will be further analyzed in the next subsection.

Figure 3.5 presents the normalized electron spectra for the decays of the four isotopes under consideration. For each transition, the spectra with and without the exchange correction are shown as solid and dashed lines, respectively.

It is important to emphasize that, due to our choice of atomic potential, the spectra without the exchange effect already incorporate finite nuclear size, diffuse nuclear surface, and atomic screening corrections. These effects are encoded in the continuum wave functions for the emitted electrons, which are used in the Fermi functions defined in Eq. (3.2). Radiative corrections, which represent non-static Coulomb effects, were not included in the calculations, as they are negligible for low Q-value β transitions [144, 167]. The inclusion of the exchange effect leads to a significant increase in the number of events in the low-energy region of the spectra and alters the overall spectral shape.

In cases where non-orthogonal bound and continuum states are used for the final atom, the spectrum with the exchange effect exhibits a downturn at low energies. This results in a mismatch between the predicted and measured spectra, as reported in [144, 164, 159]. A detailed investigation of the residuals between the measured spectra and the theoretical predictions presented here will be provided in a future study.

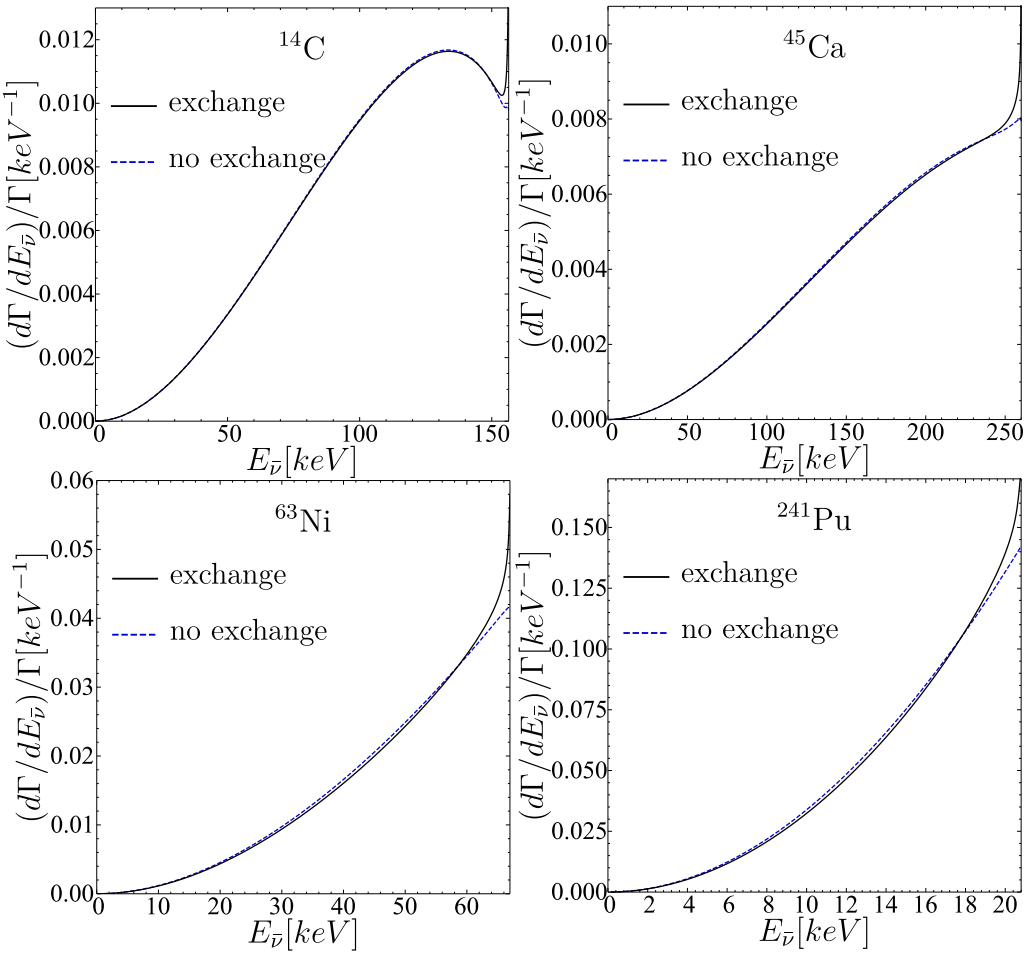

Figure 3.6: The normalized antineutrino spectra corresponding to the β transitions of ^{14}C, ^{45}Ca, ^{63}Ni and ^{241}Pu, with the exchange effect included (solid black line) and without the exchange correction (dashed blue line). The figure is taken from [165].

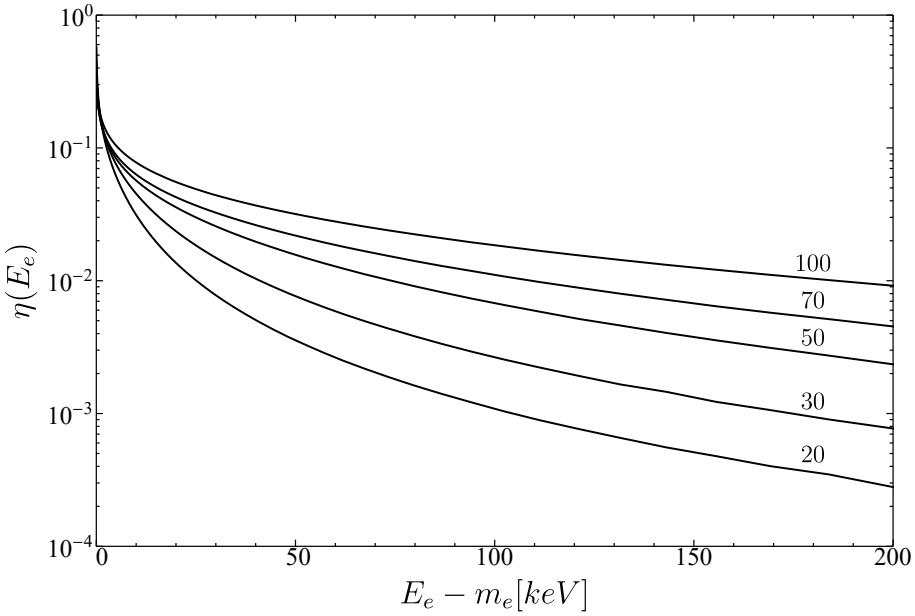

Figure 3.7: The energy dependence of the total exchange correction for β-decay of different initial nuclei with atomic numbers $Z = 20, 30, 50, 70, 100$. The quantities are computed using Eq. 3.6, which includes exchange with all occupied $s_{1/2}$ and $p_{1/2}$ orbitals. The figure is taken from [165].

For completeness, we also present the corresponding antineutrino spectra for each transition in Fig. 3.6. The antineutrino spectrum is derived by replacing $E_e \to E_0 - E_e$ in the electron spectrum defined in Eq. (3.1). Since the inversion process is symmetric, the exchange effect produces the same modifications in the shape of the antineutrino spectra as observed in the electron spectra. However, for larger Q-value β transitions, where radiative corrections cannot be ignored, the inversion symmetry no longer holds. This asymmetry arises from the distinct forms of radiative corrections for electrons and antineutrinos.

Notably, the exchange correction has a pronounced influence on the endpoint regions of the antineutrino spectra. This raises an important question regarding the potential impact of the exchange effect on the cumulative antineutrino spectrum emitted by nuclear reactors. We leave the discussion on this topic open and note that further investigations are currently underway to explore these effects in more detail.

3.4 Analytical parametrization

To estimate the impact of exchange effects on a β-decay spectrum more broadly, we conducted exchange correction calculations across a wide range of atomic numbers for the initial nucleus, spanning from 1 to 102. The emitted electrons in the β-decay process were analyzed for kinetic energies ranging between 50 eV and 200 keV.

We illustrate in Fig. 3.7 the energy dependence of the total exchange correction for β transitions of various initial isotopes with $Z = 20, 30, 50, 70, 100$. The calculations include contributions from the exchange with all occupied $s_{1/2}$ and $p_{1/2}$ orbitals. The observed decrease in the exchange effect with increasing energy of the emitted electron is neither new nor unexpected [150]. However, compared to the unscreened hydrogenic approximation employed in earlier studies [150], the DHFS self-consistent method used here yields a larger overall magnitude for the exchange correction, particularly in the very low-energy region.

Another factor contributing to this difference is that the previous calculations in

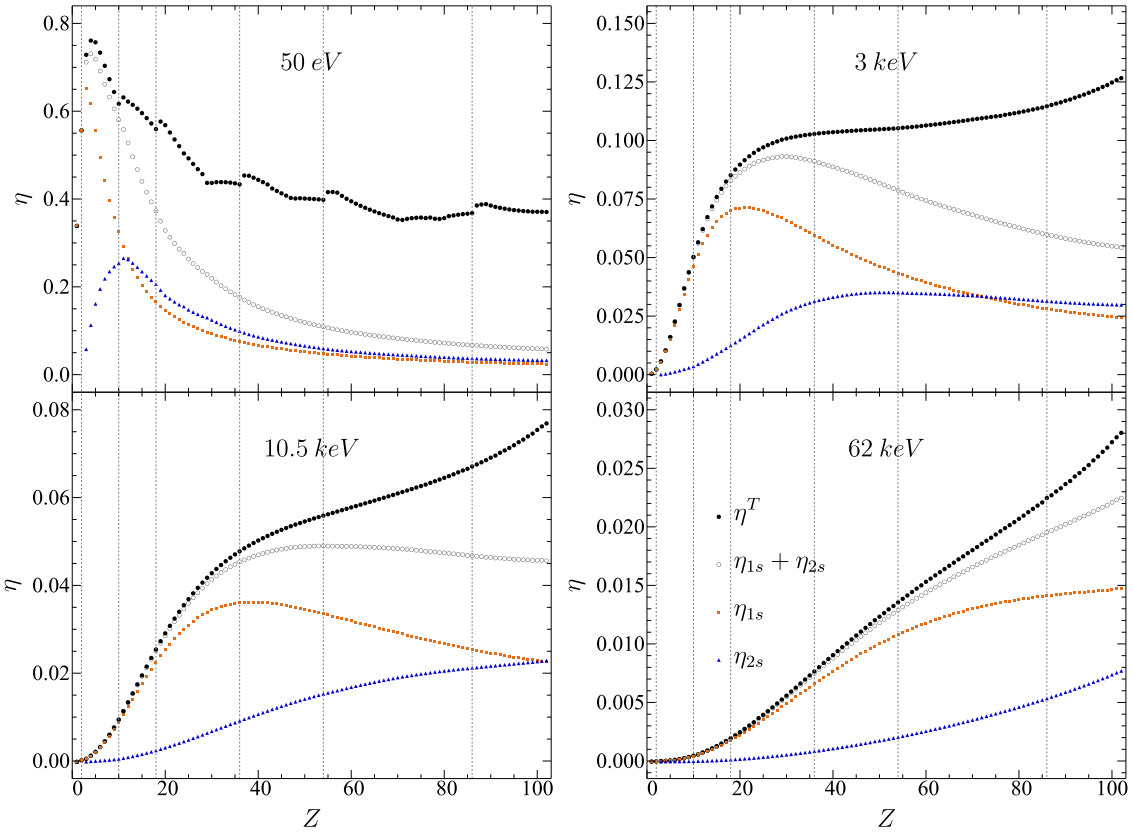

Figure 3.8: The exchange correction as function of the atomic number of the β emitter, from $Z = 1$ to $Z = 102$. The dependence is presented at four different kinetic energies of the β electron. We depict the total exchange correction, η^T, with filled black circles and the partial contributions, η_{1s} and η_{2s}, with filled orange squares and filled blue triangles, respectively. The empty black circles represent the sum of the partial contributions coming from the exchange with $1s_{1/2}$ and $2s_{1/2}$, i.e., η_{1s}+η_{2s}. We also indicate with thin dashed lines the atomic numbers where the $s_{1/2}$ orbitals are fully filled with bound electrons. The figure is taken from [165].

[150] included only the exchange contributions from occupied $s_{1/2}$ orbitals up to and including the $3s_{1/2}$ orbital, while completely neglecting the $p_{1/2}$ orbitals. Apart from the low-energy region, the total exchange correction progressively increases with nuclear charge. Nevertheless, even for $Z = 100$, the total exchange effect remains below 1% at 200 keV kinetic energy of the emitted electron, implying that its contribution can be safely ignored beyond this threshold, depending on the required level of accuracy.

In Fig. 3.8, we illustrate the exchange correction as a function of the atomic number of the β emitter, ranging from $Z = 1$ to $Z = 102$. The dependence is analyzed at four distinct kinetic energies of the β electron: 50 eV, 3 keV, 10.5 keV, and 62 keV. The total exchange correction, η^T, is represented by filled black circles, while the partial contributions, η_{1s} and η_{2s}, are depicted with filled orange squares and filled blue triangles, respectively. The sum of the partial contributions from the $1s_{1/2}$ and $2s_{1/2}$ orbitals, i.e., $\eta_{1s} + \eta_{2s}$, is indicated by empty black circles. This approach highlights the significance of contributions from the remaining occupied $s_{1/2}$ and $p_{1/2}$ orbitals, particularly at lower energies where their impact becomes more pronounced. It also emphasizes the need to account for these additional contributions to achieve a high-precision description of the exchange correction across different atomic numbers.

Table 3.2: The fit parameters for the total exchange correction are tabulated individually for each atomic number of the initial nucleus (see Eq.3.16).

Z	a	b	c	d	e	Z	a	b	c	d	e
1	40.878	41.395	1.0627	9.6525	0.2310	52	1.1568	0.6395	0.6250	2.3902	0.2457
2	11.440	13.268	1.2686	7.3986	0.2962	53	1.1788	0.6679	0.6207	2.4189	0.2429
3	5.5124	0.1003	0.2022	5.2566	0.3183	54	1.1859	0.6723	0.6192	2.4260	0.2415
4	2.8551	0.4427	1.7697	4.1501	0.3819	55	2.6675	3.8795	0.5667	3.6830	0.1882
5	2.4633	0.1412	1.7544	3.5635	0.3688	56	2.4590	3.1784	0.5810	3.5353	0.1935
6	2.1398	0.0317	1.9398	3.1399	0.3583	57	2.0825	2.2149	0.5909	3.2648	0.2026
7	1.9035	0.0043	2.2619	2.8400	0.3482	58	1.9646	2.0665	0.5747	3.2011	0.2025
8	1.8035	-0.1029	0.6761	2.6039	0.3244	59	1.8991	2.0272	0.5593	3.1752	0.2013
9	4.4452	29.653	0.6901	5.5130	0.2581	60	5.7069	-4.4807	0.0445	2.0158	0.0958
10	5.1785	39.584	0.7405	5.7240	0.2470	61	4.7160	-3.6434	0.0472	1.8830	0.1018
11	4.3112	19.394	0.6981	5.0458	0.2539	62	1.9100	2.4129	0.5209	3.2733	0.1927
12	3.8227	14.001	0.6797	4.7287	0.2549	63	1.9756	2.7329	0.5116	3.3596	0.1886
13	3.8809	13.420	0.6866	4.6739	0.2506	64	2.0675	3.1615	0.5048	3.4651	0.1843
14	3.4108	9.6263	0.6827	4.3715	0.2550	65	2.1927	3.7411	0.5007	3.5924	0.1797
15	2.8742	6.3302	0.6779	4.0086	0.2626	66	2.3524	4.4939	0.4989	3.7361	0.1751
16	2.4395	4.2232	0.6750	3.6740	0.2707	67	2.5481	5.4568	0.4998	3.8932	0.1706
17	2.1242	2.9843	0.6725	3.3994	0.2773	68	2.7706	6.6084	0.5026	4.0523	0.1665
18	1.8963	2.2428	0.6691	3.1818	0.2821	69	3.0281	8.0113	0.5070	4.2161	0.1626
19	2.5709	4.0673	0.7067	3.6467	0.2615	70	3.5968	12.385	0.5171	4.5873	0.1551
20	2.1091	2.4885	0.7326	3.2774	0.2764	71	3.3291	9.9229	0.5153	4.4002	0.1584
21	1.8382	1.8290	0.7168	3.0469	0.2815	72	2.9497	7.5192	0.5117	4.1643	0.1631
22	1.6569	1.4564	0.7006	2.8800	0.2842	73	2.5073	5.3125	0.5071	3.8723	0.1695
23	1.5267	1.2281	0.6830	2.7557	0.2850	74	2.1592	3.8373	0.5040	3.6063	0.1760
24	1.2780	0.8165	0.6507	2.4783	0.2927	75	1.9041	2.8882	0.5026	3.3813	0.1819
25	1.3602	1.0057	0.6422	2.6026	0.2823	76	2.1691	3.8474	0.5010	3.6090	0.1746
26	1.3086	0.9690	0.6203	2.5654	0.2792	77	0.0297	0.2031	-0.2002	0.3543	0.3930
27	1.2748	0.9753	0.5974	2.5548	0.2748	78	1.2728	1.1235	0.5013	2.6830	0.2041
28	1.2568	1.0258	0.5753	2.5714	0.2693	79	-0.1392	0.3445	-0.1388	0.2235	0.3614
29	1.1136	0.8685	0.5282	2.4317	0.2695	80	-0.1217	0.3229	-0.1476	0.2014	0.3780
30	1.2723	1.2967	0.5380	2.6960	0.2552	81	-0.0768	0.2711	-0.1728	0.1647	0.4341
31	1.5426	2.0748	0.5547	3.0430	0.2393	82	-0.0763	0.2694	-0.1750	0.1562	0.4366
32	1.7034	2.5015	0.5692	3.1979	0.2324	83	-0.0702	0.2624	-0.1798	0.1488	0.4456
33	1.7962	2.6806	0.5814	3.2649	0.2292	84	-0.0712	0.2625	-0.1809	0.1414	0.4469
34	1.7945	2.5440	0.5913	3.2375	0.2295	85	-0.0732	0.2638	-0.1811	0.1359	0.4454
35	1.7239	2.2223	0.5996	3.1466	0.2323	86	1.4297	1.2203	0.5313	2.7644	0.2004
36	1.6218	1.8588	0.6071	3.0246	0.2364	87	52.470	-39.955	0.0481	4.3172	0.0384
37	3.2275	6.6088	0.6445	4.0640	0.2018	88	3.4173	5.9999	0.5508	4.0237	0.1635
38	2.5377	3.9319	0.6563	3.6498	0.2150	89	0.1538	0.1231	-0.3077	0.4941	0.3504
39	2.0575	2.5016	0.6589	3.3026	0.2263	90	0.0872	0.1567	-0.2640	0.3621	0.3864
40	1.7775	1.7946	0.6630	3.0608	0.2347	91	0.0184	0.1954	-0.2298	0.2262	0.4372
41	1.5791	1.3588	0.6678	2.8673	0.2420	92	-0.0480	0.2417	-0.2002	0.1214	0.4769
42	1.4287	1.0662	0.6727	2.7055	0.2482	93	-0.0719	0.2662	-0.1847	0.1198	0.4457
43	1.2091	0.7074	0.6834	2.4424	0.2605	94	5.5119	-4.1559	0.0482	2.0596	0.0783
44	1.1287	0.5908	0.6884	2.3352	0.2651	95	4.6253	-3.5213	0.0463	1.8487	0.0863
45	1.0633	0.5044	0.6915	2.2439	0.2689	96	-0.1264	0.3340	-0.1500	0.1698	0.3550
46	1.0102	0.4394	0.6921	2.1667	0.2717	97	3.3772	-2.4923	0.0509	1.6164	0.0989
47	0.9644	0.3887	0.6921	2.0988	0.2741	98	3.0700	-2.2689	0.0504	1.5107	0.1049
48	0.9834	0.4124	0.6813	2.1319	0.2699	99	2.7323	-1.9692	0.0543	1.4570	0.1093
49	1.0483	0.4948	0.6587	2.2341	0.2607	100	1.2245	0.8824	0.4761	2.4648	0.2000
50	1.0811	0.5367	0.6463	2.2829	0.2555	101	1.2193	0.8939	0.4675	2.4613	0.1988
51	1.1207	0.5906	0.6343	2.3406	0.2502	102	1.2219	0.9252	0.4585	2.4717	0.1971

At 5 eV energy, the total exchange effect exhibits noticeable discontinuities. This behavior can be understood from the expression of η_s in Eq. 3.10. As the atomic number increases, new $s_{1/2}$ orbitals become occupied, introducing additional partial contributions to the exchange correction. These contributions, added after a shell closure, are nonzero in the low-energy region, explaining the discontinuities observed in the total exchange effect. To highlight this behavior, we use thin dashed lines to indicate the atomic numbers where $s_{1/2}$ orbitals are filled with bound electrons. A clear correlation is observed between shell closures and the jumps in the total exchange correction. While the closure of $p_{1/2}$ orbitals also contributes to this effect, its impact is more subtle. As the energy increases, these discontinuities gradually smooth out. For instance, at 3 keV, the partial contributions start from zero, resulting in a smooth dependence of the total exchange effect on the atomic number. This smooth behavior persists as the energy of the emitted electron continues to increase.

Regarding the partial contributions, η_{1s} and η_{2s}, we observe a completely different dependence on Z compared to the results reported in [8] at 3 keV. We attribute the differences in both Z dependence and magnitude to the fact that, in our study, the bound and continuum states of the final atom are orthogonal. In our calculations, η_{2s} shows a smooth dependence on the atomic number at 3 keV. In contrast, the results from [8] exhibit abrupt changes, including negative values for specific nuclear charges, leading to a downturn in the total exchange effect. Analyzing the sum of η_{1s} and η_{2s}, it becomes evident that, at very low energies, the contributions from higher orbitals are crucial for an accurate calculation of the total exchange correction. However, their significance diminishes as the energy of the continuum state increases.

The complex interplay between the spatial extension of the atomic potential, the spatial distribution of bound wave functions for different n, and the shell closures of $s_{1/2}$ and $p_{1/2}$ orbitals complicates the formulation of an analytical parametrization for the total exchange correction across the full range of $E_e - m_e$ and Z. To address this challenge, we propose the following analytical fit for the total exchange correction:

$$\eta^T(x) = (a + bx^c)\exp(-dx^e), \tag{3.16}$$

as a function of the kinetic energy of the emitted electron, i.e., $x = E_e - m_e$ in keV. The jumps in the Z dependence for low energies forced us to tabulate the required fit parameters for each Z individually. The five fitting parameters are provided in Table 3.2. Due to the orthogonality constraint implemented in our study, the proposed fit is more compact compared to the one in [8], which required nine fitting parameters. The discrepancy between these analytical fit models arises because the downturn in the exchange correction observed in [8] cannot be captured with a simple model. In our case, the deviation between the fitted and calculated exchange corrections never exceeds 10^{-3} across the entire tested energy range, from 5 eV to 200 keV. Furthermore, for the full $E_e - m_e$ and Z range, the average residuals remain below 10^{-4}, achieving a level of accuracy comparable to that of [8]. Importantly, we emphasize that our fit is also suitable for extrapolation beyond 200 keV kinetic energy of the emitted electron.

3.5 General conclusions

The investigation of β-spectrum shapes serves as a powerful tool for addressing open questions in physics beyond the SM and neutrino physics. With advancements in experimental techniques enabling measurements in the low-energy region, particularly within the first few keV, and the availability of higher statistics, it is imperative to provide accurate theoretical predictions for β-spectra. However, accurately describing these spectra poses

significant challenges due to the multitude of effects that become relevant at low energies. For allowed transitions, the dominant atomic effects arise from the screening of the emitted electron's wave function by the atomic electron cloud and the exchange interactions between continuum and bound electrons. The latter effect is referred to as the exchange correction.

We investigated the exchange correction for allowed β transitions, accounting for contributions from all occupied $s_{1/2}$ and $p_{1/2}$ orbitals. The electron wave functions were calculated using a modified DHFS self-consistent method. To ensure orthogonality between the continuum and bound electron states in the potential of the final atom, we modified the final iteration of the self-consistent procedure. Our findings demonstrate that orthogonality plays a crucial role in accurately computing the exchange correction. Failure to enforce orthogonality between the continuum and bound states in the final atom introduces errors in the overlaps between the initial atom's bound states and the final atom's continuum states, resulting in a downturn in the total exchange correction. After enforcing orthogonality, we observed significant differences in both magnitude and energy dependence compared to prior studies. We argue that our approach resolves the mismatch between other recent theoretical predictions and experimental data in the low-energy region.

To develop an analytical parametrization for the exchange correction, we extended our calculations to a broad range of β emitters, with atomic numbers spanning from $Z = 1$ to $Z = 102$. Apart from the low-energy region, the total exchange correction exhibits a progressive increase with nuclear charge. At ultra-low energies, such as 5 eV, the Z dependence of the total exchange effect is influenced by the closure of $s_{1/2}$ and $p_{1/2}$ orbitals. At higher energies, however, the exchange correction shows a smooth dependence on nuclear charge—a behavior that differs markedly from earlier studies. We attribute this discrepancy to the enforcement of orthogonality between the continuum and bound states in our approach. Additionally, we demonstrated that contributions from orbitals beyond the $2s_{1/2}$ orbital are crucial for accurately determining the total effect, especially at low energies. Finally, we provided an analytical expression for the total exchange correction for each atomic number, for a straightforward implementation in experimental analyses.

3.6 Addressing the discrepancy between experimental and theoretical spectra of ^{151}Sm β-decay

This Section highlights that the main source of deviation between the observed and theoretical β spectrum of ^{151}Sm primarily stems from the lack of orthogonality between continuum and bound electron states within the potential of the final atom, ^{151}Eu, when calculating the exchange correction. The calculations presented in this work build upon the results from the previous sections, published in [168].

The β-decay of ^{151}Sm follows two branches: a dominant one (99.31%) from the ground state to the ground state of ^{151}Eu, and a weaker branch (0.61%) from the ground state to the 21.541 keV excited state of ^{151}Eu [159]. Both transitions are classified as first non-unique β transitions. Our calculations focus on the dominant channel. Despite the demonstration that treating the transition as allowed (i.e., using the ξ approximation with $C(E_e) = 1$ in Eq. (3.1)) is only accurate within a 5% precision level, as determined by nuclear Shell Model calculations with the conserved vector current (CVC) hypothesis [159], we continue to consider the spectrum as if it were an allowed transition. Moreover, we include the exchange correction as for an allowed transition as presented in Eq. 3.6, so we neglect the possible exchange with bound electrons from $p_{3/2}$ ($\kappa = -2$) and $\bar{d} \equiv d_{3/2}$ ($\kappa = 2$) orbitals.

Our rough estimation of the electron spectrum for the ground-state-to-ground-state β transition of ^{151}Sm is shown in Figure 3.9, alongside the results from [159]. Since no

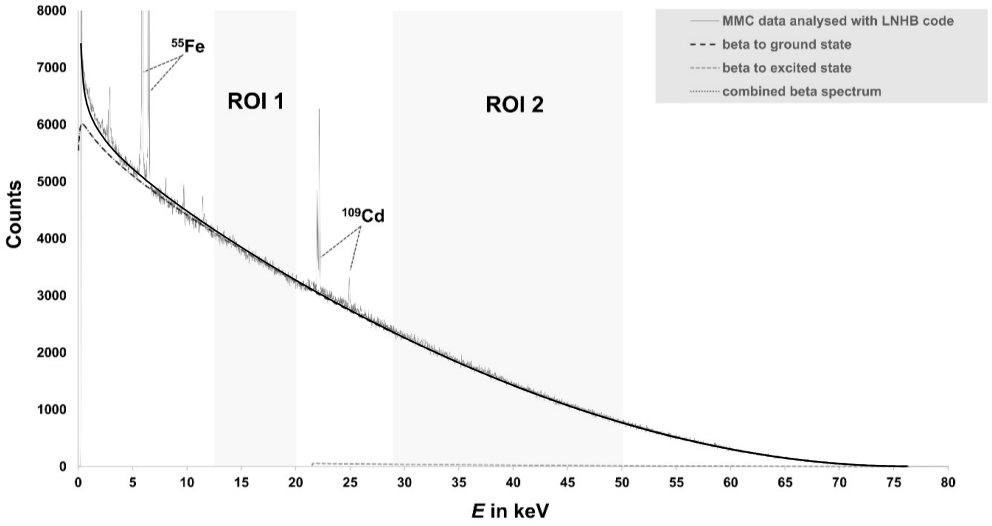

Figure 3.9: The measured and theoretical spectra for the β transitions of ^{151}Sm. Our prediction (solid black) is overlaid on Figure 9 from [159], maintaining the same aspect ratio and using the same Q-value, specifically $Q = 76.430$ keV. For further details on the original figure, including regions of interest, calibration signals, and the transition to the excited state beginning at 21.541 keV, we direct the reader to [159]. A black and white mode has been applied to the original figure.

experimental data is available (solid gray), we overlaid our prediction (solid black) on Figure 9 from [159], preserving the original aspect ratio and adopting the same Q-value, specifically $Q = 76.430$ keV. For further details on the original figure, such as calibration signals, regions of interest, and the transition to the excited state starting at 21.541 keV, we refer readers to [159].

Despite the simplifications from our approach compared to the more elaborate calculations in [159], our model exhibits better agreement with the experimental data, particularly in the low-energy region of the spectrum (below 10 keV). In our earlier work [168], we demonstrated that neglecting orthogonality between the continuum and bound wave functions in the final state leads to a downturn in the exchange correction at low energies. A similar behavior was observed for the β-decay of ^{214}Pb, as noted in [166], although no detailed explanation was provided.

We can conclude that the mismatch between the measured and theoretical β spectrum of ^{151}Sm can largely be addressed by incorporating an orthogonality condition into the atomic exchange correction calculation.

3.7 Additional experimental confirmation

Further validation of our findings from previous sections is supported by spectral measurements of the β-decay of ^{63}Ni [144] and ^{210}Pb [169]. In the absence of actual experimental data, Figures 3.10 and 3.11, corresponding to the β-decay of ^{63}Ni and ^{210}Pb, respectively, should be interpreted with caution. Nevertheless, it is noteworthy that both transitions exhibit an increase in the number of events in the low-energy region of the spectra, aligning with our theoretical predictions. Interestingly, a similar enhancement in the number of events in the low-energy region was recently observed in the β-decay spectrum of ^{99}Tc, as reported in [170].

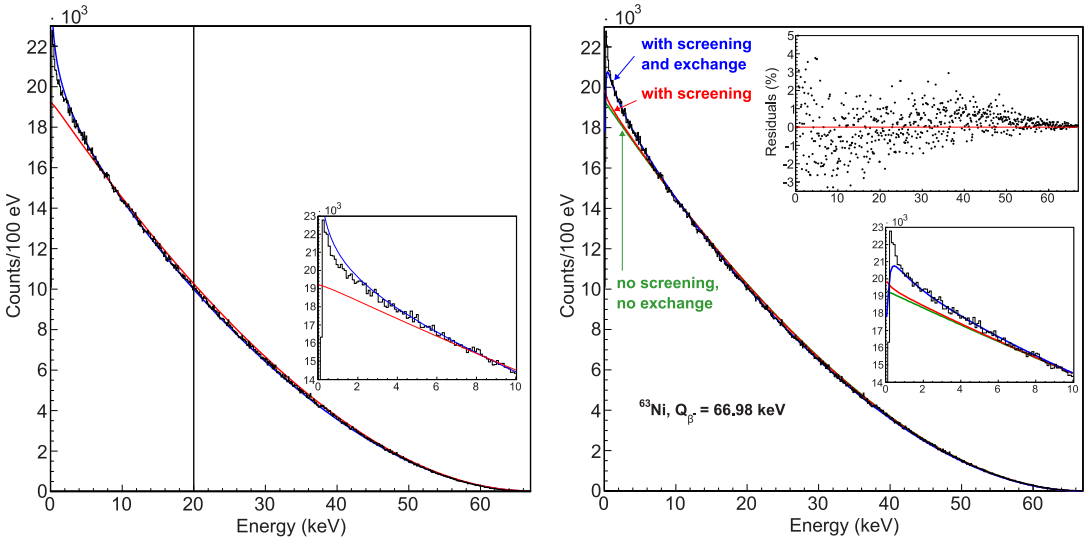

Figure 3.10: The measured and theoretical spectra for the β transitions of ^{63}Ni are presented. Our predictions in the left panel (blue-with exchange correction; red-without exchange correction) are overlaid on the experimental histogram from [144], preserving the same aspect ratio and using the same Q-value. The vertical line indicates a matching point, and the inset provides a zoom-in of the low-energy region of the spectrum. The theoretical predictions discussed in [144] are displayed in the right panel. The original figure is reproduced from [171].

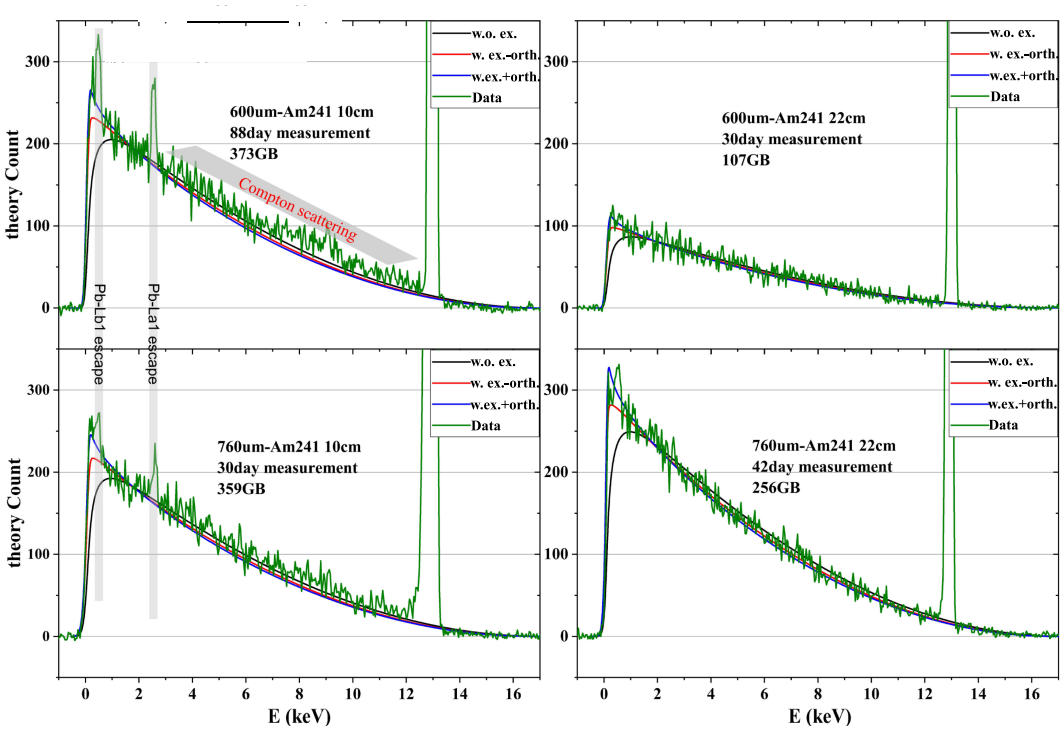

Figure 3.11: The measured and theoretical spectra for the β transitions of ^{210}Pb under four different experimental conditions are shown (see [169] for more details). The green histograms correspond to the experimental spectra, while the blue curves represent the theoretical predictions obtained using our model. The figure is reproduced from [169].

4 Accurate energy distributions in the β-decay of ^{187}Re for neutrino mass measurement

4.1 Introduction

In this Chapter, we investigate the β-decay of ^{187}Re, incorporating all relevant corrections to its spectrum. We begin with the same relativistic wave functions for the emitted electrons as used in our previous study [128]. Next, we enhance the precision of the theoretical rhenium decay spectrum by including finite nuclear size, diffuse nuclear surface, and screening corrections. The latter is calculated using the self-consistent Dirac-Hartree-Fock-Slater description of the atomic bound electrons surrounding the electron emitted during rhenium decay. We have observed significant differences in the decay rates for both emission channels compared to our previous work, but negligible modifications to the spectral shape resulting from the aforementioned corrections. We note that the results from this chapter have been published in [172] as an Editor's Suggestion, as shown in Fig. 4.1.

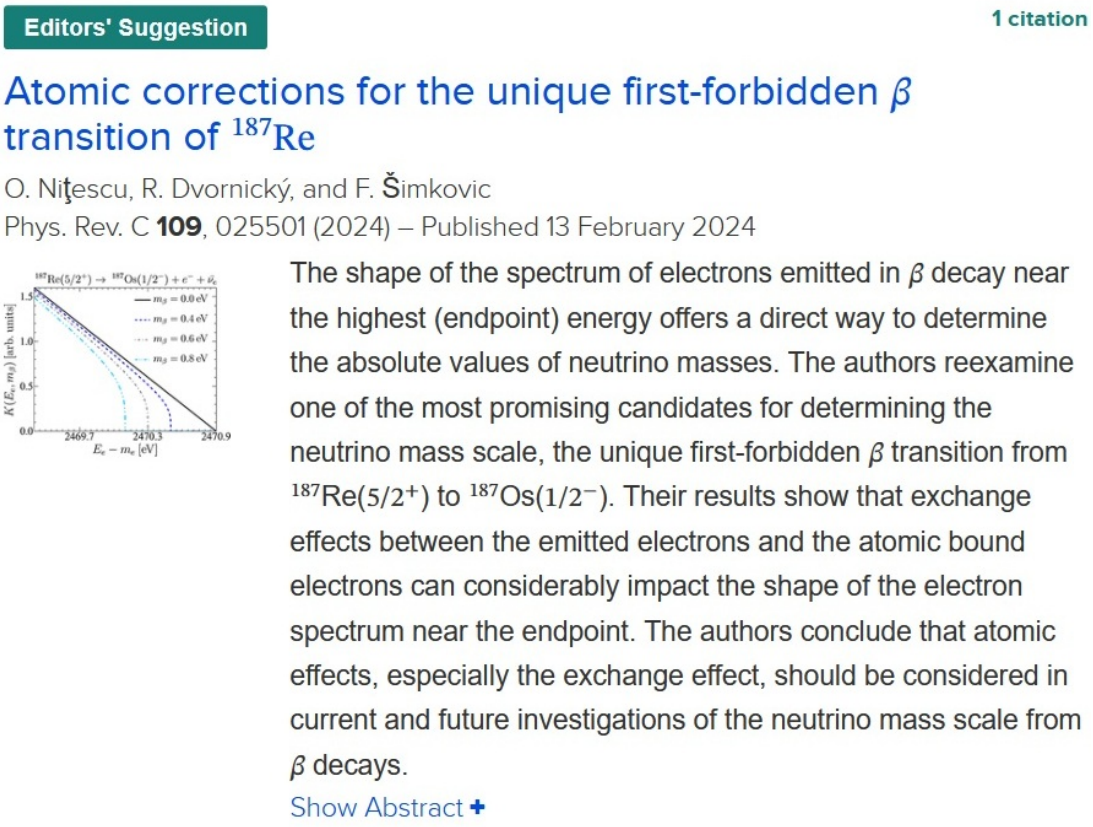

Figure 4.1: A print-screen from the Physical Review C website, Highlights section.

The central focus is the incorporation of the so-called exchange correction, which accounts for the possible interchange between emitted electrons and atomic bound electrons. This correction was discussed in detail for allowed transitions in Chapter 3. This correction not only modifies the decay rates for the $p_{3/2}$- and $s_{1/2}$-state channels but also

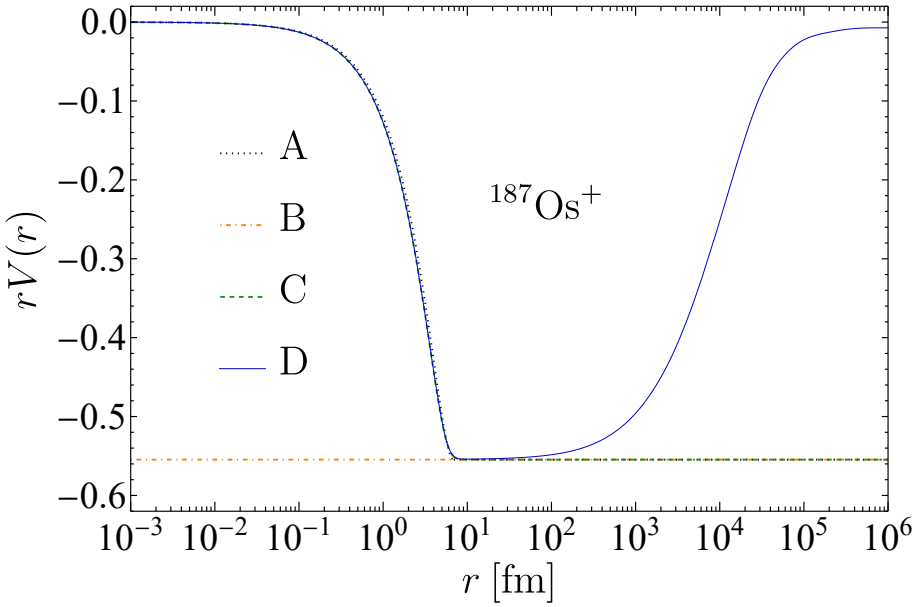

Figure 4.2: The electrostatic potential for $^{187}Os^{+}$ as function of r, where the emitted electron is located, in four different approximation schemes: (A → Subsection A.3.1) The final nucleus as an uniform charged sphere. (B → Subsection A.3.2) A point-like final nucleus. (C → Subsection A.3.3) The final nucleus as a charged sphere filled with protons following a Fermi distribution. (D → Subsection A.3.4) The same as the preceding case but the DHFS atomic electron screening is taken into account. The figure was taken from [173].

significantly influences the spectral shapes of these channels. While the most prominent shape modification occurs in the low-energy region of the total spectrum, the exchange correction remains non-negligible near the endpoint, potentially affecting analyses related to neutrino mass scale determination from rhenium β-decay.

When examining deviations of the rhenium spectrum from an allowed one, we find that the exchange correction transforms the shape factor dramatically—shifting it from an increasing linear behavior to a decreasing quadratic one. We provide the best-fit parameters for both cases. To maintain the linearity of the Kurie plot in the context of zero effective neutrino mass, we demonstrate that it is necessary to revise its definition to explicitly incorporate the exchange correction. Furthermore, we illustrate how variations in effective neutrino masses influence the Kurie plots near the endpoint of the β-decay of ^{187}Re..

We note that although the final nucleus, ^{187}Os, is predicted to exhibit an axially symmetric deformation with $\beta_2 = 0.209$ [174], deformation effects on the electron spectrum shape and the β-decay rate of ^{187}Re have not been considered in this Chapter. Previous studies on allowed β transitions [8] have demonstrated that deformation corrections exhibit very weak energy dependence for electrons with small momenta. Moreover, the overall impact of deformation on the decay rate has been found to be negligible, at the level of 10^{-4}. Another correction that has not been addressed in this work is the radiative correction, which arises from the exchange of virtual photons and the emission of real photons during the β-decay process. Based on the leading-order radiative correction estimates [175, 176], we evaluate this effect to be on the order of 10^{-5} for the low-energy electrons emitted in the β-decay of ^{187}Re.

For the wave functions of the emitted electrons from β-decay of ^{187}Re, we employed four distinct approximation schemes. In Fig. 4.2, we present the quantities $rV(r)$ as functions of r for each approximation scheme applied to the final positive ion, $^{187}Os^{+}$.

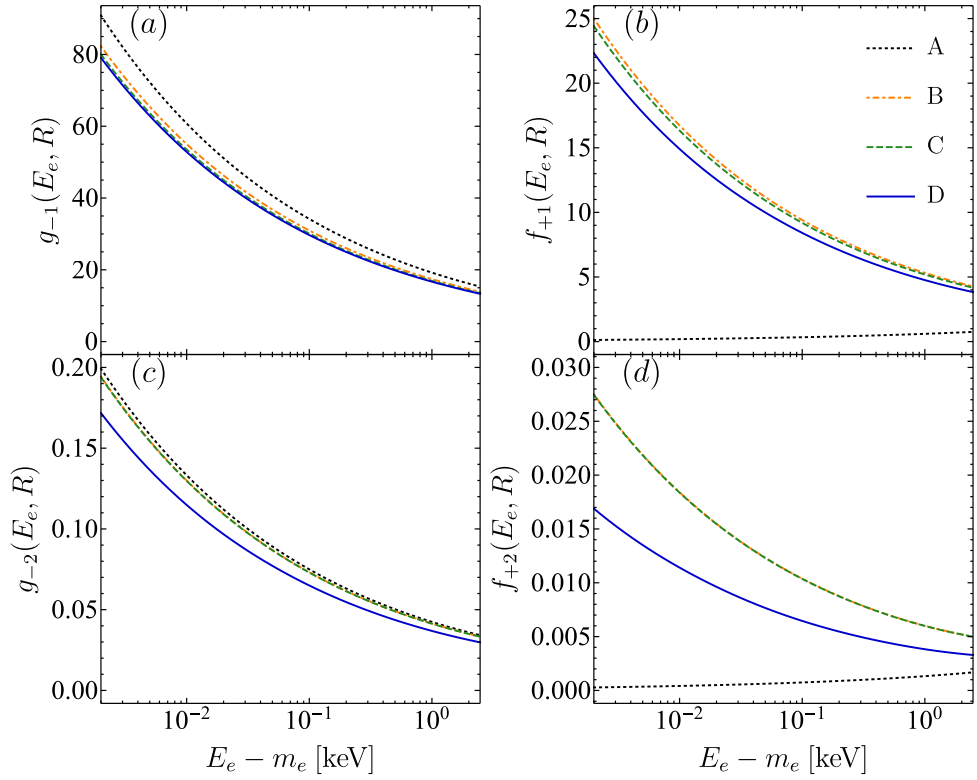

Figure 4.3: The radial wave functions for an electron emitted from the β-decay of ^{187}Re, evaluated on the nuclear surface of the final nucleus R, as functions of the electron kinetic energy $E_e - m_e$. In the top panels (a) and (b) , the components of on electron emitted in $s_{1/2}$ state, $g_{-1}(E_e, r)$ and $f_{+1}(E_e, r)$, and in the bottom panels (c) and (d), the components associated with the emission in $p_{3/2}$ state, $g_{-2}(E_e, r)$ and $f_{+2}(E_e, r)$. We consider four different approximation schemes in the evaluation of the radial wave functions (see text for details). The figure was taken from [173].

In the simplest case, corresponding to a point-like nucleus (scheme B → Subsection A.3.2), we observe that $rV(r) = -76\alpha$ yields a straight line. In contrast, the most complex scenario (scheme D → Subsection A.3.4), which incorporates finite nuclear size, diffuse nuclear surface, and atomic screening corrections, approaches $V(r) = -\alpha/r$ asymptotically for large values of r. This behavior is expected, as the potential describes the interaction of the emitted electron with a positive ion of charge +1. When transitioning from a uniformly charged sphere (scheme A → Subsection A.3.1) to a distribution of protons following a Fermi distribution (scheme C → Subsection A.3.3), the differences between the potentials are minimal and only slightly visible. However, the electron wave functions A are approximated by retaining only the lowest-order terms in the expansion of r. By numerically solving the radial Dirac equation for the potentials in schemes A and C, we confirm that the diffuse nuclear surface correction does not introduce any significant deviations in the wave functions. Hence, any discrepancies between the electron wave functions A and C arise primarily from the omission of higher-order terms in the expansion.

In Fig. 4.3, we display the radial wave functions of an electron in the $s_{1/2}$ wave state, $g_{-1}(E_e, r)$ and $f_{+1}(E_e, r)$ (panels (a) and (b)), and in the $p_{3/2}$ wave state, $g_{-2}(E_e, r)$ and $f_{+2}(E_e, r)$ (panels (c) and (d)). These wave functions are evaluated on the nuclear surface of the final nucleus, $r = R$, and plotted as functions of the electron kinetic energy, $E_e - m_e$. The results correspond to the β emitter ^{187}Re and include all approximation schemes considered in this study.

For the large component radial wave functions, $g_{-1}(E_e, r)$ and $g_{-2}(E_e, r)$, no shape deviations are observed between the approximation schemes. However, their amplitudes systematically decrease from scheme A to scheme D. In contrast, the small component radial wave functions, $f_{+1}(E_e, r)$ and $f_{+2}(E_e, r)$, exhibit significant sensitivity to the missing terms in the expansion in r in scheme A. Instead of aligning with the wave functions computed in scheme C, the small component wave functions in scheme A are nearly constant and close to zero across the entire range of electron kinetic energies. A noteworthy observation is the substantial impact of atomic screening on electrons emitted in the $p_{3/2}$ wave state, as evidenced by the results from scheme D. Since the emission of electrons in the $p_{3/2}$ wave state is dominant in the β-decay of ^{187}Re, we anticipate a significant deviation in the spectrum when the screening correction is incorporated.

4.2 The first unique forbidden β-decay of ^{187}Re

The β transition from the ground state $5/2^+$ of ^{187}Re to the ground state $1/2^-$ of ^{187}Os is classified as a first unique forbidden β transition. Given the angular momentum and parity change, $\Delta J^\pi = 2^-$, the electron and neutrino are emitted in $p_{3/2}$ and $s_{1/2}$ states, or vice versa. An intriguing feature of the first unique forbidden β-decay of ^{187}Re is that, owing to its low transition energy, $Q = 2.4709$ keV [130], the emission of electrons in the $p_{3/2}$ state is favored by approximately four orders of magnitude compared to the emission of electrons in the $s_{1/2}$ state [128]. The theoretical differential decay rate is expressed as a sum of two contributions, each corresponding to the emission of electrons in the $s_{1/2}$ and $p_{3/2}$ states:

$$\begin{aligned}\frac{d\Gamma}{dE_e} &= \frac{d\Gamma^{p_{3/2}}}{dE_e} + \frac{d\Gamma^{s_{1/2}}}{dE_e} \\ &= \sum_{k=1}^{3} |U_{ek}|^2 \, \frac{G_F^2 V_{ud}^2}{2\pi^3} \, p_e E_e (E_0 - E_e) \, [B^{p_{3/2}}(E_e, p_\nu) + B^{s_{1/2}}(E_e, p_\nu)\,] \\ &\times \sqrt{(E_0 - E_e)^2 - m_k^2} \; \theta(E_0 - E_e - m_k)\end{aligned} \tag{4.1}$$

where

$$\begin{aligned}B^{s_{1/2}} = \frac{1}{2} \, g_A^2 \Bigg(&\left| \langle \mathrm{f} \| \sum_n \tau_n^+ g_{-1}(E_e, r) \; j_1(p_\nu r) \; \{\boldsymbol{\sigma}_n \otimes \hat{\boldsymbol{r}}_n\}_2 \| \mathrm{i} \rangle \right|^2 \\ &+ \left| \langle \mathrm{f} \| \sum_n \tau_n^+ f_{+1}(E_e, r) \; j_1(p_\nu r) \; \{\boldsymbol{\sigma}_n \otimes \hat{\boldsymbol{r}}_n\}_2 \| \mathrm{i} \rangle \right|^2 \Bigg) ,\end{aligned} \tag{4.2}$$

and

$$\begin{aligned}B^{p_{3/2}} = \frac{1}{2} \, g_A^2 \Bigg(&\left| \langle \mathrm{f} \| \sum_n \tau_n^+ g_{-2}(E_e, r) \; j_0(p_\nu r) \; \{\boldsymbol{\sigma}_n \otimes \hat{\boldsymbol{r}}_n\}_2 \| \mathrm{i} \rangle \right|^2 \\ &+ \left| \langle \mathrm{f} \| \sum_n \tau_n^+ f_{+2}(E_e, r) \; j_0(p_\nu r) \; \{\boldsymbol{\sigma}_n \otimes \hat{\boldsymbol{r}}_n\}_2 \| \mathrm{i} \rangle \right|^2 \Bigg) .\end{aligned} \tag{4.3}$$

Here, G_F represents the Fermi constant, and V_{ud} is the relevant element of the Cabibbo-Kobayashi-Maskawa (CKM) matrix. The parameter E_0 denotes the maximum endpoint energy of the electron, assuming a zero neutrino mass. The neutrino momentum is given by $p_\nu = \sqrt{(E_0 - E_e)^2 - m_k^2}$, where m_k represents the neutrino mass eigenstates, and $\theta(x)$ denotes the Heaviside theta (step) function. The axial-vector coupling constant is denoted by g_A. The initial and final nuclear states, $|i\rangle$ and $|f\rangle$, correspond to ^{187}Re with $J^\pi = 5/2^+$ and ^{187}Os with $J^\pi = 1/2^-$, respectively. The quantity $\mathbf{r}_n$ refers to the coordinate of the n-th nucleon, where $r = |\mathbf{r}|$ denotes the radial distance and $\hat{\boldsymbol{r}} = \mathbf{r}/r$ represents the unit vector in the radial direction.

The differential decay rate in Eq. (4.1) depends on four distinct squared matrix elements, which are incorporated into the $B^{s_{1/2}}$ and $B^{p_{1/2}}$ terms. To separate the decay rate in the squared nuclear matrix element and the phase-space factor, the large- and small-component electron radial functions are approximated as follows [128]:

$$\begin{aligned}
g_{-1}(E_e, r) &\simeq \frac{g_{-1}(E_e, R)}{j_0(p_e R)}\ j_0(p_e r) \simeq g_{-1}(E_e, R), \\
f_{+1}(E_e, r) &\simeq \frac{f_{+1}(E_e, R)}{j_0(p_e R)}\ j_0(p_e r) \simeq f_{+1}(E_e, R), \\
g_{-2}(E_e, r) &\simeq \frac{g_{-2}(E_e, R)}{j_1(p_e R)}\ j_1(p_e r) \simeq \frac{r}{R} g_{-2}(E_e, R), \\
f_{+2}(E_e, r) &\simeq \frac{f_{+2}(E_e, R)}{j_1(p_e R)}\ j_1(p_e r) \simeq \frac{r}{R} f_{+2}(E_e, R),
\end{aligned} \tag{4.4}$$

where R is a nuclear radius. For bound states, required in the atomic exchange correction (see Sec. 4.3), the same approximation holds leading to $g_{n,-1}(r) \simeq g_{n,-1}(R)$, $f_{n,1}(r) \simeq f_{n,1}(R)$, $g_{n,-2}(r) \simeq (r/R) g_{n,-2}(R)$ and $f_{n,2}(r) \simeq (r/R) f_{n,2}(R)$. For continuum states, only the leading terms in the expansion of spherical Bessel functions $j_0(p_e r)$ and $j_1(p_e r)$ were considered. In this manner, the energy distribution is ultimately expressed as a function of a single squared matrix element [128]:

$$\begin{aligned}
\frac{d\Gamma}{dE_e} &= \frac{d\Gamma^{p_{3/2}}}{dE_e} + \frac{d\Gamma^{s_{1/2}}}{dE_e} \\
&= \sum_{k=1}^{3} |U_{ek}|^2 \frac{G_F^2 V_{ud}^2}{2\pi^3} B R^2 p_e E_e (E_0 - E_e) \\
&\times \frac{1}{3} \left[F_1(Z, E_e) p_e^2 + F_0(Z, E_e)((E_0 - E_e)^2 - m_k^2) \right] \\
&\times \sqrt{(E_0 - E_e)^2 - m_k^2}\, \theta(E_0 - E_e - m_k),
\end{aligned} \tag{4.5}$$

with

$$B = \tfrac{g_A^2}{6R^2} |\langle \mathrm{f} \| \textstyle\sum_n \tau_n^+ \{\boldsymbol{\sigma}_n \otimes \boldsymbol{r}_n\}_2 \| \mathrm{i} \rangle|^2, \tag{4.6}$$

and

$$\begin{aligned}
F_0(Z, E_e) &= \frac{g_{-1}(E_e) g_{-1}(E_e) + f_1(E_e) f_1(E_e)}{j_0(p_e R)\ j_0(p_e R)}, \\
F_1(Z, E_e) &= \frac{g_{-2}(E_e) g_{-2}(E_e) + f_2(E_e) f_2(E_e)}{j_1(p_e R)\ j_1(p_e R)}.
\end{aligned} \tag{4.7}$$

Here, $g_\kappa(E_e) \equiv g_\kappa(E_e, R)$ and $f_\kappa(E_e) \equiv f_\kappa(E_e, R)$. In the case where the Coulomb interaction is neglected, the Fermi functions simplify to $F_0(Z, E_e) = 1$ and $F_1(Z, E_e) = 1$. Different approximation schemes for the electron wave functions are denoted in the Fermi functions as $F^{\mathrm{I}}_{k-1}(Z, E_e)$, where $\mathrm{I} = \mathrm{A}, \mathrm{B}, \mathrm{C}$, or D.

4.3 Exchange correction for unique first forbidden β transitions

We have generalized the exchange effect formalism, originally developed for allowed β transitions in [150, 151], to address unique first forbidden β transitions. Our findings indicate that two distinct components of the exchange correction independently influence the spectra corresponding to the emission of electrons in the $s_{1/2}$ and $p_{3/2}$ states,

$$\begin{aligned} \frac{d\Gamma^{s_{1/2}}}{dE_e} &\Rightarrow \frac{d\Gamma^{s_{1/2}}}{dE_e} \times \left[1 + \eta_1^{\mathrm{T}}(E_e)\right] \\ \frac{d\Gamma^{p_{3/2}}}{dE_e} &\Rightarrow \frac{d\Gamma^{p_{3/2}}}{dE_e} \times \left[1 + \eta_2^{\mathrm{T}}(E_e)\right] \end{aligned} \tag{4.8}$$

The result aligns with the findings reported in [145] and, more recently, in [177], for the unique first forbidden β-decay of ^{85}Kr. The total exchange correction for each partial spectrum is expressed as:

$$\begin{aligned} \eta_k^T(E_e) &= f_k(2T_{-k} + T_{-k}^2) + (1 - f_k)(2T_{+k} + T_{+k}^2) \\ &= \eta_{-k}(E_e) + \eta_{+k}(E_e) \end{aligned} \tag{4.9}$$

where $k = |\kappa|$ can take the values 1 or 2. Here,

$$f_k = \frac{g'^2_{-k}(E_e, R)}{g'^2_{-k}(E_e, R) + f'^2_{+k}(E_e, R)}, \tag{4.10}$$

and the dimensionless quantities T_κ depend on the overlaps between the bound states of the initial atom and the continuum states of the final atom with energy E_e,

$$T_\kappa = \sum_{(n\kappa)'} T_{n\kappa} = -\sum_{(n\kappa)'} \frac{\langle \psi'_{E_e\kappa} | \psi_{n\kappa} \rangle}{\langle \psi'_{n\kappa} | \psi_{n\kappa} \rangle} \frac{g'_{n,\kappa}(R)}{g'_\kappa(E_e, R)}, \tag{4.11}$$

for electrons in $s_{1/2}$ ($\kappa = -1$) and $p_{3/2}$ ($\kappa = -2$) states, and

$$T_\kappa = \sum_{(n\kappa)'} T_{n\kappa} = -\sum_{(n\kappa)'} \frac{\langle \psi'_{E_e\kappa} | \psi_{n\kappa} \rangle}{\langle \psi'_{n\kappa} | \psi_{n\kappa} \rangle} \frac{f'_{n,\kappa}(R)}{f'_\kappa(E_e, R)}, \tag{4.12}$$

for electrons in $p_{1/2}$ ($\kappa = +1$) and $d_{3/2}$ ($\kappa = +2$) states. All primed continuum and bound states are associated with the final atom. The summations extend over all occupied orbitals in the final atom, which, under the sudden approximation, retain the electronic configuration of the parent atom.

Taking into account the sums inside the T_κ quantities, we can write

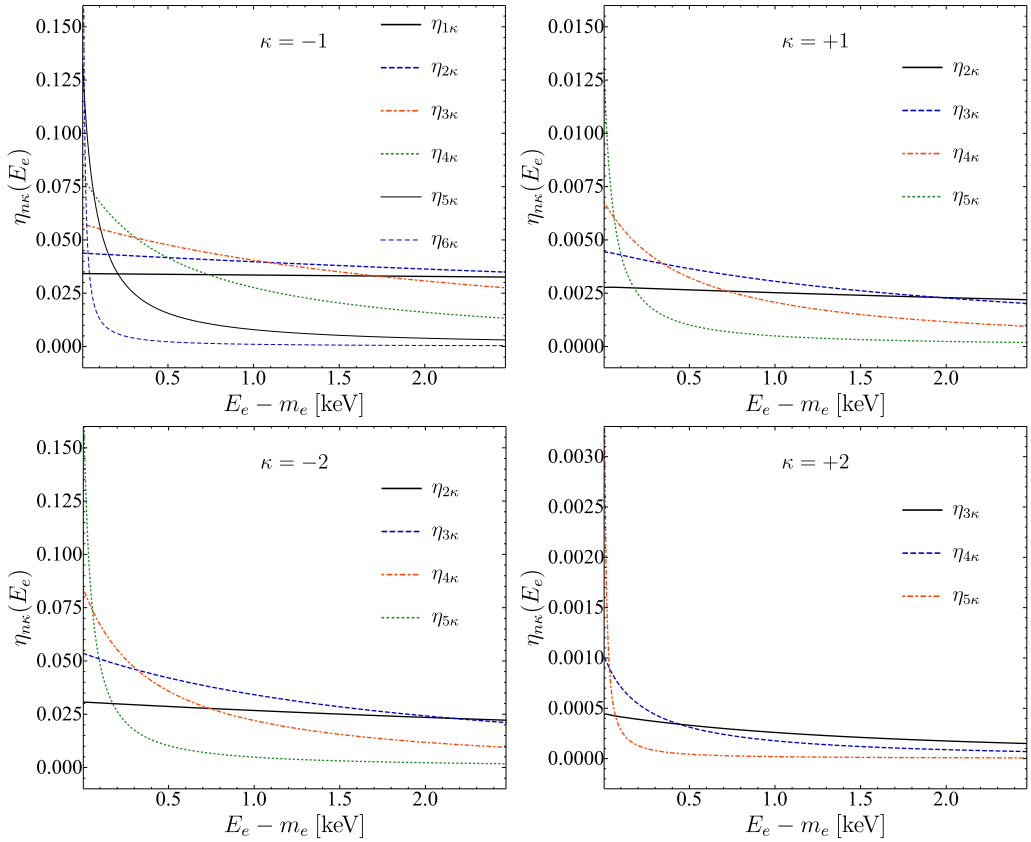

Figure 4.4: All partial exchange corrections for the decay of ^{187}Re, i.e., Eqs. (4.15) and (4.16). The results are presented for atomic electrons in $s_{1/2}$ ($\kappa = -1$), $p_{3/2}$ ($\kappa = -2$), $p_{1/2}$ ($\kappa = +1$) and $d_{3/2}$ ($\kappa = +2$) states. The figure was taken from [173].

$$\eta_\kappa(E_e) = \sum_n \eta_{n\kappa} + f_{|\kappa|} \sum_{\substack{n,m \\ n\neq m}} T_{n\kappa} T_{m\kappa} \tag{4.13}$$

for negative values of κ, and

$$\eta_\kappa(E_e) = \sum_n \eta_{n\kappa} + (1 - f_\kappa) \sum_{\substack{n,m \\ n\neq m}} T_{n\kappa} T_{m\kappa} \tag{4.14}$$

for positive values of κ. In this way, we can define the partial exchange correction contributions, $\eta_{n\kappa}$, given by

$$\eta_{n\kappa} = f_{|\kappa|}(2T_{n\kappa} + T_{n\kappa}^2) \tag{4.15}$$

for negative values of κ, and

$$\eta_{n\kappa} = (1 - f_\kappa)(2T_{n\kappa} + T_{n\kappa}^2), \tag{4.16}$$

for positive values of κ.

A key aspect in evaluating the exchange correction involves calculating the overlaps between the electron wave function in the continuum state, with energy E_e, in the final atom and the electron wave functions in the bound orbitals of the initial atom, i.e., $\langle \psi'_{E_e s} | \psi_{ns} \rangle$. The explicit expression for this overlap is provided by

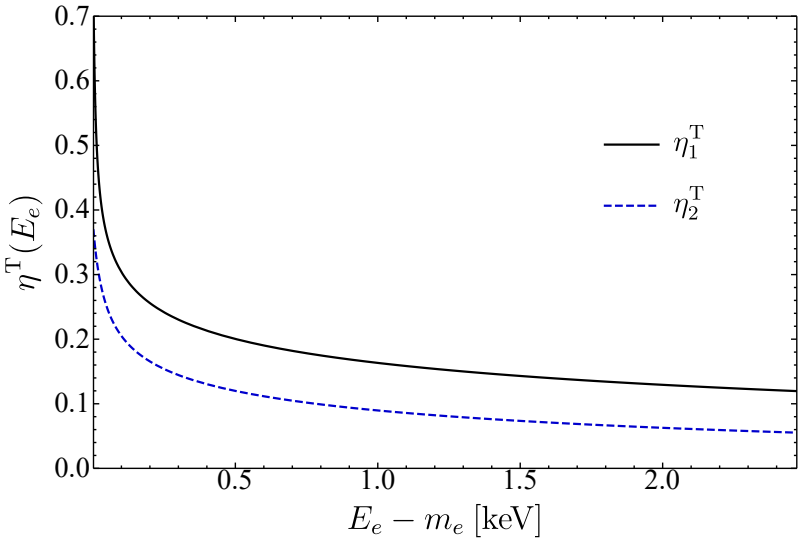

Figure 4.5: The total exchange correction for electrons emitted in $s_{1/2}$ wave state, $\eta_1^{\mathrm{T}}(E_e)$ (solid black line), and for electrons emitted in $p_{3/2}$ wave state, $\eta_2^{\mathrm{T}}(E_e)$ (dashed blue line). The figure was taken from [173].

$$\langle \psi'_{E_e\kappa} | \psi_{n\kappa} \rangle = \int_0^\infty r^2 \left[g'_\kappa(E_e, r) g_{n,\kappa}(r) + f'_\kappa(E_e, r) f_{n,\kappa}(r) \right] dr. \tag{4.17}$$

and its numerical calculation requires good knowledge of the continuum wave function over a wide region of space, from the nuclear center to where the bound wave function for the initial atom ends.

As outlined in Chapter 3, a critical requirement for computing the exchange correction is ensuring that the electron continuum wave function in the final state is orthogonal to the wave functions of the bound orbitals in the final state, i.e., $\langle \psi'_{E_e\kappa} | \psi'_{n\kappa} \rangle = 0$. Since these wave functions are eigenfunctions of the same Hamiltonian, they must inherently satisfy orthogonality. Any deviation from this condition, such as a non-zero value of $\langle \psi'_{E_e\kappa} | \psi'_{n\kappa} \rangle$, can introduce significant errors into the overlap $\langle \psi'_{E_e\kappa} | \psi_{n\kappa} \rangle$ [150]. The consequences of using non-orthogonal continuum and bound wave functions for the final state on the exchange correction have been analyzed in detail in [168]. In our approach, we employ a modified DHFS self-consistent method for bound states along with the potential described in Section A.3.5 for continuum states. This framework inherently enforces the orthogonality condition, $\langle \psi'_{E_e\kappa} | \psi'_{n\kappa} \rangle = 0$, eliminating the need for additional computationally expensive orthogonalization procedures.

In the case of ^{187}Re, there are numerous possibilities for exchanges between the β-emitted electrons and the bound electrons in the atomic cloud. For the emission of $s_{1/2}$-state electrons, ten orbitals contribute to η_1^{T}, while for the dominant emission in $p_{3/2}$-state electrons, seven orbitals contribute to η_2^{T}. In Fig. 4.4, we illustrate all partial exchange corrections for the β-decay of ^{187}Re, as expressed in Eqs.(4.15) and (4.16), plotted against the kinetic energy of the emitted electrons, $E_e - m_e$. We observe that the contributions from $p_{1/2}$ (top right panel) and $d_{3/2}$ (bottom right panel) states are significantly smaller than those from $s_{1/2}$ (top left panel) and $p_{3/2}$ (bottom left panel) states. This behavior arises because the former are linked to the small components of the Fermi functions, $f'_1(E_e)$ and $f'_2(E_e)$, respectively, as described in Eq. (4.7). Despite their smaller magnitudes, these contributions cannot be ignored in precise calculations.

Table 4.1: The partial decay rates for ^{187}Re, excluding the squared matrix element, associated with the emission of electrons in $s_{1/2}$ wave state (second colum) and $p_{3/2}$ wave state (forth column). The approximation scheme for the electron wave functions is indicated in the first column. In the last line, the addition of the exchange correction over the scheme D is indicated as D + ex. In the third and fifth column, we present the decay rate percent deviation between the scheme A and the other schemes, $\delta^{s_{1/2}} = 100(\Gamma_{\rm A}^{s_{1/2}} - \Gamma_{\rm X}^{s_{1/2}})/\Gamma_{\rm X}^{s_{1/2}}$, and $\delta^{p_{3/2}} = 100(\Gamma_{\rm A}^{p_{3/2}} - \Gamma_{\rm X}^{p_{3/2}})/\Gamma_{\rm X}^{p_{3/2}}$, respectively, where X can be B, C, D or D + ex. The last column presents the experimental squared matrix elements.

w. f.	$\frac{10^{41}}{B} \times \Gamma^{s_{1/2}}$ [MeV]	$\delta^{s_{1/2}}$ %	$\frac{10^{37}}{B} \times \Gamma^{p_{3/2}}$ [MeV]	$\delta^{p_{3/2}}$ %	$B \times 10^4$
A	9.30	-	9.19	-	3.63
B	8.33	-10.41	8.92	-2.95	3.74
C	7.88	-15.23	8.88	-3.35	3.76
D	7.58	-18.48	6.98	-24.02	4.78
D+ex	9.46	1.75	7.92	-13.84	4.22

The total exchange correction for the $s_{1/2}$ ($p_{3/2}$) electron spectrum in the β-decay of rhenium is shown as a solid (dashed) line in Fig. 4.5, plotted against the kinetic energy of the emitted electron. It is evident that the exchange corrections decrease as the kinetic energy of the emitted electron increases, starting at approximately 73% for $s_{1/2}$ electrons and 37% for $p_{3/2}$ electrons at 2 eV. Even in the Q-value region, the exchange correction remains notable, around 12% for $s_{1/2}$ electrons and 5.5% for $p_{3/2}$ electrons. Given the substantial magnitude and distinctive shape of the exchange correction, we anticipate that it will lead to significant alterations in both the decay rate and the spectrum shape of rhenium β-decay. These modifications are explored in what follows.

4.4 Results and discussions

In Table 4.1, we summarize the partial decay rates, $\Gamma^{s_{1/2}}$ (second column) and $\Gamma^{p_{3/2}}$ (fourth column), excluding the squared matrix element, B. These partial decay rates, expressed in MeV, are obtained by integrating Eq. (4.5) over the full energy range. The final row corresponds to approximation scheme D, which incorporates the atomic exchange correction discussed in Section4.3. This combined approach is denoted as D + ex. We take approximation scheme A, previously used in our earlier study, as the reference for calculating percentage deviations in the other schemes. These deviations are listed in the third (fifth) column for the partial decay rates $\Gamma^{s_{1/2}}$ ($\Gamma^{p_{3/2}}$). Finally, using the experimental half-life of 4.33×10^{10} years [178], we present our predictions for the squared matrix elements in the last column of Table 4.1.

Across all approximation schemes, the ratios between the $p_{3/2}$-state and $s_{1/2}$-state electron emission channels consistently remain around 10^4, indicating that different corrections do not alter this fundamental characteristic of rhenium decay. However, significant variations in the decay rates arise when incorporating screening and exchange corrections. In particular, the screening correction alone (scheme D) results in a 24% reduction in the partial decay rate $\Gamma^{p_{3/2}}$ and an 18.5% decrease in $\Gamma^{s_{1/2}}$ compared to scheme A. When the exchange correction is further included (scheme D + ex), the partial decay rate $\Gamma^{s_{1/2}}$ increases slightly, reaching a value only 1.7% higher than that from scheme A. Conversely, $\Gamma^{p_{3/2}}$ remains significantly lower, showing a 13.8% decrease relative to scheme A.

The most notable impact of the exchange correction is its influence on the spectrum

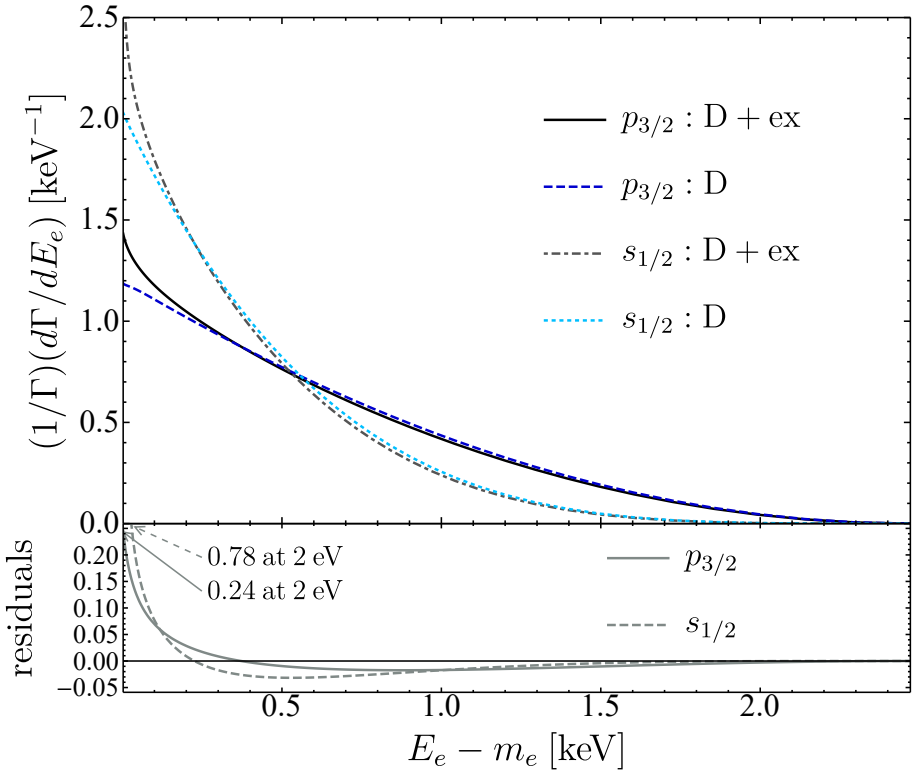

Figure 4.6: The single electron differential decay rate normalized to the particular decay rate ($\Gamma^{s_{1/2}}$ and $\Gamma^{p_{3/2}}$) for the emission of $s_{1/2}$ and $p_{3/2}$ electrons as functions of the electron kinetic energy $E_e - m_e$ for β-decay of ^{187}Re. We indicate with D the approximation scheme D and with ex the atomic exchange correction. The lower portion of the figure gives the difference between the spectra with and without the exchange correction for $s_{1/2}$ wave state electrons with a dashed line and $p_{3/2}$ wave state electrons with a solid line. Spectra are normalized over the full energy range. The figure was taken from [173].

shape of rhenium decay. In Fig. 4.6, we display the normalized single-electron spectra for both $s_{1/2}$- and $p_{3/2}$-state emissions, calculated using approximation schemes D and D + ex. Notably, there are no significant shape differences among approximation schemes A, B, C, and D. In the lower panel of Fig. 4.6, the residuals between the spectra are also shown. While the dominant $p_{3/2}$ spectrum is less affected by the exchange correction compared to the $s_{1/2}$ spectrum, the alteration is substantial enough to modify the overall shape of the total decay spectrum.

We present the total spectrum of rhenium β-decay in Fig. 4.7, following the same conventions as in Fig. 4.6. Here, however, the electron kinetic energy spans from 700 keV up to the Q-value, and the residuals are expressed as percentages. The spectra are normalized to unity over the full kinetic energy range. It is evident that the inclusion of the exchange correction results in a distinct modification of the total electron spectrum shape for rhenium decay. The significant alteration in the spectrum caused by the exchange correction underscores the necessity of incorporating this effect in analyses related to neutrino mass determination from rhenium decay. More broadly, it highlights the importance of considering such corrections in other low Q-value β transitions.

To evaluate the deviation from an allowed spectrum, we write the β spectrum of ^{187}Re as,

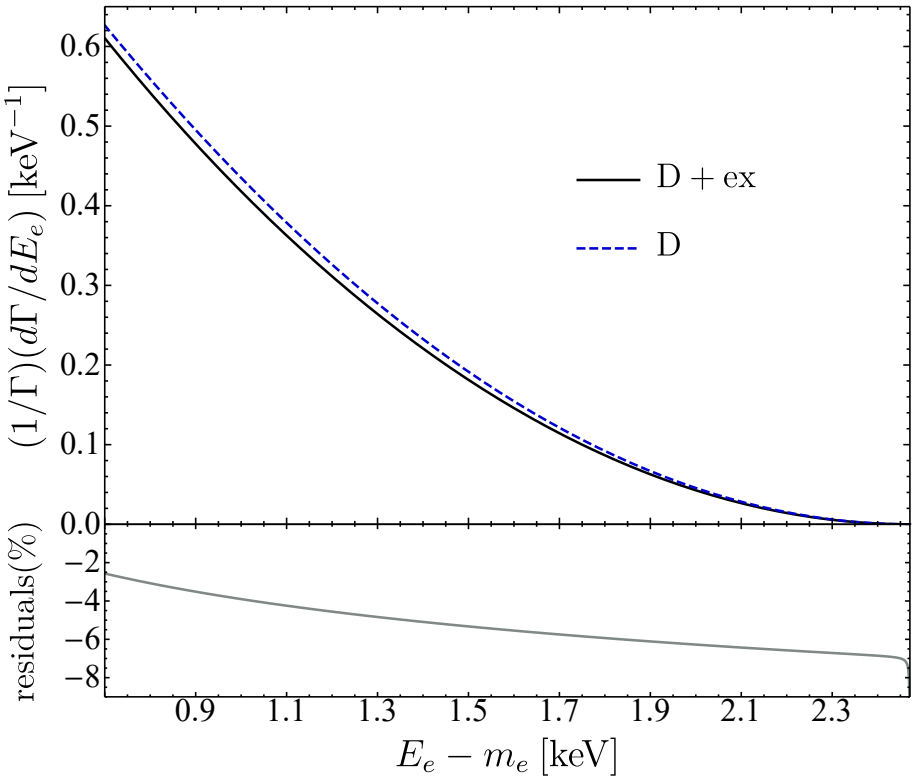

Figure 4.7: The differential decay rate normalized to the total decay rate (Γ) as function of the electron kinetic energy $E_e - m_e$ for β-decay of ^{187}Re. We indicate with D the approximation scheme D and with ex the atomic exchange correction. The lower portion of the figure gives the percentage residuals between the spectrum with and without the exchange correction. Spectra are normalized over the full energy range. The figure was taken from [173].

$$\frac{d\Gamma}{dE_e} = \frac{G_F^2 V_{ud}^2}{2\pi^3} B p_e E_e F_0^{\mathrm{I}}(Z, E_e)(E_0 - E_e)^2 A_F^{\mathrm{I}} \tag{4.18}$$

where, for the moment, the neutrino masses are neglected and I = A, B, C, or D. The shape factor $A_F^{\mathrm{I}} = 1$ for the allowed transitions, but for unique first forbidden,

$$A_F^{\mathrm{I}} = \frac{R^2}{3}\left[p_e \frac{F_1^{\mathrm{I}}(Z, E_e)}{F_0^{\mathrm{I}}(Z, E_e)} + (E_0 - E_e)^2\right], \tag{4.19}$$

where we did not include the exchange with bound electrons. If we want to take into account this effect, the shape factor becomes,

$$A_F^{\mathrm{D+ex}} = \frac{R^2}{3}\left\{p_e \frac{F_1^{\mathrm{D}}(Z, E_e)}{F_0^{\mathrm{D}}(Z, E_e)}\left[1 + \eta_2^{\mathrm{T}}(E_e)\right] + (E_0 - E_e)^2\left[1 + \eta_1^{\mathrm{T}}(E_e)\right]\right\}. \tag{4.20}$$

As shown in Fig. 4.8, all A_F^{I} exhibit a linear increase with energy within the experimentally accessible range, spanning from 700 eV to the Q-value. The behavior of A_F^{I} is accurately reproduced by employing the following model fit:

$$A_F^{\mathrm{I}} = a^{\mathrm{I}}\left(1 + b_1 T_e + b_2 T_e^2\right) \tag{4.21}$$

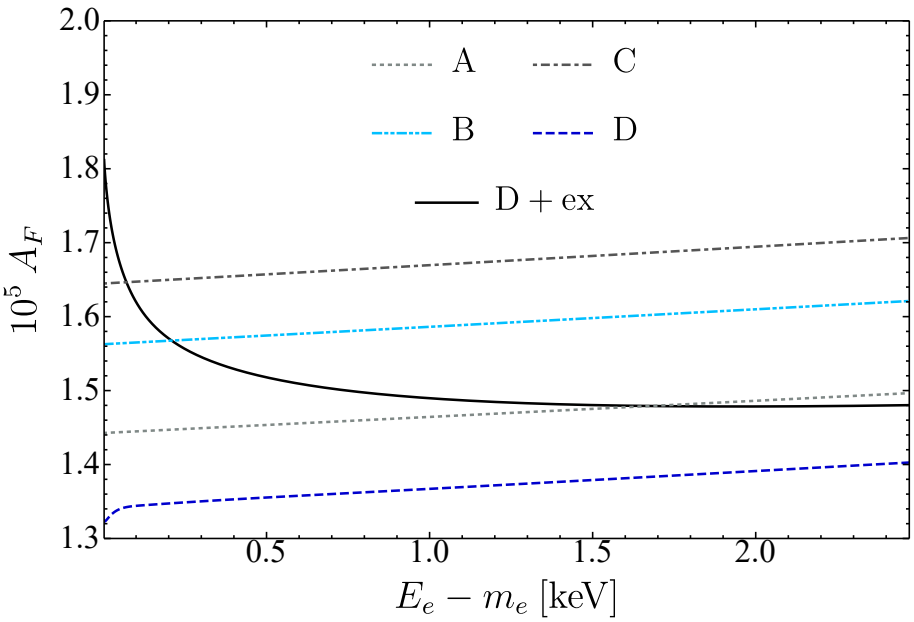

Figure 4.8: The shape factor A_F^{I}, i.e. Eq. (4.19), for different approximation schemes, I = A, B, C and D, and the shape factor $A_F^{\mathrm{D+ex}}$, i.e. Eq. (4.20). The figure was taken from [173].

with $T_e = E_e - m_e$ in eV. The optimal fit parameters are $b_1 = 1.50 \times 10^{-5}$ eV^{-1} and $b_2 = 4.82 \times 10^{-11}$ eV^{-2}. The coefficients a^{I} merely act as scaling factors across different approximations of the Fermi functions (e.g., $a^{\mathrm{A}} = 1.44 \times 10^{-5}$). However, they do not alter the linear increasing trend observed in A_F^{I}.

In contrast, $A_F^{\mathrm{D+ex}}$ exhibits a decreasing trend with energy, and its shape becomes more intricate due to the inclusion of the exchange correction. The optimal fit within the energy range from 700 eV to the Q-value is achieved by adopting the following assumption,

$$A_F^{\mathrm{D+ex}} = a^{\mathrm{D+ex}} \left(\frac{b_{-1}}{T_e} + 1 + b_1 T_e + b_2 T_e^2 \right), \tag{4.22}$$

where we found the best fit parameters $b_{-1} = 19.95$ eV, $b_1 = -6.80 \times 10^{-6}$ eV^{-1} and $b_2 = 3.05 \times 10^{-9}$ eV^{-2} with $a^{\mathrm{D+ex}} = 1.46 \times 10^{-5}$. It is important to highlight the sign change of b_1 when the exchange correction is incorporated. The selection of a fit model that includes terms proportional to T_e^{-1} is motivated by experimental shape factors, which have been shown to involve similar terms [167].

The most recent and stringent upper limit on the effective neutrino mass, $m_\beta \leqslant 0.8$ eV, was reported by the KATRIN experiment [124]. This constraint applies within the degenerate neutrino mass region, where $m_1 \simeq m_2 \simeq m_3 \simeq m_\beta = \sum_{k=1}^{3} |U_{ek}|^2 m_k$. Consequently, we substitute all individual neutrino masses, m_k ($k = 1, 2, 3$), with the effective neutrino mass, m_β. For the following analysis, we adopt approximation scheme D for the electron wave functions and incorporate the atomic exchange correction.

The Kurie functions for the unique first forbidden transitions is given by

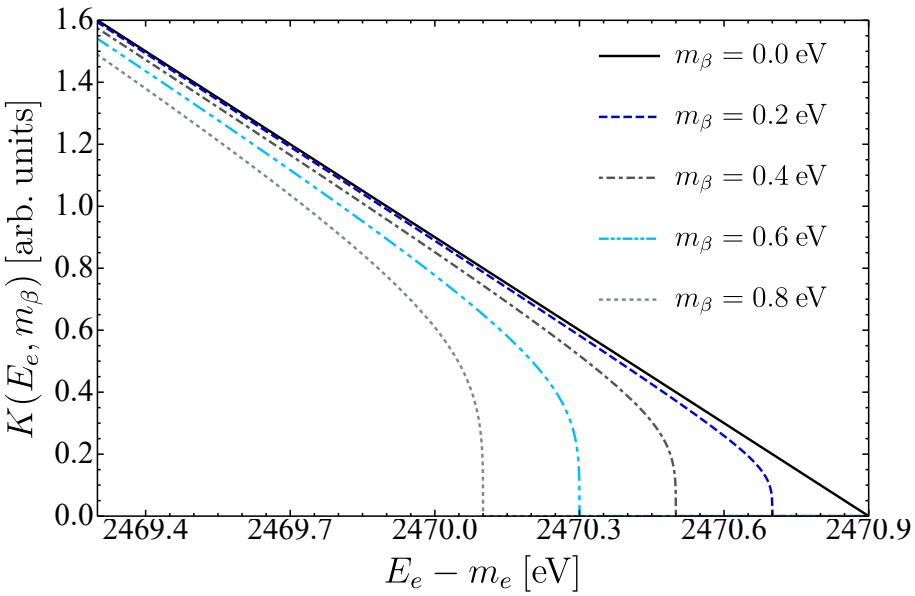

Figure 4.9: The Kurie plots in arbitrary units (a.u.) for the β-decay of ^{187}Re with different values of the effective neutrino mass: $m_\beta = 0.0$, 0.2, 0.4, 0.6, and 0.8 eV. The Q-value considered is 2470.9 eV [130]. The figure was taken from [173].

$$
\begin{aligned}
K(E_e, m_\beta) &= \sqrt{\frac{d\Gamma/dE_e}{p_e E_e (p_e R)^2 F_1(Z, E_e)(1+\eta_2^{\mathrm{T}}(E_e))}} \\
&= G_F V_{ud} \sqrt{\frac{B}{6\pi^3}} (E_0 - E_e) \sqrt[4]{1 - \frac{m_\beta^2}{(E_0 - E_e)^2}} \\
&\times \left[1 + \frac{p_\nu}{p_e} \frac{F_0(Z, E_e)}{F_1(Z, E_e)} \frac{(1+\eta_1^{\mathrm{T}}(E_e))}{(1+\eta_2^{\mathrm{T}}(E_e))}\right]^{1/2} . \qquad (4.23)
\end{aligned}
$$

The Kurie functions for the β-decay of ^{187}Re are shown in Fig. 4.9 for different values of the effective neutrino mass. For the case of $m_\beta = 0$, the Kurie plot, which represents $K(E_e, m_\beta)$ versus E_e, maintains linearity by incorporating the exchange correction for $p_{3/2}$ wave state electrons in the denominator of its definition. The only term capable of altering this linear behavior is the last term in the squared brackets. However, its deviation from unity is minimal–remaining below 6×10^{-5} for kinetic energies above 1000 eV. In the region of interest, ranging from 2300 eV to the Q-value, the deviation further reduces to less than 10^{-6}.

4.5 Conclusions

The distortion observed in endpoint measurements of low Q-value β-decay spectra serves as a direct method for probing neutrino masses. Current experiments primarily focus on ground-state-to-ground-state β transitions, while next-generation investigations may consider ultra-low Q-value (below 1 keV) ground-state-to-excited-state β transitions as promising candidates. With the growing interest in extracting neutrino masses from β-decays, providing precise theoretical predictions for the β-spectrum has become essential. However, these predictions pose challenges due to the classification of β transitions and the multitude of atomic effects influencing the low-energy region.

In this study, we investigated the ground-state-to-ground-state unique first forbidden β transition from $^{187}\mathrm{Re}(5/2^+)$ to $^{187}\mathrm{Os}(1/2^-)$, incorporating all relevant corrections to both the spectrum and decay rate. Building upon our earlier work, we included additional corrections for finite nuclear size, diffuse nuclear surface, screening, and exchange effects in the rhenium β-decay model. The latter two effects were calculated using a self-consistent Dirac-Hartree-Fock-Slater description for the atomic bound electrons of the final atom. Given that rhenium β emission involves a mixture of $s_{1/2}$-state and $p_{3/2}$-state electrons, our exchange correction accounts for all possible contributions from exchanges with $s_{1/2}$, $p_{3/2}$, $p_{1/2}$, and $d_{3/2}$ bound orbitals. Our results reveal significant modifications to the partial decay rates of both $s_{1/2}$- and $p_{3/2}$-state emission channels due to screening and exchange effects, while preserving the experimentally established dominance of $p_{3/2}$-state emission.

A key outcome of this work is that, beyond altering the partial decay rates, the exchange correction induces substantial modifications in the shape of the total electron spectrum for rhenium β-decay. By analyzing deviations from an allowed spectrum, we show that calculations with and without the exchange effect produce entirely different shape factors, changing from an increasing linear behavior to a decreasing quadratic one. We provided best-fit parameters for both cases.

The impact of this shape modification is significant enough to incorporate the exchange correction into the definition of the Kurie plot to preserve its linearity in scenarios with zero effective neutrino mass. Furthermore, we showed how varying effective neutrino masses influence the Kurie plots near the endpoint of $^{187}\mathrm{Re}$ β-decay.

In conclusion, our findings highlight the critical role of atomic effects, particularly the exchange correction, in current and future investigations of the neutrino mass scale using β-decay.

5 Improved formalism for $2\nu\beta\beta$-decay

5.1 Introduction

The accuracy of observables such as the single and summed energy distributions, as well as the angular correlation between emitted electrons, plays a pivotal role in testing hypotheses related to $2\nu\beta\beta$-decay [75, 76] and in probing the underlying mechanisms responsible for $0\nu\beta\beta$-decay [77, 73, 78, 79, 80]. Furthermore, the current experimental constraints on various strength parameters associated with beyond the Standard Model (BSM) scenarios are derived by analyzing the shape of the summed electron energy distribution in $2\nu\beta\beta$-decay [86].

Standard Model predictions for $2\nu\beta\beta$-decay are also crucial in searches for weakly interacting massive particles (WIMPs) and coherent elastic neutrino-nucleus scattering (CEνNS). In particular, for liquid Xenon experiments, the $2\nu\beta\beta$-decay of ^{136}Xe serves as an unavoidable source of background. Consequently, precise theoretical descriptions of $2\nu\beta\beta$-decay are essential for upcoming experiments targeting WIMPs and CEνNS [81, 82, 83, 84].

In this Chapter, we enhance the precision of theoretical predictions for observables in $2\nu\beta\beta$-decay by incorporating radiative and atomic exchange corrections for the emitted electrons. Our primary analysis focuses on the $2\nu\beta\beta$-decay of ^{100}Mo, but the results are expected to be broadly applicable to other nuclei undergoing $2\nu\beta\beta$-decay. These corrections build upon our earlier work [78, 179], where we improved the $2\nu\beta\beta$-decay description using a Taylor expansion formalism that accounts for the lepton energies within the NMEs denominators. This approach allows for a decomposition of observables into partial components governed by the parameters ξ_{31} and ξ_{51}. The formalism also establishes connections with the single state dominance (SSD) and higher state dominance (HSD) hypotheses.

The radiative correction accounts for processes involving the exchange of a virtual photon or the emission of a real photon during $2\nu\beta\beta$-decay. For the atomic exchange correction, we consider scenarios where an electron emitted during the decay can exchange places with an atomic bound electron, while the bound electron transitions into a continuum state of the final atom. The required bound and continuum states for the atomic exchange calculation are modeled using the Dirac-Hartree-Fock-Slater self-consistent framework. Our results indicate a roughly 5% increase in the $2\nu\beta\beta$-decay rate of ^{100}Mo, predominantly due to radiative correction. Additionally, we observe the following effects: (i) A sharp increase in low-energy single-electron events caused by the exchange correction, consistent with prior β-decay studies [150, 151, 168, 172]; (ii) A 10 keV leftward shift in the maximum of the summed electron spectrum, driven by the combined influence of both corrections. Finally, we present the fully corrected single and summed electron spectra for the $2\nu\beta\beta$-decay of ^{100}Mo, evaluated for three sets of $\xi_{31}^{2\nu}$ and $\xi_{51}^{2\nu}$ parameters. These include predictions under the HSD hypothesis, the SSD hypothesis, and values based on experimental measurements.

In the final part of this Chapter, we present the Taylor expansion formalism applied to $2\nu\beta\beta$-decay for $0^+ \to 2^+$ transitions. Measurements of various transitions in ^{150}Nd and ^{148}Nd to different excited states were carried out over 5.845 years using a four-crystal low-background HPGe γ spectrometry system at the STELLA underground low-background laboratory of LNGS-INFN. Although the specifics of the experimental setup and methodology are not included here, the experimentally determined half-life values

and limits provide a practical benchmark for evaluating the accuracy of our theoretical predictions. We demonstrate that our model, which incorporates the Taylor expansion formalism, radiative and exchange corrections, and QRPA calculations for the NMEs, achieves excellent agreement with the experimental half-lives and limits for the $2\nu\beta\beta$-decay of ^{150}Nd and ^{148}Nd to various excited states.

5.2 The standard $2\nu\beta\beta$-decay formalism for $0^+ \to 0^+$ transitions

The inverse half-life of the $2\nu\beta\beta$-decay, $0^+ \to 0^+$ nuclear transition, is defined as

$$\left[T^{2\nu}_{1/2}\right]^{-1} = \frac{\Gamma^{2\nu}}{\ln(2)}, \tag{5.1}$$

where $\Gamma^{2\nu}$ is the decay rate.

The differential decay rate for a $0^+ \to 0^+$ nuclear transition with respect to the angle $0 \leq \theta \leq \pi$ between the emitted electrons can be written as [87]

$$\frac{d\Gamma^{2\nu}}{d(\cos\theta)} = \frac{\Gamma^{2\nu}}{2}\left(1 + K^{2\nu}\cos\theta\right), \tag{5.2}$$

where

$$K^{2\nu} = -\frac{\Lambda^{2\nu}}{\Gamma^{2\nu}}, \tag{5.3}$$

is the angular correlation coefficient. The decay rates are given by

$$\begin{aligned}\begin{Bmatrix}\Gamma^{2\nu}\\ \Lambda^{2\nu}\end{Bmatrix} =& \frac{m_e(G_\beta m_e^2)^4}{8\pi^7}(g_A^{\text{eff}})^4\frac{1}{m_e^{11}}\int_{m_e}^{E_i-E_f-m_e} p_{e_1}E_{e_1}\int_{m_e}^{E_i-E_f-E_{e_1}} p_{e_2}E_{e_2}\\ &\times\int_0^{E_i-E_f-E_{e_1}-E_{e_2}} E_{\nu_1}^2E_{\nu_2}^2\begin{Bmatrix}\mathcal{A}^{2\nu}F_{ss}(E_{e_1})F_{ss}(E_{e_2})\\ \mathcal{B}^{2\nu}E_{ss}(E_{e_1})E_{ss}(E_{e_2})\end{Bmatrix}dE_{\nu_1}dE_{e_2}dE_{e_1}\end{aligned} \tag{5.4}$$

where $G_\beta = G_F\cos\theta_C$ (G_F is the Fermi constant and θ_C is the Cabbibo angle [180]) and m_e is the mass of electron. E_i, E_f, E_{e_i} ($E_{e_i} = \sqrt{p_{e_i}^2 + m_e^2}$, $i = 1, 2$) and E_{ν_i} are the energies of initial and final nuclei, electrons and antineutrinos, respectively. The energy of the second antineutrino can be obtained from the energy conservation, $E_{\nu_2} = E_i - E_f - E_{e_1} - E_{e_2} - E_{\nu_1}$. The difference $E_i - E_f$ represents the energy difference between the initial and final 0^+ nuclear states, which can be determined by relating it to the Q-value of the $2\nu\beta\beta$-decay, given as $Q = E_i - E_f - 2m_e$.

The functions F_{ss} and E_{ss} are given by

$$\begin{aligned}F_{ss}(E_e) =& |\tilde{g}_{-1}(E_e, R)|^2 + \left|\tilde{f}_1(E_e, R)\right|^2,\\ E_{ss}(E_e) =& 2\,\text{Re}\{\tilde{g}_{-1}(E_e, R)\tilde{f}_1^*(E_e, R)\}.\end{aligned} \tag{5.5}$$

where the electron radial wave functions, $\tilde{g}_\kappa(E_e, r)$ and $\tilde{f}_\kappa(E_e, r)$, discussed in Section A.3, are evaluated on the nuclear surface $R = 1.2A^{1/3}$. Note that the functions $f_{11}^{(0)}$ and $f_{11}^{(1)}$ defined in [181] are equivalent in our notation with $F_{ss}(E_{e_1})F_{ss}(E_{e_2})$ and $-E_{ss}(E_{e_1})E_{ss}(E_{e_2})$, respectively. $\mathcal{A}^{2\nu}$ and $\mathcal{B}^{2\nu}$ consist of products of the Fermi (F) and Gamow-Teller (GT) nuclear matrix elements, which depend on lepton energies,

$$
\begin{aligned}
\mathcal{A}^{2\nu} =& \frac{1}{4}\left|\left(\frac{g_V}{g_A^{\text{eff}}}\right)^2\left(M_F^K+M_F^L\right)-\left(M_{GT}^K+M_{GT}^L\right)\right|^2 \\
&+\frac{3}{4}\left|\left(\frac{g_V}{g_A^{\text{eff}}}\right)^2\left(M_F^K-M_F^L\right)+\frac{1}{3}\left(M_{GT}^K-M_{GT}^L\right)\right|^2,
\end{aligned}
\tag{5.6}
$$

$$
\begin{aligned}
\mathcal{B}^{2\nu} =& \frac{1}{4}\left|\left(\frac{g_V}{g_A^{\text{eff}}}\right)^2\left(M_F^K+M_F^L\right)-\left(M_{GT}^K+M_{GT}^L\right)\right|^2 \\
&-\frac{1}{4}\left|\left(\frac{g_V}{g_A^{\text{eff}}}\right)^2\left(M_F^K-M_F^L\right)+\frac{1}{3}\left(M_{GT}^K-M_{GT}^L\right)\right|^2,
\end{aligned}
\tag{5.7}
$$

where $g_V = 1$ and g_A^{eff} are the vector and the effective axial-vector coupling constants, respectively. The latter is usually model-dependent and remains an open question in nuclear weak interaction processes [182]. The Fermi and Gamow-Teller nuclear matrix elements (NMEs) are given by,

$$
\begin{aligned}
M_F^{K,L} &= m_e \sum_n M_F(n) \frac{E_n(0^+)-(E_i-E_f)/2}{\left[E_n(0^+)-(E_i+E_f)/2\right]^2-\varepsilon_{K,L}^2}, \\
M_{GT}^{K,L} &= m_e \sum_n M_{GT}(n) \frac{E_n(1^+)-(E_i-E_f)/2}{\left[E_n(1^+)-(E_i+E_f)/2\right]^2-\varepsilon_{K,L}^2},
\end{aligned}
\tag{5.8}
$$

with

$$
\begin{aligned}
M_F(n) &= \langle 0_f^+ \| \sum_j \tau_j^+ \| 0_n^+ \rangle \langle 0_n^+ \| \sum_k \tau_k^+ \| 0_i^+ \rangle, \\
M_{GT}(n) &= \langle 0_f^+ \| \sum_j \tau_j^+ \sigma_j \| 1_n^+ \rangle \langle 1_n^+ \| \sum_k \tau_k^+ \sigma_k \| 0_i^+ \rangle.
\end{aligned}
\tag{5.9}
$$

Here, $|0_i^+\rangle$, $|0_f^+\rangle$ are the 0^+ ground states of the initial and final even-even nuclei, respectively, and $|1_n^+\rangle$ ($|0_n^+\rangle$) are all possible states of the intermediate nucleus with angular momentum and parity $J^\pi = 1^+$ ($J^\pi = 0^+$) and energy $E_n(1^+)$ ($E_n(0^+)$). The summations run over all states the intermediate odd-odd nucleus and over all j, k nucleons inside the nucleus. The operator $\sigma_{j,k}$ is the nucleon spin operator, and $\tau_{j,k}^+$ represents the isospin-ladder operator transforming a neutron into a proton. The lepton energies enter in the factors

$$
\begin{aligned}
\varepsilon_K &= \left(E_{e_2}+E_{\nu_2}-E_{e_1}-E_{\nu_1}\right)/2, \\
\varepsilon_L &= \left(E_{e_1}+E_{\nu_2}-E_{e_2}-E_{\nu_1}\right)/2.
\end{aligned}
\tag{5.10}
$$

The maximal value of $|\varepsilon_K|$ and $|\varepsilon_L|$ is the of Q-value of the process ($\varepsilon_{K,L} \in (-Q/2, Q/2)$). For $2\nu\beta\beta$-decay with energetically forbidden transition to intermediate nucleus ($E_n - E_i > -m_e$) the quantity $E_n - (E_i + E_f)/2 = Q/2 + m_e + (E_n - E_i)$ is always larger than half of the Q-value.

The Fermi (Gamow-Teller) operator, which determines the matrix elements $M_F(n)$ ($M_{GT}(n)$) as defined in Eq. (5.9), acts as a generator of an isospin SU(2) (spin-isospin

SU(4)) multiplet symmetry. If both isospin and spin-isospin symmetries were exact in nuclei, the $2\nu\beta\beta$-decay would be strictly forbidden because the ground states of the initial and final nuclei would belong to different multiplets. Typically, it is assumed that the Fermi matrix elements contribute negligibly to the $2\nu\beta\beta$-decay amplitude, as isospin is considered a reasonably accurate symmetry in nuclei. The primary contribution instead arises from the Gamow-Teller matrix elements. This assumption is partially supported by nuclear structure studies, though these results are model-dependent. An open question remains as to whether it is possible to experimentally demonstrate the dominance of the Gamow-Teller contribution over the Fermi contribution in the $2\nu\beta\beta$-decay process.

Commonly, the calculation of the $2\nu\beta\beta$-decay distributions and decay rate is simplified by neglecting $\varepsilon_{K,L}$ in energy denominators of the NMEs from which

$$M^{2\nu}_{F(GT)} \equiv M^{K}_{F(GT)} = M^{L}_{F(GT)} \tag{5.11}$$

and

$$\mathcal{A}^{2\nu} = \mathcal{B}^{2\nu} = \left| \left(\frac{g_V}{g_A^{\text{eff}}} \right)^2 M^{2\nu}_F - M^{2\nu}_{GT} \right|^2 , \tag{5.12}$$

where Fermi and Gamow-Teller matrix elements are given by

$$\begin{aligned} M^{2\nu}_F &= m_e \sum_n \frac{\langle 0^+_f \| \sum_j \tau^+_j \| 0^+_n \rangle \langle 0^+_n \| \sum_k \tau^+_k \| 0^+_i \rangle}{E_n(0^+) - (E_i + E_f)/2}, \\ M^{2\nu}_{GT} &= m_e \sum_n \frac{\langle 0^+_f \| \sum_j \tau^+_j \sigma_j \| 1^+_n \rangle \langle 1^+_n \| \sum_k \tau^+_k \sigma_k \| 0^+_i \rangle}{E_n(1^+) - (E_i + E_f)/2}. \end{aligned} \tag{5.13}$$

We note that this approximation of neglecting $\varepsilon_{K,L}$ in Eq. is justified under the assumption that higher-lying states (0^+_n, 1^+_n) of the intermediate nucleus dominate the contribution to the $2\nu\beta\beta$-decay rate. This theoretical assumption is referred to as the higher state dominance (HSD) hypothesis. Experimental observations reveal that the Fermi strength distribution from the initial to the intermediate nucleus is primarily concentrated in the region of the Isobaric Analog State, at excitation energies above 10 MeV. This behavior reflects the preservation of isospin symmetry, which prevents significant fragmentation of the Fermi transition. In contrast, the Gamow-Teller strength distribution is fragmented across numerous states of the intermediate nucleus, spanning both the region of the Gamow-Teller resonance and the region of low-lying states. Consequently, while the HSD assumption is well-justified for the Fermi matrix elements $M^{K,L}_F$, it remains an open question whether the dominant contribution to $M^{K,L}_{GT}$ arises from transitions through low-lying 1^+ states, higher-lying states in the Gamow-Teller resonance region, or a mutual cancellation of these contributions.

Another popular assumption, proposed in [183, 184], is that the $2\nu\beta\beta$-decay is governed only by the transition through the first 1^+ state of the intermediate nucleus with energy E_1. This assumption is known as the single state dominance (SSD) hypothesis. Under this assumption, the NMEs are given by,

$$M^{K,L}_{GT} = m_e \frac{M_{GT}(1)\,[E_1 - (E_i + E_f)/2]}{[E_1 - (E_i + E_f)/2]^2 - \varepsilon^2_{K,L}}, \tag{5.14}$$

and $M^{K,L}_F = 0$. In this case, the $2\nu\beta\beta$-decay observables are independent of $M_{GT}(1)$, but are influenced by the lepton energies incorporated in $\varepsilon_{K,L}$ which can not be longer neglected

[75, 76]. Experimental studies of energy distributions conducted for the $2\nu\beta\beta$-decay of ^{82}Se [185] and ^{100}Mo [108] have shown a clear preference for the SSD hypothesis over the HSD hypothesis. However, a more accurate interpretation of the experimental data requires an improved theoretical description of the $2\nu\beta\beta$-decay process.

5.3 Taylor expansion $2\nu\beta\beta$-decay formalism for $0^+ \to 0^+$ transitions

The refined expressions for the $2\nu\beta\beta$ differential decay rates can be derived by applying a Taylor expansion of the denominators in the NMEs over the parameters $\varepsilon_{K,L}$ in Eq. (5.9). The expansion is explicitly given by

$$\begin{aligned} M_{F,GT}^{K,L} &= m_e \sum_n M_{F,GT}(n) \frac{E_n - (E_i + E_f)/2}{[E_n - (E_i + E_f)/2]^2 - \epsilon_{K,L}^2} \\ &= m_e \sum_n M_{F,GT}(n) \frac{1}{E_n - (E_i + E_f)/2} \\ &\times \left\{ 1 + \left(\frac{\epsilon_{K,L}}{E_n - (E_i + E_f)/2} \right)^2 + \left(\frac{\epsilon_{K,L}}{E_n - (E_i + E_f)/2} \right)^4 + \dots \right\} \end{aligned} \tag{5.15}$$

Note that the series was firstly proposed in [78], where only the GT component of the NME was considered and the angular correlation part of the decay rate was omitted. For this part of the thesis, our assumptions are as follows: i) The Fermi nuclear matrix element $M_F^{K,L}$ is predominantly determined by transitions through the isobaric analog state, located at an energy exceeding 10 MeV. Consequently, the impact of lepton energies in the energy denominators is negligible, implying $M_F^{K,L} \simeq M_F$; ii) The Gamow-Teller nuclear matrix element $M_{GT}^{K,L}$ exhibits a non-negligible dependence on lepton energies.

By limiting the expansion to the fourth power in $\varepsilon_{K,L}$, the separation of the decay rates is possible in the following form,

$$\begin{aligned} \Gamma^{2\nu} &= \Gamma_0^{2\nu} + \Gamma_2^{2\nu} + \Gamma_{22}^{2\nu} + \Gamma_4^{2\nu}, \\ \Lambda^{2\nu} &= \Lambda_0^{2\nu} + \Lambda_2^{2\nu} + \Lambda_{22}^{2\nu} + \Lambda_4^{2\nu}. \end{aligned} \tag{5.16}$$

Here, the leading $\Gamma_0^{2\nu}$ ($\Lambda_0^{2\nu}$), next to leading $\Gamma_2^{2\nu}$ ($\Lambda_2^{2\nu}$) and next-to-next to leading $\Gamma_{22}^{2\nu}$ and $\Gamma_4^{2\nu}$ ($\Lambda_{22}^{2\nu}$ and $\Lambda_4^{2\nu}$) orders of the Taylor expansion are given by

$$\begin{aligned} \frac{\Gamma_0^{2\nu}}{\ln(2)} &= \left(g_A^{\text{eff}}\right)^4 \mathcal{M}_0 G_0^{2\nu}, \quad \frac{\Gamma_2^{2\nu}}{\ln(2)} = \left(g_A^{\text{eff}}\right)^4 \mathcal{M}_2 G_2^{2\nu}, \\ \frac{\Gamma_{22}^{2\nu}}{\ln(2)} &= \left(g_A^{\text{eff}}\right)^4 \mathcal{M}_{22} G_{22}^{2\nu}, \quad \frac{\Gamma_4^{2\nu}}{\ln(2)} = \left(g_A^{\text{eff}}\right)^4 \mathcal{M}_4 G_4^{2\nu}, \end{aligned} \tag{5.17}$$

and

$$\begin{aligned} \frac{\Lambda_0^{2\nu}}{\ln(2)} &= \left(g_A^{\text{eff}}\right)^4 \mathcal{N}_0 H_0^{2\nu}, \quad \frac{\Lambda_2^{2\nu}}{\ln(2)} = \left(g_A^{\text{eff}}\right)^4 \mathcal{N}_2 H_2^{2\nu}, \\ \frac{\Lambda_{22}^{2\nu}}{\ln(2)} &= \left(g_A^{\text{eff}}\right)^4 \mathcal{N}_{22} H_{22}^{2\nu}, \quad \frac{\Lambda_4^{2\nu}}{\ln(2)} = \left(g_A^{\text{eff}}\right)^4 \mathcal{N}_4 H_4^{2\nu}. \end{aligned} \tag{5.18}$$

The phase-space factors (PSFs) are defined as

$$\begin{aligned}\left\{\begin{matrix} G_N^{2\nu} \\ H_N^{2\nu} \end{matrix}\right\} =& \frac{m_e (G_\beta m_e^2)^4}{8\pi^7 \ln(2)} \frac{1}{m_e^{11}} \int_{m_e}^{E_i - E_f - m_e} p_{e_1} E_{e_1} \int_{m_e}^{E_i - E_f - E_{e_1}} p_{e_2} E_{e_2} \\ & \times \int_0^{E_i - E_f - E_{e_1} - E_{e_2}} E_{\nu_1}^2 E_{\nu_2}^2 \mathcal{A}_N^{2\nu} \left\{\begin{matrix} F_{ss}(E_{e_1}) F_{ss}(E_{e_2}) \\ E_{ss}(E_{e_1}) E_{ss}(E_{e_2}) \end{matrix}\right\} dE_{\nu_1} dE_{e_2} dE_{e_1}\end{aligned} \tag{5.19}$$

for $N = \{0, 2, 22, 4\}$ and with

$$\begin{aligned}\mathcal{A}_0^{2\nu} &= 1, & \mathcal{A}_2^{2\nu} &= \frac{\varepsilon_K^2 + \varepsilon_L^2}{(2m_e)^2}, \\ \mathcal{A}_{22}^{2\nu} &= \frac{\varepsilon_K^2 \varepsilon_L^2}{(2m_e)^4}, & \mathcal{A}_4^{2\nu} &= \frac{\varepsilon_K^4 + \varepsilon_L^4}{(2m_e)^4},\end{aligned} \tag{5.20}$$

The products of nuclear matrix elements are given by

$$\begin{aligned}\mathcal{M}_0 =& \left[\left(\frac{g_V}{g_A^{\text{eff}}}\right)^2 M_{F-1}^{2\nu} - M_{GT-1}^{2\nu}\right]^2 \\ \mathcal{M}_2 =& -\left[\left(\frac{g_V}{g_A^{\text{eff}}}\right)^2 M_{F-1}^{2\nu} - M_{GT-1}^{2\nu}\right] M_{GT-3}^{2\nu} \\ \mathcal{M}_{22} =& \frac{1}{3}\left(M_{GT-3}^{2\nu}\right)^2 \\ \mathcal{M}_4 =& \frac{1}{3}\left(M_{GT-3}^{2\nu}\right)^2 - \left[\left(\frac{g_V}{g_A^{\text{eff}}}\right)^2 M_{F-1}^{2\nu} - M_{GT-1}^{2\nu}\right] M_{GT-5}^{2\nu}\end{aligned} \tag{5.21}$$

and

$$\begin{aligned}\mathcal{N}_0 =& \left[\left(\frac{g_V}{g_A^{\text{eff}}}\right)^2 M_{F-1}^{2\nu} - M_{GT-1}^{2\nu}\right]^2 \\ \mathcal{N}_2 =& -\left[\left(\frac{g_V}{g_A^{\text{eff}}}\right)^2 M_{F-1}^{2\nu} - M_{GT-1}^{2\nu}\right] M_{GT-3}^{2\nu} \\ \mathcal{N}_{22} =& \frac{5}{9}\left(M_{GT-3}^{2\nu}\right)^2 \\ \mathcal{N}_4 =& \frac{2}{9}\left(M_{GT-3}^{2\nu}\right)^2 - \left[\left(\frac{g_V}{g_A^{\text{eff}}}\right)^2 M_{F-1}^{2\nu} - M_{GT-1}^{2\nu}\right] M_{GT-5}^{2\nu}\end{aligned} \tag{5.22}$$

where nuclear matrix elements take the forms

$$\begin{aligned}M_{GT-1}^{2\nu} &\equiv M_{GT}^{2\nu} \\ M_{F-1}^{2\nu} &\equiv M_F^{2\nu} \\ M_{GT-3}^{2\nu} &= \sum_n M_{GT}(n) \frac{4\ m_e^3}{(E_n(1^+) - (E_i + E_f)/2)^3}, \\ M_{GT-5}^{2\nu} &= \sum_n M_{GT}(n) \frac{16\ m_e^5}{(E_n(1^+) - (E_i + E_f)/2)^5},\end{aligned} \tag{5.23}$$

By introducing following ratios of NMEs,

$$\xi_{31} = \frac{M^{2\nu}_{GT-3}}{M^{2\nu}_{GT} - \left(\frac{g_V}{g_A^{\rm eff}}\right)^2 M^{2\nu}_F}, \qquad \xi_{51} = \frac{M^{2\nu}_{GT-5}}{M^{2\nu}_{GT} - \left(\frac{g_V}{g_A^{\rm eff}}\right)^2 M^{2\nu}_F}, \tag{5.24}$$

one can write the $2\nu\beta\beta$-decay rate as a function of those ratios,

$$\begin{aligned}\left[T^{2\nu}_{1/2}\right]^{-1} = \frac{\Gamma^{2\nu}}{\ln(2)} = \left(g_A^{\rm eff}\right)^4 \left| \left(\frac{g_V}{g_A^{\rm eff}}\right)^2 M^{2\nu}_F - M^{2\nu}_{GT} \right|^2 \\ \times \left[G^{2\nu}_0 + \xi_{31} G^{2\nu}_2 + \frac{1}{3}\xi^2_{31} G^{2\nu}_{22} + \left(\frac{1}{3}\xi^2_{31} + \xi_{51}\right) G^{2\nu}_4 \right].\end{aligned} \tag{5.25}$$

The observables associated with $2\nu\beta\beta$-decay, such as the half-life and the single and summed electron distributions, are influenced by the parameters ξ_{31} and ξ_{51}. Implicitly, the angular correlation distributions also depend on ξ_{31} and ξ_{51}, as detailed in Chapter 6. Theoretically, these parameters can be predicted by calculating the NMEs within various nuclear models, such as the pn-QRPA with partial isospin restoration [78] or the NSM and pn-QRPA calculations presented in [186].

Experimentally, ξ_{31} and ξ_{51} can be treated as free parameters that control the observables of $2\nu\beta\beta$-decay. The first experimental constraint on ξ_{31} was established by the KamLAND-Zen collaboration through the analysis of the $2\nu\beta\beta$-decay of ^{136}Xe [186]. More recently, the parameters ξ_{31} and ξ_{51} have been explored by the CUPID-Mo experiment [55]. Combining these experimental results with theoretical predictions could provide insights into the effective axial-vector coupling constant $g_A^{\rm eff}$ and into the interplay between contributions from various intermediate states on the NMEs [78].

5.3.1 Analytical integration over the antineutrino energy

Motivated to obtain a simplified expression for the PSFs from Eq. (5.19), we performed the integration over the neutrino energy analytically. In what follows, we denote the integrals with,

$$\mathcal{I}_N = \int_0^{E_i - E_f - E_{e_1} - E_{e_2}} E^2_{\nu_1} E^2_{\nu_2} \mathcal{A}^{2\nu}_N dE_{\nu_1}, \tag{5.26}$$

where $N = \{0, 2, 22, 4\}$, $\mathcal{A}^{2\nu}_N$ functions are defined in Eq. (5.20) and $E_{\nu_2} = E_i - E_f - E_{e_1} - E_{e_2} - E_{\nu_1}$. We used the following standard integrals,

$$\int x^2 (rx+s)^n dx = \frac{1}{r^2}\left(\frac{(rx+s)^{n+3}}{n+3} + 2s\frac{(rx+s)^{n+2}}{n+2} + s\frac{(rx+s)^{n+1}}{n+1} \right), \tag{5.27}$$

with $n \neq -1, -2$, and

$$\begin{aligned}\int x^m (rx+s)^n dx &= \frac{1}{r(m+n+1)}\left(x^m (rx+s)^{n+1} - ms \int x^{m-1}(rx+s)^n dx \right) \\ &= \frac{1}{m+n+1}\left(x^{m+1}(rx+s)^n - ns \int x^m (rx+s)^{n-1} dx \right),\end{aligned} \tag{5.28}$$

with $m > 0$ and $m + n + 1 \neq 0$.

The results can be expressed in the following compact form

$$\begin{aligned}
\mathcal{I}_0 &= \frac{1}{30}a^5, \\
\mathcal{I}_2 &= \frac{1}{420}a^5\frac{1}{(2m_e)^2}(a^2+7b^2), \\
\mathcal{I}_{22} &= \frac{1}{10080}a^5\frac{1}{(2m_e)^4}(a^4-6a^2b^2+21b^4), \\
\mathcal{I}_4 &= \frac{1}{5040}a^5\frac{1}{(2m_e)^4}(a^4+18a^2b^2+21b^4),
\end{aligned} \tag{5.29}$$

where

$$\begin{aligned}
a &= E_i - E_f - E_{e_1} - E_{e_2}, \\
b &= E_{e_1} - E_{e_2}.
\end{aligned} \tag{5.30}$$

5.4 Exchange and radiative corrections for $2\nu\beta\beta$-decay

As in Chapters 3 and 4, we consider the scenario where one electron produced in the $2\nu\beta\beta$-decay is created in a bound orbital of the final atom, corresponding to an occupied orbital in the initial atom. Simultaneously, an atomic electron from that bound orbital transitions to a continuum state of the final atom. This process, known as the atomic exchange correction, has been extensively investigated in β-decay [152, 153, 150, 151, 143, 144, 8, 166, 145, 168, 172]. Here, we extend, for the first time, the study of the exchange correction to the $2\nu\beta\beta$-decay, accounting for the exchange effect for both emitted electrons. Furthermore, we include the first-order radiative correction due to the exchange of a virtual photon or the emission of a real photon during the $2\nu\beta\beta$-decay process.

The leading order radiative correction is given by [8],

$$R(E_e, E_e^{\max}) = 1 + \frac{\alpha}{2\pi}g(E_e, E_e^{\max}) \tag{5.31}$$

where the function $g(E_e, E_e^{\max})$ is given by [175, 176]

$$\begin{aligned}
g(E_e, E_e^{\max}) = {} & 3\ln(m_p) - \frac{3}{4} - \frac{4}{\beta}\mathrm{Li}_2\left(\frac{2\beta}{1+\beta}\right) \\
& + \frac{\tanh^{-1}\beta}{\beta}\left[2\left(1+\beta^2\right) + \frac{(E_e^{\max}-E_e)^2}{6E_e^2} - 4\tanh^{-1}\beta\right] \\
& + 4\left(\frac{\tanh^{-1}\beta}{\beta} - 1\right)\left[\frac{E_e^{\max}-E_e}{3E_e} - \frac{3}{2} + \ln\left[2\left(E_e^{\max}-E_e\right)\right]\right],
\end{aligned} \tag{5.32}$$

Here, $\beta = p_e/E_e$, $E_e^{\max}$ is the maximum total energy of the electron, m_p is the proton mass and $\mathrm{Li}_2(x)$ is the dilogarithm function.

Since only $s_{1/2}$-wave state electron emissions are considered in $2\nu\beta\beta$-decay, the exchange correction is calculated similarly to the allowed β-decay [150, 151]:

$$\begin{aligned}
\eta^T(E_e) &= f_s(2T_s + T_s^2) + (1-f_s)(2T_{\bar{p}} + T_{\bar{p}}^2) \\
&= \eta_s(E_e) + \eta_{\bar{p}}(E_e)
\end{aligned} \tag{5.33}$$

Here,

$$f_s = \frac{g'^2_{-1}(E_e, R)}{g'^2_{-1}(E_e, R) + f'^2_{+1}(E_e, R)}, \tag{5.34}$$

where $g'_\kappa(E_e, r)$ and $f'_\kappa(E_e, r)$ are the real large- and small-component radial wave functions, respectively, for electrons emitted in the continuum states corresponding to the final atom. All primed quantities pertain to the final atomic system. As in the case of β-decay, since we work with the modulus of the radial components, the phase shifts can be omitted. The quantities T_s and $T_{\bar{p}}$ depend respectively on the overlaps between the bound $s_{1/2}$ ($\kappa = -1$) and $\bar{p} \equiv p_{1/2}$ ($\kappa = 1$) orbitals wave functions in the initial state atom and the continuum states wave functions in the final state atom,

$$T_s = \sum_{(ns)'} T_{ns} = -\sum_{(ns)'} \frac{\langle \psi'_{E_e s} | \psi_{ns} \rangle}{\langle \psi'_{ns} | \psi_{ns} \rangle} \frac{g'_{n,-1}(R)}{g'_{-1}(E_e, R)} \tag{5.35}$$

and

$$T_{\bar{p}} = \sum_{(n\bar{p})'} T_{n\bar{p}} = -\sum_{(n\bar{p})'} \frac{\langle \psi'_{E_e \bar{p}} | \psi_{n\bar{p}} \rangle}{\langle \psi'_{n\bar{p}} | \psi_{n\bar{p}} \rangle} \frac{f'_{n,+1}(R)}{f'_{+1}(E_e, R)}. \tag{5.36}$$

where $g_{n,\kappa}(r)$ and $f_{n,\kappa}(r)$ are the large- and small-component radial wave functions, respectively, for bound electrons. The summations in T_s and $T_{\bar{p}}$ are performed over all occupied orbitals of the final atom, which, under the sudden approximation, correspond to the electronic configuration of the initial atom.

As discussed in Chapter 3, the correct calculation of the exchange correction requires maintaining orthogonality between the continuum and bound wave functions of the electron in the final atomic system, i.e., $\langle \psi'_{E_e \kappa} | \psi'_{n\kappa} \rangle = 0$ [150, 151]. We have shown that non-orthogonal states significantly influence the overall behavior of the exchange correction as a function of the emitted electron's kinetic energy. Consequently, we adopt the same approach as outlined in [168, 172], employing a modified self-consistent DHFS framework to compute the electron wave functions.

We emphasize that the exchange correction in $2\nu\beta\beta$-decay differs from that in β-decay due to the distinct charge changes occurring in the two processes. In $2\nu\beta\beta$-decay, the initial nucleus undergoes a charge change of two units, whereas in β-decay, the charge change is only by one unit. Consequently, although we use the same notation (with single primes for the final states) as in [168], the overlaps described in Eqs. (5.35) and (5.36) involve wave functions corresponding to atomic systems with a charge change of two units.

In Fig. 5.1, we present the total exchange correction for one electron emitted during the $2\nu\beta\beta$-decay (solid line) and β-decay (dashed line) of molybdenum isotopes. The figure shows that the exchange effect is consistently larger for $2\nu\beta\beta$-decay than for β-decay across the entire energy spectrum. For β-decay, the analytical parametrization introduced in [168] was used to determine η^T. It is noteworthy that ^{100}Mo does not undergo β-decay. However, the exchange correction exhibits only minor variation with respect to the molybdenum isotopic mass number. Thus, the corrections depicted in Fig. 5.1 are applicable to all molybdenum isotopes.

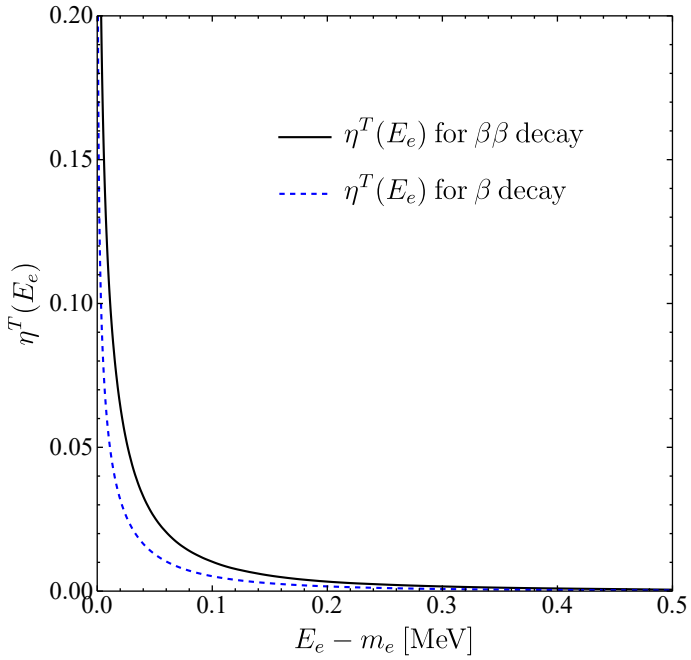

Figure 5.1: The total atomic exchange correction for β-decay (dashed blue) and $2\nu\beta\beta$-decay (solid black) of molybdenum. The figure is taken from [187].

5.5 The $2\nu\beta\beta$-decay of ^{100}Mo, $0^+ \to 0^+$ transition

We investigate the influence of the exchange and radiative corrections in the $2\nu\beta\beta$-decay of ^{100}Mo to the ground state of ^{100}Ru. The corrections are introduced on top of the Taylor expansion formalism, but for simplicity we have omitted the Fermi component of the NMEs. Under these assumptions the parameters ξ_{31} and ξ_{51} from Eq. (5.24) are simplified to

$$\xi_{31} = \frac{M^{2\nu}_{GT-3}}{M^{2\nu}_{GT-1}}, \qquad \xi_{51} = \frac{M^{2\nu}_{GT-5}}{M^{2\nu}_{GT-1}}, \tag{5.37}$$

Taking advantage of the analytical integration over the antineutrino energy preformed in [179] (see Eq. (5.29)), the PSFs, in the Taylor expansion formalism, are given by,

$$\begin{aligned} G^{2\nu}_N = \frac{(G_F\,|V_{ud}|)^4}{8\pi^7 m_e^2 \ln 2} \int_{m_e}^{E_i - E_f - m_e} \int_{m_e}^{E_i - E_f - E_{e_1}} \\ \times p_{e_1} E_{e_1} \left[1 + \eta^T(E_{e_1})\right] R(E_{e_1}, E_i - E_f - m_e) \\ \times p_{e_2} E_{e_2} \left[1 + \eta^T(E_{e_2})\right] R(E_{e_2}, E_i - E_f - E_{e_1}) \\ \times F_{ss}(E_{e_1}) F_{ss}(E_{e_2}) \mathcal{I}_N dE_{e_2} dE_{e_1} \end{aligned} \tag{5.38}$$

with $N = \{0, 2, 22, 4\}$. Recall that the quantity $E_i - E_f$ represents the energy difference between the initial and final 0^+ nuclear states, and can be determined by relating it to the Q-value of the $2\nu\beta\beta$-decay, given as $Q = E_i - E_f - 2m_e$. For our study, we used $Q = 3.0344$ MeV [188]. The functions $\left[1 + \eta^T(E_e)\right]$ and $R(E_e, E_e^{\max})$ account for the exchange and radiative corrections discussed in Section 5.4.

5.5.1 The SSD hypothesis

The inverse half-life for the $2\nu\beta\beta$-decay under the SSD hypothesis, for a $0^+ \to 0^+$ transition, can be written in the following form,

$$\left[T^{2\nu}_{1/2}\right]^{-1} = \left(g_A^{\text{eff}}\right)^4 \left|M^{2\nu}_{GT}(1)\right|^2 G^{2\nu}_{\text{SSD}}, \tag{5.39}$$

where the square of the single state Gamow-Teller NME is given by

$$\left|M^{2\nu}_{GT}(1)\right|^2 = \left|M^f_1(0^+)M^i_1(0^+)\right|^2, \tag{5.40}$$

where we have used the notation from [75, 76],

$$M^f_n(0^+) \equiv \langle 0^+_f \| \sum_j \tau^+_j \sigma_j \| 1^+_n \rangle, \qquad M^i_n(0^+) \equiv \langle 1^+_n \| \sum_k \tau^+_k \sigma_k \| 0^+_i \rangle. \tag{5.41}$$

Under the SSD hypothesis, the PSF is given by (derived in [187])

$$\begin{aligned} G^{2\nu}_{\text{SSD}} = & \frac{\left(G_F \left|V_{ud}\right|\right)^4}{8\pi^7 m_e^2 \ln(2)} \int_{m_e}^{E_i - E_f - m_e} \int_{m_e}^{E_i - E_f - E_{e_1}} \int_0^{E_i - E_f - E_{e_1} - E_{e_2}} p_{e_1} E_{e_1} p_{e_2} E_{e_2} \\ & \times \left[1 + \eta^T(E_{e_1})\right] R(E_{e_1}, E_i - E_f - m_e) \\ & \times \left[1 + \eta^T(E_{e_2})\right] R(E_{e_2}, E_i - E_f - E_{e_1}) \\ & \times F_{ss}(E_{e_1}) F_{ss}(E_{e_2}) E^2_{\nu_1} E^2_{\nu_2} \frac{K^2 + L^2 + KL}{3} dE_{\nu_1} dE_{e_2} dE_{e_1}. \end{aligned} \tag{5.42}$$

where the dimensionless quantities K and L are given by,

$$K = \frac{m_e \left[E_1 - (E_i + E_f)/2\right]}{\left[E_1 - (E_i + E_f)/2\right]^2 - \varepsilon_K^2}, \qquad L = \frac{m_e \left[E_1 - (E_i + E_f)/2\right]}{\left[E_1 - (E_i + E_f)/2\right]^2 - \varepsilon_L^2}. \tag{5.43}$$

An advantage of the SSD hypothesis is that $M^{2\nu}_{GT}(1)$ can be directly related to the electron capture (EC) and β^--decay processes of the first 1^+ state in the intermediate nucleus. For the $2\nu\beta\beta$-decay of ^{100}Mo, this 1^+ state corresponds to the ground state of the intermediate nucleus, ^{100}Tc. Taking into account the recent experimental half-life for $2\nu\beta\beta$-decay of ^{100}Mo, $T^{2\nu-\text{exp}}_{1/2} = (7.07 \pm 0.11) \times 10^{18}$ yr [55], and our calculation for the PSF, $G^{2\nu}_{\text{SSD}} = 4.008 \times 10^{-19}$ yr^{-1}, one can obtain,

$$\left(g_A^{\text{eff}}\right)^2 \left|M^{2\nu}_{GT}(1)\right| = \frac{1}{\sqrt{T^{2\nu-\text{exp}}_{1/2} G^{2\nu}_{\text{SSD}}}} = 0.594 \pm 0.005 \tag{5.44}$$

On the other hand, $M^f_1(0^+)$ and $M^i_1(0^+)$ can be deduced from the $\log(ft)$ values of the EC and β^--decay of the ground state of ^{100}Tc,

$$M^f_1(0^+) = \frac{1}{g_A^{\text{eff}}} \sqrt{\frac{3D}{(ft)_{\beta^-}}}, \quad M^i_1(0^+) = \frac{1}{g_A^{\text{eff}}} \sqrt{\frac{3D}{(ft)_{\text{EC}}}}, \tag{5.45}$$

where $D = \left[2\pi^3 \ln(2)\right] / \left[(G_F \left|V_{ud}\right|)^2 m_e^5\right]$. Taking into account that $\log(ft)_{\text{EC}} = 4.3 \pm 0.1$ and $\log(ft)_{\beta^-} = 4.598 \pm 0.004$ [189], one can obtain,

$$\left(g_A^{\text{eff}}\right)^2 \left|M^{2\nu}_{GT}(1)\right| = \frac{3D}{\sqrt{(ft)_{\beta^-}(ft)_{\text{EC}}}} = 0.671^{+0.085}_{-0.076}, \tag{5.46}$$

where the large variation interval is mainly due to the significant uncertainty in $\log(ft)_{\text{EC}}$, highlighting the need for more precise measurements. The observed disagreement between

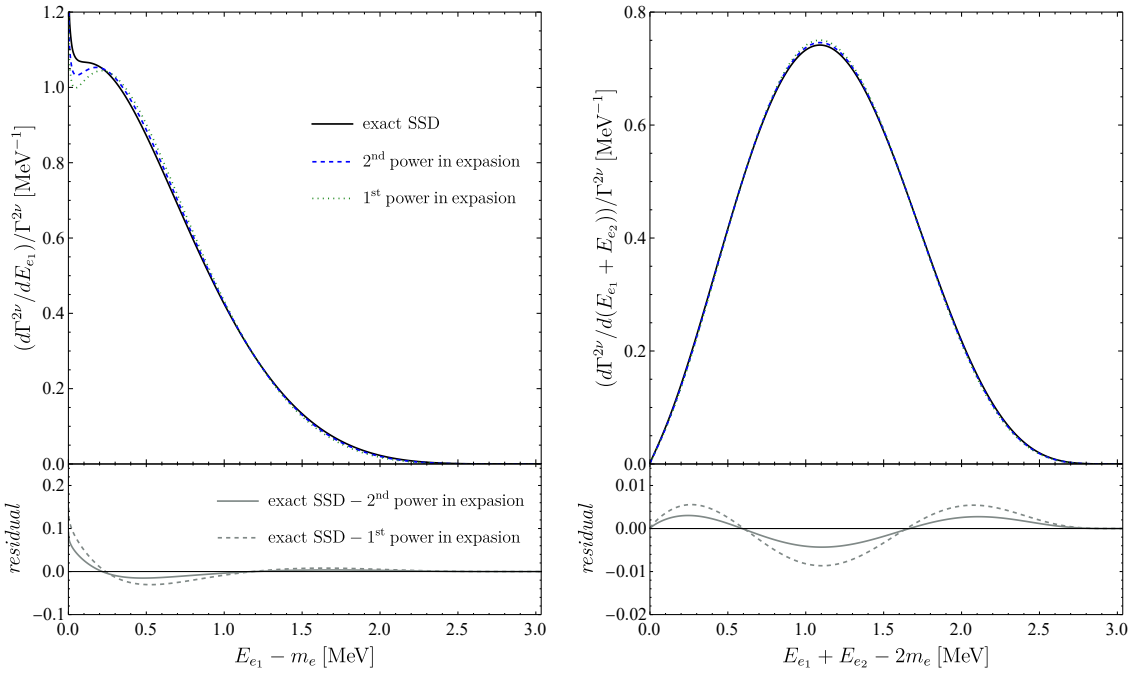

Figure 5.2: The single (left panel) and summed (right panel) electron spectra for $2\nu\beta\beta$-decay of ^{100}Mo from: (solid) the exact SSD formalism, (dashed) Taylor expansion with contributions up to next-to-next to leading order, i.e., $\Gamma^{2\nu} = \Gamma^{2\nu}_0 + \Gamma^{2\nu}_2 + \Gamma^{2\nu}_{22} + \Gamma^{2\nu}_4$, (dotted) Taylor expansion with contributions up to next to leading order, i.e., $\Gamma^{2\nu} = \Gamma^{2\nu}_0 + \Gamma^{2\nu}_2$. All spectra are normalized to unity and they include radiative and exchange corrections. The lower panels display the residuals. The figure is taken from [187].

the experimental NME and the value derived from the $\log(ft)$ suggests that the SSD hypothesis alone does not fully explain the $2\nu\beta\beta$ transition of ^{100}Mo. Contributions from higher 1^+ states in ^{100}Tc are likely necessary for an accurate NME calculation. This discrepancy could potentially be clarified by considering the cancellation effects that arise from the interplay between low-lying and higher-lying states.

Under the SSD hypothesis, the expressions for ξ_{31} and ξ_{51} from Eq. (5.37) are simplified, as only one term contributes in the summations in the NMEs, i.e.,

$$\xi^{\rm SSD}_{31} = \frac{4\ m_e^2}{[E_1 - (E_i + E_f)/2]^2}, \qquad \xi^{\rm SSD}_{51} = \frac{16\ m_e^4}{[E_1 - (E_i + E_f)/2]^4}. \tag{5.47}$$

In the particular case of the $2\nu\beta\beta$-decay of ^{100}Mo, using the nuclear states energy differences $E_1 - (E_i + E_f)/2 = (E_1 - E_i) + (E_i - E_f)/2 = 1.685$ MeV [189], one can find $\xi^{\rm SSD}_{31} = 0.368$ and $\xi^{\rm SSD}_{51} = 0.135$.

Although the SSD hypothesis is an assumption for $2\nu\beta\beta$-decay, it has a theoretical advantage in that the inverse half-life separation from Eq. (5.39) does not neglect the leptonic energy dependence in the decay rate. This makes SSD observables useful for verifying those derived from the Taylor expansion formalism with fixed $\xi^{\rm SSD}_{31} = 0.368$ and $\xi^{\rm SSD}_{51} = 0.135$.

The results are shown in Fig. 5.2, displaying the single (left panel) and summed (right panel) electron spectra for the $2\nu\beta\beta$-decay of ^{100}Mo. Spectra labeled "exact SSD" are calculated using Eq. (5.42). For the Taylor expansion formalism, two scenarios are considered: (i) up to next-to-next-to-leading-order contributions are included, i.e., $\Gamma^{2\nu} = \Gamma^{2\nu}_0 + \Gamma^{2\nu}_2 + \Gamma^{2\nu}_{22} + \Gamma^{2\nu}_4$ (dashed curves); (ii) up to next-to-leading-order contributions

are included, i.e., $\Gamma^{2\nu} = \Gamma^{2\nu}_0 + \Gamma^{2\nu}_2$ (dotted curves). All spectra are normalized to unity, incorporate radiative and exchange corrections, and use DHFS electron wave functions. As expected, adding more terms in the Taylor expansion improves agreement with the exact SSD for both single and summed electron spectra, as shown by the residuals in the bottom panels of Fig. 5.2.

A similar verification of the Taylor expansion formalism was previously performed in [179] for the single-electron spectra of $2\nu\beta\beta$-decay of ^{82}Se, ^{100}Mo, and ^{150}Nd. The same verification is presented in Chapter 6. However, additional corrections applied in this study were not included in that earlier work. Overall, we observe good agreement between the spectra, indicating that including up to next-to-next-to-leading-order terms in the decay rate provides a sufficiently precise description of the $2\nu\beta\beta$-decay of ^{100}Mo. For experiments with higher statistics, higher-order terms could also be incorporated.

5.5.2 The HSD hypothesis

In contrast to the SSD hypothesis, the HSD hypothesis assumes that the transition is primarily governed by the Gamow-Teller resonance (GTR) states, which are typically located approximately $10-12$ MeV above the ground state of the initial nucleus. This allows for a clear separation between the nuclear structure contributions and the phase-space integration,

$$\left[T^{2\nu}_{1/2}\right]^{-1} = \left(g_A^{\text{eff}}\right)^4 \left|M^{2\nu}_{GT}\right|^2 G^{2\nu}_0. \tag{5.48}$$

Because no experimental information is available for the EC and β^- decay of the GTR state of the intermediate nucleus, one can approximate,

$$\left(g_A^{\text{eff}}\right)^2 \left|M^{2\nu}_{GT}\right| = \frac{1}{\sqrt{T^{2\nu-\text{exp}}_{1/2} G^{2\nu}_0}} = 0.202 \pm 0.002, \tag{5.49}$$

where the $G^{2\nu}_0$ calculated in this work (see Table 5.1) is the leading order PSF from the Taylor expansion formalism.

Assuming that only one state from the GTR region, with energy E_{GTR}, dominates the transition, the ratios of the NMEs from the Taylor expansion formalism can be estimated from,

$$\xi^{\text{HSD}}_{31} = \frac{4\ m_e^2}{\left[E_{\text{GTR}} - (E_i + E_f)/2\right]^2}, \quad \xi^{\text{HSD}}_{51} = \frac{16\ m_e^4}{\left[E_{\text{GTR}} - (E_i + E_f)/2\right]^4}, \tag{5.50}$$

For $E_{\text{GTR}} > 10$ MeV, and consequently $(E_{\text{GTR}} - E_i) + (E_i - E_f)/2 > 11.685$ MeV, it becomes clear that the ratios are negligible. Specifically, for the $2\nu\beta\beta$-decay of ^{100}Mo, we find $\xi^{\text{HSD}}_{31} < 7.6 \times 10^{-3}$ and $\xi^{\text{HSD}}_{51} < 5.9 \times 10^{-5}$. While a more precise determination of the GTR energy can be obtained from [190], the conclusion remains unchanged. Additionally, it is worth mentioning that a toy model was proposed in [191] to represent the $2\nu\beta\beta$-decay NME as a combination of contributions from the first state and a single GTR state of the intermediate nucleus.

5.5.3 The corrected spectra for the $2\nu\beta\beta$-decay of ^{100}Mo

We begin by investigating the impact of radiative and exchange corrections on the single-electron spectra in the $2\nu\beta\beta$-decay of ^{100}Mo. Our focus is on the first two terms

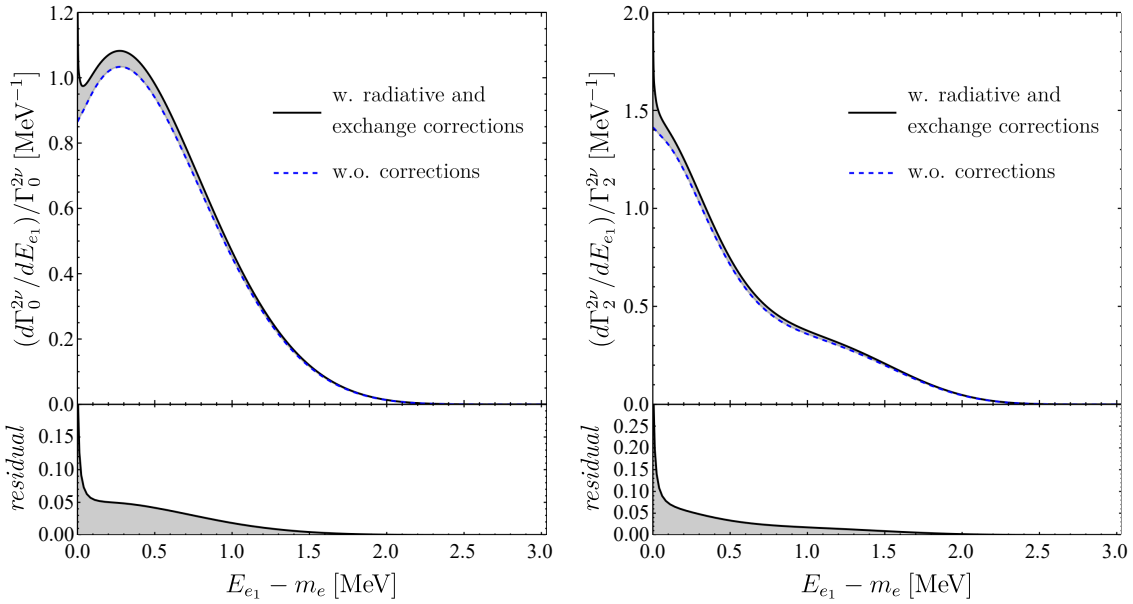

Figure 5.3: The first two contributions to the single electron spectrum of $2\nu\beta\beta$-decay of ^{100}Mo, i.e., $d\Gamma_0/dE_e$ and $d\Gamma_2/dE_e$ with (solid curve) and without (dashed curve) radiative and exchange corrections. Only the uncorrected spectra are normalized to unity and the lower panels present the residuals. The figure is taken from [187].

of the Taylor expansion formalism, $d\Gamma_0/dE_e$ and $d\Gamma_2/dE_e$. The combined effect of these corrections is depicted in Fig. 5.3. The uncorrected spectra (dashed lines) are normalized to unity, while the corrected spectra (solid lines) are normalized to the total decay rate of the uncorrected distribution.

A significant modification is observed in the low-energy region (0–100 keV), where the atomic exchange correction leads to a steep increase. This finding aligns with previous results from β-decay studies [150, 151, 168, 172]. Unlike the exchange correction, the radiative correction has little effect on the shape of the spectra, as evidenced by the residuals (lower panels), which closely follow the spectral distributions. These results indicate that atomic exchange corrections significantly affect the low-energy spectrum shape, while radiative corrections primarily alter the overall decay rate.

The influence of radiative and exchange corrections on the total decay rate of the

Table 5.1: The phase space factors $G_N^{2\nu}$ with $N = \{0, 2, 22, 4\}$ for the $2\nu\beta\beta$-decay of ^{100}Mo. The results are obtained from Ref. [179] (first row) and within the DHFS framework without additional corrections (second row). The third row corresponds to the results with the exchange correction, the fourth includes the radiative correction, and the fifth presents the calculations with both corrections. The last row displays the percentage deviations from the uncorrected DHFS results due to the radiative and exchange corrections. All values are given in units of yr^{-1}.

Correction(s)	$G_0^{2\nu}$	$G_2^{2\nu}$	$G_{22}^{2\nu}$	$G_4^{2\nu}$
Ref. [179]	3.279×10^{-18}	1.498×10^{-18}	1.972×10^{-19}	8.576×10^{-19}
DHFS	3.307×10^{-18}	1.511×10^{-18}	1.989×10^{-19}	8.652×10^{-19}
Exchange	3.343×10^{-18}	1.536×10^{-18}	2.031×10^{-19}	8.835×10^{-19}
Radiative	3.432×10^{-18}	1.568×10^{-18}	2.066×10^{-19}	8.974×10^{-19}
Radiative and Exchange	3.470×10^{-18}	1.593×10^{-18}	2.109×10^{-19}	9.164×10^{-19}
δ	4.91%	5.42%	5.97%	5.92%

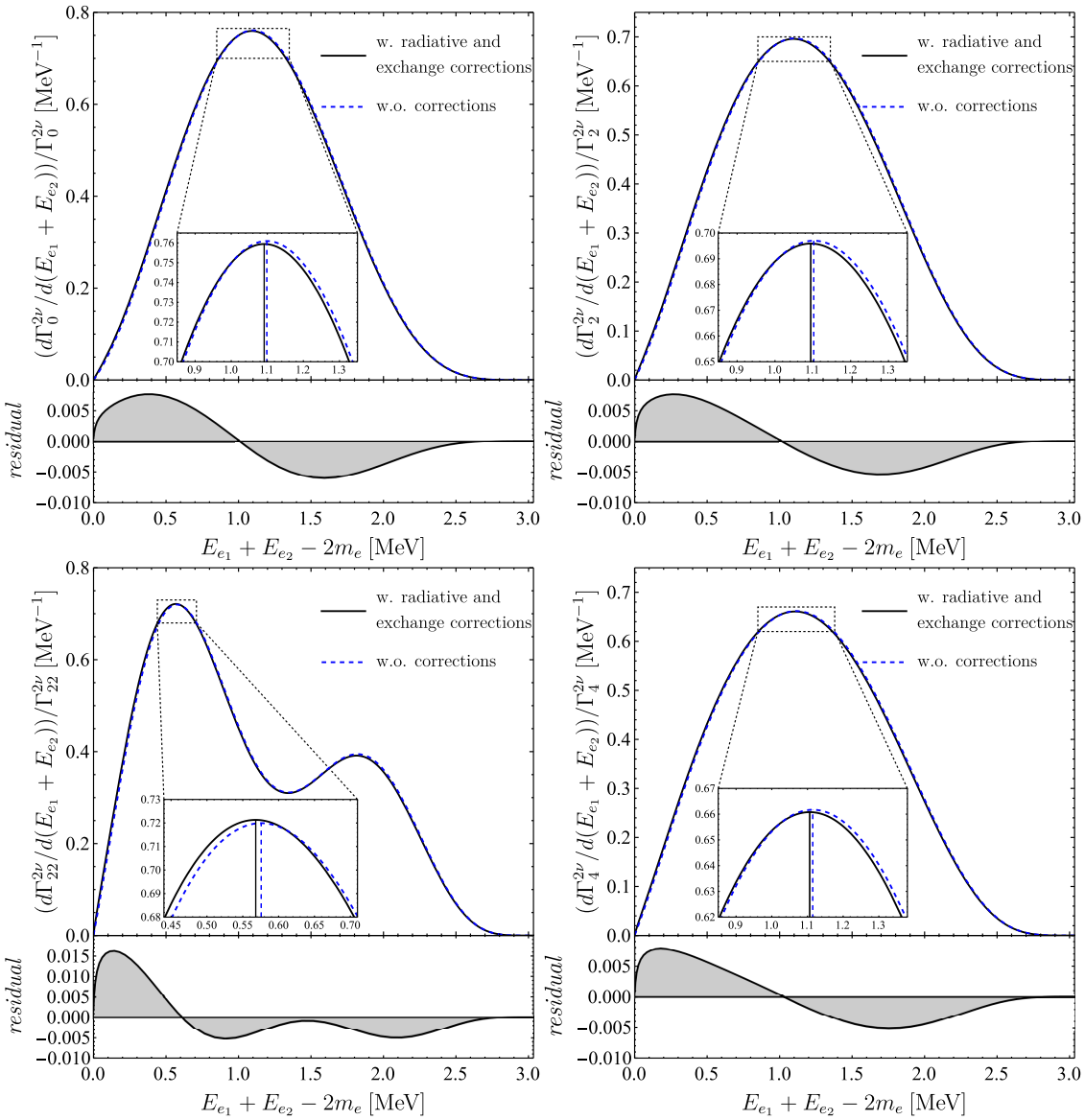

Figure 5.4: The uncorrected (dashed curve) and corrected (solid curve) summed electron spectra for $2\nu\beta\beta$-decay of ^{100}Mo. In the corrected spectra both radiative and exchange corrections are included. All spectra are normalized to unity, and the lower panels display the residuals. The insets provide a closer view of the maxima of the spectra, with vertical lines intersecting at those points. The figure is taken from [187].

$2\nu\beta\beta$-decay in ^{100}Mo is evaluated by examining the PSFs summarized in Table 5.1. For comparison, we include results from [179] (first row), where atomic screening corrections were calculated using the Thomas-Fermi equation, consistent with previous studies [192, 193, 194, 72, 78, 195]. In contrast, the second row presents results derived from the self-consistent DHFS framework, which provides a more refined treatment of atomic screening corrections and a more accurate description of the atomic structure in the final system. The deviations observed between the first and second rows are attributed to this increased precision of the model.

The subsequent rows in Table 5.1 incorporate radiative corrections, exchange corrections, and both corrections combined. The final row quantifies the percentage change between the corrected and uncorrected PSFs using the DHFS framework. From this analysis, it is evident that the radiative and exchange corrections collectively modify each contribution to the decay rate by approximately 5% for the $2\nu\beta\beta$-decay of ^{100}Mo. Among these, the radiative correction is the dominant factor driving the increase in the decay rate.

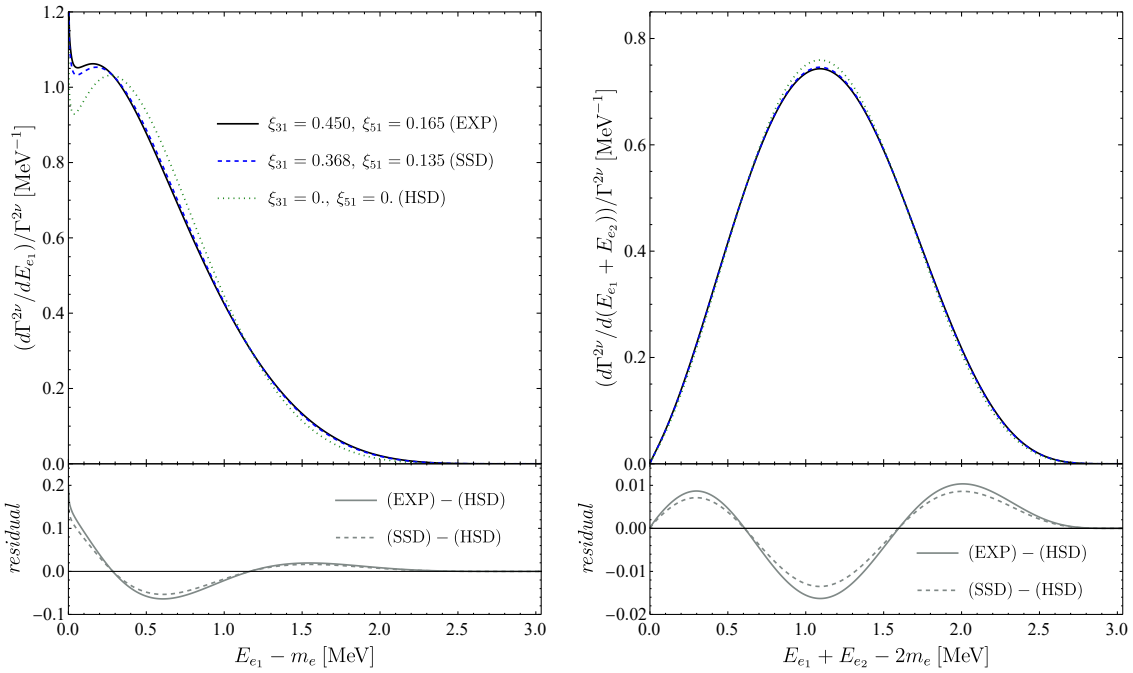

Figure 5.5: The corrected total single (left panel) and total summed (right panel) electron spectra for $2\nu\beta\beta$-decay of ^{100}Mo, for different values of the ratios of NMEs: $\xi_{31} = 0$ and $\xi_{51} = 0$ which correspond to the HSD hypothesis (dotted line); $\xi_{31} = 0.368$ and $\xi_{51} = 0.135$ which correspond to the SSD hypothesis (dashed line); $\xi_{31} = 0.450$ and $\xi_{51} = 0.165$ from the experimental (EXP) measurement [55] (solid line). All spectra are normalized to unity, and the lower panels display the residuals between the spectra corresponding to the experimental and HSD values (solid line) and between the spectra corresponding to the SSD and HSD values (dashed line). The figure is taken from [187].

The impact of radiative and exchange corrections on the shape of the summed energy electron spectra for the $2\nu\beta\beta$-decay of ^{100}Mo was analyzed by considering the first four contributions to the summed electron spectrum, as shown in Fig. 5.4. When both corrections are included, the spectra consistently exhibit a leftward shift, indicating an increase in events in the lower-energy region. This shift is a combined effect of both corrections, as they both influence the spectral maxima in the same direction, resulting in no observable cancellations between their contributions.

The insets in Fig. 5.4 provide a detailed view of the shifts in the spectral maxima,

highlighted by intersecting vertical lines. While these shifts are relatively small—around 10 keV—they are potentially significant given the precision of current and future experimental data. Such shifts may play a crucial role in constraining strength parameters associated with new physics scenarios, as deviations from the SM predictions often manifest as shifts in the spectral maxima.

Finally, we analyze the effect of varying the values of ξ_{31} and ξ_{51} on the total corrected single and summed electron spectra, derived from Eq. (5.25) and considering the PSFs defined in Eq. (5.38). We consider three distinct assumptions: (i) the HSD hypothesis, in which $\xi_{31}^{\rm HSD} = 0$ and $\xi_{51}^{\rm HSD} = 0$, (ii) the SSD hypothesis, in which $\xi_{31}^{\rm SSD} = 0.368$ and $\xi_{51}^{\rm SSD} = 0.135$, and (iii) the experimental measurements of CUPID-Mo collaboration for $\xi_{31}^{\rm EXP} = 0.450$ and $\xi_{51}^{\rm EXP} = 0.165$ [55]. The results are shown in Fig. 5.5, with the single electron spectrum displayed in the left panel and the summed electron spectrum in the right panel. Both type of distributions are normalized to unity and include the effects of radiative and exchange corrections.

The single electron spectrum demonstrates significant sensitivity to the values of ξ_{31} and ξ_{51}. The differences among the scenarios are most pronounced in the low-energy region, although these low-energy events are challenging to detect experimentally. This sensitivity is further illustrated in the bottom panel, which shows the residuals between the different assumptions. For the summed electron spectrum, variations in ξ_{31} and ξ_{51} are most noticeable near the peak of the spectrum, around 1.1 MeV for the $2\nu\beta\beta$-decay of ^{100}Mo, as highlighted by the residuals in the bottom panel. Additionally, the summed spectrum also exhibits non-negligible variations in the regions near 0.3 MeV and 2 MeV. These regions are experimentally accessible and do not require a tracking system for individual electrons, unlike the single electron spectrum.

5.5.4 Conclusions

In this Section, we investigated the $2\nu\beta\beta$-decay of ^{100}Mo by incorporating radiative and atomic exchange corrections. As these corrections are introduced on top of our previous Taylor expansion formalism, we presented a connection between this approach and the SSD and HSD hypotheses. Additionally, we demonstrated that while the SSD hypothesis is an approximation for separating the decay rate, it remains useful in testing the truncation order of the Taylor series. To calculate the atomic exchange correction we employed a modified DHFS self-consistent framework that ensures orthogonality between continuum and bound states. We found that the exchange effect for one electron emitted in $\beta\beta$-decay is larger than in β-decay, as the atomic system's charge changes by two units in the former case.

We found a steep increase in the number of event in the low-energy region of the single electron distribution due to the atomic exchange correction, which is in accordance with the previous studies on β-decay. Although the radiative correction leave the shape of the single electron spectrum unchanged, it is responsible for an overall increase in the decay rate of about 5%. We also found that the both correction contribute constructively to a leftward shift of the maximum in the summed electron spectrum, amounting to about 10 keV for the $2\nu\beta\beta$-decay of ^{100}Mo. Since similar shifts are predicted by new physics scenarios in $2\nu\beta\beta$-decay, our finding might influence the experimental constrains of the BSM parameters. Additionally, this corrections might affect the future ξ_{31} and ξ_{51} measurements. Finally, we provided the corrected single and summed electron spectra for the $2\nu\beta\beta$-decay of ^{100}Mo under the assumptions of the SSD and HSD hypotheses, as well as for experimentally measured values of the ξ_{31} and ξ_{51} parameters.

5.6 Taylor expansion $2\nu\beta\beta$-decay formalism for $0^+ \to 2^+$ transitions

In this Section, we provide the key formulas for the Taylor expansion formalism of $2\nu\beta\beta$-decay, specifically for $0^+ \to 2^+$ nuclear transitions. While the expressions for $0^+ \to 0^+$ transitions are covered in Section 5.3, the following formulas are presented for both 0^+ and 2^+ final states of the nucleus, for comparison and symmetry purposes.

The inverse half-life of the $2\nu\beta\beta$-decay transition to both 0^+ and 2^+ states of the final nucleus takes the form

$$\begin{aligned}\left\{\begin{matrix}\left[T^{2\nu}_{1/2}(0^+)\right]^{-1}\\ \left[T^{2\nu}_{1/2}(2^+)\right]^{-1}\end{matrix}\right\} = &\frac{m_e (G_\beta m_e^2)^4}{8\pi^7 \ln(2)} (g_A^{\text{eff}})^4 \frac{1}{m_e^{11}} \int_{m_e}^{E_i - E_f - m_e} p_{e_1} E_{e_1} \\ &\times \int_{m_e}^{E_i - E_f - E_{e_1}} p_{e_2} E_{e_2} \int_0^{E_i - E_f - E_{e_1} - E_{e_2}} E^2_{\nu_1} E^2_{\nu_2} F_{ss}(E_{e_1}) F_{ss}(E_{e_2}) \\ &\times \left\{\begin{matrix}\mathcal{A}^{2\nu}(0^+)\\ \mathcal{A}^{2\nu}(2^+)\end{matrix}\right\} dE_{\nu_1} dE_{e_2} dE_{e_1}\end{aligned} \tag{5.51}$$

where

$$\begin{aligned}\mathcal{A}^{2\nu}(0^+) &= \frac{1}{4}\left|M^K_{GT}(0^+) + M^L_{GT}(0^+)\right|^2 + \frac{1}{12}\left|M^K_{GT}(0^+) - M^L_{GT}(0^+)\right|^2, \\ \mathcal{A}^{2\nu}(2^+) &= \left|M^K_{GT}(2^+) - M^L_{GT}(2^+)\right|^2,\end{aligned} \tag{5.52}$$

with

$$\frac{M^{K,L}_{GT}(J^\pi)}{m_e} = \sum_n \frac{M_n(J^\pi)\left[E_n(1^+) - (E_i + E_f)/2\right]}{\left[E_n(1^+) - (E_i + E_f)/2\right]^2 - \epsilon^2_{K,L}}. \tag{5.53}$$

The partial transition matrix elements take the form

$$\begin{aligned}M_n(0^+) =& \langle 0^+_f \| \sum_j \tau^+_j \sigma_j \| 1^+_n \rangle \langle 1^+_n \| \sum_k \tau^+_k \sigma_k \| 0^+_i \rangle \\ M_n(2^+) =& \frac{1}{\sqrt{3}} \langle 2^+_f \| \sum_j \tau^+_j \sigma_j \| 1^+_n \rangle \langle 1^+_n \| \sum_k \tau^+_k \sigma_k \| 0^+_i \rangle.\end{aligned} \tag{5.54}$$

Here, $|0^+_i\rangle$ and $|J^+_f\rangle$ ($J^\pi = 0^+,\ 2^+$) are the initial (ground) and final (ground or excited) states with angular momentum and parity 0^+ and J^π, respectively. Additionally, $|1^+_n\rangle$ denote all possible states of the intermediate nucleus with angular momentum and parity 1^+ and energy $E_n(1^+)$.

The dependence of the GT nuclear matrix element $M^{K,L}_{GT}(J^\pi)$ on lepton energies is taken into account by performing a Taylor expansion over the ratio $\varepsilon_{K,L}/\left[E_n - (E_i + E_f)/2\right]$ in the denominator of Eq. (5.53). By limiting our consideration to the fourth (sixth) power in $\varepsilon_{K,L}$ for $J^\pi = 0^+$ ($J^\pi = 2^+$) we get:

$$
\begin{aligned}
\frac{\left[T^{2\nu}_{1/2}(0^+)\right]^{-1}}{(g_A^{\rm eff})^4} =& \mathcal{M}_0(0^+)G_0^{2\nu}(0^+) + \mathcal{M}_2(0^+)G_2^{2\nu}(0^+) \\
&+\mathcal{M}_{22}(0^+)G_{22}^{2\nu}(0^+) + \mathcal{M}_4(0^+)G_4^{2\nu}(0^+), \\
\frac{\left[T^{2\nu}_{1/2}(2^+)\right]^{-1}}{(g_A^{\rm eff})^4} =& \mathcal{M}_{22}(2^+)G_{22}^{2\nu}(2^+) + \mathcal{M}_6(2^+)G_6^{2\nu}(2^+).
\end{aligned}
\tag{5.55}
$$

The products of the NMEs for $2\nu\beta\beta$-decay, transitions to 0^+ states, are given by (see also Eq. (5.21))

$$
\begin{aligned}
\mathcal{M}_0(0^+) &= \left[M^{2\nu}_{GT-1}(0^+)\right]^2, \\
\mathcal{M}_2(0^+) &= M^{2\nu}_{GT-1}(0^+)M^{2\nu}_{GT-3}(0^+), \\
\mathcal{M}_{22}(0^+) &= \frac{1}{3}\left[M^{2\nu}_{GT-3}(0^+)\right]^2, \\
\mathcal{M}_4(0^+) &= \frac{1}{3}\left[M^{2\nu}_{GT-3}(0^+)\right]^2 + M^{2\nu}_{GT-1}(0^+)M^{2\nu}_{GT-5}(0^+)
\end{aligned}
\tag{5.56}
$$

and for transitions to 2^+ states,

$$
\begin{aligned}
\mathcal{M}_{22}(2^+) &= \left[M^{2\nu}_{GT-3}(2^+)\right]^2, \\
\mathcal{M}_6(2^+) &= M^{2\nu}_{GT-3}(2^+)M^{2\nu}_{GT-5}(2^+).
\end{aligned}
\tag{5.57}
$$

The explicit expressions for the NMEs are the following:

$$
\begin{aligned}
M^{2\nu}_{GT-1}(0^+) &= \sum_n M_n(0^+)\frac{m_e}{E_n(1^+) - (E_i+E_f)/2}, \\
M^{2\nu}_{GT-3}(0^+) &= \sum_n M_n(0^+)\frac{4\ m_e^3}{\left(E_n(1^+) - (E_i+E_f)/2\right)^3}, \\
M^{2\nu}_{GT-5}(0^+) &= \sum_n M_n(0^+)\frac{16\ m_e^5}{\left(E_n(1^+) - (E_i+E_f)/2\right)^5},
\end{aligned}
\tag{5.58}
$$

and

$$
\begin{aligned}
M^{2\nu}_{GT-3}(2^+) &= \sum_n M_n(2^+)\frac{4\ m_e^3}{\left(E_n(1^+) - (E_i+E_f)/2\right)^3}, \\
M^{2\nu}_{GT-5}(2^+) &= \sum_n M_n(2^+)\frac{16\ m_e^5}{\left(E_n(1^+) - (E_i+E_f)/2\right)^5}.
\end{aligned}
\tag{5.59}
$$

The PSFs for $2\nu\beta\beta$-decay for transitions to 0^+ and 2^+ states are given by

$$
\begin{aligned}
\begin{Bmatrix} G_N^{2\nu}(0^+) \\ G_{N'}^{2\nu}(2^+) \end{Bmatrix} =& \frac{m_e (G_\beta m_e^2)^4}{8\pi^7 \ln 2} \frac{1}{m_e^{11}} \\
&\times \int_{m_e}^{E_i - E_f - m_e} p_{e_1} E_{e_1} F_{ss}(E_{e_1}) \left[1 + \eta^T(E_{e_1})\right] R(E_{e_1}, E_i - E_f - m_e) \\
&\times \int_{m_e}^{E_i - E_f - E_{e_1}} p_{e_2} E_{e_2} F_{ss}(E_{e_2}) \left[1 + \eta^T(E_{e_2})\right] R(E_{e_2}, E_i - E_f - E_{e_1}) \\
&\times \int_{0}^{E_i - E_f - E_{e_1} - E_{e_2}} E_{\nu_1}^2 E_{\nu_2}^2 \begin{Bmatrix} \mathcal{A}_N^{2\nu}(0^+) \\ \mathcal{A}_{N'}^{2\nu}(2^+) \end{Bmatrix} dE_{\nu_1} dE_{e_2} dE_{e_1}
\end{aligned}
\tag{5.60}
$$

with $N = \{0, 2, 22, 4\}$ and $N' = \{22, 6\}$. It should be noted that we have included the radiative and exchange corrections as in Section 5.4. In the phase space expressions the functions $\mathcal{A}_N^{2\nu}(0^+)$ are equivalent with the ones from Eq. (5.20) and

$$
\begin{aligned}
\mathcal{A}_{22}^{2\nu}(2^+) &= \frac{\left(\varepsilon_K^2 - \varepsilon_L^2\right)^2}{(2m_e)^4}, \\
\mathcal{A}_{6}^{2\nu}(2^+) &= 2\frac{\left(\varepsilon_K^2 - \varepsilon_L^2\right)^2 \left(\varepsilon_K^2 + \varepsilon_L^2\right)}{(2m_e)^6}.
\end{aligned}
\tag{5.61}
$$

5.7 The $2\nu\beta\beta$-decay of ^{150}Nd and ^{148}Nd, $0^+ \to 0^+$ and $0^+ \to 2^+$ transitions

The Taylor expansion formalism is tested for the $2\nu\beta\beta$-decay of ^{150}Nd and ^{148}Nd. Measurements of various transitions of these isotopes to different excited states were conducted over a period of 5.845 years using a four-crystal low-background HPGe γ spectrometry system at the STELLA underground low-background laboratory of LNGS-INFN. While the experimental setup and procedures are not detailed here, the experimentally determined half-life values and limits serve as a practical benchmark for assessing the accuracy of the theoretical predictions. The decay schemes of ^{150}Nd and ^{148}Nd are shown in Fig. 5.6 and Fig. 5.7, respectively.

For the computation of the NMEs from Eqs. (5.58-5.59), we utilize the spherical proton-neutron QRPA method with isospin symmetry restoration [199]. The pairing and residual interactions, along with the two-nucleon short-range correlations, are derived from the same modern, realistic nucleon-nucleon potentials—specifically, the charge-dependent Bonn potential [200]. Pairing correlations between like nucleons are treated consistently in both cases using the Bardeen–Cooper–Schrieffer (BCS) approximation with fixed gap parameters for protons and neutrons (see Table 5.2).

The intermediate nuclear states are constructed using pn-QRPA phonons, while the ground states of the initial and final nuclei are represented as BCS states. As shown in [201], deformation primarily affects the overlap factors of these BCS states. Consequently, in this study, deformation effects are incorporated via BCS overlap factors derived from deformed BCS calculations [202], yielding values of 0.52 for the ^{150}Nd system and 0.73 for the ^{148}Nd system.

The wave functions for the 2^+ states are constructed using spherical QRPA methods, with the detailed expressions for decay transitions from the intermediate states to these final 2^+ states provided in [203, 204]. For the first excited 0_1^+ state, the so-called Boson Expansion Method (BEM) is employed. This method represents the 0_1^+ state as a polynomial of 2^+

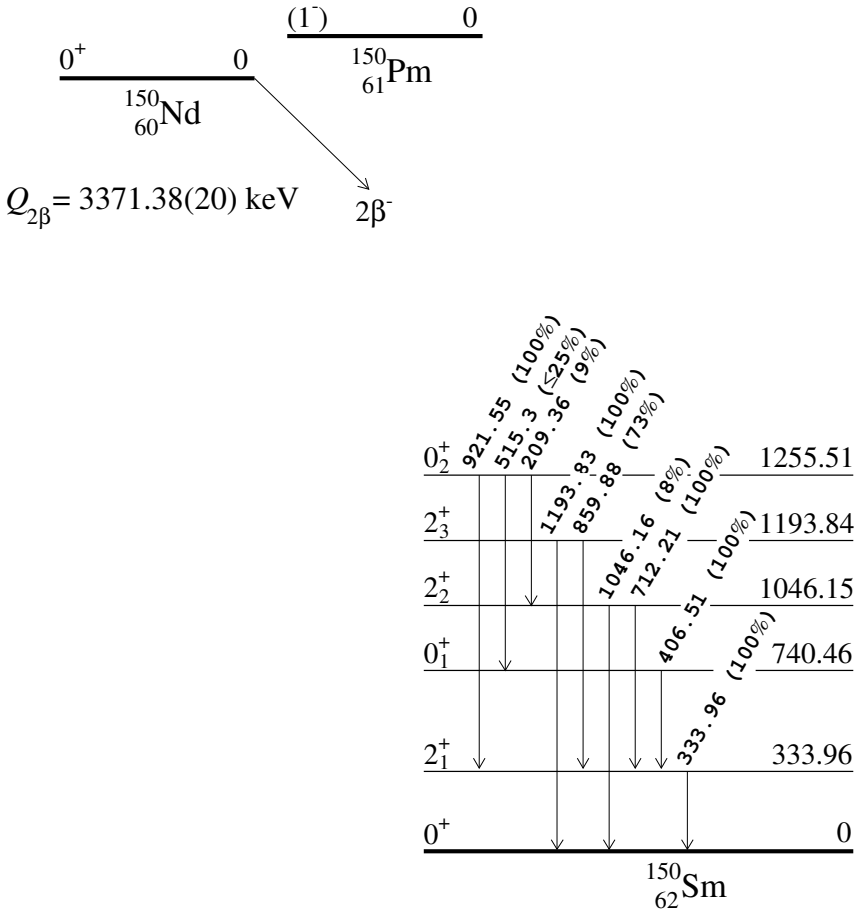

Figure 5.6: A simplified decay scheme of ^{150}Nd [196]. The energies of the excited levels and of the emitted γ quanta are given in keV (the relative intensities of the γ quanta are given in parentheses). The Q-value for double-β-decay energy of ^{150}Nd is taken from [197].

QRPA phonons. The detailed expression for the transitions from intermediate states to this 0_1^+ state is outlined in [205].

In the calculation of NMEs, it is essential to determine the key parameters for pn-QRPA, namely g_{pp}, the particle-particle interaction strength. Following the methodology outlined in [199], for the decay of ^{150}Nd to the ground state, $g_{pp}^{T=1}$ for the iso-vector channel is set by ensuring $M_F^{2\nu}$ vanishes. The iso-scalar channel parameter $g_{pp}^{T=0}$ is then determined by reproducing the experimental half-life of ^{150}Nd using Eq. (5.55) for a specified g_A^{eff}. For ^{148}Nd, in the absence of a measured half-life, $g_{pp}^{T=0}$ is fixed by imposing the condition $M_{GT-cl}^{2\nu} = 0$ [206]. In the case of like-nucleon QRPA calculations, $g_{pp}^{T=1}$ is set equal to the value obtained from the pn-QRPA calculation with isospin symmetry restoration.

For the decay of ^{150}Nd to 2^+ states, our results suggest that the NMEs are not as sensitive to the $g_{pp}^{T=0}$ value as the ones for the decay to the ground states. Therefore, the half-lives are then solely determined by the g_A^{eff} values used. For the decay to first 0_1^+ excited states, $M_{GT-1}(0^+)$ is slightly sensitive to $g_{pp}^{T=0}$ but the other two NMEs are not sensitive to the $g_{pp}^{T=0}$ values we choose.

For ^{148}Nd, the NMEs for decay to the ground state are significantly larger than those for ^{150}Nd. This is primarily attributed to the greater overlap factor derived within the BCS framework for nuclei and the notably larger proton pairing gap, Δ_p. As the half-life for the $2\nu\beta\beta$-decay of ^{148}Nd has not yet been measured, pseudo spin-isospin SU(4) symmetry is applied as a guiding assumption [206]. Future experimental data could provide insights

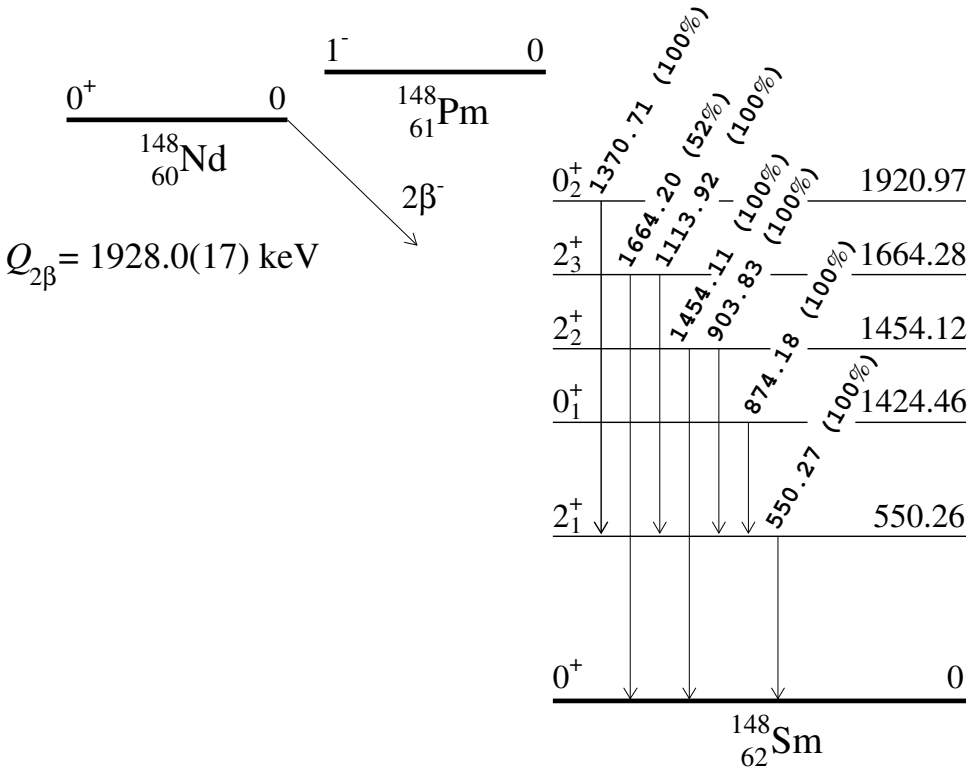

Figure 5.7: A simplified decay scheme of ^{148}Nd [198]. The energies of the excited levels and of the emitted γ quanta are given in keV (the relative intensities of the γ quanta are shown in parentheses). The Q-value for double-β-decay energy of ^{148}Nd is taken from [197].

Table 5.2: Pairing gaps for protons (Δ_p) and neutrons (Δ_n) determined phenomenologically from the odd-even mass differences through a symmetric five-term formula involving the experimental binding energies. β_2 is the deformation parameter extracted from the measured E2 probability.

Isotope	Δ_p [MeV]	Δ_n [MeV]	β_2
^{150}Nd	1.193	1.045	0.285
^{150}Sm	1.444	1.195	0.193
^{148}Nd	1.387	1.121	0.201
^{148}Sm	1.347	1.057	0.142

into the validity of this assumption. For decays to 2^+ states, the NMEs are also larger compared to those of ^{150}Nd. However, for decays to 0^+ states, the NMEs are relatively suppressed. It is worth noting that NMEs associated with decays to excited states are generally less sensitive to the model parameters, such as g_{pp}.

The calculation of the PSFs with exchange and radiative corrections, as given by Eq. (5.60), requires good knowledge of both the bound and continuum states for electrons within the potential of the final positively charged ion, as well as the bound states for electrons within the potential of the initial neutral atom. In this study, we employ the modified self-consistent Dirac-Hartree-Fock-Slater (DHFS) framework to determine the electron wave functions. Detailed descriptions of the nuclear, electronic, and exchange components of the DHFS potential, as well as the convergence of the method, are provided in Appendix A. Our calculations are based on the RADIAL subroutine package [207]. Notably, the modified self-consistent DHFS framework offers not only realistic screening for the continuum wave functions but also ensures orthogonality between the continuum and bound wave functions of the electrons in the final atomic system, i.e., $\langle \psi'_{E_e\kappa} | \psi'_{n\kappa} \rangle = 0$. It has been shown that non-orthogonal states significantly affect the behavior of the exchange correction with respect to the kinetic energy of the emitted electron [168].

The results for $G_N^{2\nu}(0^+)$ with $N = \{0, 2, 22, 4\}$ and $G_{N'}^{2\nu}(2^+)$ with $N' = \{22, 6\}$ are presented in Table 5.3 for the $2\nu\beta\beta$-decay of ^{148,150}Nd to various 0^+ and 2^+ states of ^{148,150}Sm. For transitions to 0^+ states, the trend of the PSFs from different orders of the Taylor expansion aligns with our previous results [78, 179]. We note that for the $2\nu\beta\beta$-decay of ^{150}Nd to the ground state of ^{150}Sm, increasing the precision for the screening correction and adding the radiative and exchange corrections, leads to a 6% increase in the decay rate when compared to the result from [179]. A detailed investigation regarding the interplay between these corrections is discussed in Section 5.5.

The NMEs for the $2\nu\beta\beta$-decay of ^{150}Nd and ^{148}Nd to both ground and excited states are summarized in Table 5.4, alongside their corresponding theoretical and experimental half-life values (or limits). For the decays of ^{150}Nd, two sets of results are provided: one assuming the unquenched g_A value, i.e., $g_A^{\text{eff}} = 1.276$ [209], and the other using a moderately quenched g_A, i.e., $g_A^{\text{eff}} = 0.75 \times 1.276$. Notably, the predicted half-life for the decay of ^{150}Nd to the first 0_1^+ state using the moderately quenched g_A lies within the experimental uncertainty limits, whereas the prediction with unquenched g_A is about two times shorter. For this reason, results for the decay of ^{148}Nd are presented only with $g_A^{\text{eff}} = 0.75 \times 1.276$. Overall, the theoretical predictions for all transitions show a good agreement with the experimental limits.

Besides the half-lives presented in Table 5.4 for ^{150}Nd, we also investigated the $2\nu\beta\beta$ transitions to higher excited states of ^{150}Sm, namely the second 2^+ state (1046.1 keV), the third 2^+ state (1193.8 keV), and the second 0^+ state (1255.5 keV). This analysis was performed to determine whether the first 2^+ excited state at 334 keV is predominantly populated directly through the $2\nu\beta\beta$-decay or if a significant populating probability exists via γ transitions originating from these higher excited 2^+ and 0^+ states, which are themselves populated by $2\nu\beta\beta$ transitions (see Fig. 5.6). To estimate the half-lives for $2\nu\beta\beta$ transitions to the second and third 2^+ states, the NMEs were assumed to be the same as those for the $2\nu\beta\beta$ transition to the first 2^+ state. Similarly, for the $2\nu\beta\beta$-decay to the 0^+ state at 1255.5 keV, the NMEs for the ground-state-to-ground-state transition were considered. However, this assumption overestimates the NMEs, as the 0^+ excited state at 1255.5 keV appears to correspond to a triple-phonon state, and the associated NMEs are expected to be significantly suppressed. Using $g_A^{\text{eff}} = 1.276$ and the phase-space factors (PSFs) provided in Table 5.3, the following theoretical half-lives were determined: $T_{1/2}^{2\nu-\text{th}}(2_2^+) = 4.408 \times 10^{21}$ yr, $T_{1/2}^{2\nu-\text{th}}(2_3^+) = 1.025 \times 10^{22}$ yr and $T_{1/2}^{2\nu-\text{th}}(0_2^+) = 5.820 \times 10^{20}$

Table 5.3: The phase-space factors $G_N^{2\nu}(0^+)$ with $N = \{0, 2, 22, 4\}$ and $G_{N'}^{2\nu}(2^+)$ with $N' = \{22, 6\}$, i.e., Eq. (5.60), for the $2\nu\beta\beta$-decays of ^{150}Nd and ^{148}Nd to different excited states of ^{150}Sm and ^{148}Sm, respectively. The excited states of ^{150}Sm and ^{148}Sm are the ones displayed in Fig. 5.6 and Fig. 5.7, respectively.

Nuclear Transition	$E_i - E_f - 2m_e$ [MeV]	$G_0^{2\nu}(0^+)$ [yr^{-1}]	$G_2^{2\nu}(0^+)$ [yr^{-1}]	$G_{22}^{2\nu}(0^+)$ [yr^{-1}]	$G_4^{2\nu}(0^+)$ [yr^{-1}]	$G_{22}^{2\nu}(2^+)$ [yr^{-1}]	$G_6^{2\nu}(2^+)$ [yr^{-1}]
$^{150}\text{Nd} \to {}^{150}\text{Sm}$							
$0^+ \to 0^+$	3.37138	3.851×10^{-17}	2.191×10^{-17}	3.617×10^{-18}	1.560×10^{-17}	–	–
$0^+ \to 2_1^+$	3.03742	–	–	–	–	2.256×10^{-18}	4.478×10^{-18}
$0^+ \to 0_1^+$	2.63092	4.602×10^{-18}	1.627×10^{-18}	1.698×10^{-19}	7.160×10^{-19}	–	–
$0^+ \to 2_2^+$	2.32523	–	–	–	–	8.177×10^{-20}	9.616×10^{-20}
$0^+ \to 2_3^+$	2.17754	–	–	–	–	3.649×10^{-20}	3.772×10^{-20}
$0^+ \to 0_2^+$	2.11587	7.459×10^{-19}	1.731×10^{-19}	1.206×10^{-20}	4.979×10^{-20}	–	–
$^{148}\text{Nd} \to {}^{48}\text{Sm}$							
$0^+ \to 0^+$	1.9280	3.482×10^{-19}	6.746×10^{-20}	3.957×10^{-21}	1.617×10^{-20}	–	–
$0^+ \to 2_1^+$	1.3777	–	–	–	–	1.433×10^{-22}	6.000×10^{-23}
$0^+ \to 0_1^+$	0.5035	1.152×10^{-23}	1.573×10^{-25}	7.369×10^{-28}	2.631×10^{-27}	–	–
$0^+ \to 2_2^+$	0.4739	–	–	–	–	5.798×10^{-28}	2.904×10^{-29}
$0^+ \to 2_3^+$	0.2637	–	–	–	–	7.901×10^{-31}	1.227×10^{-32}
$0^+ \to 0_2^+$	0.0070	1.468×10^{-36}	3.940×10^{-42}	4.006×10^{-48}	1.295×10^{-47}	–	–

Table 5.4: The NMEs and the theoretical and experimental half-lives (limits) for the $2\nu\beta\beta$-decay of ^{150}Nd and ^{148}Nd to ground and excited states. The experimental results without reference are obtained in the STELLA laboratory (to be published).

Nuc. Tran.	g_A^{eff}	$M^{2\nu}_{GT-1}(0^+)$	$M^{2\nu}_{GT-3}(0^+)$	$M^{2\nu}_{GT-5}(0^+)$	$M^{2\nu}_{GT-3}(2^+)$	$M^{2\nu}_{GT-5}(2^+)$	$T^{2\nu-\text{th}}_{1/2}$ [yr]	$T^{2\nu-\text{exp}}_{1/2}$ [yr]
$^{150}\text{Nd} \rightarrow {}^{150}\text{Sm}$								
$0^+ \rightarrow 0^+$	1.276	0.0255	0.0189	0.0059	–	–	9.34×10^{18}	$9.34^{+0.66}_{-0.64} \times 10^{18}$ [60]
	0.957	0.0491	0.0240	0.0075	–	–	9.31×10^{18}	
$0^+ \rightarrow 0^+_1$	1.276	0.039	0.021	0.011	–	–	0.43×10^{20}	$1.03^{+0.38}_{-0.28} \times 10^{20}$
	0.957	0.042	0.021	0.010	–	–	1.19×10^{20}	
$0^+ \rightarrow 2^+_1$	1.276	–	–	–	0.027	0.010	1.32×10^{20}	$1.5^{+2.4}_{-0.7} \times 10^{20}$
	0.957	–	–	–	0.027	0.010	4.18×10^{20}	
$^{148}\text{Nd} \rightarrow {}^{48}\text{Sm}$								
$0^+ \rightarrow 0^+$	0.957	0.135	0.051	0.017	–	–	1.74×10^{20}	-
$0^+ \rightarrow 0^+_1$	0.957	0.025	0.013	0.007	–	–	1.64×10^{26}	$\geq 8.8 \times 10^{20}$
$0^+ \rightarrow 2^+_1$	0.957	–	–	–	0.043	0.021	3.74×10^{23}	$\geq 6.6 \times 10^{20}$ [208]

yr. The $2\nu\beta\beta$ transitions to the second 2^+, third 2^+, and second 0^+ excited states are suppressed relative to the transition to the first 2^+ state by factors of 0.030, 0.013, and 0.227, respectively. Based on these results, it can be concluded that the 2^+ state at 334 keV is only weakly fed via $2\nu\beta\beta$ transitions to higher excited states.

In Table 5.5, we compare our NMEs and half-life predictions with those reported in [210, 211, 212] for the $2\nu\beta\beta$-decay of ^{150}Nd to the ground state and to the first 2_1^+ state of ^{150}Sm. The NMEs reported in the papers [210, 211, 212] have been properly scaled, as detailed in Table 5.5's caption, to ensure consistency with our definitions of the NMEs, namely Eqs. (5.58) and (5.59). The last column presents the half-lives obtained as,

$$\left[T_{1/2}^{2\nu}(0^+)\right]^{-1} = \left(g_A^{\text{eff}}\right)^4 \left|M_{GT-1}^{2\nu}(0^+)\right|^2 G_0^{2\nu}(0^+), \tag{5.62}$$

for the transition to ground state and

$$\left[T_{1/2}^{2\nu}(2^+)\right]^{-1} = \left(g_A^{\text{eff}}\right)^4 \left|M_{GT-3}^{2\nu}(2^+)\right|^2 G_{22}^{2\nu}(2^+) \tag{5.63}$$

for the transition to first 2_1^+ state. These can be obtained from Eq. (5.55) by keeping only the first term from the Taylor expansion of the decay rates. The comparison between these half-lives and the published ones [210, 211, 212] in Table 5.5 highlights two main aspects: (i) for our work, it underscores the importance of the additional terms arising from the Taylor expansion of the decay rate, and (ii) for the previous papers, it reveals the differences between our first order PSF and the ones used in those studies.

Table 5.5: The comparison between the NMEs and half-lives predictions from this work and the ones reported in [210, 211, 212] for the $2\nu\beta\beta$-decay of ^{150}Nd to the ground state (top part) and to the first 2_1^+ state (bottom part) of ^{150}Sm. For the $0^+ \to 0^+$ transition, the NMEs reported in [211, 212] have been scaled by a factor m_e. For the $0^+ \to 2_1^+$ transition, the NMEs reported in [210] have been scaled by a factor 4, and the NMEs reported in [211, 212] have been scaled by a factor $4m_e^3$. The g_A^{eff} used in the calculations is presented in the fourth column. The fifth column shows the published half-lives in each paper. The last column presents the half-lives obtained with the revised PSFs (see Table 5.3) using only the first term from the Taylor expansion of the decay rates, i.e., Eqs. (5.62) and (5.63).

				$T_{1/2}^{2\nu-\text{th}}(0^+)$[yr]	
Nucl. Trans.	Paper	$\left\|M_{GT-1}^{2\nu}(0^+)\right\|$	g_A^{eff}	Published	Revised PSF
$0^+ \to 0^+$	This work	2.55×10^{-2}	1.276	–	1.50×10^{19}
	This work	4.91×10^{-2}	0.957	–	1.28×10^{19}
	Ref. [210]	5.49×10^{-2}	1.000	6.73×10^{18}	8.61×10^{18}
	Ref. [210]	5.50×10^{-2}	1.000	6.68×10^{18}	8.58×10^{18}
	Ref. [211]	2.79×10^{-1}	1.254	–	1.35×10^{17}
	Ref. [212]	3.80×10^{-1}	1.254	7.89×10^{16}	7.26×10^{16}
				$T_{1/2}^{2\nu-\text{th}}(2^+)$[yr]	
Nucl. Trans.	Paper	$\left\|M_{GT-3}^{2\nu}(2^+)\right\|$	g_A^{eff}	Published	Revised PSF
$0^+ \to 2_1^+$	This work	2.70×10^{-2}	1.276	–	2.29×10^{20}
	This work	2.70×10^{-2}	0.957	–	7.25×10^{20}
	Ref. [210]	2.15×10^{-4}	1.000	7.21×10^{24}	9.57×10^{24}
	Ref. [210]	1.65×10^{-4}	1.000	1.23×10^{25}	1.63×10^{25}
	Ref. [211]	1.42×10^{-3}	1.254	1.50×10^{23}	8.84×10^{22}
	Ref. [212]	1.69×10^{-3}	1.254	4.61×10^{20}	6.26×10^{22}

For the $2\nu\beta\beta$ transition to the ground state, the NMEs from [210] are of the same order of magnitude as ours, while those from [211, 212] are approximately one order of magnitude larger. As a consequence, the NMEs from [211, 212] predict smaller half-lives than the ones obtained in this work. For the $2\nu\beta\beta$ transition to the first 2_1^+ state, the NMEs from [210] are two orders of magnitude smaller than ours, while those from [211, 212] are one order of magnitude smaller. One would expect half-lives two to four orders of magnitude larger than ours in these studies. However, in [212], a half-life of 4.61×10^{20} yr is reported, quite close to our prediction for the moderately quenched g_A. The comparison between the last two columns of Table 5.5 reveals that our calculated PSFs are approximately 30% smaller compared to those reported in [210], which are based on calculations from [63], for both transitions to the ground state and to the first 2^+ state. This validates the computation of $G_0^{2\nu}(0^+)$ and $G_{22}^{2\nu}(2^+)$ from this work, as we have previously demonstrated a 30% decrease in the $2\nu\beta\beta$-decay rate of ^{150}Nd due to a more precise description for the emitted electrons [179]. However, the PSF value for the $2\nu\beta\beta$ transition to the first 2_1^+ state extracted from [212] contradicts those reported in [63, 65] and the value listed in Table 5.3 by a factor of 10^2. For other nuclei, the PSFs from [63, 65] and those derived from [212] generally agree within one order of magnitude. Therefore, the predicted half-life for the $2\nu\beta\beta$-decay of ^{150}Nd to the first 2_1^+ state of ^{150}Sm reported in [212] likely contains a misprint.

6 The angular correlation between the electrons emitted in $2\nu\beta\beta$-decay and $0\nu\beta\beta$-decay

6.1 Introduction

The increasing statistical precision of $2\nu\beta\beta$-decay experiments has opened the door to testing new physics beyond the Standard Model (BSM). Current BSM models extending $2\nu\beta\beta$-decay involve three main approaches [86]: (i) non-standard interactions, (ii) violation of fundamental symmetries, and (iii) emission of new bosons or fermions emitted in the decay. Examples include right-handed neutrino interactions [87], neutrino self-interactions [88], violations of the Pauli exclusion principle [89], Lorentz invariance violation [90, 91, 92, 93], sterile neutrinos within the Q-value range [94, 95], Majoron-emitting $0\nu\beta\beta$ decays [96, 97, 98], and even quadruple-β-decay [107].

While current constraints on BSM parameters rely heavily on analyzing the summed electron energy distribution [86], several BSM scenarios predict their most prominent signatures in the angular correlation distributions between emitted electrons [87, 88, 92, 93]. For instance, right-handed currents in $2\nu\beta\beta$-decay are expected to produce a direction flip in electron emissions [87]. Next-generation experiments, such as SuperNEMO [109] and NEXT-100 [110], aim to measure individual electron tracks. This capability will provide crucial insights into the mechanism underlying $0\nu\beta\beta$-decay [77, 73, 72, 79, 80] and significantly enhance sensitivity to BSM scenarios in $2\nu\beta\beta$-decay.

In this Chapter, we revisit the angular correlation distributions of emitted electrons in both $2\nu\beta\beta$-decay and $0\nu\beta\beta$-decay. In the first part, we deliberately exclude the electronic phase shifts from the calculations to examine how different approximation schemes for the electrostatic potential of the final atom affect angular correlations. We analyze the angular correlations for the eleven most promising $2\nu\beta\beta$-decay nuclei and propose a novel approach for determining the effective axial-vector coupling constant.

In the second part, we focus specifically on the angular correlation between the emitted electrons in the double beta decay (DBD) of ^{100}Mo, paying particular attention to the impact of phase shifts in electronic wave functions. To model the electron wave functions and phase shifts, we employ a modified self-consistent Dirac-Hartree-Fock-Slater potential for the final positive ion ^{100}Ru. This framework provides a realistic description of the nuclear environment, incorporating finite size, diffuse surface effects, and atomic screening.

Our findings demonstrate that phase shifts in electron wave functions have a measurable impact on emission patterns in both $2\nu\beta\beta$-decay and $0\nu\beta\beta$-decay: (i) For $2\nu\beta\beta$-decay, angular correlation coefficients increase by approximately 7% when phase shifts are included. Additionally, we observe a notable energy-dependent feature where electrons are preferentially emitted in the same direction below a specific energy threshold; (ii) For $0\nu\beta\beta$-decay, the angular correlation factor exhibits only a 2% change when phase shifts are included. However, the directional preference remains, potentially influencing the interpretation of mechanisms beyond the light neutrino exchange studied here.

These results suggest that electron phase shifts could influence emission patterns associated with various BSM scenarios in $2\nu\beta\beta$-decay. Moreover, incorporating phase shifts into calculations may refine theoretical tools needed to probe the mechanisms driving $0\nu\beta\beta$-decay. Further investigations in this direction, particularly for alternative decay mechanisms, are left for future studies.

6.2 Formalism

The differential DBD rate for a $0^+ \to 0^+$ nuclear transition with respect to the angle $0 \leq \theta \leq \pi$ between the emitted electrons can be written as [87]

$$\frac{d\Gamma}{d(\cos\theta)} = \frac{\Gamma}{2}(1 + K\cos\theta), \tag{6.1}$$

where

$$K = -\frac{\Lambda}{\Gamma}, \tag{6.2}$$

is the angular correlation coefficient. The above expressions are valid for both $2\nu\beta\beta$-decay and $0\nu\beta\beta$-decay.

6.2.1 The $2\nu\beta\beta$-decay

We have shown in Section 5.3 that the $2\nu\beta\beta$-decay rates are given by [78, 179],

$$\begin{Bmatrix}\Gamma^{2\nu}\\ \Lambda^{2\nu}\end{Bmatrix} = (g_A^{\text{eff}})^4 \left|M_{GT}^{2\nu}\right|^2 \ln(2) \begin{Bmatrix} G_0^{2\nu} + \xi_{31} G_2^{2\nu} + \frac{1}{3}\xi_{31}^2 G_{22}^{2\nu} + \left(\frac{1}{3}\xi_{31}^2 + \xi_{51}\right) G_4^{2\nu} \\ H_0^{2\nu} + \xi_{31} H_2^{2\nu} + \frac{5}{9}\xi_{31}^2 H_{22}^{2\nu} + \left(\frac{2}{9}\xi_{31}^2 + \xi_{51}\right) H_4^{2\nu} \end{Bmatrix} \tag{6.3}$$

where PSFs are given by,

$$\begin{aligned}\begin{Bmatrix} G_N^{2\nu} \\ H_N^{2\nu} \end{Bmatrix} =& \frac{m_e (G_F |V_{ud}| m_e^2)^4}{8\pi^7 \ln(2)} \frac{1}{m_e^{11}} \int_{m_e}^{E_i - E_f - m_e} p_{e_1} E_{e_1} \\ &\times \int_{m_e}^{E_i - E_f - E_{e_1}} p_{e_2} E_{e_2} \mathcal{I}_N \begin{Bmatrix} F_{ss}(E_{e_1}) F_{ss}(E_{e_2}) \\ E_{ss}(E_{e_1}) E_{ss}(E_{e_2}) \end{Bmatrix} dE_{e_2} dE_{e_1}\end{aligned} \tag{6.4}$$

with $N = \{0, 2, 22, 4\}$ and $\mathcal{I}_N$ are given in Eq. (5.29). Using the same analytical integration over the antineutrino energy write the normalized total double electron distribution as

$$\begin{aligned}\frac{1}{\Gamma^{2\nu}} \frac{d\Gamma^{2\nu}}{dE_{e_1} dE_{e_2}} =& \frac{c^{2\nu}}{G_0^{2\nu} + \xi_{31} G_2^{2\nu} + \frac{1}{3}\xi_{31}^2 G_{22}^{2\nu} + \left(\frac{1}{3}\xi_{31}^2 + \xi_{51}\right) G_4^{2\nu}} p_{e_1} E_{e_1} p_{e_2} E_{e_2} \\ &\times F_{ss}(E_{e_1}) F_{ss}(E_{e_2}) \left[\mathcal{I}_0 + \xi_{31}\mathcal{I}_2 + \frac{1}{3}\xi_{31}^2 \mathcal{I}_{22} + \left(\frac{1}{3}\xi_{31}^2 + \xi_{51}\right)\mathcal{I}_4\right],\end{aligned} \tag{6.5}$$

and the total single electron distribution,

$$\begin{aligned}\frac{1}{\Gamma^{2\nu}} \frac{d\Gamma^{2\nu}}{dE_{e_1}} =& \frac{c^{2\nu}}{G_0^{2\nu} + \xi_{31} G_2^{2\nu} + \frac{1}{3}\xi_{31}^2 G_{22}^{2\nu} + \left(\frac{1}{3}\xi_{31}^2 + \xi_{51}\right) G_4^{2\nu}} \\ &\times p_{e_1} E_{e_1} F_{ss}(E_{e_1}) \int_{m_e}^{E_i - E_f - E_{e_1}} p_{e_2} E_{e_2} F_{ss}(E_{e_2}) \\ &\times \left[\mathcal{I}_0 + \xi_{31}\mathcal{I}_2 + \frac{1}{3}\xi_{31}^2 \mathcal{I}_{22} + \left(\frac{1}{3}\xi_{31}^2 + \xi_{51}\right)\mathcal{I}_4\right] dE_{e_2},\end{aligned} \tag{6.6}$$

where

$$c^{2\nu} = \frac{m_e (G_\beta m_e^2)^4}{8\pi^7 \ln 2} \frac{1}{m_e^{11}}. \tag{6.7}$$

We can also define the partial double distributions normalized to the corresponding partial decay rate as

$$\frac{1}{\Gamma_N^{2\nu}}\frac{d\Gamma_N^{2\nu}}{dE_{e_1}dE_{e_2}} = \frac{c^{2\nu}}{G_N^{2\nu}} p_{e_1}E_{e_1}p_{e_2}E_{e_2}F_{ss}(E_{e_1})F_{ss}(E_{e_2})\mathcal{I}_N. \tag{6.8}$$

The angular correlation coefficient is given by,

$$K^{2\nu}(\xi_{31}^{2\nu},\xi_{51}^{2\nu}) = -\frac{H_0^{2\nu}+\xi_{31}H_2^{2\nu}+\frac{5}{9}\xi_{31}^2H_{22}^{2\nu}+\left(\frac{2}{9}\xi_{31}^2+\xi_{51}\right)H_4^{2\nu}}{G_0^{2\nu}+\xi_{31}G_2^{2\nu}+\frac{1}{3}\xi_{31}^2G_{22}^{2\nu}+\left(\frac{1}{3}\xi_{31}^2+\xi_{51}\right)G_4^{2\nu}}. \tag{6.9}$$

One can also define the energy-dependent angular correlation distributions [192, 87],

$$\alpha^{2\nu}(E_e) = -\frac{d\Lambda^{2\nu}/dE_e}{d\Gamma^{2\nu}/dE_e}, \qquad \kappa^{2\nu}(E_{e_1},E_{e_2}) = -\frac{d^2\Lambda^{2\nu}/\left(dE_{e_1}dE_{e_2}\right)}{d^2\Gamma^{2\nu}/\left(dE_{e_1}dE_{e_2}\right)} \tag{6.10}$$

which offer information about the direction of electron emission for given energies. The latter can be written in the following compact form,

$$\kappa(E_{e_1},E_{e_2},\xi_{31}) = -\frac{E_{ss}(E_{e_1})E_{ss}(E_{e_2})}{F_{ss}(E_{e_1})F_{ss}(E_{e_2})}\frac{\left[1+\xi_{31}\tilde{\mathcal{I}}_2+\frac{5}{9}\xi_{31}^2\tilde{\mathcal{I}}_{22}+\left(\frac{2}{9}\xi_{31}^2+\xi_{51}\right)\tilde{\mathcal{I}}_4\right]}{\left[1+\xi_{31}\tilde{\mathcal{I}}_2+\frac{1}{3}\xi_{31}^2\tilde{\mathcal{I}}_{22}+\left(\frac{1}{3}\xi_{31}^2+\xi_{51}\right)\tilde{\mathcal{I}}_4\right]}, \tag{6.11}$$

where the dimensionless quantities are

$$\begin{aligned}
\tilde{\mathcal{I}}_2 &= \frac{1}{14}\frac{1}{(2m_e)^2}(a^2+7b^2)\\
\tilde{\mathcal{I}}_{22} &= \frac{1}{336}\frac{1}{(2m_e)^4}(a^4-6a^2b^2+21b^4)\\
\tilde{\mathcal{I}}_4 &= \frac{1}{168}\frac{1}{(2m_e)^4}(a^4+18a^2b^2+21b^4)
\end{aligned} \tag{6.12}$$

where recall that a and b is given by Eq. (5.30).

6.2.2 The $0\nu\beta\beta$-decay

Assuming only the light-neutrino exchange produced by left-handed currents as the dominant mechanism, the $0\nu\beta\beta$-decay rates are given by [181, 72]

$$\begin{aligned}
\begin{Bmatrix}\Gamma^{0\nu}\\ \Lambda^{0\nu}\end{Bmatrix} =& \frac{(G_F\left|V_{ud}\right|)^4m_e^2}{32\pi^5R^2}(g_A)^4\left|M^{0\nu}\right|^2\frac{\left|m_{\beta\beta}\right|^2}{m_e^2}\\
&\times\int_{m_e}^{E_i-E_f-m_e} p_{e_1}E_{e_1}p_{e_2}E_{e_2}\begin{Bmatrix}F_{ss}(E_{e_1})F_{ss}(E_{e_2})\\ E_{ss}(E_{e_1})E_{ss}(E_{e_2})\end{Bmatrix}dE_{e_1}\\
=&(g_A)^4\left|M^{0\nu}\right|^2\frac{\left|m_{\beta\beta}\right|^2}{m_e^2}\ln(2)\begin{Bmatrix}G^{0\nu}\\ H^{0\nu}\end{Bmatrix},
\end{aligned} \tag{6.13}$$

where $E_{e_2} = E_i - E_f - E_{e_1}$, from the energy conservation, and the effective Majorana neutrino mass is given by

$$m_{\beta\beta} = \sum_{k=1}^{3} U_{ek}^2 m_k. \tag{6.14}$$

Here, U_{ek} and m_k, with $k = 1, 2, 3$, are elements of the PMNS neutrino mixing matrix and the values of neutrino masses, respectively. A recent and comprehensive review on the calculation of the $0\nu\beta\beta$-decay NME, $M^{0\nu}$, can be found in [213]. In this case, one angular correlation distribution can be defined, i.e.,

$$\alpha^{0\nu}(E_e) = -\frac{d\Lambda^{0\nu}/dE_e}{d\Gamma^{0\nu}/dE_e}. \tag{6.15}$$

6.3 The $2\nu\beta\beta$-decay angular correlations without electron phase shift

6.3.1 Results and discussion

In this section, we examine the observables of $2\nu\beta\beta$-decay without accounting for the electron phase shift in the wave functions of the emitted electrons. As elaborated in Section A.3, the functions $\tilde{g}_\kappa$ and $\tilde{f}_\kappa$ are [63, 181]

$$\begin{Bmatrix} \tilde{g}_\kappa(E_e, r) \\ \tilde{f}_\kappa(E_e, r) \end{Bmatrix} = \exp\left(-i\bar{\Delta}_\kappa\right) \begin{Bmatrix} g_\kappa(E_e, r) \\ f_\kappa(E_e, r) \end{Bmatrix} \tag{6.16}$$

where $\bar{\Delta}_\kappa$ is the overall phase shift. We deliberately disregard the phase shift by employing the following expressions:

$$\begin{aligned} F_{ss}(E_e) =& g^2_{-1}(E_e, R) + f^2_1(E_e, R), \\ E_{ss}(E_e) \simeq& 2g_{-1}(E_e, R) f_1(E_e, R), \end{aligned} \tag{6.17}$$

in place of Eq. (5.5).

In our calculations, we adopt three distinct approximation schemes for the emitted electron wave functions—scheme A (see Section A.3.1), scheme B (see Section A.3.2), and scheme C (see Section A.3.4). These schemes differ in their treatment of the Coulomb potential of the final nucleus and the accuracy of the electronic wave functions. Scheme A incorporates the finite nuclear size correction but approximates the radial wave functions for the $s_{1/2}$ state by retaining only the leading-order term in the expansion of r. Scheme B improves upon this by employing exact radial wave functions, although it models the final nucleus as a point-like charge, thereby neglecting finite size corrections. Scheme C offers the most precise approach, using exact radial wave functions while accounting for both finite nuclear size corrections and the screening effect of atomic electrons.

In Figure 6.1, we present the radial wave functions of an electron in the $s_{1/2}$ spherical wave state emitted from the double-β emitter ^{136}Xe. These wave functions are plotted as functions of the electron's kinetic energy, $E_e - m_e$, and evaluated at the surface of the daughter nucleus. The results demonstrate that approximation scheme A, which incorporates the leading finite-size Coulomb correction, agrees well with the other two schemes for $g_{-1}(E_e, R)$. However, it exhibits significant deviations for $f_{+1}(E_e, R)$, especially at low electron energies. Notably, approximation schemes B and C yield consistent results across the entire range of representation intervals.

In Table 6.1, we provide the phase-space factors contributing to the decay rate, as defined in Eq. (6.4), for the $2\nu\beta\beta$-decay of ^{100}Mo, ^{136}Xe, and ^{150}Nd. These calculations employ approximation schemes A, B, and C. Consistent with prior findings in [78], the G_N phase-space factors calculated with exact relativistic electron wave functions (scheme C) are smaller compared to those obtained using approximation scheme A. The results from scheme B fall between the values produced by schemes A and C. For the angular

Table 6.1: Phase space factors $G_N^{2\nu}$ and $H_N^{2\nu}$ with $N = \{0, 2, 22, 4\}$ for $2\nu\beta\beta$-decay of ^{100}Mo, ^{136}Xe and ^{150}Nd. The results are obtained using different approximations for the radial wave functions $g_{-1}(E_e)$ and $f_1(E_e)$ of the electron: (A) The standard approximation of Doi *et al.* [63] (see Section A.3.1). (B) The analytical solution of the Dirac equation for a point-like nucleus [214] (see Section A.3.2). (C) The exact solution of the Dirac equation for an uniform charge distribution of the nucleus screened by the atomic electronic cloud (see Section A.3.4). The results are presented in yr^{-1}. For each nucleus and each phase space factor we present the percent deviation between approximation schemes A and B, $\delta_{AB} = 100(X^A - X^B)/X^B$, and the percent deviation between approximation schemes A and C, $\delta_{AB} = 100(X^A - X^C)/X^C$, with $X = G_N^{2\nu}$ or $X = H_N^{2\nu}$.

Nucleus	Elec. w. f.	$G_0^{2\nu}$	$G_2^{2\nu}$	$G_{22}^{2\nu}$	$G_4^{2\nu}$
^{100}Mo	A	3.820×10^{-18}	1.748×10^{-18}	2.302×10^{-19}	1.001×10^{-18}
	B	3.490×10^{-18}	1.597×10^{-18}	2.105×10^{-19}	9.145×10^{-19}
	C	3.279×10^{-18}	1.498×10^{-18}	1.972×10^{-19}	8.576×10^{-19}
	δ_{AB}	9.44%	9.49%	9.38%	9.52%
	δ_{AC}	16.49%	16.67%	16.76%	16.80%
^{136}Xe	A	1.794×10^{-18}	5.519×10^{-19}	4.998×10^{-20}	2.112×10^{-19}
	B	1.566×10^{-18}	4.815×10^{-19}	4.367×10^{-20}	1.842×10^{-19}
	C	1.406×10^{-18}	4.318×10^{-19}	3.908×10^{-20}	1.651×10^{-19}
	δ_{AB}	14.57%	14.63%	14.45%	14.67%
	δ_{AC}	27.62%	27.81%	27.87%	27.95%
^{150}Nd	A	4.820×10^{-17}	2.733×10^{-17}	4.483×10^{-18}	1.938×10^{-17}
	B	4.043×10^{-17}	2.291×10^{-17}	3.765×10^{-18}	1.624×10^{-17}
	C	3.604×10^{-17}	2.038×10^{-17}	3.343×10^{-18}	1.443×10^{-17}
	δ_{AB}	19.21%	19.29%	19.04%	19.36%
	δ_{AC}	33.76%	34.08%	34.10%	34.30%
Nucleus	Elec.w.f.	$H_0^{2\nu}$	$H_2^{2\nu}$	$H_{22}^{2\nu}$	$H_4^{2\nu}$
^{100}Mo	A	2.466×10^{-18}	1.034×10^{-18}	1.239×10^{-19}	5.491×10^{-19}
	B	2.406×10^{-18}	1.030×10^{-18}	1.260×10^{-19}	5.582×10^{-19}
	C	2.244×10^{-18}	9.566×10^{-19}	1.165×10^{-19}	5.163×10^{-19}
	δ_{AB}	2.49%	0.37%	−1.71%	−1.64%
	δ_{AC}	9.86%	8.08%	6.34%	6.35%
^{136}Xe	A	1.025×10^{-18}	2.872×10^{-19}	2.329×10^{-20}	1.015×10^{-19}
	B	1.026×10^{-18}	2.982×10^{-19}	2.512×10^{-20}	1.090×10^{-19}
	C	9.103×10^{-19}	2.630×10^{-19}	2.201×10^{-20}	9.566×10^{-20}
	δ_{AB}	−0.12%	−3.69%	−7.28%	−6.89%
	δ_{AC}	12.63%	9.20%	5.78%	6.06%
^{150}Nd	A	3.201×10^{-17}	1.668×10^{-17}	2.497×10^{-18}	1.099×10^{-17}
	B	3.005×10^{-17}	1.618×10^{-17}	2.507×10^{-18}	1.100×10^{-17}
	C	2.658×10^{-17}	1.424×10^{-17}	2.194×10^{-18}	9.637×10^{-18}
	δ_{AB}	6.50%	3.07%	−0.42%	−0.08%
	δ_{AC}	20.43%	17.14%	13.81%	14.07%

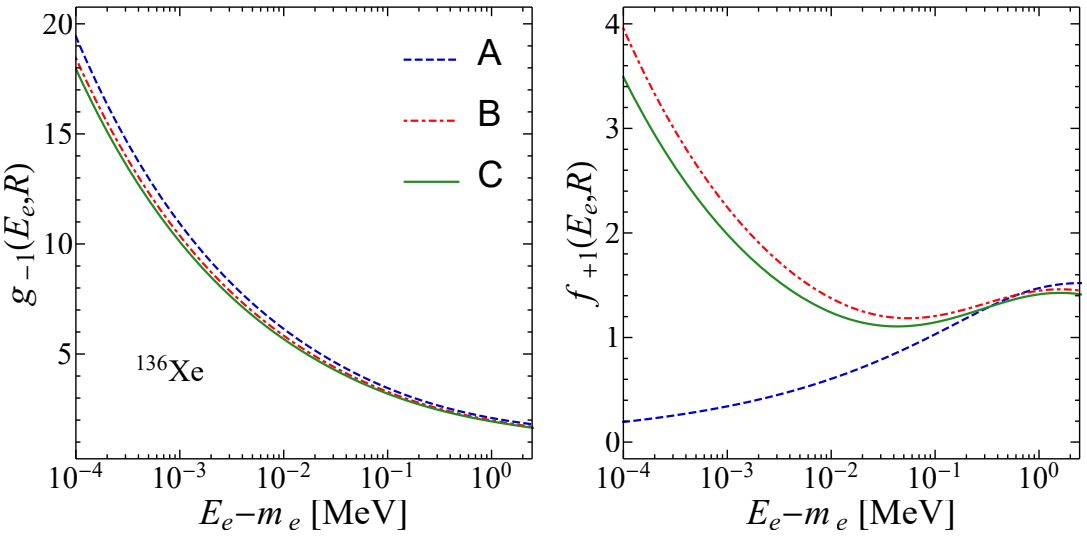

Figure 6.1: Electron radial wave functions in $s_{1/2}$ spherical wave state for an electron emitted in the double-β-decay of ^{136}Xe, as functions of the kinetic energy $E_e - m_e$ evaluated on the surface of the final nucleus $R = 6.17$ fm. The original figure can be found in [179].

Table 6.2: Phase space factors $G_N^{2\nu}$ and $H_N^{2\nu}$ with $N = \{0, 2, 22, 4\}$, in yr^{-1}, obtained using the screened exact finite-size Coulomb wave functions for $s_{1/2}$ electron state. The Q values are taken from the experiments with the smallest uncertainty when available, or from tables of recommended value [197].

Nucleus	Q [MeV]	$G_0^{2\nu}$	$G_2^{2\nu}$	$G_{22}^{2\nu}$	$G_4^{2\nu}$
^{48}Ca	4.268121 [215]	1.517×10^{-17}	1.290×10^{-17}	3.094×10^{-18}	1.392×10^{-17}
^{76}Ge	2.039061 [216]	4.779×10^{-20}	1.007×10^{-20}	6.236×10^{-22}	2.644×10^{-21}
^{82}Se	2.9979 [217]	1.596×10^{-18}	7.069×10^{-19}	8.986×10^{-20}	3.928×10^{-19}
^{96}Zr	3.356097 [218]	6.837×10^{-18}	3.780×10^{-18}	5.979×10^{-19}	2.624×10^{-18}
^{100}Mo	3.0344 [188]	3.279×10^{-18}	1.498×10^{-18}	1.972×10^{-19}	8.576×10^{-19}
^{110}Pd	2.01785 [219]	1.357×10^{-19}	2.835×10^{-20}	1.760×10^{-21}	7.350×10^{-21}
^{116}Cd	2.8135 [220]	2.728×10^{-18}	1.083×10^{-18}	1.250×10^{-19}	5.374×10^{-19}
^{124}Sn	2.2927 [197]	5.609×10^{-19}	1.503×10^{-19}	1.190×10^{-20}	5.010×10^{-20}
^{130}Te	2.527518 [221]	1.498×10^{-18}	4.851×10^{-19}	4.612×10^{-20}	1.957×10^{-19}
^{136}Xe	2.45783 [222]	1.406×10^{-18}	4.318×10^{-19}	3.908×10^{-20}	1.651×10^{-19}
^{150}Nd	3.37138 [223]	3.604×10^{-17}	2.038×10^{-17}	3.343×10^{-18}	1.443×10^{-17}
Nucleus	Q [MeV]	$H_0^{2\nu}$	$H_2^{2\nu}$	$H_{22}^{2\nu}$	$H_4^{2\nu}$
^{48}Ca	4.268121 [215]	1.165×10^{-17}	9.277×10^{-18}	2.083×10^{-18}	9.428×10^{-18}
^{76}Ge	2.039061 [216]	2.678×10^{-20}	5.197×10^{-21}	2.906×10^{-22}	1.274×10^{-21}
^{82}Se	2.9979 [217]	1.076×10^{-18}	4.423×10^{-19}	5.181×10^{-20}	2.306×10^{-19}
^{96}Zr	3.356097 [218]	4.852×10^{-18}	2.504×10^{-18}	3.679×10^{-19}	1.639×10^{-18}
^{100}Mo	3.0344 [188]	2.244×10^{-18}	9.567×10^{-19}	1.165×10^{-19}	5.163×10^{-19}
^{110}Pd	2.01785 [219]	7.845×10^{-20}	1.529×10^{-20}	8.659×10^{-22}	3.750×10^{-21}
^{116}Cd	2.8135 [220]	1.833×10^{-18}	6.815×10^{-19}	7.277×10^{-20}	3.201×10^{-19}
^{124}Sn	2.2927 [197]	3.482×10^{-19}	8.744×10^{-20}	6.362×10^{-21}	2.764×10^{-20}
^{130}Te	2.527518 [221]	9.745×10^{-19}	2.963×10^{-19}	2.604×10^{-20}	1.135×10^{-19}
^{136}Xe	2.45783 [222]	9.103×10^{-19}	2.630×10^{-19}	2.201×10^{-20}	9.566×10^{-20}
^{150}Nd	3.37138 [223]	2.658×10^{-17}	1.424×10^{-17}	2.194×10^{-18}	9.637×10^{-18}

Table 6.3: The values of the angular correlation coefficient for different values of ξ_{31}. We assume the approximation scheme A and C for the relativistic wave function of the emitted electrons. For each nuclei, we display the energy difference $E(1^+) - E_i$ in MeV, necessary to calculate ξ_{51} via Eq. (5.47).

				A	C
Nucleus	$E(1^+) - E_i$	$\xi_{51}^{2\nu}$	$\xi_{31}^{2\nu}$	$K^{2\nu}$	$K^{2\nu}$
^{82}Se	-0.338	0.139	-0.2	-0.649	-0.675
			0.0	-0.645	-0.671
			0.2	-0.641	-0.667
			0.4	-0.636	-0.662
			0.6	-0.630	-0.657
^{96}Zr	0.021	0.046	-0.2	-0.681	-0.713
			0.0	-0.676	-0.708
			0.2	-0.669	-0.703
			0.4	-0.663	-0.697
			0.6	-0.656	-0.690
^{100}Mo	-0.343	0.135	-0.2	-0.646	-0.685
			0.0	-0.642	-0.682
			0.2	-0.637	-0.677
			0.4	-0.632	-0.673
			0.6	-0.627	-0.668
^{116}Cd	-0.043	0.088	-0.2	-0.620	-0.674
			0.0	-0.616	-0.671
			0.2	-0.612	-0.667
			0.4	-0.607	-0.663
			0.6	-0.603	-0.659
^{150}Nd	-0.315	0.087	-0.2	-0.666	-0.738
			0.0	-0.661	-0.735
			0.2	-0.655	-0.731
			0.4	-0.648	-0.725
			0.6	-0.641	-0.719

phase-space factors H_N, schemes A and B exhibit good agreement, whereas scheme C again predicts smaller values. This disparity in the behavior of G_N and H_N across the same approximation schemes underscores the sensitivity of angular correlations to the treatment of the Coulomb interaction experienced by the emitted electrons.

In Table 6.2, we present updated phase-space factor values computed using approximation scheme C for eleven experimentally relevant nuclei. The Q-values for each nucleus were sourced from experiments reporting the smallest uncertainties or, where unavailable, from recommended value tables [197], as exemplified by the $2\nu\beta\beta$-decay of ^{124}Sn. These selected Q-values were subsequently employed to determine the maximum sum of the kinetic energies of the emitted electrons.

In Table 6.3, we present the angular correlation coefficient $K^{2\nu}$, as defined in Eq. (6.9), for several nuclei of interest, considering ξ_{31} values of -0.2, 0, 0.2, 0.4, and 0.6. For each nucleus, the ξ_{51} parameter was determined based on the SSD hypothesis, along with the energy difference between the lowest 1^+ state of the intermediate nucleus and the ground state of the initial nucleus, as specified in Eq. (5.47). Columns 5 and 6 of Table 6.3 provide the $K^{2\nu}$ results obtained using electronic wave functions derived from approximation schemes A and C, respectively. While scheme C consistently produces smaller $K^{2\nu}$ values compared to scheme A, it is clear that the dependence of $K^{2\nu}$ on ξ_{31} is inherently nonlinear.

To illustrate the dependence on the ratio of nuclear matrix elements, Figure 6.2 shows the angular correlation coefficient $K^{2\nu}$ as a function of ξ_{31}, covering the range from

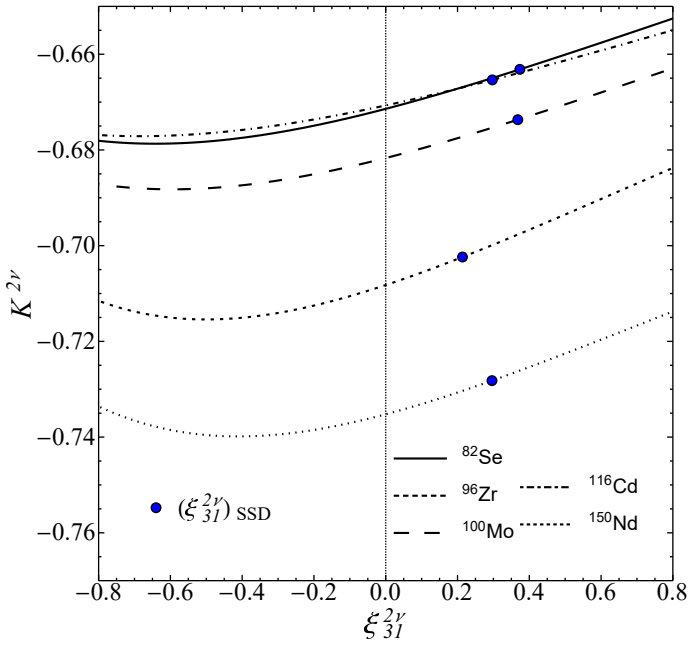

Figure 6.2: The angular correlation coefficient between the electrons emitted in $2\nu\beta\beta$-decay of ^{82}Se, ^{96}Zr, ^{100}Mo, ^{116}Cd, and ^{150}Nd, as functions of $\xi^{2\nu}_{31}$. The filled blue circles indicate the values of $K^{2\nu}$ for the ratio of the nuclear matrix elements fixed by the SSD assumption, $\left(\xi^{2\nu}_{31}\right)_{\rm SSD}$. In the case of ^{82}Se and ^{116}Cd, the right filled circle correspond to ^{82}Se and the left one to ^{116}Cd. We used the approximation scheme C for the relativistic wave function of the emitted electrons. The original figure can be found in [179].

$\xi_{31} = -0.8$ to $\xi_{31} = 0.8$ for all nuclei considered. The figure demonstrates that $K^{2\nu}$ exhibits a quadratic dependence on ξ_{31} across the entire representation interval for all nuclei. Under the SSD assumption for the $2\nu\beta\beta$ process, the parameter ξ_{31} is uniquely determined and fixed to the value $\xi^{\rm SSD}_{31}$ (see Eq. (5.47)). These specific values of the angular correlation coefficient, evaluated at $\xi^{\rm SSD}_{31}$, are highlighted with filled blue circles in Figure 6.2.

From the analytical expressions of the partial double distributions in Eq. (6.8), it is evident that they exhibit distinctly different behaviors as functions of the electron energies, E_{e_1} and E_{e_2}. This observation is illustrated in Figure 6.3, where we show the contour plots of the partial double electron distribution for the $2\nu\beta\beta$-decay of ^{100}Mo. These distributions are normalized to the corresponding partial decay rate. The normalization procedure ensures that the normalized partial distributions are independent of the nuclear matrix element ratios ξ_{31} and ξ_{51}.

The angular correlation distribution κ, expressed as a function of the electron energies and the ratios of the nuclear matrix elements, is provided in Eq.(6.11). Figure 6.4 illustrates the contour plots of the angular distributions for the $2\nu\beta\beta$-decay of ^{100}Mo, considering different values of ξ_{31}. The left, middle, and right panels correspond to $\xi_{31} = -1$, 0, and 1, respectively. Notably, the middle panel represents the standard approximation angular distribution.

We compared the enhanced formalism introduced in this work with the exact SSD formalism for $2\nu\beta\beta$-decay, as outlined in [75, 76]. Under the SSD assumption, the ratios ξ_{31} and ξ_{51} are fixed. Figure 6.5 presents the single-electron differential decay rates, normalized to the full width, for ^{82}Se, ^{100}Mo, and ^{150}Nd. The solid black line represents the normalized single-electron spectra obtained using the exact SSD formalism [75, 76], while the blue dashed line corresponds to the spectra described by Eq. (6.6). The legends in the plots indicate the values of ξ_{31} fixed by the SSD assumption. The lower panels display the

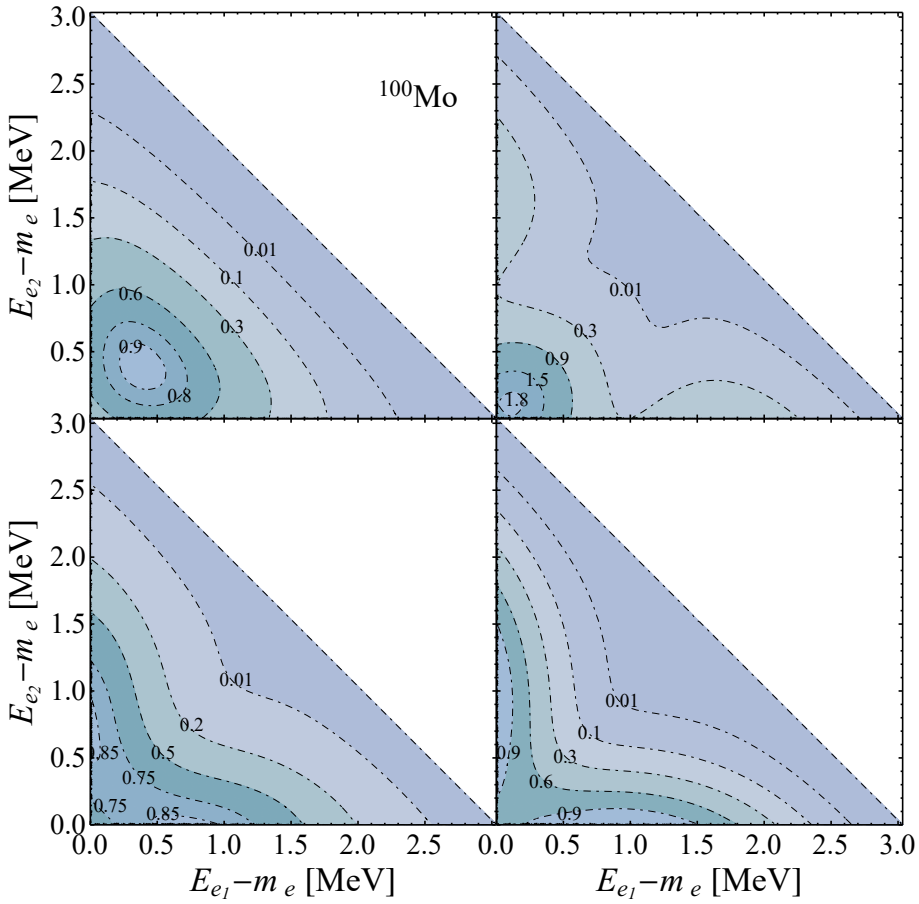

Figure 6.3: Normalized to unity partial double energy distributions $(1/\Gamma_N)(d\Gamma_N/(dE_{e_1}dE_{e_2}))$, as functions of the kinetic energies of the electrons, for $N = 0$ (top left), $N = 2$ (bottom left), $N = 22$ (top right) and $N = 4$ (bottom right). All distributions are in units of MeV^{-2} for electrons emitted in double β-decay of ^{100}Mo. The distributions are obtained using the screened exact finite-size Coulomb wave functions for $s_{1/2}$ electron state. The original figure can be found in [179].

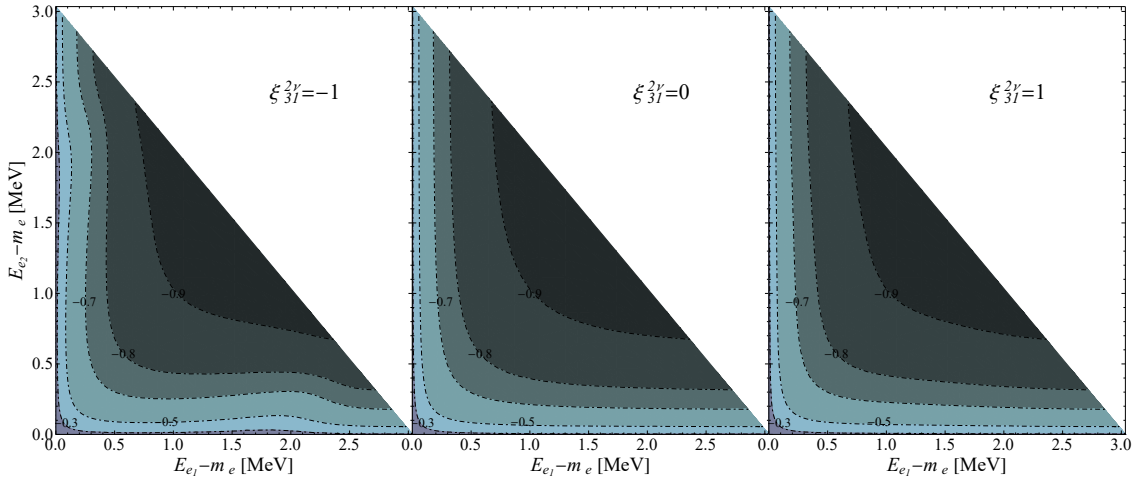

Figure 6.4: The angular correlation $\kappa^{2\nu}$ as function of electron energies emitted in the $2\nu\beta\beta$-decay of ^{100}Mo. The distributions are obtained using $\xi^{2\nu}_{31} = -1$, 0 and 1. The distributions were calculated by using the screened exact finite-size Coulomb wave functions for $s_{1/2}$ electron state. The original figure can be found in [179].

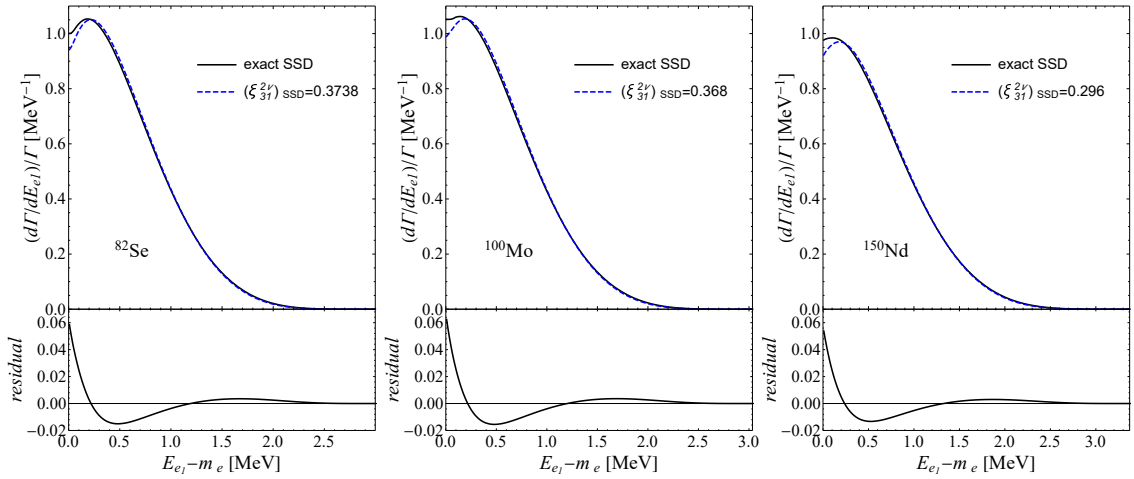

Figure 6.5: Normalized single electron spectra for ^{82}Se, ^{100}Mo and ^{150}Nd assuming the single state dominance. We compare the exact SSD [75, 76] with the Taylor expansion with ratio of the nuclear matrix elements fixed by SSD. The original figure can be found in [179].

residuals between the exact and improved formalisms. Overall, the spectra demonstrate good agreement, with only slight deviations appearing at low electron energies, a region that is typically inaccessible in double-beta decay experiments due to high background events.

To compare the angular correlation distributions obtained from the exact SSD formalism and the improved formalism, we present in Figure 6.6 the distribution reproduced using the exact SSD approach. Notably, this distribution shows no significant deviations from the one corresponding to a positive ξ_{31} in Figure 6.4. Based on the comparisons of both the single-electron spectra and angular distributions, we conclude that the improved formalism introduced in this work, with ξ_{31} fixed by the SSD assumption, demonstrates excellent agreement with the exact SSD formalism.

6.3.2 Towards to detection of effective axial-vector coupling g_A^{eff}

As noted earlier in [78], the calculation of $M^{2\nu}_{GT-3}$ is generally more reliable than that of $M^{2\nu}_{GT-1}$, as $M^{2\nu}_{GT-3}$ is predominantly saturated by contributions from the lowest-energy states of the intermediate nucleus. The half-life of $2\nu\beta\beta$-decay can be expressed in terms of $M^{2\nu}_{GT-3}$, ξ_{31}, and ξ_{51} as follows:

$$\begin{aligned}\left[T^{2\nu\beta\beta}_{1/2}\right]^{-1} \simeq \left(g_A^{\text{eff}}\right)^4 \left|M^{2\nu}_{GT-3}\right|^2 \frac{1}{|\xi_{31}|^2} \\ \times \left[G^{2\nu}_0 + \xi_{31} G^{2\nu}_2 + \frac{1}{3}\left(\xi_{31}\right)^2 G^{2\nu}_{22} + \left(\frac{1}{3}\left(\xi_{31}\right)^2 + \xi_{51}\right) G^{2\nu}_4\right],\end{aligned} \tag{6.18}$$

i.e., without explicit dependence on nuclear structure factor $(M^{2\nu}_{GT} - (g_V/g_A^{\text{eff}})^2 M^{2\nu}_F)$. The nuclear structure parameter ξ_{31} can be deduced from the energy distribution of the emitted electrons or from the angular correlation factor $K^{2\nu}$ as solution

$$\xi_{31} = \frac{-B \pm \sqrt{B^2 - 4AC}}{2A} \tag{6.19}$$

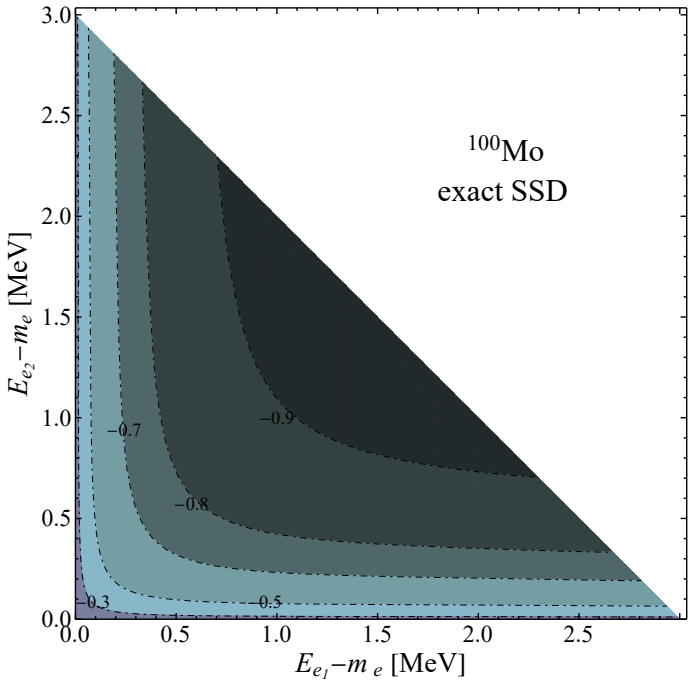

Figure 6.6: The angular correlation $\kappa^{2\nu}$ as function of energies of electrons emitted in $2\nu\beta\beta$-decay of ^{100}Mo. The distribution is obtained using the exact SSD formalism presented in [75, 76] and the screened exact finite-size Coulomb wave functions for $s_{1/2}$ electron state. The original figure can be found in [179].

of a quadratic equation with coefficients A, B and C, which are functions of the measured angular correlation factor:

$$\begin{aligned} A &= \frac{1}{9}\left(5H_{22}^{2\nu} + 2H_{4}^{2\nu} + 3K^{2\nu}G_{22}^{2\nu} + 3K^{2\nu}G_{4}^{2\nu}\right) \\ B &= H_{2}^{2\nu} + K^{2\nu}G_{2}^{2\nu} \\ C &= H_{0}^{2\nu} + \xi_{51}^{2\nu}H_{4}^{2\nu} + K^{2\nu}G_{0}^{2\nu} + \xi_{51}^{2\nu}K^{2\nu}G_{4}^{2\nu} \end{aligned} \tag{6.20}$$

The existence of two possible values for ξ_{31} corresponding to a measured angular correlation coefficient is also evident from Figure 6.2. Resolving this ambiguity requires a cross-check with the determination of ξ_{31} based on the energy distribution.

If $M_{GT-3}^{2\nu}$ is reliably calculated and ξ_{31} is accurately extracted from both angular and energy measurements, the effective axial-vector coupling constant, g_A^{eff}, can be determined from the measured $2\nu\beta\beta$-decay half-life using Eq. (6.18). Any discrepancy between the values of ξ_{31} obtained from energy and angular distributions may point to the presence of new physics effects manifesting in the $2\nu\beta\beta$-decay data analysis.

6.4 The impact of electron phase shifts on $\beta\beta$-decay kinematics

6.4.1 Electron wave function and phase shift

For electrons emitted in DBD, we consider the modified DHFS potential (see more details in Section A.2.1),

$$V(r) = V_{\text{nuc}}(r) + V_{\text{el}}(r) + V_{\text{ex}}^{\text{Slater}}(r), \tag{6.21}$$

whose components have been detailed in [168, 172], based on the RADIAL subroutine package [207], that we employ in the actual calculations. The electron charge density required to construct the electronic and exchange components of the potential is obtained through a self-consistent DHFS atomic structure calculation of the final positive ion with the electronic configuration of the initial neutral atom, known as sudden approximation. This approximation is avoided in [224, 225, 226, 227], where more complex models that account for overlap correction, and shake-up and shake-off effects have been considered. In particular, while the last two effects might influence the potential $V(r)$, the conclusions presented below remain valid. Nevertheless, the potential used in our model respects the correct asymptotic condition, i.e., $\lim_{r\to\infty} rV(r) = \alpha Z_\infty$. The charge $Z_\infty = Z_e Z_f$ can be obtained in DBD from the electron charge $Z_e = -1$ and the charge of the final positive ion, i.e., $Z_f = 2$.

In the potential from Eq. (6.21), the functions $\tilde{g}_\kappa$ and $\tilde{f}_\kappa$ must following asymptotic behavior,

$$\begin{Bmatrix} \tilde{g}_\kappa(E_e, r) \\ \tilde{f}_\kappa(E_e, r) \end{Bmatrix} \xrightarrow[r\to\infty]{} \frac{\exp\left(-i\bar{\Delta}_\kappa\right)}{p_e r} \begin{Bmatrix} \sqrt{\frac{E_e+m_e}{2E_e}}\sin\left(p_e r - \ell_\kappa\frac{\pi}{2} + \eta\ln(2p_e r) + \bar{\Delta}_\kappa\right) \\ \sqrt{\frac{E_e-m_e}{2E_e}}\cos\left(p_e r - \ell_\kappa\frac{\pi}{2} + \eta\ln(2p_e r) + \bar{\Delta}_\kappa\right) \end{Bmatrix}, \tag{6.22}$$

where $\bar{\Delta}_\kappa = \Delta_\kappa + \delta_\kappa$ is the overall phase shift. Here, δ_κ is the inner phase shift induced by the finite-range component of final system potential, i.e., $V_{\text{f.r.}}(r) = V(r) - \alpha Z_\infty/r$, and $\eta = -\alpha Z_\infty E_e/p_e$ is the Sommerfeld parameter. The effect of the pure Coulomb potential, i.e., $V_c(r) = \alpha Z_\infty/r$, is accounted for by the logarithmic phase, $\eta\ln(2p_e r)$, and the Coulomb phase shift [207],

$$\Delta_\kappa = \nu - (\gamma_\kappa - \ell_\kappa - 1)\frac{\pi}{2} + \arg\Gamma(\gamma_\kappa - i\eta) - \mathcal{S}_{Z_\infty,\kappa}\pi \tag{6.23}$$

with

$$\nu = \arg\left[\alpha Z_\infty(E_e + m_e) - i(\kappa + \gamma_\kappa)p_e\right], \tag{6.24}$$

$$\gamma_\kappa = \sqrt{\kappa^2 - (\alpha Z_\infty)^2}, \tag{6.25}$$

and

$$\ell_\kappa = \begin{cases} |\kappa| - 1 & \text{if} \quad \kappa < 0 \\ \kappa & \text{if} \quad \kappa > 0 \end{cases}, \qquad \mathcal{S}_{Z_\infty,\kappa} = \begin{cases} 1 & \text{if} \quad \kappa < 0, \;\; Z_\infty < 0 \\ 0 & \text{otherwise} \end{cases}. \tag{6.26}$$

The phase shifts for electrons emitted in the DBD of ^{100}Mo were calculated by solving Eq. (A.54) within the potential generated by the final ion, ^{100}Ru. The numerical inner phase shift for electrons with $\kappa = -1$ is shown in the top-left panel of Figure 6.7 as a function of kinetic energy.

Due to the attractive nature of the finite-range component of the DHFS potential generated by the final positive ion ^{100}Ru, the absolute phase shift must be positive. However, the numerical inner phase shift appears negative because the RADIAL subroutine package [207] confines its calculation to the interval $(-\pi/2, \pi/2)$. The relationship between the absolute and numerical inner phase shifts was established using the graphical method. Unfortunately, since $\lim_{r\to 0} rV_{\text{f.r.}}(r) \neq 0$, the high-energy limit of $\delta_\kappa(E_e)$ cannot be determined by integrating the finite-range potential, as proposed in [228].

Three points from distinct regions of $\delta_\kappa(E_e)$ are highlighted in the top-left panel of Figure 6.7. For each fixed energy, the radial dependence of the function $rg_{-1}(E_e, r)$ is shown in the remaining panels of Figure 6.7, comparing results obtained using the modified DHFS potential (solid line) and the pure Coulomb potential (dashed line).

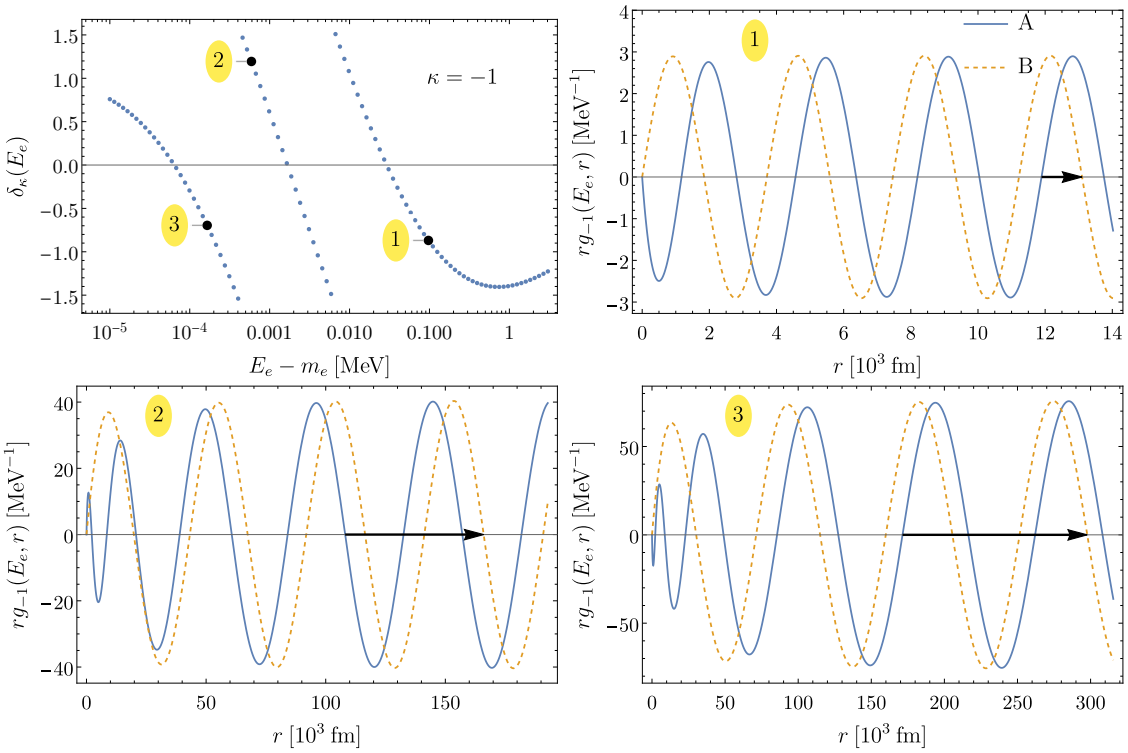

Figure 6.7: (Top-left panel): The numerical inner phase shifts for electrons emitted in DBD of ^{100}Mo with energy E_e and $\kappa = -1$. Inner phase shifts labeled 1, 2, and 3 are highlighted for three distinct electron energies, chosen from different branches of the numerical inner phase shift, which are separated by discontinuities. For each energy, the radial dependence of the real functions $rg_{-1}(E_e, r)$ is shown for both (A) the modified DHFS potential and (B) the pure Coulomb potential. The absolute inner phase shifts for these chosen energies are represented by arrows connecting the nodes of the functions where they reach their asymptotic behavior. The figure is taken from [229].

The radial ranges are carefully selected to ensure that all functions exhibit their asymptotic behavior. By examining the radial differences between the nodes of these functions, indicated by arrows, the absolute inner phase shift is determined. Specifically, for the regions corresponding to the points labeled "1", "2", and "3", it is necessary to add π, 2π, and 3π, respectively, to the numerical phase shift to compute the absolute phase shift. The same behavior is observed for electrons with $\kappa = 1$.

The energy dependence of the total phase shift, which incorporates the Coulomb phase shift, is shown in the left panel of Figure 6.8 for electrons with $\kappa = -1$ (solid line) and $\kappa = 1$ (dashed line). This representation highlights the behavior of the phase shifts across the electron's kinetic energy spectrum. In the right panel of Figure 6.8, we plot the function $\cos\left(\bar{\Delta}_{-1} - \bar{\Delta}_{+1}\right)$, which plays a crucial role in the construction of the $E_{ss}(E_e)$ function as defined in Eq. (5.5). An intriguing feature observed in this plot is a sign change in the cosine function occurring near a kinetic energy of approximately 2 keV for the emitted electron.

6.4.2 Results and discussions

In Figure 6.9, we present the quantities F_{ss} and E_{ss}, comparing cases where phase shifts are either included or omitted in their definitions. Since F_{ss} is expressed in terms of the modulus squared of the scattering wave functions, it remains identical in both

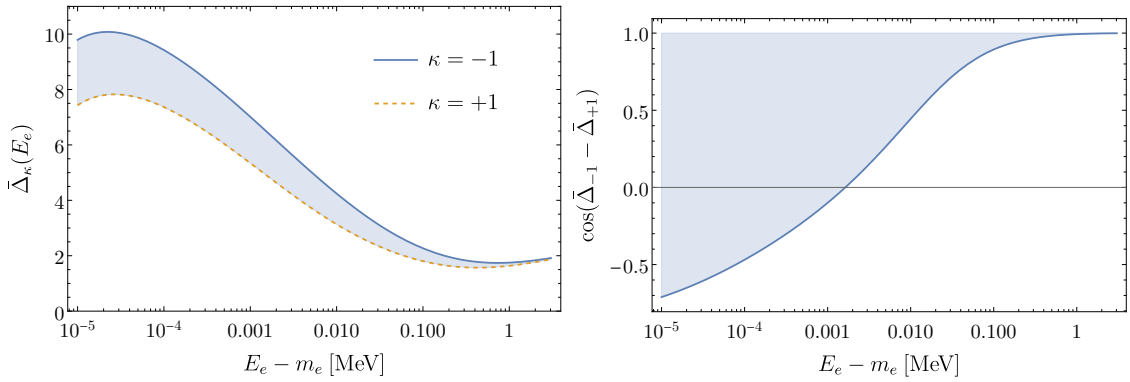

Figure 6.8: (Left panel): The total phase shifts for electrons emitted in DBD of ^{100}Mo with energy E_e and $\kappa = -1$ (solid) or $\kappa = +1$ (dashed). (Right panel): The real part of $\exp\left[-i\left(\bar{\Delta}_{-1} - \bar{\Delta}_{+1}\right)\right]$, required in the construction of $E_{ss}(E_e)$ function from Eq. (5.5). The figure is taken from [229].

scenarios. In contrast, the quantity E_{ss} exhibits a pronounced difference between the two cases, particularly for electron energies below 100 keV. Notably, it becomes significantly smaller when phase shifts are included, even turning negative around 2 keV.

The angular correlation functions α are shown in Figure 6.10. In both DBD modes, α becomes positive at electron energies below a few tens of keV when phase shifts are included in the calculations. A similar observation was reported in [195], although the implications for electron emission patterns were not addressed. In this low-energy range, events where the electrons are emitted with an opening angle smaller than $\pi/2$ occur more frequently than those with angles exceeding $\pi/2$. The most probable emission angle is 0, indicating a preference for collinear electron emission. In the two-neutrino mode, such collinear emission is feasible because the antineutrinos can be emitted in the opposite direction, conserving momentum. However, in the neutrinoless mode, momentum conservation with collinear electron emission is only possible if the nucleus recoils. It is important to note that the recoil energy is not included in Eqs. (6.3) and (6.13), so care must be taken when interpreting this intuitive picture.

An intriguing feature observed in Figure 6.10 emerges at electron energies above a few tens of keV. In the two-neutrino mode, the angular correlation function α calculated with phase shifts deviates significantly from the result obtained without phase shifts across the entire energy range. Conversely, in the neutrinoless mode, the two curves remain nearly identical, except near the energy boundaries. Furthermore, the inclusion of phase shifts amplifies the relative difference between $\alpha^{2\nu}$ and $\alpha^{0\nu}$, indicating that the angular correlation function could serve as a valuable tool for distinguishing between neutrinoless and two-neutrino double beta decay—provided sufficiently high statistical precision can be achieved in experimental measurements..

In Figure 6.11, we present the $\kappa^{2\nu}$ function, both with and without the inclusion of phase shifts. When phase shifts are taken into account, the negative contours shift toward higher electron energies and exhibit noticeable distortions in shape compared to the case where phase shifts are omitted. More intriguingly, in the case with phase shifts, positive contours appear, producing a physical picture similar to that discussed for the $\alpha^{2\nu}$ function. Given that $\kappa^{2\nu}$ is a continuous function, the presence of both positive and negative contours implies the existence of two contour lines where $\kappa^{2\nu} = 0$. For ^{100}Mo, these zero-contour lines correspond to scenarios in which one electron has an energy close to 2 keV. In this energy range, the electrons are emitted isotropically, assuming nuclear recoil is neglected.

Finally, we examine the angular correlation coefficients defined in Eq. (6.2). Table 6.4

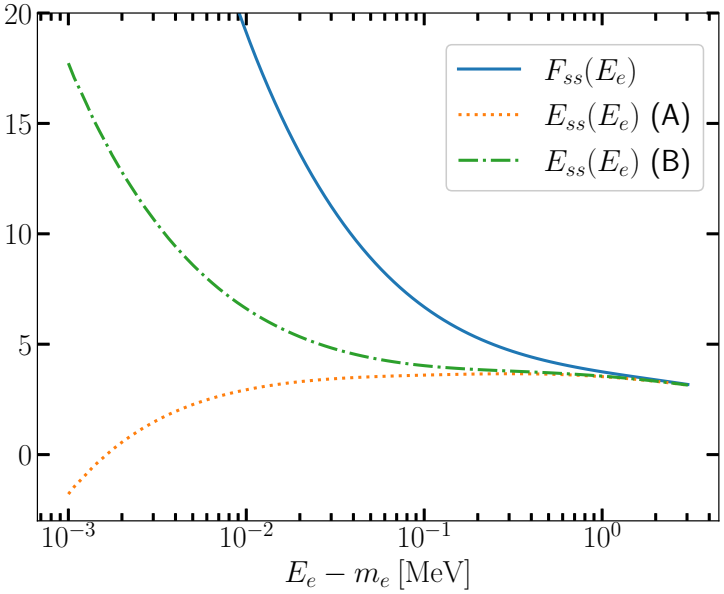

Figure 6.9: The functions $F_{ss}(E_e)$ and $E_{ss}(E_e)$ for the DBD of ^{100}Mo obtained from: (A) the modified DHFS potential and intentionally omitting the phase shifts in Eq. (5.5), i.e., Eq. (6.17); (B) the modified DHFS potential and including the phase shifts in Eq. (5.5). The figure is taken from [229].

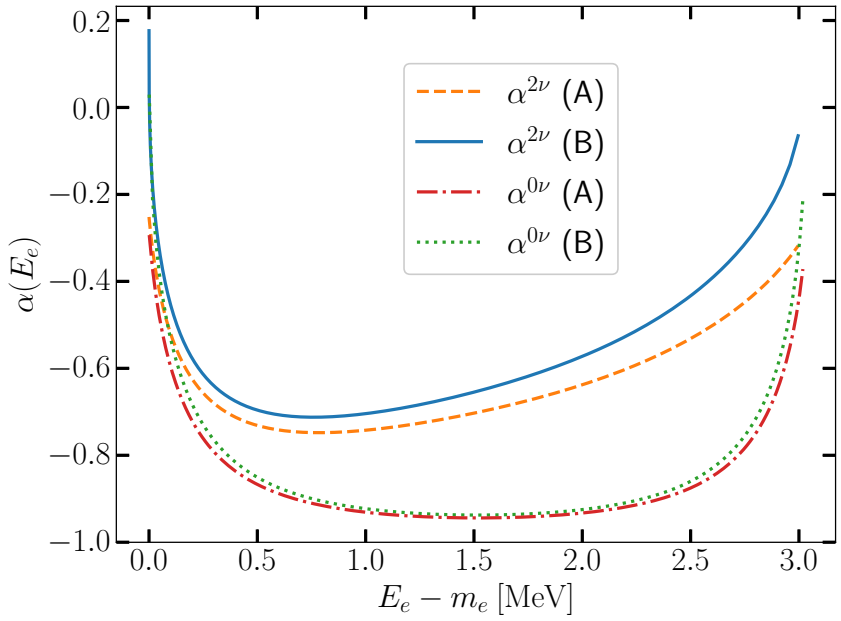

Figure 6.10: The functions $\alpha^{2\nu}(E_e)$ and $\alpha^{0\nu}(E_e)$ for the DBD of ^{100}Mo obtained from: (A) the modified DHFS potential and intentionally omitting the phase shifts in Eq. (5.5), i.e., Eq. (6.17); (B) the modified DHFS potential and including the phase shifts in Eq. (5.5). The values $\xi_{31} = 0.45$ and $\xi_{51} = 0.165$ are used, in accordance with [55]. The figure is taken from [229].

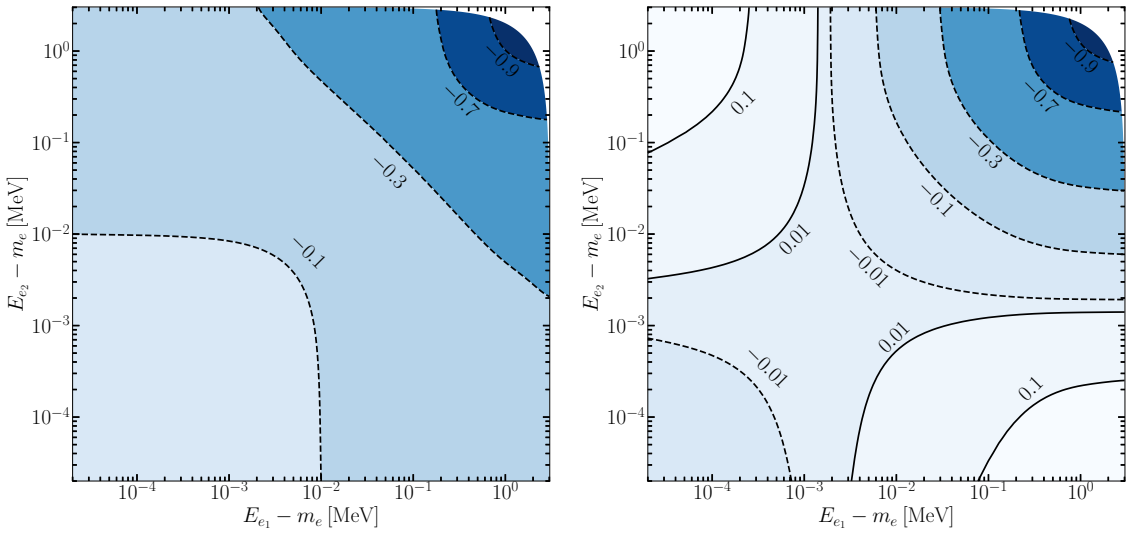

Figure 6.11: The angular correlation distribution $\kappa^{2\nu}(E_{e_1}, E_{e_2})$ for the DBD of ^{100}Mo obtained by: (left) intentionally omitting the phase shifts in Eq. (5.5), i.e., Eq. (6.17); (right) including the phase shifts in Eq. (5.5). Contour lines are drawn at selected levels to guide the eye. The same values for ξ_{31} and ξ_{51} as those in Figure 6.10 are used. The figure is taken from [229].

Table 6.4: The values of $K^{2\nu}$ for the DBD of ^{100}Mo decay for multiple sets of ξ_{31} and ξ_{51} parameters, corresponding to the HSD and SSD hypotheses, along with experimental measurements. The values from this work are labeled as "TW" and for the other, the reference next to the values indicates the original papers. For cases where the angular correlation coefficient value is not explicitly provided, we have derived it based on the reported PSFs. The "No screening" case refers to the standard Fermi function approximation [63], while "Realistic screening" involves models where atomic screening is derived from either the Thomas-Fermi equation or the DHFS method. Values in the second and third columns are computed either by neglecting phase shifts or by considering them approximately, while the final column includes results that fully account for phase shifts.

	$K^{2\nu}$ without phase shifts		$K^{2\nu}$ with phase shifts
	No screening	Realistic screening	Realistic screening
HSD	-0.650 [88]	-0.684 [179]	-0.640 (TW)
($\xi_{31} = 0$; $\xi_{51} = 0$)	-0.646 [89]	-0.684 [192]	
	-0.646 [179]	-0.685 (TW)	
	-0.646 [75]		
SSD	-0.627 [89]	-0.668 [92]	-0.627 (TW)
($\xi_{31} = 0.368$; $\xi_{51} = 0.135$)	-0.627 [75]	-0.669 [93]	
	-0.633 [179]	-0.668 [192]	
		-0.674 [179]	
		-0.675 (TW)	
EXP	-0.630 [179]	-0.671 [179]	-0.624 (TW)
($\xi_{31} = 0.450$; $\xi_{51} = 0.165$ [55])		-0.672 (TW)	

summarizes the $K^{2\nu}$ values calculated with and without phase shifts for various parameter sets of ξ_{31} and ξ_{51}, corresponding to the HSD hypothesis, SSD hypothesis, and experimental measurements. For studies where explicit angular correlation coefficient values were unavailable, we derived them using the reported PSFs. Our results without phase shifts are consistent with prior calculations that included atomic screening, whereas those neglecting screening predict larger $K^{2\nu}$ values. Notably, the HSD hypothesis yields the smallest $K^{2\nu}$ values, while the experimentally measured parameters [55] produce the largest values. Incorporating phase shifts into the decay rate calculation (last column of Table 6.4) results in $K^{2\nu}$ values approximately 7% higher than those obtained without phase shifts. This observation suggests that similar effects may arise in other studies if phase shifts are included. For the $0\nu\beta\beta$-decay of ^{100}Mo, we calculate $K^{0\nu} = -0.896$ when phase shifts are excluded and measured ξ_{31} and ξ_{51} values are used. Incorporating phase shifts increases this value to $K^{0\nu} = -0.882$, reflecting a change of about 2%. This difference is expected, as phase shifts affect a smaller portion of the integration domain in Eq. (6.13) compared to Eq. (6.3). While this analysis focuses on the light neutrino exchange mechanism, we emphasize that the impact of phase shifts may vary for alternative mechanisms driving $0\nu\beta\beta$-decay.

6.4.3 Conclusions

In conclusion, we have investigated the impact of phase shifts on the kinematics of $\beta\beta$-decay in ^{100}Mo, considering both 0ν and 2ν modes. Our analysis of the angular correlation distributions, α and κ, revealed a striking feature: when electron phase shifts are included, electrons are most likely emitted in the same direction if one has an energy below 2 keV. While a similar observation was previously reported in [195], our study provides a more detailed examination of the implications for electron emission patterns.

Through a systematic review of the previously reported $K^{2\nu}$ values, we demonstrated that incorporating phase shifts influences the results, irrespective of the approximations employed in factorizing the $2\nu\beta\beta$-decay rate or accounting for atomic screening effects. Specifically, we found that properly accounting for phase shifts increases the angular correlation coefficient, K, by 7% in the 2ν mode and 2% in the 0ν mode.

These findings could have significant implications for proposals aimed at constraining new physics parameters based on angular correlation coefficients in $2\nu\beta\beta$-decay [87, 88, 94, 89, 92, 93, 90, 105, 104]. Furthermore, phase shifts might influence methods to differentiate between mechanisms driving $0\nu\beta\beta$-decay [72, 79, 80]. However, as this study is limited to the light neutrino exchange mechanism, a more detailed exploration of alternative scenarios will be addressed in future work.

7 Two-neutrino double electron capture

7.1 Introduction

Besides the $2\nu\beta\beta$-decay, double beta decay of proton-rich isotopes is also possible and remains in the early stages of experimental investigation [36]. There are three distinct DBD modes associated with proton-rich nuclei [33, 34]: the double-positron emission mode ($0\nu/2\nu\beta^+\beta^+$), the single electron capture accompanied by positron emission mode ($0\nu/2\nu\mathrm{EC}\beta^+$), and the double electron capture mode ($0\nu/2\nu$ECEC). Compared to the well-studied $2\nu\beta\beta$ decay mode, experimental studies of these processes have faced challenges due to their longer half-lives and lower Q-values. However, their distinct signatures, particularly when employing coincidence trigger logic, could facilitate their detection [36]. Notably, there have been positive indications of the 2νECEC mode in ^{130}Ba and ^{132}Ba through geochemical measurements [41, 42, 43], as well as in ^{78}Kr [44, 45]. More recently, the XENON1T collaboration directly observed the 2νECEC mode in ^{124}Xe [46, 47].

On the theoretical front, initial estimates of 2νECEC decay rates were provided by Primakoff and Rosen [230, 231], followed by refinements from Vergados [232] and Kim and Kubodera [233]. These early calculations relied on a non-relativistic treatment of captured electrons. A significant advancement was made by Doi and Kotani, who developed a detailed theoretical formulation that incorporated relativistic effects [33]. However, these calculations assumed a point-like nucleus, enabling the analytical treatment of electron bound states. Around the same time, Boehm and Vogel published results for selected 2νECEC cases, albeit without providing detailed computational procedures [234].

More recently, theoretical models have been improved by including atomic screening effects through the Thomas-Fermi approximation for the electron cloud [235, 194, 195]. Diffuse nuclear surface effects have also been incorporated by adopting realistic charge distributions within the nucleus [194, 195]. These advancements provide more precise predictions for the decay rates of proton-rich isotopes undergoing double beta decay.

Although 2νECEC inherently bridges nuclear and atomic physics, several aspects of atomic structure calculations have been either overlooked or treated simplistically in earlier studies. In the first part of this Chapter, we adopt the DHFS self-consistent framework to provide a more accurate treatment of atomic screening effects and a rigorous estimation of the binding energies for the captured electrons. The DHFS atomic potential incorporates both finite nuclear size and diffuse nuclear surface corrections. Additionally, we extend our analysis to include all available s-wave electrons for capture, going beyond the K and L_1 orbitals considered in previous investigations.

Our findings reveal that, for light atoms undergoing the 2νECEC process, the decay rate reduction caused by improved atomic screening is compensated by an increase due to the inclusion of higher-orbital captures beyond K and L_1. However, this compensatory effect is not observed in medium and heavy atoms, where the inclusion of higher orbitals leads to a significant enhancement in the decay rate—up to 10% for the heaviest nuclei. For all 2νECEC transitions analyzed, we provide the capture fractions corresponding to the most dominant channels. We also focus on low Q-value 2νECEC transitions in ^{152}Gd, ^{164}Er, and ^{242}Cm, where the simultaneous capture of both K shell electrons is energetically forbidden. Finally, using the updated phase-space factors, we reexamine the effective nuclear matrix elements and evaluate their spread relative to those associated with $2\nu\beta\beta$.

In the second part of this Chapter, we present a comprehensive analysis of the 2νECEC

process in ^{124}Xe. The formalism is refined using the Taylor expansion method [78, 179], incorporating terms up to the fourth power of the lepton energies in the derivation of the decay rate. This approach not only enhances the theoretical rigor but also introduces new NME ratios, $\xi_{31}^{2\nu\text{ECEC}}$ and $\xi_{51}^{2\nu\text{ECEC}}$. Measuring these ratios could offer valuable insights into the interplay between low- and higher-lying intermediate nuclear states involved in NME calculations.

In addition to this methodological improvement, we revisit both the atomic and nuclear components of the calculation. For the atomic part, we use again the DHFS self-consistent framework to determine the electron wave functions, ensuring an accurate treatment of atomic screening and electron binding energies. The PSF calculations are refined by accounting for Pauli blocking effects on the decay of innermost nucleon states and by including all s-wave electrons available for capture, extending beyond the K and L_1 orbitals considered in previous studies. Furthermore, we calculate the atomic de-excitation energies within the DHFS framework. These values, along with the capture fractions, can serve as inputs for background modeling in liquid xenon experiments.

For the nuclear part, we employ the interacting shell model (ISM) [236, 237, 238, 239, 240, 241] and the proton-neutron quasiparticle random-phase approximation (pn-QRPA) with isospin restoration[199]. Similar to $2\nu\beta\beta$ NMEs, the 2νECEC NMEs can only be reliably calculated if the sum over excited 1^+ states of the intermediate nucleus is included (see Eqs. (7.17)), which is inherently supported by the ISM and pn-QRPA approaches. Methods that bypass this full summation by adopting the closure approximation or the single-state dominance (SSD) approximation often fail to produce accurate results. Within the ISM, we replace the direct summation over intermediate states with a strength function approach, which converges more rapidly to the exact result. A complete description of this approach can be found in Section 4 of Ref.[241]. In this work, we extend the strength function approach to account for higher-order terms in the denominators required by the Taylor expansion formalism (see Eqs. (7.17)). The updated ISM NMEs, combined with the improved PSFs, enable predictions of capture fractions for 2νECEC channels that remain unobserved. For consistency, we analyze two widely used effective Hamiltonians, which yield compatible nuclear structure results, reinforcing the reliability of our computed NMEs and predicted capture fractions.

Additionally, we calculate the NMEs using the pn-QRPA method with isospin restoration, where the particle-particle strength parameter is fixed to reproduce the experimental half-life. Interestingly, we find that our pn-QRPA NME values are significantly smaller than those reported in earlier pn-QRPA studies [242, 243].

7.2 A systematic study of two-neutrino double electron capture

7.2.1 The usual formalism for the 2νECEC

We investigate the two neutrino double electron capture (2νECEC) process,

$$2e^- + (A, Z+2) \rightarrow (A, Z) + 2\nu_e, \tag{7.1}$$

in which the initial nucleus $(A, Z+2)$ captures two atomic electrons, changing its atomic number by two units and emitting two neutrinos. If the electrons are captured from the x and y atomic orbitals, we denote the process as 2νxy. For simplicity, we adopt the X-ray notation for the orbitals, where x and y = K, L_1, M_1, N_1, etc. Following the 2νxy process, the final atomic system remains electrically neutral but exists in an excited atomic state, characterized by vacancies in the orbitals x and y from which the electrons were

initially captured. As a result, the 2νECEC process is accompanied by atomic de-excitation, involving a cascade of X-ray emissions and Auger electrons originating from the outer shells.

Figure 7.1 schematically illustrates two possible channels for the 2νECEC process in ^{124}Xe. In the top panel, both electrons are captured from the K orbital ($2\nu KK$), whereas in the bottom panel, both electrons are captured from the L_1 orbital ($2\nu L_1 L_1$). It is important to emphasize that the atomic de-excitation yields different energy depositions in the detector, depending on whether the capture occurs from the K or L_1 shells. Specifically, atomic relaxation following $L_1 L_1$ capture emits less energy compared to the KK capture, leading to distinct experimental signatures for each capture mode.

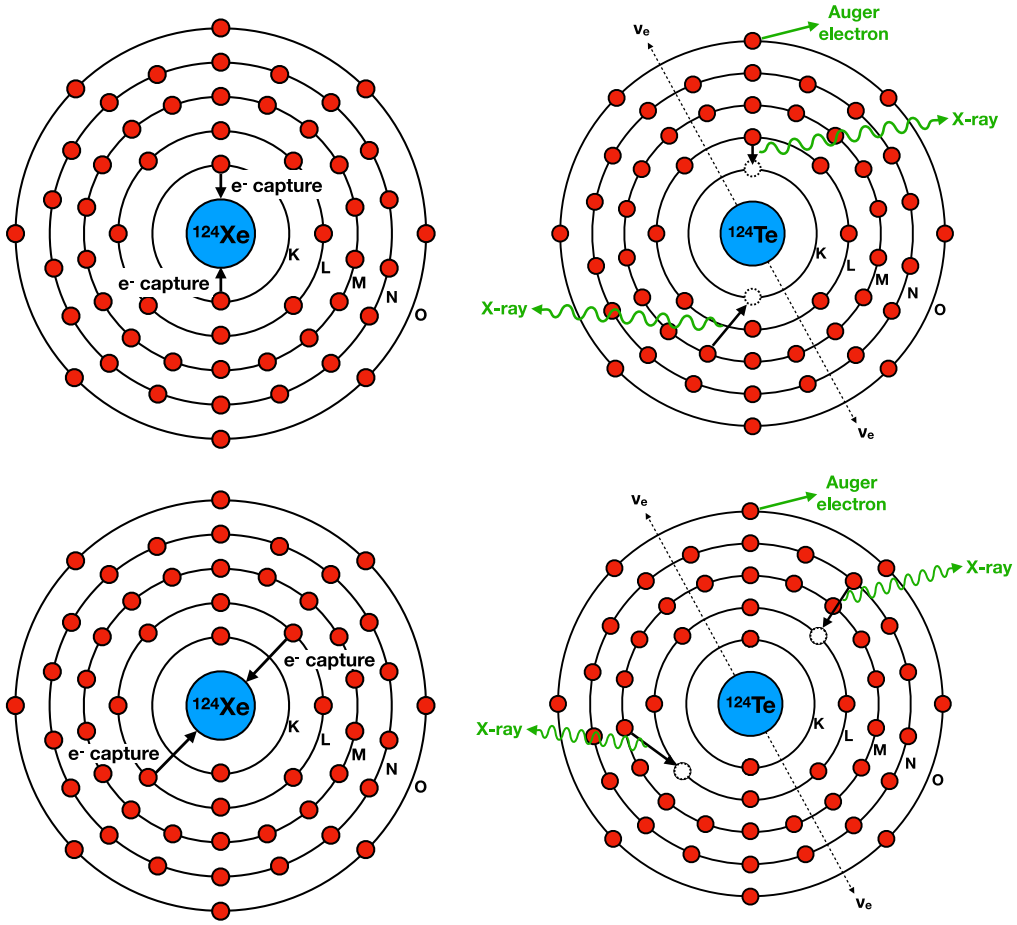

Figure 7.1: A simplified schematic representation of the 2νECEC process in ^{124}Xe. Top panels: both electrons are captured from K shell. Bottom panels: both electrons are captured from L shell. Left panels: two bound electrons from K (top) or L (bottom) shell are captured by the initial nucleus ^{124}Xe. Right panels: the atomic relaxation of the final neutral atomic system ^{124}Te, with two holes in K (top) or L (bottom) shell. The de-excitation is done via X-ray emissions and Auger electrons from outer shells. The figure is reproduced from [244] by adding the schematic representation of the $2\nu L_1 L_1$ process in ^{124}Xe. The figure is taken from [245].

We adopt the following energy balance,

$$\mathcal{M}_{\rm gs}(A, Z+2) - \mathcal{M}_{\rm gs}(A, Z) = \omega_{\rm x} + \omega_{\rm y} + \mathcal{M}_{\rm xy}(A, Z) - \mathcal{M}_{\rm gs}(A, Z), \tag{7.2}$$

which implies that the energy difference between the atomic masses of the initial and final

systems in their ground states, typically expressed as $Q = \mathcal{M}_{\rm gs}(A, Z+2) - \mathcal{M}_{\rm gs}(A, Z)$, is distributed among the neutrinos, with energies $\omega_{\rm x}$ and $\omega_{\rm y}$, and the atomic relaxation energy of the final atom. The mass $\mathcal{M}_{\rm xy}(A, Z)$ corresponds to an excited atomic state of the final neutral system, featuring vacancies in the shells x and y from which the electrons were captured in the initial atom. It can be expressed as,

$$\mathcal{M}_{\rm xy}(A, Z) = E_f + Zm_e - B_{\rm xy}(Z) \tag{7.3}$$

where E_f is the nuclear mass (energy) of the final nucleus, Zm_e is the rest energy of the final atomic cloud (m_e is the mass of the electron), and $B_{\rm xy}(Z)$ is the total electron binding energy of the final system with a configuration with two holes. We adopt the units in which $\hbar = c = 1$. One can see that the atomic relaxation energy can be written as a difference in the total electron binding energies of the final atom with gs and xy configurations,

$$R_{\rm xy} = B_{\rm gs}(Z) - B_{\rm xy}(Z). \tag{7.4}$$

The total energy of the emitted neutrinos can be written as,

$$\omega_{\rm x} + \omega_{\rm y} = Q - R_{\rm xy} \tag{7.5}$$

and making the usual approximation that $B_{\rm xy}(Z) - B_{\rm gs}(Z+2) = -|t_{\rm x}| - |t_{\rm y}|$, we finally obtain [33, 235, 195]

$$\begin{aligned} \omega_{\rm x} + \omega_{\rm y} &= E_i - E_f + 2m_e - |t_{\rm x}| - |t_{\rm y}| \\ &= E_i - E_f + e_{\rm x} + e_{\rm y}, \end{aligned} \tag{7.6}$$

where $t_{\rm x}$ and $e_{\rm x} = m_e - |t_{\rm x}|$ are respectively the binding and the total energy for the electrons in shell x.

Based on the formalism outlined in [33, 235], the inverse half-life for the 2νECEC process, transitioning from the 0^+ ground state of the initial nucleus to the 0^+ ground state of the final nucleus, can be expressed as:

$$\left[T_{1/2}^{2\nu\rm ECEC}\right]^{-1} = g_A^4 \left|M^{2\nu\rm ECEC}\right|^2 G_{K\to\rm edge}^{2\nu\rm ECEC}, \tag{7.7}$$

where g_A is the axial coupling constant, $G_{K\to\rm edge}^{2\nu\rm ECEC}$ is the phase-space factor (PSF) discussed later, and $M^{2\nu\rm ECEC}$, the nuclear matrix element (NME), is given by

$$M^{2\nu\rm ECEC} = -\frac{m_e}{\tilde{A}} \left[M_{\rm GT}^{2\nu\rm ECEC} - \left(\frac{g_V}{g_A}\right)^2 M_{\rm F}^{2\nu\rm ECEC} \right]. \tag{7.8}$$

Here, $\tilde{A} = 1.12A^{1/2}$ in MeV and g_V is the vector coupling constant. This choice of $\tilde{A}$ reproduces the average excitation energies in the intermediate nucleus for a wide range of isotopes [64]. Nevertheless, there are reasons supporting the use of a single value for both, as discussed in [64]. The double Gamow-Teller (GT) and Fermi (F) transition matrix elements, in closure approximation, are $M_{\rm GT}^{2\nu\rm ECEC} = \langle 0_f^+ \left| \sum_{j,k} \tau_j^- \tau_k^- \boldsymbol{\sigma}_j \boldsymbol{\sigma}_k \right| 0_i^+ \rangle$ and $M_{\rm F}^{2\nu\rm ECEC} = \langle 0_f^+ \left| \sum_{j,k} \tau_j^- \tau_k^- \right| 0_i^+ \rangle$ [235]. Here, $\tau_{j,k}^-$ is the isospin-lowering operator, transforming a proton into a neutron and $\boldsymbol{\sigma}_{j,k}$ is the nucleon spin operator.

It is important to emphasize that the factorization of the half-life in Equation 7.7 is based on the closure approximation [33]. As a result, the PSFs provided here must be used in conjunction with NMEs computed under the same approximation. Nevertheless, several prior studies have calculated NMEs beyond the closure approximation while disregarding

this constraint [242, 243, 246]. Despite this inconsistency, the predicted half-lives in those studies are remarkably close to the experimental values. In the present work, we adopt the closure approximation for direct comparisons. It is worth noting that an alternative formulation for the 2νECEC half-life, which does not rely on the closure approximation, will be presented in the second part of this Chapter.

We assume that electron captures can take place from any occupied $s_{1/2}$ orbitals of the initial atom, including $K, L_1, M_1, \ldots$. Captures from other orbitals are significantly suppressed for two primary reasons. First, the higher orbital angular momentum associated with these orbitals reduces the capture probability. Second, the NMEs corresponding to captures from non-$s_{1/2}$ orbitals are comparatively smaller [33]. Under these assumptions, we found that the PSF expression is

$$\begin{aligned} G^{2\nu\mathrm{ECEC}}_{K\to\mathrm{edge}} =& \frac{m_e(G_F\,|V_{ud}|\,m_e^2)^4}{16\pi^3}\frac{2\tilde{A}}{3m_e^2}\frac{1}{m_e^3}\sum_{\substack{\mathrm{x,y}=K \\ E_I-E_F+e_\mathrm{x}+e_\mathrm{y}>0}}^{\mathrm{edge}} \mathcal{B}^2_\mathrm{x}\mathcal{B}^2_\mathrm{y} \\ &\times\int_0^{E_I-E_F+e_\mathrm{x}+e_\mathrm{y}} \left[\langle K_{n,\mathrm{xy}}\rangle^2+\langle L_{n,\mathrm{xy}}\rangle^2+\langle K_{n,\mathrm{xy}}\rangle\langle L_{n,\mathrm{xy}}\rangle\right]\omega_\mathrm{x}^2\omega_\mathrm{y}^2 d\omega_\mathrm{x} \\ =& \sum_{\substack{\mathrm{x,y}=K \\ E_I-E_F+e_\mathrm{x}+e_\mathrm{y}>0}}^{\mathrm{edge}} G^{2\nu\mathrm{xy}}. \end{aligned} \tag{7.9}$$

where G_F is the Fermi coupling constant and V_{ud} the first element of the Cabibbo-Kobayashi-Maskawa (CKM) matrix. The summations extend over all occupied orbitals of the initial atomic system that are potential sources for electron capture. The term "edge" designates the outermost orbital eligible for capture. The probability of locating an electron from shell x at the nuclear surface can be expressed as [33, 235],

$$\mathcal{B}^2_\mathrm{x} = \frac{1}{4\pi m_e^3}\left[g^2_\mathrm{x}(R)+f^2_\mathrm{x}(R)\right], \tag{7.10}$$

in terms of the large- and small-component radial wave functions describing the bound state, $g_\mathrm{x}(r)$ and $f_\mathrm{x}(r)$, respectively, evaluated on the nuclear surface $R = 1.2A^{1/3}$. These are described in Section A.2. The factors $\langle K_{n,\mathrm{xy}}\rangle$ and $\langle L_{n,\mathrm{xy}}\rangle$ can be written as,

$$\begin{aligned} \langle K_{n,\mathrm{xy}}\rangle =& \frac{1}{-e_\mathrm{x}+\omega_\mathrm{x}+\langle E_n\rangle-E_i}+\frac{1}{-e_\mathrm{y}+\omega_\mathrm{y}+\langle E_n\rangle-E_i} \\ \langle L_{n,\mathrm{xy}}\rangle =& \frac{1}{-e_\mathrm{x}+\omega_\mathrm{y}+\langle E_n\rangle-E_i}+\frac{1}{-e_\mathrm{y}+\omega_\mathrm{x}+\langle E_n\rangle-E_i} \end{aligned} \tag{7.11}$$

where $\langle E_n\rangle$ is a suitably chosen excitation energy for the intermediate nucleus, $(A, Z+1)$. In the actual calculations, the energy difference $\langle E_n\rangle - E_i = \tilde{A} - Q/2 + m_e$.

For comparison with the results of the previous investigations, we define also the PSF for captures from K and L_1 orbitals only,

$$G^{2\nu\mathrm{ECEC}}_{K\to L_1} = G^{2\nu KK} + 2G^{2\nu KL_1} + G^{2\nu L_1L_1} \tag{7.12}$$

which is a particularization of Equation 7.9. The factor of 2 stems from the equal contributions of 2νxy and 2νyx captures in the total decay rate for any $\mathrm{x}\neq\mathrm{y}$ orbitals.

7.2.2 Electron bound states description

Accurate computation of the PSFs for any 2νECEC process necessitates precise atomic structure calculations for the atomic systems involved. To achieve this, we used the DHFS self-consistent framework. Details regarding the nuclear, electronic, and exchange components of the DHFS potential, along with the convergence of the self-consistent method, were previously outlined in [168, 247]. Our implementation is based on the RADIAL subroutine package [207], which we also employed in our calculations (see Subsection A.2.1 for more details). In earlier sections, the electron shells denoted as x or y are uniquely specified by the state $n\kappa$, where n is the principal quantum number and κ is the relativistic quantum number.

Table 7.1 compares experimental binding energies with theoretical predictions from various models for selected isotopes (Kr, Xe, and Ba) undergoing the 2νECEC process. The model presented in [33], which assumes a uniform nuclear charge distribution and neglects atomic screening, fails to reproduce the experimental data accurately. Approaches that incorporate atomic screening and diffuse nuclear surface effects, such as those in [194, 195], offer improved predictions by employing a Thomas-Fermi screening function and realistic proton density profiles within the nucleus. However, these models still overestimate binding energies relative to experimental values. In contrast, the DHFS self-consistent method employed in this work demonstrates superior accuracy, successfully reproducing experimental binding energies within a 1% margin. It should be noted that the binding energies for all orbitals of ^{124}Xe can be found in Section A.2.2.

Table 7.1: The binding energies, t_x, in units of eV, for all occupied $s_{1/2}$ orbitals of the neutral atoms, Kr, Xe and Ba, undergoing 2νECEC process. The experimental data are sourced from [248], our values are obtained with the DHFS self-consistent method, and values from prior studies are taken from [33] and [194, 195].

Shell($n\ell_j$)	t_x[33] (eV)	t_x[194, 195] (eV)	t_x [This work] (eV)	t_x [Experiment] [248] (eV)
		Kr		
$K(1s_{1/2})$	-17936	-17700	-14280	-14327 ± 2
$L_1(2s_{1/2})$	-4507	-3100	-1902	-1927 ± 2
$M_1(3s_{1/2})$	–	–	-278	-292 ± 2
$N_1(4s_{1/2})$	–	–	-27.46	-27.51 ± 0.1
		Xe		
$K(1s_{1/2})$	-41340	-39400	-34556	-34565 ± 2
$L_1(2s_{1/2})$	-10424	-7800	-5417	-5452 ± 2
$M_1(3s_{1/2})$	–	–	-1122	-1149 ± 2
$N_1(4s_{1/2})$	–	–	-208	-213 ± 2
$O_1(5s_{1/2})$	–	–	-23.63	-23.40 ± 0.1
		Ba		
$K(1s_{1/2})$	-44610	-42400	-37450	-37442 ± 2
$L_1(2s_{1/2})$	-11293	-8500	-5961	-5991 ± 2
$M_1(3s_{1/2})$	–	–	-1274	-1293 ± 2
$N_1(4s_{1/2})$	–	–	-256	-254 ± 2
$O_1(5s_{1/2})$	–	–	-38	-31 ± 2
$P_1(6s_{1/2})$	–	–	-4.64	-5.21 ± 0.1

7.2.3 Results and discussions

The PSFs for captures from K and L_1 shells only, $G^{2\nu\mathrm{ECEC}}_{K\to L_1}$, calculated for the 2νECEC cases previously studied, are presented in Table 7.2. In this analysis, we adopted the same Q-

values as used in [235]. Our results are consistently lower, by approximately 5%, compared to those reported in [235], with the exceptions of ^{92}Mo and ^{180}W, where deviations are more pronounced. Compared to the values reported in [194, 195], our PSFs generally fall within 70%, showing a noticeable dependence on the mass number A. For lighter nuclei, our values are systematically lower than those in [194, 195], but as the mass number increases, our results tend to converge and even surpass the previously reported values. This trend suggests differences in the underlying models, particularly in the treatment of screening and nuclear size effects. In contrast, the $G^{2\nu\mathrm{ECEC}}_{K\to L_1}$ values obtained in this study show a consistent reduction of 10%-20% relative to those presented in [33]. This discrepancy can likely be attributed to the absence of screening effects in [33]. We opted not to include comparisons with the values reported in [234], as their definition of the PSF differs due to an alternative separation of the decay rate.

In Table 7.3, we present the total PSFs, $G^{2\nu\mathrm{ECEC}}_{K\to\mathrm{edge}}$, along with the capture fractions for selected shell pairs, for all nuclei where 2νECEC is energetically allowed and single-electron capture (EC) is energetically forbidden. A comparison with one of the most precise calculations available [235] (column four of Table 7.2) reveals the following trends. For light atoms, the more rigorous treatment of atomic screening employed in our calculations effectively compensates for the inclusion of all $\kappa = -1$ shells, resulting in PSF values comparable to those reported in [235]. An exception is ^{40}Ca, where our calculated PSF value, incorporating all $\kappa = -1$ shells, is approximately 7.5% higher. This discrepancy arises from the interplay between binding energies and the Q-value in the PSF integral (see Equation 7.9). For medium and heavy atoms, our results show a consistent increase in the decay rate relative to [235]. This increase is almost linear with Z, reaching approximately 10% for the heaviest elements considered.

The low Q-value transitions of ^{152}Gd, ^{164}Er, and ^{242}Cm exhibit unique behavior. In these cases, both the KK and KL_1 capture channels are energetically forbidden. Consequently, the dominant contributions to the total PSF originate from the L_1L_1, M_1M_1, and L_1M_1 capture channels. Table 7.4 provides the values of the PSFs and capture fractions for these low Q-value transitions. These results emphasize the role of higher-order electron shells in the decay process and highlight the importance of including all energetically allowed capture channels when evaluating decay rates for low Q-value transitions. Such contributions, which are often neglected in simpler models, become significant in the case of forbidden captures from lower-energy shells.

The inverse of the PSF, which is proportional to the half-life for each transition (as given by Equation 7.7), is plotted in Figure 7.2 for all nuclei listed in Table 7.3 as a function of the atomic number. The results indicate a clear trend: the half-life decreases as both the Q-value and the atomic number increase. This behavior is driven primarily by the larger phase-space factors associated with higher atomic numbers, which result in a higher decay rate and consequently shorter half-lives.

Finally, we investigate the effective matrix elements for the 2νECEC process of ^{78}Kr, ^{124}Xe, ^{130}Ba and ^{132}Ba. These can be obtained as,

$$\begin{aligned}\left|M^{2\nu\mathrm{ECEC}}_{\mathrm{eff}}\right| &= \frac{1}{\sqrt{T^{2\nu\mathrm{ECEC}}_{1/2} G^{2\nu\mathrm{ECEC}}_{K\to\mathrm{edge}}}} \\ &= \frac{m_e}{\tilde{A}} \left| g_A^2 M^{2\nu\mathrm{ECEC}}_{\mathrm{GT}} - g_V^2 M^{2\nu\mathrm{ECEC}}_{\mathrm{F}} \right| .\end{aligned} \tag{7.13}$$

using the experimental half-lives and the PSFs from Table 7.3. The effective NME values are summarized in Table 7.5. It is important to highlight that, for ^{132}Ba, an experimental half-life measurement has been reported in [42]. However, the authors emphasized that this value

Table 7.2: Comparison of the $G^{2\nu\mathrm{ECEC}}_{K\to L_1}$ (in units of 10^{-24} yr^{-1}) values from [33], [235], and [194, 195], with values obtained through the method explained in this study. The Q-values cited in [235] were utilized. In cases where these values were not available, the Q was calculated using atomic masses provided in [197].

Nucleus	Q (MeV) (MeV)	$G^{2\nu\mathrm{ECEC}}_{K\to L_1}$[33] $(10^{-24}\mathrm{yr}^{-1})$	$G^{2\nu\mathrm{ECEC}}_{K\to L_1}$[235] $(10^{-24}\mathrm{yr}^{-1})$	$G^{2\nu\mathrm{ECEC}}_{K\to L_1}$[194, 195] $(10^{-24}\mathrm{yr}^{-1})$	$G^{2\nu\mathrm{ECEC}}_{K\to L_1}$[This work] $(10^{-24}\mathrm{yr}^{-1})$
^{36}Ar	0.43259	–	–	2.900×10^{-4}	4.168×10^{-4}
^{40}Ca	0.19351	–	1.250×10^{-5}	1.020×10^{-5}	1.314×10^{-5}
^{50}Cr	1.1688	–	4.220×10^{-1}	2.380×10^{-1}	4.161×10^{-1}
^{54}Fe	0.6798	–	4.690×10^{-2}	3.021×10^{-2}	4.553×10^{-2}
^{58}Ni	1.9263	17.00	15.30	9.900	14.79
^{64}Zn	1.0948	–	1.410	1.030	1.364
^{74}Se	1.209169	–	5.656	3.410	5.454
^{78}Kr	2.8463	774.0	660.0	410.0	637.0
^{84}Sr	1.79	–	93.60	64.62	90.58
^{92}Mo	1.651	–	208.0	82.32	128.2
^{96}Ru	2.71451	2.740×10^{3}	2.400×10^{3}	1.450×10^{3}	2.328×10^{3}
^{102}Pd	1.1727	–	46.00	42.09	44.64
^{106}Cd	2.77539	6.220×10^{3}	5.410×10^{3}	4.299×10^{3}	5.269×10^{3}
^{108}Cd	0.27204	–	2.070×10^{-2}	6.820×10^{-2}	1.975×10^{-2}
^{112}Sn	1.91982	–	1.150×10^{3}	869.7	1.120×10^{3}
^{120}Te	1.71481	–	888.0	840.3	866.3
^{124}Xe	2.8654	2.020×10^{4}	1.720×10^{4}	1.510×10^{4}	1.685×10^{4}
^{126}Xe	0.92	–	46.10	60.59	44.98
^{130}Ba	2.619	1.630×10^{4}	1.500×10^{4}	1.477×10^{4}	1.464×10^{4}
^{132}Ba	0.844	–	39.10	61.98	38.12
^{136}Ce	2.37853	1.580×10^{4}	1.250×10^{4}	1.222×10^{4}	1.224×10^{4}
^{138}Ce	0.698	–	18.40	34.47	17.92
^{144}Sm	1.78259	–	5.150×10^{3}	6.436×10^{3}	5.055×10^{3}
^{152}Gd	0.0557	–	–	1.120×10^{-2}	5.989×10^{-7}
^{156}Dy	2.012	–	1.760×10^{4}	2.208×10^{4}	1.734×10^{4}
^{158}Dy	0.284	–	1.830×10^{-1}	3.191	1.751×10^{-1}
^{162}Er	1.844	1.810×10^{4}	1.500×10^{4}	2.008×10^{4}	1.470×10^{4}
^{164}Er	0.02507	–	–	8.300×10^{-3}	7.392×10^{-11}
^{168}Yb	1.40927	–	4.710×10^{3}	7.872×10^{3}	4.647×10^{3}
^{174}Hf	1.0988	–	1.580×10^{3}	3.432×10^{3}	1.563×10^{3}
^{180}W	0.1432	–	1.560×10^{-3}	1.478	1.321×10^{-3}
^{184}Os	1.453	–	1.290×10^{4}	2.422×10^{4}	1.275×10^{4}
^{190}Pt	1.384	–	1.290×10^{4}	2.815×10^{4}	1.285×10^{4}
^{196}Hg	0.82	–	821.0	3.587×10^{3}	815.8

Table 7.3: Values of the $G^{2\nu\mathrm{ECEC}}_{K\to\mathrm{edge}}$ (in units of 10^{-24} yr^{-1}) and of the capture fractions for various shell pairs. The Q-values are computed using atomic masses provided in [197].

Nucleus	Q (MeV)	$G^{2\nu\mathrm{ECEC}}_{K\to\mathrm{edge}}$ $(10^{-24}\mathrm{yr}^{-1})$	KK (%)	KL_1 (%)	KM_1 (%)	KN_1 (%)	L_1L_1 (%)
^{36}Ar	0.4326	4.244×10^{-4}	83.40	14.23	1.62	–	0.61
^{40}Ca	0.1935	1.347×10^{-5}	81.38	15.44	2.07	0.16	0.73
^{50}Cr	1.1705	4.301×10^{-1}	81.35	15.39	2.18	0.12	0.73
^{54}Fe	0.68076	4.717×10^{-2}	80.41	16.01	2.35	0.16	0.80
^{58}Ni	1.9264	15.22	80.45	15.97	2.37	0.15	0.79
^{64}Zn	1.09502	1.407	79.73	16.50	2.48	0.14	0.85
^{74}Se	1.20924	5.648	78.64	17.03	2.74	0.30	0.92
^{78}Kr	2.84767	661.9	78.64	16.92	2.81	0.35	0.91
^{84}Sr	1.78977	94.16	77.83	17.33	2.98	0.44	0.96
^{92}Mo	1.65044	133.8	76.69	17.89	3.25	0.56	1.04
^{96}Ru	2.7145	2.437×10^{3}	76.64	17.85	3.31	0.60	1.04
^{102}Pd	1.20347	53.70	75.16	18.77	3.59	0.68	1.17
^{106}Cd	2.77539	5.540×10^{3}	75.71	18.31	3.55	0.69	1.11
^{108}Cd	0.27179	2.122×10^{-2}	65.39	24.87	5.12	1.01	2.26
^{112}Sn	1.91981	1.181×10^{3}	74.78	18.82	3.72	0.76	1.18
^{120}Te	1.73558	975.8	74.06	19.20	3.87	0.83	1.24
^{124}Xe	2.85674	1.756×10^{4}	74.22	19.00	3.88	0.86	1.22
^{126}Xe	0.91778	47.36	71.66	20.62	4.28	0.95	1.48
^{130}Ba	2.6237	1.570×10^{4}	73.57	19.31	4.00	0.92	1.27
^{132}Ba	0.84407	40.87	70.45	21.26	4.50	1.03	1.59
^{136}Ce	2.37853	1.303×10^{4}	72.88	19.67	4.14	0.97	1.33
^{138}Ce	0.69594	19.03	68.37	22.43	4.86	1.14	1.82
^{144}Sm	1.7824	5.417×10^{3}	71.11	20.67	4.49	1.07	1.50
^{150}Gd	1.28728	1.301×10^{3}	69.29	21.72	4.81	1.16	1.69
^{152}Gd	0.05567	1.547×10^{-6}	–	–	7.40×10^{-4}	1.04×10^{-3}	38.56
^{154}Dy	3.31234	2.490×10^{5}	71.29	20.48	4.51	1.09	1.47
^{156}Dy	2.00595	1.837×10^{4}	70.19	21.14	4.69	1.14	1.59
^{158}Dy	0.28282	2.028×10^{-1}	42.31	35.46	9.04	2.26	6.01
^{162}Er	1.84696	1.601×10^{4}	69.29	21.64	4.87	1.19	1.68
^{164}Er	0.02508	8.606×10^{-9}	–	–	–	–	0.87
^{168}Yb	1.40936	5.052×10^{3}	67.42	22.71	5.20	1.27	1.90
^{174}Hf	1.09994	1.724×10^{3}	64.94	24.06	5.62	1.39	2.20
^{180}W	0.14323	2.522×10^{-3}	5.94×10^{-5}	17.72	8.08	2.34	34.73
^{184}Os	1.45289	1.399×10^{4}	65.02	23.90	5.64	1.43	2.17
^{190}Pt	1.40132	1.519×10^{4}	63.83	24.50	5.84	1.50	2.32
^{196}Hg	0.81859	916.2	56.49	28.25	7.04	1.84	3.38
^{212}Rn	1.71019	1.400×10^{5}	61.36	25.58	6.27	1.68	2.63
^{214}Rn	0.15031	1.376×10^{-2}	–	1.07	1.38	0.52	39.52
^{218}Ra	1.42814	6.758×10^{4}	58.58	26.92	6.72	1.83	3.03
^{224}Th	1.16975	2.802×10^{4}	54.68	28.74	7.34	2.03	3.64
^{230}U	0.75251	2.393×10^{3}	42.80	33.66	9.16	2.59	5.87
^{236}Pu	0.45693	95.16	16.51	39.25	12.33	3.64	13.66
^{242}Cm	0.08682	1.243×10^{-3}	–	–	–	–	9.66
^{252}Fm	0.782	8.121×10^{3}	34.11	36.07	10.34	3.05	7.96
^{258}No	1.051	7.188×10^{4}	41.77	33.61	9.28	2.73	6.14

Table 7.4: Values of the $G^{2\nu\mathrm{ECEC}}_{K\to\mathrm{edge}}$ (in units of 10^{-24} yr^{-1}) and of the capture fractions for the dominant shell pairs in case of low Q-value transitions. The Q-values are computed using atomic masses provided in [197].

Nucleus	Q (MeV)	$G^{2\nu\mathrm{ECEC}}_{K\to\mathrm{edge}}$ $(10^{-24}\mathrm{yr}^{-1})$	L_1L_1 (%)	L_1M_1 (%)	L_1N_1 (%)	L_1O_1 (%)	M_1M_1 (%)	M_1N_1 (%)	M_1O_1 (%)	N_1N_1 (%)	N_1O_1 (%)
^{152}Gd	0.05567	1.547×10^{-6}	38.56	35.94	10.12	1.84	7.56	4.17	0.75	0.57	0.21
^{164}Er	0.02508	8.606×10^{-9}	0.87	26.59	12.06	2.33	28.11	20.49	3.79	3.62	1.33
^{242}Cm	0.08682	1.243×10^{-3}	9.66	33.49	13.91	4.16	16.55	12.49	3.65	2.32	1.35

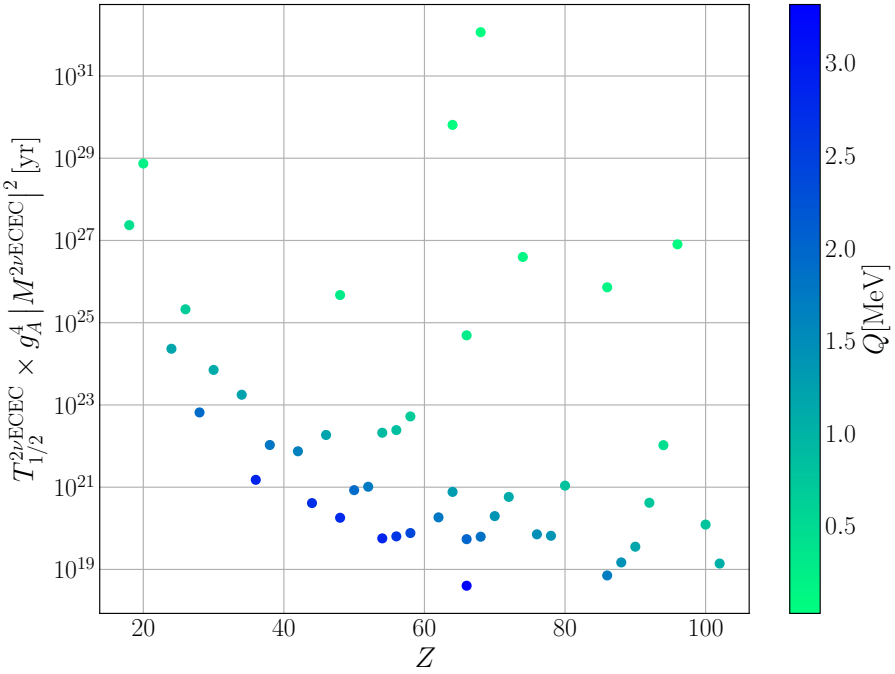

Figure 7.2: Theoretical half-life scaled by $g_A^4 \left|M^{2\nu\mathrm{ECEC}}\right|^2$ as function of atomic number for nuclei presented in Table 7.3. The color scale indicates the Q-value for each transition. The figure is taken from [245].

is tentative. Indeed, our analysis yields an effective NME value for ^{132}Ba that is more than an order of magnitude larger than those obtained for other nuclei. Consequently, we adopt the more conservative half-life limit provided in [41]. Future experimental measurements may help resolve this discrepancy. However, it is worth noting that geochemical measurements often tend to underestimate half-lives, leading to an overestimation of effective NMEs. This could be attributed to challenges in accurately identifying the relevant production channels of the final atom [36]. Another intriguing possibility is that variations in the weak interaction constant over time might be influencing these measurements, as discussed in [249, 250, 251].

In Figure 7.3, we compare the effective NMEs listed in Table 7.5 for the 2νECEC process with those corresponding to the $2\nu\beta\beta$-decay. The latter are defined analogously to the ECEC effective NMEs, but with isospin-lowering operators replaced by isospin-raising operators in the definitions of the Gamow-Teller and Fermi matrix elements. Interestingly, the effective NMEs obtained from both processes exhibit similar ranges, suggesting a comparable underlying nuclear structure and dynamics governing these transitions.

Table 7.5: Values or limits of the experimental half-life $M_{\text{eff}}^{2\nu\text{ECEC}}$. The Q-values are computed using atomic masses provided in [197]. The bottom row corresponds to the $2\nu\beta\beta$ decay of ^{134}Xe. For this case, the value of the effective NME was obtained from the lower half-life limit, and the PSF computed following [192] (0.225×10^{-22} yr^{-1} using $Q = 0.8258$ MeV).

Nucleus	$T_{1/2}^{2\nu\text{ECEC}}$ (yr)	$\lvert M_{\text{eff}}^{2\nu\text{ECEC}} \rvert$
^{78}Kr	$9.2^{+5.7}_{-2.9} \times 10^{21}$ [44]	$0.457^{+0.095}_{-0.098}$
	$1.9^{+1.3}_{-0.8} \times 10^{22}$ [45]	$0.318^{+0.100}_{-0.073}$
^{124}Xe	$(1.1 \pm 0.2) \times 10^{22}$ [47]	$0.072^{+0.008}_{-0.006}$
^{130}Ba	$(2.2 \pm 0.5) \times 10^{21}$ [42]	$0.170^{+0.023}_{-0.017}$
	$(6.0 \pm 1.1) \times 10^{20}$ [43]	$0.326^{+0.035}_{-0.026}$
^{132}Ba	$\geq 2.2 \times 10^{21}$ [41]	≤ 3.335
Nucleus	$T_{1/2}^{2\nu\beta\beta}$ (yr)	$\lvert M_{\text{eff}}^{2\nu\beta\beta} \rvert$
^{134}Xe	$\geq 2.8 \times 10^{22}$ [252]	≤ 0.398

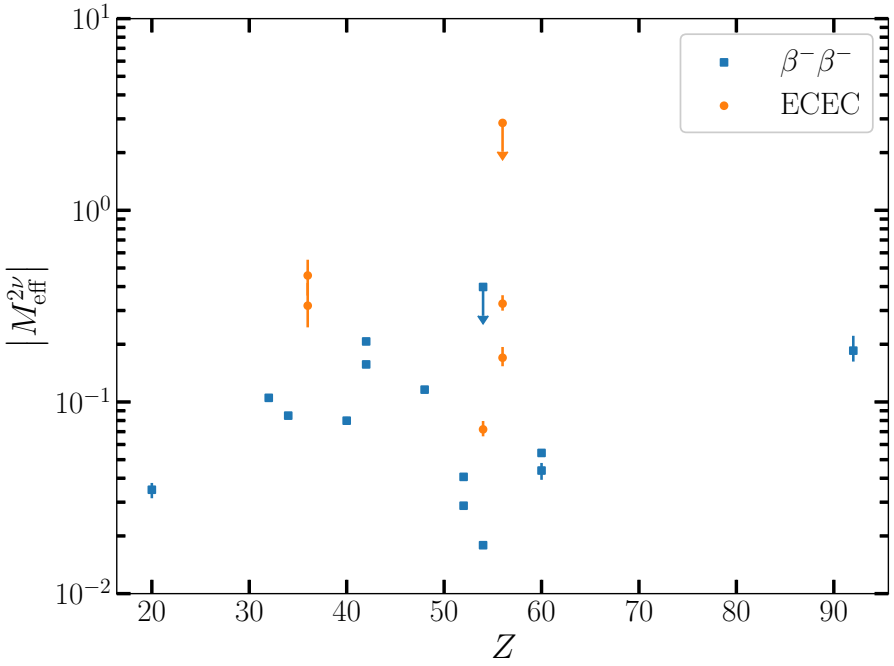

Figure 7.3: Absolute values of the effective nuclear matrix elements for the measured nuclei undergoing 2νECEC process or $2\nu\beta\beta$ decay. The values for 2νECEC processes and $2\nu\beta\beta$ decay of ^{134}Xe are the ones from Table 7.5. The other $2\nu\beta\beta$ values are the ones reported in [253], computed using the PSFs from [192]. Vertical bars indicate uncertainties derived from the ones of the measured half-lives. Arrows indicate that the corresponding point is an upper limit for the effective nuclear matrix element. The figure is taken from [245].

7.2.4 Uncertainties and further improvements

We first conduct a sensitivity analysis on the input parameters, specifically the Q-value, the average energy of the excited 1^+ states $\langle E_N \rangle$, and the nuclear radius. The relative variations in the PSFs resulting from changes in these parameters are summarized in Table 7.6. Among these, the Q-value exhibits the greatest influence. Nevertheless, we emphasize that modern measurements of the Q-value are highly precise, rendering the absolute PSF values effectively insensitive to minor variations in this parameter. In contrast, the sensitivities of the PSFs to $\langle E_N \rangle$ and the nuclear radius are significantly smaller, in agreement with earlier findings reported in [235].

Table 7.6: Summary of uncertainties in the PSFs due to input parameters.

Source	$\delta G^{2\nu\text{ECEC}}_{K\rightarrow\text{edge}}/G^{2\nu\text{ECEC}}_{K\rightarrow\text{edge}}$
Q-value	(5-7)$\times\delta Q/Q$
$\langle E_N \rangle$	0.07 $\times\delta\langle E_N\rangle/\langle E_N\rangle$
Nuclear radius	0.2 $\times\delta R/R$

Another source of uncertainty arises from the use of the DHFS model for atomic structure computations. The DHFS approach achieves an accuracy of approximately 1% in binding energies relative to experimental values [247]. These binding energies influence the PSFs through their role in defining integration limits, determining neutrino energies, and contributing to the $\langle K_N \rangle$ and $\langle L_N \rangle$ factors, where they always appear as additive terms to the Q-value. Consequently, this uncertainty has a negligible impact, translating to a relative variation of $\mathcal{O}(10^{-4})$ in the Q-value of the process. However, low Q-value transitions are an exception, where binding energy uncertainties become dominant.

Uncertainty in the values of wave functions at the nuclear surface also contributes to PSF errors. This effect was analyzed in [247] by comparing Coulomb amplitudes, proportional to the wave function values on the nuclear surface, obtained using the DHFS model with those derived from the more advanced Dirac-Hartree-Fock (DHF) model. The study found that Coulomb amplitudes in the DHFS model agree within 0.25% with those in the DHF model for the $1s_{1/2}$ and $2s_{1/2}$ shells, particularly for atomic numbers above 20. Assuming this value as the uncertainty in our model, we estimate a relative error in the PSFs of approximately 1%, as wave functions enter the PSF definition raised to the fourth power. It is worth noting that this uncertainty is systematic, with DHFS Coulomb amplitudes consistently overestimating those obtained in the DHF model.

Beyond the uncertainties discussed earlier, additional variations in the PSFs may arise from enhancements to the overall modeling of the 2νECEC process. Firstly, the determination of the summed neutrino energy, currently approximated using Equation 7.6, can be refined by employing the exact relation provided in Equation 7.5. Such refinements are particularly relevant for low Q-value transitions. For instance, the DHFS framework predicts $R_{KL_1} = 55.05$keV for ^{152}Sm. As a result, the $2\nu KL_1$ process in ^{152}Gd becomes energetically allowed, contrary to the findings presented in Table7.3. This outcome is consistent with earlier studies of resonant neutrinoless double electron capture, such as those reported in [254, 255, 256]. Secondly, our current model does not include the Pauli blocking effect on the decay of the innermost nucleon states. This limitation can be addressed by averaging the bound electron wave function, weighted by a realistic nuclear charge distribution, as described in [192, 257]. Preliminary results indicate that incorporating this effect could lead to an increase of a few percent in the PSFs. Some of these aspects are discussed in the second part of this Chapter dedicated to 2νECEC of ^{124}Xe.

7.2.5 Conclusions

In this part of Chapter 7, we have performed a comprehensive study of atoms undergoing the 2νECEC process. While 2νECEC inherently bridges nuclear and atomic physics, prior investigations have often treated atomic structure calculations simplistically or overlooked key aspects. To address these gaps, we introduced two major improvements in modeling the atomic component of double electron capture transitions. First, we employed the DHFS self-consistent framework to refine the description of bound wave function and to improve the accuracy of binding energy estimates for captured electrons. Second, we extended our analysis to include captures from outer orbitals, beyond the K and L_1 shells considered in previous studies.

Using this enhanced model, we updated the phase-space values for all atoms undergoing the 2νECEC process. For lighter atoms, we observed minimal differences relative to earlier models that assumed simplified atomic screening and restricted captures to the K and L_1 orbitals. This similarity arises from a cancellation effect, where the decay rate reduction caused by more precise screening is balanced by the increase resulting from higher-orbital captures. However, for medium and heavy atoms, our model predicted a nearly linear increase in the decay rate with atomic number, reaching enhancements of approximately 10% in the decay rates for the heaviest cases.

Additionally, we provided detailed capture fractions for the dominant partial channels and examined low Q-value 2νECEC transitions in ^{152}Gd, ^{164}Er, and ^{242}Cm, where the KK capture is energetically forbidden. Finally, we demonstrated that the effective nuclear matrix elements for 2νECEC processes exhibit ranges comparable to those of $2\nu\beta\beta$-decays.

7.3 Theoretical analysis and predictions for the two-neutrino double electron capture of ^{124}Xe

7.3.1 Improved formalism for 2νECEC

We improve the 2νECEC formalism by employing a Taylor expansion approach. Building upon the methodology used for $2\nu\beta\beta$ decay [78, 179] (see Chapter 5), and extending the expansion to include terms up to the fourth power in the lepton energies, we derive the total inverse half-life of the 2νECEC process in an analogous form:

$$\begin{aligned}\left[T_{1/2}^{2\nu\mathrm{ECEC}}\right]^{-1} = \left(g_A^{\mathrm{eff}}\right)^4 \left|M_{GT-1}^{2\nu\mathrm{ECEC}}\right|^2 \Big\{ & G_0^{2\nu\mathrm{ECEC}} \\ & + \xi_{31}^{2\nu\mathrm{ECEC}} G_2^{2\nu\mathrm{ECEC}} + \frac{1}{3}\left(\xi_{31}^{2\nu\mathrm{ECEC}}\right)^2 G_{22}^{2\nu\mathrm{ECEC}} \\ & + \left[\frac{1}{3}\left(\xi_{31}^{2\nu\mathrm{ECEC}}\right)^2 + \xi_{51}^{2\nu\mathrm{ECEC}}\right] G_4^{2\nu\mathrm{ECEC}} \Big\},\end{aligned} \tag{7.14}$$

The partial inverse half-life for the 2νxy process, in which atomic electrons are captured exclusively from the x and y shells, can be expressed as:

$$\begin{aligned}\left[T_{1/2}^{2\nu\mathrm{xy}}\right]^{-1} = (2-\delta_{\mathrm{xy}}) \left(g_A^{\mathrm{eff}}\right)^4 \left|M_{GT-1}^{2\nu\mathrm{ECEC}}\right|^2 \Big\{ & G_0^{2\nu\mathrm{xy}} + \\ & + \xi_{31}^{2\nu\mathrm{ECEC}} G_2^{2\nu\mathrm{xy}} + \frac{1}{3}\left(\xi_{31}^{2\nu\mathrm{ECEC}}\right)^2 G_{22}^{2\nu\mathrm{xy}} + \\ & + \left[\frac{1}{3}\left(\xi_{31}^{2\nu\mathrm{ECEC}}\right)^2 + \xi_{51}^{2\nu\mathrm{ECEC}}\right] G_4^{2\nu\mathrm{xy}} \Big\}.\end{aligned} \tag{7.15}$$

Here, g_A^{eff} is an effective axial coupling constant and the parameters:

$$\xi_{31}^{2\nu\text{ECEC}} = \frac{M_{GT-3}^{2\nu\text{ECEC}}}{M_{GT-1}^{2\nu\text{ECEC}}}, \qquad \xi_{51}^{2\nu\text{ECEC}} = \frac{M_{GT-5}^{2\nu\text{ECEC}}}{M_{GT-1}^{2\nu\text{ECEC}}} \tag{7.16}$$

are NME ratios arising from the Taylor expansion, with

$$\begin{aligned} M_{GT-1}^{2\nu\text{ECEC}} &= \sum_n M_{GT}^{2\nu}(n) \frac{m_e}{E_n(1^+) - (E_i + E_f)/2}, \\ M_{GT-3}^{2\nu\text{ECEC}} &= \sum_n M_{GT}^{2\nu}(n) \frac{4\ m_e^3}{\left[E_n(1^+) - (E_i + E_f)/2\right]^3}, \\ M_{GT-5}^{2\nu\text{ECEC}} &= \sum_n M_{GT}^{2\nu}(n) \frac{16\ m_e^5}{\left[E_n(1^+) - (E_i + E_f)/2\right]^5}. \end{aligned} \tag{7.17}$$

The summations are over all 1^+ states of the intermediate nucleus and $M_{GT}^{2\nu}(n)$ matrix elements depend on the n^{th} 1^+ intermediate state, with energy $E_n(1^+)$, as well as on the ground states $|0_i^+\rangle$ and $|0_f^+\rangle$ of the initial and final nuclei, with the energies E_i and E_f:

$$M_{GT}^{2\nu}(n) = \langle 0_f^+ \| \sum_m \tau_m^- \sigma_m \| 1_n^+ \rangle \langle 1_n^+ \| \sum_m \tau_m^- \sigma_m \| 0_i^+ \rangle, \tag{7.18}$$

where τ_m^- is the isospin-lowering operator transforming a proton into a neutron, and σ_m is the nucleon spin operator.

The PSFs entering the inverse half-lives are given by

$$\begin{aligned} G_N^{2\nu\text{ECEC}} &= \frac{m_e (G_F\, |V_{ud}|\, m_e^2)^4}{2\pi^3 \ln(2)} \frac{1}{m_e^5} \sum_{\text{x,y}} \mathcal{B}_{\text{x}}^2 \mathcal{B}_{\text{y}}^2 \mathcal{I}_{N,\text{xy}} \\ &= \sum_{\text{x,y}} G_N^{2\nu\text{xy}}, \end{aligned} \tag{7.19}$$

where G_F is the Fermi coupling constant, V_{ud} represents the first element of the Cabibbo-Kobayashi-Maskawa (CKM) matrix, and the summations extend over all occupied atomic shells in the initial atom. The functions $\mathcal{I}_{N,\text{xy}}$ depend on the total energies of the electrons occupying the x and y orbitals in the initial atom, denoted as e_{x} and e_{y}, respectively. Their explicit forms can be derived from Eqs. (5.29) and (5.30) by substituting $E_{e_1} \to -e_{\text{x}}$ and $E_{e_2} \to -e_{\text{y}}$. The probability of localizing an electron from shell x inside the nucleus is expressed as:

$$\mathcal{B}_{\text{x}}^2 = \frac{1}{4\pi m_e^3} \left[\langle g_{\text{x}} \rangle^2 + \langle f_{\text{x}} \rangle^2 \right], \tag{7.20}$$

where

$$\langle g_{\text{x}} \rangle = \frac{\int g_{\text{x}}(r) \rho(r) r^2 dr}{\int \rho(r) r^2 dr} \qquad \langle f_{\text{x}} \rangle = \frac{\int f_{\text{x}}(r) \rho(r) r^2 dr}{\int \rho(r) r^2 dr} \tag{7.21}$$

Here, $g_{\text{x}}(r)$ and $f_{\text{x}}(r)$ represent the large- and small-component radial wave functions, respectively, for the bound electron in shell x. The nuclear charge distribution, normalized to Z, is expressed as:

$$\rho(r) = \frac{1}{1 + e^{(r - c_{\text{rms}})/a}} \tag{7.22}$$

	$N=0$	$N=2$	$N=22$	$N=4$
$G_N^{2\nu\mathrm{ECEC}}$	18332.0	9802.2	3056.1	6116.3
$G_N^{2\nu\mathrm{KK}}$	13605.3	7230.0	2241.2	4482.4
$G_N^{2\nu\mathrm{KL_1}}$	1741.9	945.8	298.9	599.4
$G_N^{2\nu\mathrm{KM_1}}$	355.4	193.6	61.3	123.1
$G_N^{2\nu\mathrm{KN_1}}$	78.6	42.8	13.6	27.3
$G_N^{2\nu\mathrm{KO_1}}$	11.8	6.4	2.0	4.1
$G_N^{2\nu\mathrm{L_1L_1}}$	222.9	123.4	39.9	79.8
$G_N^{2\nu\mathrm{L_1M_1}}$	45.5	25.3	8.2	16.4

Table 7.7: The evaluated PSFs (Eq. 7.19) units of $10^{-24}\mathrm{yr}^{-1}$ for the total 2νECEC process (first line) and the partial 2νxy processes (the following lines) of ^{124}Xe. We have used $Q = 2856.73$ keV [259].

Using a surface thickness of $a = 0.545$ fm, we determined that $c_{\mathrm{rms}} = 5.569$ fm reproduces the experimental root-mean-square (rms) radius, $\sqrt{\langle r^2 \rangle} = 4.7661$ fm, for ^{124}Xe [258]. The weighted average of the bound electron wave function, incorporating the nuclear charge distribution, effectively accounts for Pauli blocking of the decay of innermost nucleon states while retaining the intuitive interpretation of electron capture occurring on the nuclear surface.

7.3.2 PSFs calculation and atomic relaxation energies

In most studies of the 2νECEC process, electron captures are primarily considered from the K shell and L_1 subshell [33, 235, 195]. However, in the specific case of double electron capture in ^{124}Xe, even electrons from the O shell exhibit a small but non-negligible probability of being captured. In this work, we assume that neutrinos are emitted with anti-parallel spins and allow electron capture from all occupied shells of the initial atom, extending the summations in Eq. 7.19 up to the O_1 subshell. We restrict our analysis to subshells with $\kappa = -1$, as captures involving configurations where not all four leptons occupy s-wave states are strongly suppressed due to additional terms in the NMEs [33]. This assumption may impact the interpretation of experimental data. For instance, the signal model employed in [47] includes captures from all subshell combinations. In our model, each subshell accommodates only two electrons, resulting in two pairs of electrons available for capture when $\mathrm{x} \neq \mathrm{y}$. This condition is incorporated into Eq. (7.19) by not imposing the requirement $\mathrm{x} < \mathrm{y}$.

The results of the PSFs calculated using the Taylor expansion formalism for the 2νECEC process in ^{124}Xe are presented in Table 7.7, based on Eq. (7.19). The first row reports the total PSFs, while subsequent rows detail the contributions from the most probable capture channels. As expected, the PSF values decrease with higher-order terms in the Taylor expansion, consistent with trends observed for $2\nu\beta\beta$-decay [78, 179].

While the first entry in Table 7.7 can be directly compared to older results, such as 17200×10^{-24} yr^{-1} from [235], caution is required for a meaningful comparison. First, the value from [235] is based on the closure approximation for the NME, whereas our results are for NMEs derived within the Taylor expansion framework. Second, the older calculations include only captures from the K and L_1 shells, while our results incorporate contributions from all occupied shells in ^{124}Xe. Overall, we observe that employing the DHFS framework for screening reduces the total PSF compared to the Thomas-Fermi screening model used in [235, 195]. However, this reduction is offset by the inclusion of Pauli blocking effects and the consideration of captures beyond the K and L_1 shells, leading to an increase in the total PSF value.

Following the capture process, the final atom is left in an excited state. Experimentally, the detection of de-excitation energies, released as X-rays and Auger electrons, serves as a signature for identifying 2νECEC events. However, this energy release can also contribute to background noise in experiments where the decay of ^{124}Xe is an unavoidable source of interference. The atomic relaxation energy associated with the 2νxy process can be expressed in terms of the total electron binding energies of ^{124}Te, both in its ground state and in its excited state, which features vacancies in the x and y orbitals, as:

$$R_{\mathrm{xy}} = B_{\mathrm{g.s.}}(^{124}\mathrm{Te}) - B_{\mathrm{xy}}(^{124}\mathrm{Te}). \tag{7.23}$$

The relaxation energies obtained using the DHFS framework are presented in Table 7.12. The details of the calculation of the atomic relaxation energies can be found in Section A.2.3. Based on the findings in [247], these R_{xy} estimates are expected to have an accuracy better than 1%. Given the current experimental energy resolution of a few keV [47], our estimations provide a reliable basis for identifying the position of background peaks in liquid xenon experiments [47, 83, 84].

7.3.3 The ISM evaluation of the NMEs

The NMEs, as defined in Eq. (7.17), were calculated following the approach described in [246], but with several important modifications: (i) no single-state dominance (SSD) assumption was made [241]; (ii) two effective Hamiltonians were utilized, including GCN5082 [246] (abbreviated as GCN in the tables below) and SVD [260]; (iii) distinct quenching factors (q_H) for the GT $\tau^-\sigma$ operator were adopted for each effective Hamiltonian, calibrated to match the two-neutrino double-beta decay data of ^{136}Xe—specifically, $q_{GCN} = 0.4$ [246] and $q_{SVD} = 0.7$ [239, 240]; and (iv) up to four nucleons were excited from the lower $g_{7/2}d_{5/2}$ orbitals into the higher $jj55$-space orbitals to account for configuration mixing.

Following [246], we calculate the NMEs in the $jj55$ model space, which includes the $0g_{7/2}$, $1d_{5/2}$, $1d_{3/2}$, $2s_{1/2}$, and $0h_{11/2}$ orbitals for both protons and neutrons. Full shell model calculations in this space are computationally challenging due to the large basis dimensions required, particularly for ^{124}Xe. Therefore, as in [246], we rely on truncations by promoting nucleons from the lower $g_{7/2}d_{5/2}$ orbitals into the higher $d_{3/2}s_{1/2}h_{11/2}$ orbitals. We extend beyond the truncations used in [246] by allowing up to four nucleon excitations. Additionally, we improve upon the single-state dominance approximation assumed in [246] by performing a full summation over the intermediate 1^+ states in Eq. (7.17). This summation is carried out using the strength function approach described in Section 4 of Ref.[241].

Notably, the full summation leads to a reduction of about 25% in the NME for the GCN5082 Hamiltonian. Furthermore, instead of assuming a wide range of quenching factors, we adopt quenching factors that accurately reproduce the NMEs for the two-neutrino double-beta decay of ^{136}Xe, calculated within the same model space and effective Hamiltonians.

The results for the dominant nuclear matrix elements, $M^{2\nu\mathrm{ECEC}}_{GT-1}$, are displayed in Fig. 7.4. The notation "g7d5-jump" represents the number of nucleons allowed to be excited (jump) from the lower $g_{7/2}d_{5/2}$ orbitals into the higher $jj55$-space orbitals, with a maximum of 14. Both effective Hamiltonians yield similar results, and although the NMEs have not yet fully converged, their values exhibit only minor variations, especially for the SVD effective Hamiltonian.

We also computed the other two nuclear matrix elements, $M^{2\nu\mathrm{ECEC}}_{GT-3}$ and $M^{2\nu\mathrm{ECEC}}_{GT-5}$, by extending the techniques outlined in Section 4 of [241]. These calculations involve the Gamow-Teller $\tau^-\sigma$ operator in Eq. (7.18), which was quenched by the q_H factors specified

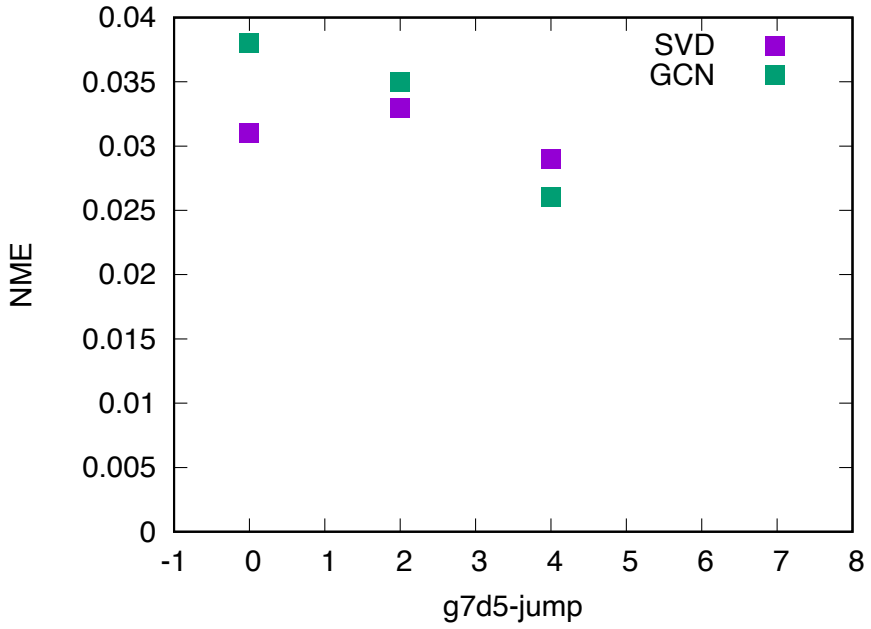

Figure 7.4: The $M^{2\nu\text{ECEC}}_{GT-1}$ NME as a function of the number of nucleons that were allowed to get excited from the lower $g_{7/2}d_{5/2}$ orbitals.

Model	NME type	jump=0	jump=2	jump=4
SVD	$M^{2\nu\text{ECEC}}_{GT-1}$	0.0305	0.0329	0.0291
	$M^{2\nu\text{ECEC}}_{GT-3}$	0.0066	0.0087	0.0064
	$M^{2\nu\text{ECEC}}_{GT-5}$	0.0018	0.0026	0.0018
GCN	$M^{2\nu\text{ECEC}}_{GT-1}$	0.0379	0.0354	0.0264
	$M^{2\nu\text{ECEC}}_{GT-3}$	0.0108	0.0092	0.0057
	$M^{2\nu\text{ECEC}}_{GT-5}$	0.0032	0.0027	0.0016

Table 7.8: ISM results for the NMEs of Eq. (7.17) (see text for details).

earlier ($q_{SVD} = 0.7$, $q_{GCN} = 0.4$). Within the ISM framework, this quenching effect reflects the renormalization of the $\tau^-\sigma$ operator in reduced model spaces [261, 262, 263], while the axial coupling constant retains its free nucleon value, $g_A = 1.276$ [209].

The NME results are summarized in Table 7.8, where "jump" denotes the g7d5-jump configuration. These results are further employed to extract the parameters $\xi^{2\nu\text{ECEC}}_{31}$ and $\xi^{2\nu\text{ECEC}}_{51}$, shown in Table 7.9. These parameters are essential for calculating the Taylor expansion corrections to the decay half-lives, as given by Eqs. (7.14)–(7.15). It is important to note that the NMEs $M^{2\nu\text{ECEC}}_{GT-3}$ and $M^{2\nu\text{ECEC}}_{GT-5}$ exhibit trends similar to those of $M^{2\nu\text{ECEC}}_{GT-1}$, as shown in Fig. 7.4.

Model	$\xi^{2\nu\text{ECEC}}_i$	jump=0	jump=2	jump=4
SVD	$\xi^{2\nu\text{ECEC}}_{31}$	0.216	0.264	0.220
	$\xi^{2\nu\text{ECEC}}_{51}$	0.059	0.079	0.062
GCN	$\xi^{2\nu\text{ECEC}}_{31}$	0.285	0.260	0.216
	$\xi^{2\nu\text{ECEC}}_{51}$	0.084	0.076	0.061

Table 7.9: ISM results for the ξ_i parameters of Eq. (7.16) (see text for details).

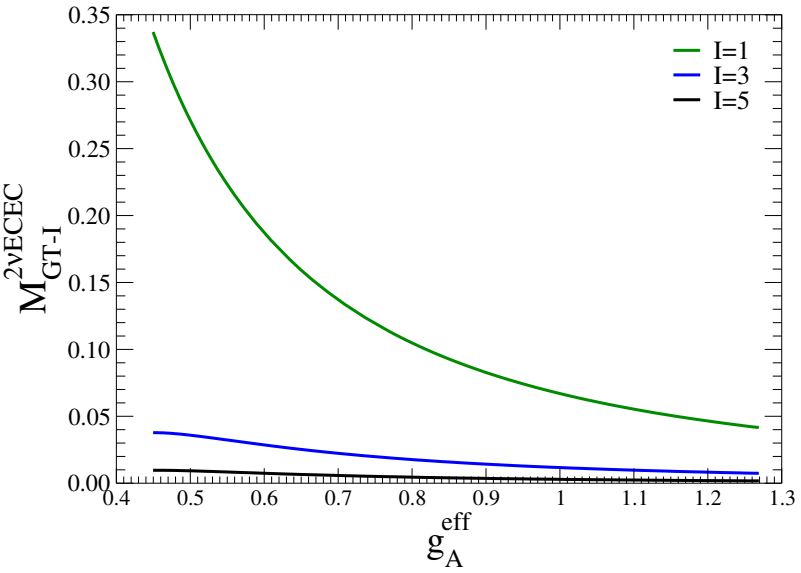

Figure 7.5: Dependence of the matrix elements $M^{2\nu\text{ECEC}}_{GT-1}$, $M^{2\nu\text{ECEC}}_{GT-3}$, and $M^{2\nu\text{ECEC}}_{GT-5}$ on the effective value of axial-vector coupling constant g_A^{eff} for the case the calculated 2νECEC half-life is the same as its experimental value, i.e., $T^{2\nu\text{ECEC}}_{1/2}(^{124}\text{Xe}) = 1.1 \times 10^{22}$ yrs [47]. Results were obtained within the QRPA with the restoration of the isospin by assuming the realistic Argonne V18 nucleon-nucleon potential.

7.3.4 The pn-QRPA evaluation of the NMEs

The nuclear matrix elements $M^{2\nu\text{ECEC}}_{GT-1}$, $M^{2\nu\text{ECEC}}_{GT-3}$, and $M^{2\nu\text{ECEC}}_{GT-5}$ are computed using the proton-neutron Quasiparticle Random Phase Approximation (pn-QRPA) with isospin restoration, as described in [199]. These calculations employ the same extensive model space, consisting of 23 subshells within the N = 0–5 oscillator shells, supplemented by the $i11/2$ and $i_{13/2}$ orbitals, and use the same mean fields as those applied in the study of double-beta decay in ^{128,130}Te and ^{136}Xe. Pairing and residual interactions are derived from modern realistic nucleon-nucleon potentials, specifically the charge-dependent Bonn potential (CD-Bonn) and the Argonne V18 potential. In solving the BCS pairing equations, the pairing interaction strengths are slightly adjusted to accurately reproduce the experimental pairing gaps [199].

The pn-QRPA equations involve three adjustable renormalization parameters: g_{ph} for the particle-hole interaction, and $g_{pp}^{T=1}$ and $g_{pp}^{T=0}$ for the isovector and isoscalar components of the particle-particle interaction, respectively. While the parameter $g_{ph} = 1.0$ is typically used [199], the value of $g_{pp}^{T=1}$ is fixed to ensure that the $2\nu\beta\beta$ Fermi matrix element vanishes, as required by isospin symmetry. Meanwhile, $g_{pp}^{T=0}$ is tuned to reproduce the half-life of the 2νECEC process in ^{124}Xe for each considered value of the effective axial coupling constant, g_A^{eff}. Unlike earlier QRPA calculations of $2\nu\beta\beta$ nuclear matrix elements, this approach incorporates the overlap of the initial and final BCS vacua. This inclusion leads to a reduction in the nuclear matrix elements by a factor of 0.828, as demonstrated in [202].

In Fig. 7.5, we present the NMEs for the 2νECEC process in ^{124}Xe, calculated within the pn-QRPA framework with isospin restoration, as functions of the effective axial-vector coupling constant, g_A^{eff}. These NMEs are computed for a fixed 2νECEC half-life corresponding to its experimental value. A notable observation is that $M^{2\nu\text{ECEC}}GT-1$ exhibits a strong dependence on g_A^{eff}, whereas $M^{2\nu\text{ECEC}}GT-3$ and $M^{2\nu\text{ECEC}}_{GT-5}$ show much weaker dependencies. In Table 7.10, we list the calculated values of $M^{2\nu\text{ECEC}}_{GT-K}$ (for $K = 1, 3, 5$) using both the Argonne V18 and CD-Bonn potentials. These values are reported for three

Table 7.10: Nuclear matrix elements $M^{M}_{\mathrm{GT-K}}$ (M = 2νECEC and $2\nu\beta\beta$, K=1,3 and 5) for 2νECEC of ^{124}Xe and $2\nu\beta\beta$-decay of ^{128,130}Te calculated within pn-QRPA with isospin restoration. Δ_p and Δ_n denote experimental proton and neutron pairing gap, respectively. g_A^{eff} is the effective axial-vector coupling constant. A and B stand for the Argonne V18 and CD-Bonn nucleon-nucleon potential, respectively. The fixed value of the particle-particle strength parameter in the isovector channel $g_{pp}^{T=1}$ is 0.9626 (0.8884), 0.9672 (0.8934) and 0.9893 (0.9151) for 2νECEC of ^{124}Xe, $2\nu\beta\beta$-decay of ^{128}Te and ^{130}Te, respectively, by exploiting the realistic Argonne V18 (CD-Bonn) nucleon-nucleon potential. $g_{pp}^{T=0}$ is the renormalization constant of particle-particle neutron-proton interaction in the isoscalar channel, which is fitted from the requirement that the calculated 2νECEC or $2\nu\beta\beta$ half-life is the same as its experimental value. $T_{1/2}^{2\nu\mathrm{ECEC}}(^{124}\mathrm{Xe}) = 1.1 \times 10^{22}$ yrs [47], $T_{1/2}^{2\nu\beta\beta}(^{128}\mathrm{Te}) = 2.3 \times 10^{24}$ yrs [40] and $T_{1/2}^{2\nu\beta\beta}(^{130}\mathrm{Te}) = 7.71 \times 10^{20}$ yrs [57] are considered.

Nucl. tran.	Δ_p^{Te}	Δ_n^{Te}	Δ_p^{Xe}	Δ_n^{Xe}	g_A^{eff}	pot.	$g_{pp}^{T=0}$	$M_{\mathrm{GT-1}}$	$M_{\mathrm{GT-3}}$	$M_{\mathrm{GT-5}}$	ξ_{31}	ξ_{51}
^{124}Xe$\rightarrow^{124}$Te	1.249	1.344	1.357	1.339	0.80	A	0.706	0.104	0.018	0.0045	0.169	0.043
						B	0.635	0.105	0.019	0.0049	0.181	0.047
					1.00	A	0.737	0.066	0.016	0.0029	0.175	0.043
						B	0.664	0.068	0.014	0.0035	0.201	0.051
					1.27	A	0.754	0.042	0.007	0.0017	0.178	0.041
						B	0.681	0.041	0.009	0.0023	0.231	0.057
^{128}Te$\rightarrow^{128}$Xe	1.129	1.280	1.319	1.265	0.80	A	0.743	0.063	0.012	0.0038	0.196	0.060
						B	0.667	0.063	0.014	0.0043	0.219	0.068
					1.00	A	0.764	0.040	0.008	0.0023	0.200	0.057
						B	0.689	0.040	0.010	0.0030	0.244	0.073
					1.27	A	0.777	0.025	0.005	0.0013	0.202	0.051
						B	0.701	0.025	0.007	0.0020	0.282	0.081
^{130}Te$\rightarrow^{130}$Xe	1.058	1.179	1.297	1.248	0.80	A	0.749	0.044	0.008	0.0023	0.185	0.052
						B	0.673	0.044	0.009	0.0027	0.209	0.060
					1.00	A	0.768	0.028	0.005	0.0014	0.192	0.049
						B	0.691	0.028	0.007	0.0018	0.237	0.065
					1.27	A	0.780	0.018	0.003	0.0008	0.199	0.044
						B	0.703	0.017	0.005	0.0013	0.281	0.072

choices of g_A^{eff}—1.27 (unquenched), 1.00, and 0.80 (modestly quenched). For comparison, we also include NMEs for the $2\nu\beta\beta$ processes of ^{128}Te and ^{130}Te. Since these transitions connect the ground states of tellurium and xenon isotopes, their NMEs provide a meaningful context for evaluating the 2νECEC NMEs. We observe that the 2νECEC NMEs are only slightly larger, by about a factor of 2, than those for $2\nu\beta\beta$. This similarity reflects comparable experimental pairing gaps for all isotopes involved, as shown in Table 7.10. Additionally, we present the ratios of NMEs, ξ_{13} and ξ_{15}, in Table 7.10. The maximum value of ξ_{13}, computed for an unquenched g_A^{eff}, is 0.231, 0.282, and 0.281 for the 2νECEC process of ^{124}Xe and the $2\nu\beta\beta$ decays of ^{128}Te and ^{130}Te, respectively, using the CD-Bonn potential. It is important to note that $\xi_{13} > 0.26$ was excluded for the $2\nu\beta\beta$ decay of ^{136}Xe by the KamLAND-Zen Collaboration [186]. However, a measured value of $\xi_{13} = 0.45 \pm 0.03(\text{stat}) \pm 0.05(\text{syst})$ was reported by the CUPID-Mo experiment [55].

Prior to the experimental determination of the half-life for the 2νECEC process in ^{124}Xe, NMEs for this decay were computed using the pn-QRPA method with alternative approaches for adjusting the particle-particle interaction strength parameter, g_{pp}. One method utilized experimental data from single β-decays [242], while another employed a statistical formalism to reconcile QRPA results with experimental observations [264, 243]. Results of the second approach favor a strong quenching of axial-vector coupling constant with $g_A^{\text{eff}} \simeq 0.4 - 0.6$. The obtained nuclear matrix elements in these studies are as follows: $M_{GT}^{2\nu\text{ECEC}} = 0.10 - 0.20$ ($g_A^{\text{eff}} = 1.25$), $0.34 - 0.71$ ($g_A^{\text{eff}} = 1.00$) [242] and $M_{GT}^{2\nu\text{ECEC}} = 0.296$ ($g_A^{\text{eff}} = 0.60$) [243]. By comparing them with NMEs values in Table 7.10 and with $M_{GT}^{2\nu\text{ECEC}} = 0.191$ and 0.186 (Argonne and CD-Bonn potentials) for g_A^{eff} =0.60 calculated in the presented formalism, we see that they are too large leading to a significant disagreement with measured half-life for 2νECEC of ^{124}Xe.

7.3.5 Total and partial half-lives predictions

Table 7.11 provides the calculated total half-life for the 2νECEC process, as well as the half-life specifically for the KK capture channel. These results were obtained using Eqs. (7.14) and (7.15), incorporating the phase-space factors listed in Table 7.7, the NMEs presented in Table 7.8. Overall, the results indicate that the ISM provides robust predictions that are relatively insensitive to changes in truncation schemes or effective Hamiltonians. Moreover, the calculated half-lives demonstrate good agreement with experimental measurements. It is also noteworthy that the inclusion of Taylor expansion corrections, combined with the updated and more accurate PSFs, plays a significant role in improving the alignment between theoretical predictions and experimental data.

Model	Channel	jump=0	jump=2	jump=4
SVD	Total	1.94	1.61	2.12
	KK	2.61	2.17	2.86
GCN	Total	1.20	1.40	2.58
	KK	1.62	1.88	3.48

Table 7.11: The predicted 2νECEC half-lives for ^{124}Xe (in units of 10^{22} yr) from Eqs. (7.14) and (7.15). To be compared with experimental data for the total half-life, $(1.1 \pm 0.2_{stat} \pm 0.1_{sys}) \times 10^{22}$ yr and the inferred data for the KK half-life, $(1.5 \pm 0.3_{stat} \pm 0.1_{sys}) \times 10^{22}$ yr (see section III.F of [47]).

For comparison, we note that several estimates of the half-life of ^{124}Xe for the 2νECEC process exist in the literature, based on different models for NME calculations. For instance, the pn-QRPA studies in [242, 243] and the ISM results in [246] provide a wide range of predictions. In [242], the predicted half-life spans (0.04–0.88) $\times 10^{22}$yr. However, the NMEs

Decay Chanel	R_{xy} (keV)	ISM CF (%)
KK	64.62	74.13-74.15
KL_1	37.05	18.76-18.83
KM_1	32.98	3.83-3.84
KN_1	32.11	0.83-0.85
KO_1	31.93	0.13
L_1L_1	10.04	1.22
L_1M_1	6.01	0.49
Other	< 6	0.52-0.55

Table 7.12: The atomic relaxation energies (Eq. 7.23) obtained within the DHFS model (second column) and the capture fractions (CF) predicted by ISM (third column). The captures with atomic relaxation energies below 6 keV are subsumed under the label "other". The ranges presented for the KK and KL_1 channels correspond to the minimum and maximum values of the $\xi_{31}^{2\nu\text{ECEC}}$ parameter predicted from ISM.

reported in that work are approximately five times larger than the values obtained here, rendering them incompatible with the more accurate PSFs presented here. Moreover, the PSFs in [242] are calculated using the expressions from [33], which rely on the closure approximation. Similarly, [243] provides an estimated half-life range of $(1.4–1.8) \times 10^{22}$ yr, but the calculations also rely on the closure approximation for PSFs. Consequently, the results may not fully capture the effects included in the more refined models adopted in this work. Ref. [246] presents two additional ranges for the partial half-life of ^{124}Xe, derived using the ISM and an effective theory (ET) extension applied to truncated ISM NMEs. The half-life predictions for the KK capture are $(1.3–18) \times 10^{22}$ yr for ISM and $(0.43–2.9) \times 10^{22}$yr for ET. However, the PSF values employed in this work are based on [235], which also include contributions from KL_1 and L_1L_1 capture channels. As a result, the ranges reported in [246] are underestimated by approximately 20%. Additionally, their PSF calculations assume the closure approximation, whereas their NMEs are computed either by summing over all intermediate 1^+ states in the ISM or by assuming the SSD hypothesis in the ET approach.

Building on the good prediction of the experimental data for the total 2νECEC half-life of ^{124}Xe and the partial half-life for the KK channel, we provide predictions for additional possible decay channels. Table 7.12 lists the relaxation energies calculated using Eq. 7.23 and the predicted capture fractions (CFs) for various decay channels, including the measured total and KK channels[47]. The ISM CF column presents the predicted capture fractions (in %) derived using the interacting shell model (ISM). Detailed results for different truncations and effective Hamiltonians will be published elsewhere. We note that the predicted CF for the KK channel is 74.1%, slightly higher than the previously adopted value of 72.4% from [47]. This difference arises from our more restrictive treatment, which considers only s-wave electrons, whereas [47] included contributions from all electron orbitals. Additionally, the incorporation of Taylor expansion terms and the updated PSFs leads to minor adjustments in the new capture fractions. Our analysis also identifies the KL_1 channel as the next most probable decay mode after KK, with a predicted CF of approximately 19%. Given the proximity of the relaxation energies associated with the KL_1–KO_1 channels, we predict a cumulative CF of about 24% for these channels, roughly one-third of the KK channel. This result suggests that future experimental searches may be able to observe contributions from the KL_1–KO_1 channels, providing further insights into the 2νECEC process in ^{124}Xe.

It is important to emphasize that observables related to the 2νECEC process, such as the total and partial half-lives, depend on the $\xi_{31}^{2\nu\text{ECEC}}$ and $\xi_{51}^{2\nu\text{ECEC}}$ parameters within the

Taylor expansion formalism. From an experimental standpoint, the parameter $\xi_{31}^{2\nu\mathrm{ECEC}}$ can be treated as a free variable when analyzing these observables, while $\xi_{51}^{2\nu\mathrm{ECEC}}$ can be fixed based on theoretical predictions due to its relatively smaller influence. Consequently, experimental constraints on $\xi_{31}^{2\nu\mathrm{ECEC}}$ can be derived by measuring the ratio of half-lives between different decay channels, such as $T^{2\nu\mathrm{KK}}1/2/T^{2\nu\mathrm{KL1}}1/2$. This approach parallels the method proposed in [179], where $\xi 31$ was constrained in $2\nu\beta\beta$ decays using the angular correlation coefficient of the emitted electrons. Although the dependence of half-life ratios on $\xi_{31}^{2\nu\mathrm{ECEC}}$ is relatively weak, future experimental constraints on this parameter could offer valuable insights and serve as a cross-check for the reliability of different NME calculations.

7.3.6 Conclusions

In conclusion, we analyzed the 2νECEC decay rates for the ^{124}Xe isotope, recently investigated experimentally [46, 47], and improved the calculation of both the PSFs and the NMEs. The decay rate was derived more rigorously by employing the Taylor expansion approach, which incorporates higher-order contributions for enhanced accuracy.

For the new PSF calculations, we implemented the following improvements: (i) the use of the DHFS self-consistent framework, which accounts for atomic screening, diffuse nuclear surface corrections, realistic nuclear charge densities, and electron exchange-correlation effects; and (ii) the inclusion of Pauli blocking effects for the decay of innermost nucleon states. Additionally, we considered electron captures from all s-wave orbitals, extending beyond the previously studied K and L_1 shells. Our findings reveal that while refined screening corrections for bound states decrease the decay rate, Pauli blocking effects and contributions from additional capture channels increase it.

For the nuclear component, we employed both the ISM and the pn-QRPA methods. In the ISM approach, we extended the summation over 1^+ states of the intermediate nucleus to include Taylor expansion terms in Eqs. (7.14) and (7.17). We also expanded the shell model truncation in the $jj55$ single-particle model space and validated the results using two widely adopted effective Hamiltonians. New NMEs, $M_{GT-3}^{2\nu\mathrm{ECEC}}$ and $M_{GT-5}^{2\nu\mathrm{ECEC}}$, were calculated using an extended framework based on [241]. The agreement between ISM-calculated NMEs and those extracted from experimental data reinforces the validity of similar predictions for the $2\nu\beta\beta$ decay of ^{124}Sn [240].

With the ISM approach, we achieved a good description of the total half-life within a factor of two compared to experimental data. We also predicted the capture fraction of the KK channel to be 74.1%, which deviates slightly from the 72.4% value used in earlier experimental searches [47]. Furthermore, new predictions for capture fractions in additional decay channels were provided (see Table 7.12). Notably, we obtained a cumulative capture fraction of approximately 24%, about one-third of the KK channel's contribution, suggesting that the KL_1-KO_1 channels, with relaxation energies between 37.05 keV and 31.93 keV, could be experimentally observed in the near future.

For the pn-QRPA method, we incorporated isospin symmetry restoration to calculate NMEs associated with the 2νECEC decay of ^{124}Xe. The particle-particle interaction strength parameter, $g_{pp}^{T=0}$, was adjusted based on experimental 2νECEC decay rates. Compared to earlier pn-QRPA calculations [242, 243], our results yielded significantly smaller values for $M_{GT-1}^{2\nu\mathrm{ECEC}}$. We found that NMEs for 2νECEC in ^{124}Xe are comparable to those for $2\nu\beta\beta$ in ^{128,130}Te. This similarity reflects the analogous nuclear systems, which differ only in neutron numbers and exhibit comparable experimental pairing gaps—an essential input for pn-QRPA calculations.

8 A semi-empirical formula for two-neutrino DBD

8.1 Introduction

Despite recent progress in measuring $2\nu\beta\beta$-decay and ongoing efforts to develop a robust theoretical framework, discrepancies between theoretical predictions and experimental data remain unresolved. A key challenge lies in the significant variation observed in experimental NMEs for $2\nu\beta\beta$-decay. These discrepancies cannot be consistently addressed within existing nuclear models without resorting to case-specific fine-tuning of parameters.

In this Chapter, we introduce a semi-empirical formula (SEF) designed to calculate NMEs for two-neutrino double-beta decay. The SEF incorporates dependencies on proton and neutron numbers, pairing effects, isospin, and deformation properties of the initial and final nuclei. This approach draws inspiration from nuclear many-body methods and observed experimental trends, effectively capturing essential physical correlations and symmetries.

Compared to previous phenomenological and nuclear models, the SEF provides the best agreement with experimental NMEs. The reliability of the SEF is further confirmed through cross-validation against available experimental data. Additionally, we present predictions for NMEs in nuclear systems of experimental interest, paving the way for more precise evaluations of $2\nu\beta\beta$-decay observables in future studies.

8.2 Current state

The inverse $2\nu\beta\beta$-decay half-life is commonly presented as

$$\left(T_{1/2}^{2\nu}\right)^{-1} = \left|M^{2\nu}\right|^2 \; G^{2\nu}, \tag{8.1}$$

where $G^{2\nu}$ is the PSF, and

$$M^{2\nu} = g_A^2 M_{GT}^{2\nu} - g_V^2 M_F^{2\nu}, \tag{8.2}$$

is the NME governing the transition. It should be noted that we consider here only the first order of the Taylor expansion formalism provided in Chapter 5. The vector and axial-vector coupling constants, denoted as $g_V = 1$ and g_A, respectively, are fundamental parameters in nuclear weak interaction processes. While g_V is well-established, g_A is typically model-dependent and remains an open issue in the theoretical description of these interactions [182]. In this analysis, we adopt the impulse approximation for nucleon currents and consider only $s_{1/2}$ wave states of the emitted electrons. The nuclear matrix elements, $M_F^{2\nu}$ and $M_{GT}^{2\nu}$, correspond to the Fermi and Gamow-Teller (GT) transitions, which are governed by the Fermi and GT operators. These operators act as generators of isospin SU(2) and spin-isospin SU(4) symmetries, respectively. Since isospin symmetry is a good approximation in nuclei, it is generally assumed that $M_F^{2\nu}$ contributes negligibly to the decay rate. Consequently, the dominant contribution arises from $M_{GT}^{2\nu}$, which can be expressed as

$$M_{GT}^{2\nu} = m_e \sum_n \frac{M_n}{E_n - (E_i + E_f)/2}, \tag{8.3}$$

with

$$M_n = \langle 0_f^+ \| \sum_j \tau_j^+ \sigma_j \| 1_n^+ \rangle \langle 1_n^+ \| \sum_k \tau_k^+ \sigma_k \| 0_i^+ \rangle. \tag{8.4}$$

Here, $|0_i^+\rangle$ ($|0_f^+\rangle$) is the ground state of the initial (final) even-even nucleus with energy E_i (E_f), and the summations run over all $|1_n^+\rangle$ states the intermediate odd-odd nucleus with energies E_n and over all j, k nucleons inside the nucleus.

The phase-space component of the decay rate can be accurately determined using a relativistic treatment of the emitted (captured) electrons within a realistic potential of the final (initial) atomic system. The most precise PSFs, computed using the self-consistent Dirac-Hartree-Fock-Slater method and incorporating radiative and atomic exchange corrections [168, 172] (see also Chapter 5), are presented in Table 8.1. In contrast, the computation of the $2\nu\beta\beta$-decay NMEs remains a long-standing and challenging problem in this field. With the increasing interest in detecting neutrinoless modes, there has been a notable reduction in the uncertainties of half-lives for two-neutrino modes (see column 11 in Table 8.1) and, consequently, in the corresponding experimental NMEs, calculated as $M^{2\nu-\text{exp}} = (T_{1/2}^{2\nu-\text{exp}} G^{2\nu})^{-1/2}$ (see Table 8.2 and Table 8.3). Despite these advancements, the distribution and structure of the experimental NMEs remain poorly understood. A theoretical model that accurately reproduces the current experimental NMEs could offer valuable insights and realistic predictions for future experimental searches across the nuclear chart.

Predictions of the $2\nu\beta\beta$-decay NMEs rely on a variety of nuclear structure models, each offering distinct approaches to address the complexities of nuclear systems. Prominent methods include the proton-neutron quasiparticle random phase approximation (pn-QRPA) and its variants [270, 271, 272, 273, 65, 274, 275, 202, 276, 277, 278, 199, 243, 78], which are widely used due to their ability to handle correlations in particle-particle and particle-hole channels effectively. The nuclear shell model (NSM) also plays a central role in these predictions [279, 280, 236, 281, 239, 282, 240, 283, 284], offering detailed microscopic descriptions by explicitly accounting for nucleon interactions within a limited valence space. Other approaches include the interacting boson model (IBM) [285, 286, 287, 288], which maps nucleon pairs onto bosons, and the projected Hartree-Fock-Bogoliubov (PHFB) method [289], which incorporates deformation and pairing correlations effectively. Alternative models, such as the Fermi surface quasi-particle (FSQP) model [290, 291], effective theory (ET) frameworks [292], and other approaches [293, 294], further expand the theoretical landscape. Additionally, phenomenological models [295, 296, 297] provide empirical fits to experimental data, offering simplified but often insightful descriptions of decay rates. Despite this diversity, calculating $2\nu\beta\beta$-decay NMEs remains a formidable task due to the complex structure of open-shell medium and heavy nuclei and the requirement to describe a complete set of intermediate nuclear states. Consequently, discrepancies among theoretical predictions persist, highlighting the ongoing need for refined models and improved methodologies to better capture the physics of double-beta decay.

Two widely used approaches for studying double-beta decay are the pn-QRPA and the NSM. While the NSM is limited to low-lying excitations, it effectively incorporates all correlations within the valence space. Higher-lying excitations can also be accessed through the Lanczos strength function method [280]. To reproduce $2\nu\beta\beta$-decay data, the Gamow–Teller operator is typically quenched to match results from single β-decays or charge exchange reactions, assuming an unquenched g_A [279, 281]. In contrast, the pn-QRPA extends to orbitals far from the Fermi surface, accounting for high-lying excited states up to 20–30 MeV, though it incorporates fewer correlations. The $M_{GT}^{2\nu}$ and $M_F^{2\nu}$ matrix

Table 8.1: The decay properties for various $2\nu\beta\beta$-decays (right arrow) and 2νECEC processes (left arrow). T_f represents the total isospin of the final nucleus. Δ_p and Δ_n denote experimental proton and neutron pairing gaps in units of MeV, respectively. The quadrupole deformation parameters, $\beta^{\mathrm{Z,Z+2}}$, deduced from the corresponding B(E2) transitions, are taken from Brookhaven Nuclear Database [265]. $G^{2\nu}$ in yr^{-1} is the most precise PSF computed in this work for $2\nu\beta\beta$ cases and taken from [245] (^{78}Kr, ^{106}Cd, ^{130}Ba, and ^{132}Ba) and [266] (^{124}Xe) for the 2νECEC cases. $T_{1/2}^{2\nu-\mathrm{ph}}$ and $T_{1/2}^{2\nu-\mathrm{exp}}$ are the half-lives predicted by the SEF and the experimental half-lives with the smallest uncertainties, respectively. The ^{78}Kr data are for double electron capture from K orbital. For ^{128}Te, the experimental half-life is obtained using the ratio $T_{1/2}^{2\nu-\mathrm{exp}}(^{130}\mathrm{Te})/T_{1/2}^{2\nu-\mathrm{exp}}(^{128}\mathrm{Te}) = (3.52 \pm 0.11) \times 10^{-4}$ [50]. The transitions under the "Fitted" label are used as input for the SEF, while those under the "Predicted" label are its predictions.

Nuclear transition	T_f	Δ_p^{Z}	Δ_n^{Z}	$\Delta_p^{\mathrm{Z+2}}$	$\Delta_n^{\mathrm{Z+2}}$	β^{Z}	β^{Z+2}	$G^{2\nu}$	$T_{1/2}^{2\nu-\mathrm{ph}}$	$T_{1/2}^{2\nu-\mathrm{exp}}$
Fitted										
$^{48}_{20}\mathrm{Ca}_{28} \rightarrow {}^{48}_{22}\mathrm{Ti}_{26}$	2	2.179	1.688	1.896	1.564	0.107	0.262	1.58×10^{-17}	1.2×10^{20}	$6.4^{+1.3}_{-1.1} \times 10^{19}$ [51]
$^{76}_{32}\mathrm{Ge}_{44} \rightarrow {}^{76}_{34}\mathrm{Se}_{42}$	4	1.561	1.535	1.751	1.710	0.188	0.219	5.07×10^{-20}	1.8×10^{21}	$2.022^{+0.042}_{-0.042} \times 10^{21}$ [52]
$^{82}_{34}\mathrm{Se}_{48} \rightarrow {}^{82}_{36}\mathrm{Kr}_{46}$	5	1.401	1.544	1.734	1.644	0.194	0.203	1.68×10^{-18}	9.1×10^{19}	$8.69^{+0.10}_{-0.07} \times 10^{19}$ [53]
$^{96}_{40}\mathrm{Zr}_{56} \rightarrow {}^{96}_{42}\mathrm{Mo}_{54}$	6	1.539	0.846	1.528	1.034	0.060	0.172	7.24×10^{-18}	3.4×10^{19}	$2.35^{+0.21}_{-0.21} \times 10^{19}$ [54]
$^{100}_{42}\mathrm{Mo}_{58} \rightarrow {}^{100}_{44}\mathrm{Ru}_{56}$	6	1.612	1.358	1.548	1.296	0.231	0.215	3.47×10^{-18}	7.2×10^{18}	$7.07^{+0.11}_{-0.11} \times 10^{18}$ [55]
$^{116}_{48}\mathrm{Cd}_{68} \rightarrow {}^{116}_{50}\mathrm{Sn}_{66}$	8	1.493	1.377	1.763	1.204	0.135	0.112	2.91×10^{-18}	2.3×10^{19}	$2.63^{+0.11}_{-0.12} \times 10^{19}$ [56]
$^{130}_{52}\mathrm{Te}_{78} \rightarrow {}^{130}_{54}\mathrm{Xe}_{76}$	11	1.104	1.180	1.307	1.248	0.118	0.128	1.62×10^{-18}	7.5×10^{20}	$8.76^{+0.17}_{-0.18} \times 10^{20}$ [57, 58]
$^{136}_{54}\mathrm{Xe}_{82} \rightarrow {}^{136}_{56}\mathrm{Ba}_{80}$	12	1.009	1.436	1.265	1.031	0.091	0.125	1.52×10^{-18}	2.5×10^{21}	$2.17^{+0.06}_{-0.06} \times 10^{21}$ [59]
$^{150}_{60}\mathrm{Nd}_{90} \rightarrow {}^{150}_{62}\mathrm{Sm}_{88}$	13	1.224	1.046	1.444	1.193	0.285	0.193	3.85×10^{-17}	2.5×10^{19}	$9.3^{+0.7}_{-0.6} \times 10^{18}$ [60]
$^{238}_{92}\mathrm{U}_{146} \rightarrow {}^{238}_{94}\mathrm{Pu}_{144}$	25	0.813	0.606	0.662	0.589	0.289	0.285	1.65×10^{-19}	9.1×10^{21}	$2.0^{+0.6}_{-0.6} \times 10^{21}$ [61]
Predicted										
$^{110}_{46}\mathrm{Pd}_{64} \rightarrow {}^{110}_{48}\mathrm{Cd}_{62}$	7	1.422	1.442	1.479	1.362	0.257	0.172	1.46×10^{-19}	3.1×10^{20}	$> 10^{18}$ [267]
$^{124}_{50}\mathrm{Sn}_{74} \rightarrow {}^{124}_{52}\mathrm{Te}_{72}$	10	1.671	1.314	1.248	1.343	0.095	0.170	6.00×10^{-19}	1.9×10^{21}	–
$^{128}_{52}\mathrm{Te}_{76} \rightarrow {}^{128}_{54}\mathrm{Xe}_{74}$	10	1.129	1.280	1.319	1.265	0.135	0.202	3.00×10^{-22}	1.5×10^{24}	$2.49^{+0.09}_{-0.09} \times 10^{24}$
$^{134}_{54}\mathrm{Xe}_{80} \rightarrow {}^{134}_{56}\mathrm{Ba}_{78}$	11	1.134	1.029	1.329	1.176	0.115	0.163	2.25×10^{-23}	4.0×10^{25}	$> 2.8 \times 10^{22}$ [268]
Fitted										
$^{78}_{34}\mathrm{Se}_{44} \leftarrow {}^{78}_{36}\mathrm{Kr}_{42}$	5	1.442	1.637	1.577	1.691	0.270	0.256	5.20×10^{-22}	1.7×10^{23}	$1.9^{+1.3}_{-0.8} \times 10^{22}$ [45]
$^{124}_{52}\mathrm{Te}_{72} \leftarrow {}^{124}_{54}\mathrm{Xe}_{70}$	10	1.249	1.344	1.357	1.339	0.170	0.223	1.83×10^{-20}	2.0×10^{22}	$1.10^{+0.22}_{-0.22} \times 10^{22}$ [47]
Predicted										
$^{106}_{46}\mathrm{Pd}_{60} \leftarrow {}^{106}_{48}\mathrm{Cd}_{58}$	7	1.472	1.401	1.460	1.338	0.162	0.168	5.54×10^{-21}	2.1×10^{21}	$> 4.7 \times 10^{20}$ [269]
$^{130}_{54}\mathrm{Xe}_{76} \leftarrow {}^{130}_{56}\mathrm{Ba}_{74}$	11	1.308	1.248	1.351	1.298	0.128	0.215	1.57×10^{-20}	6.0×10^{22}	$2.2^{+0.5}_{-0.5} \times 10^{21}$ [42]
$^{132}_{54}\mathrm{Xe}_{78} \leftarrow {}^{132}_{56}\mathrm{Ba}_{76}$	12	1.240	1.181	1.390	1.236	0.141	0.185	4.09×10^{-23}	1.0×10^{26}	$> 2.2 \times 10^{21}$ [41]

elements have been shown to exhibit a strong dependence on the isoscalar and isovector particle-particle interactions of the nuclear Hamiltonian [72, 78]. The IBM simplifies nuclear structure by representing low-lying states as $L = 0$ (s boson) or $L = 2$ (d boson) pairs, focusing on transitions involving 0^+ and 2^+ neutron pairs converting into protons. Meanwhile, the PHFB formalism constructs nuclear wave functions with good particle number and angular momentum by projecting onto axially symmetric intrinsic HFB states, although it limits the nuclear Hamiltonian to quadrupole interactions. While not addressed in this work due to challenges in obtaining systematic results, recent advancements in *ab initio* methods show promise for describing $2\nu\beta\beta$-decay transitions. Notable developments include coupled-cluster calculations for ^{48}Ca [298] and hybrid approaches that combine chiral effective-field theory with the NSM for ^{48}Ca, ^{76}Ge, and ^{82}Se [299]. These advances may enhance theoretical predictions and further reduce uncertainties in nuclear matrix element calculations.

Phenomenological models simplify the description of $2\nu\beta\beta$-decay processes. For instance, as outlined in [183, 184], when the intermediate nucleus has a 1^+ ground state, the decay is assumed to be dominated by two virtual β-decay transitions. The first transition connects the initial nucleus to the 1^+ ground state of the intermediate nucleus, while the second transition connects this 1^+ state to the final ground state. This framework is referred to as the single-state dominance (SSD) hypothesis. A key advantage of the SSD hypothesis is that it minimizes dependence on detailed nuclear structure models. Instead, the nuclear matrix element $M^{2\nu}$ can be derived directly from experimental data, such as measured $\log ft$ values or charge-changing reactions. However, recent experimental results challenge the SSD hypothesis. A study on electron energy distributions in the $2\nu\beta\beta$-decay of ^{100}Mo [55] indicates that transitions through higher-lying states in the intermediate nucleus cannot be neglected. These additional transitions can contribute significantly to $M^{2\nu}$, and their interference effects, particularly destructive interference, must be accounted for to accurately describe the decay process.

To date, three additional phenomenological models have been proposed to predict $2\nu\beta\beta$-decay half-lives or NMEs. One such model [295] draws parallels with the Geiger-Nuttall law, which describes α decay half-lives. The other two models [296, 297] suggest that half-lives or NMEs depend on specific nuclear properties, including the Coulomb energy parameter ($\xi \approx ZA^{-1/3}$), the Q-value, and the quadrupole deformation parameter of the initial nucleus. Despite their utility, these models exhibit limitations in capturing the full complexity of $2\nu\beta\beta$-decay dynamics. As discussed later, refinements to these approaches could enhance their predictive accuracy and provide a more comprehensive framework for describing double-beta decay processes.

8.3 Phenomenological model

We propose a phenomenological approach to describe $2\nu\beta\beta$-decay NMEs, drawing inspiration from nuclear theory insights and patterns observed in experimental data. The proposed semi-empirical formula (SEF) is

$$M^{2\nu-ph} = \left(\frac{Z_f}{N_f}\right)^{\alpha} \left(\frac{\Delta_{\rm pn}}{1-\beta_</\beta_>}\right)^{\gamma} (T_f)^{\sigma}\,, \tag{8.5}$$

where Z_f, N_f, and T_f are the proton number, neutron number, and the isospin of the final nuclear ground state, respectively. We note that the ground state of the initial (final) even-even nucleus belongs to the isospin multiplet with $T_i = (N_i - Z_i)/2$ ($T_f = (N_f - Z_f)/2$), representing the only state in the nucleus where the isospin projection equals the total isospin.

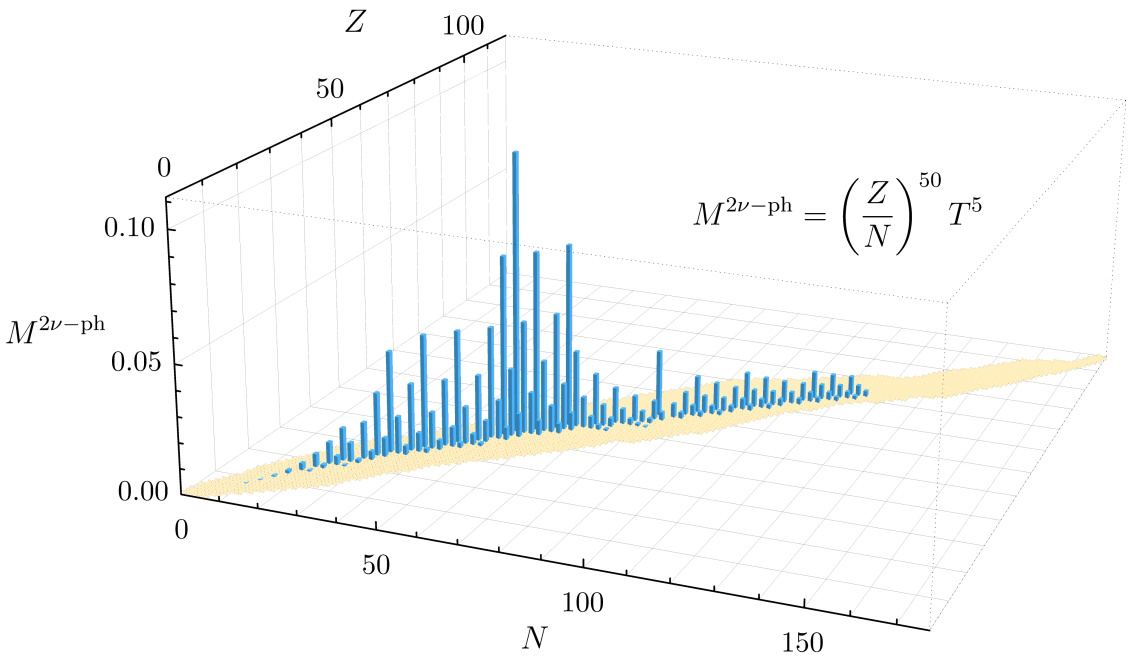

Figure 8.1: The phenomenological NMEs, obtained using a simplified model $M^{2\nu-ph} = (Z/N)^{50}\ T^5$, are represented in the (Z, N) space for stable even-even nuclei. The base of the representation, shown in orange, corresponds to the known nuclear chart. The figure is taken from [303].

The dependence of $M^{2\nu}_{GT}$ on isospin was explored in an exactly solvable model [72]. Observations indicate that the values of $(Z_f/N_f)^{50}T^5_f$, as shown in Figure 8.1 and Table 8.3, exhibit a spread comparable to $M^{2\nu-\mathrm{exp}}$. The six largest peaks correspond to NMEs for the $2\nu\beta\beta$-decay of ^{98}Mo, ^{114}Cd, ^{104}Ru, ^{94}Zr, ^{110}Pd, and ^{100}Mo, in this order. While ^{100}Mo has the largest experimentally measured NMEs, theoretical predictions [300, 301, 243] suggest that some of these cases could exceed ^{100}Mo's NME, though measurements are limited by their lower Q-values [302]. Interestingly, the simple form $(Z_f/N_f)^{50}\ T^5_f$ accurately predicts the ordering of $2\nu\beta\beta$-decay NMEs and serves as a robust foundation for further refinement.

The quantities $\beta_< = \min(\beta^Z, \beta^{Z+2})$ and $\beta_> = \max(\beta^Z, \beta^{Z+2})$, appearing in Eq. (8.5), are defined using the quadrupole deformation parameters β^Z and β^{Z+2} for the ground states of the initial and final nuclei, respectively. It is important to highlight that only prolate shapes have been considered for these nuclear configurations, as the signs of the quadrupole deformation parameters cannot be deduced from the associated electric quadrupole transition probabilities, B(E2). Future experimental studies offering insights into the nuclear shapes involved in $2\nu\beta\beta$-decay may enable further refinements to the model. For this analysis, however, we adopt the positive quadrupole deformation parameters provided in the Brookhaven Nuclear Database [265].

The dependence on deformation parameters reflects findings from pn-QRPA [202, 276], PHFB [304, 305], and NSM [306] calculations, which indicate that discrepancies between the deformations of initial and final states tend to suppress the NMEs for $2\nu\beta\beta$-decay. Furthermore, the pairing parameter Δ_{pn}, defined as the product of experimental pairing gaps [307], is also included to capture pairing effects influencing the decay rates,

$$\Delta_{\mathrm{pn}} = \Delta^{\mathrm{Z}}_p\ \Delta^{\mathrm{Z}}_n\ \Delta^{\mathrm{Z+2}}_p\ \Delta^{\mathrm{Z+2}}_n. \tag{8.6}$$

This highlights the importance of transitions involving the lowest 1^+ states of the interme-

diate nucleus. The associated β transition amplitudes are directly connected to the BCS u and v occupation amplitudes, which, in turn, can be determined from the gap parameter.

8.4 Results and discussions

The best fitting parameters α, γ, and σ have been obtained from the minimization of the chi-squared

$$\chi^2 = \sum_{i=1}^{N} \frac{(O_i - P_i)^2}{\sigma_i^2}, \tag{8.7}$$

where O_i is the experimental NME with uncertainty σ_i, and P_i is the predicted NME. The sum includes data from both direct counter experiments and radiochemical observations. For the $2\nu\beta\beta$-decay transitions categorized under the "Fitted" label in Table 8.1 ($N = 10$), the resulting $2\nu\beta\beta$-SEF yielded parameters $\alpha = 46.94$, $\gamma = 0.22$, and $\sigma = 4.90$. Interestingly, when "Fitted" 2νECEC cases were incorporated as additional inputs ($N = 12$), but with $T_f \to T_f + 1$, the same fit parameters were obtained. This observation suggests a potential multilevel modeling framework for both types of transitions. However, further half-life measurements for proton-rich nuclei are necessary to confirm this hypothesis.

Table 8.2 provides a comparative analysis of $2\nu\beta\beta$-decay NMEs derived from the SEF, the SSD hypothesis, and the latest computations using various nuclear models. The datasets are also displayed in Fig. 8.2. The comparisons are quantified through χ^2/N values. Among the approaches, the $2\nu\beta\beta$-SEF demonstrates the closest agreement with experimental NMEs, consistently producing χ^2/N values that are roughly two orders of magnitude lower than those obtained from other models. It is worth noting that the NME values listed for nuclear models in Table 8.2 correspond to the calculated $M^{2\nu}_{GT}$, each scaled by the square of the effective g_A adopted in the respective studies. While the SSD hypothesis and NSM and FSQP calculations also show relatively smaller χ^2/N values, broader conclusions remain challenging due to the limited number of cases analyzed within these datasets. It is also noteworthy that the pn-QRPA results from [78], which incorporate SU(4) symmetry restoration and an effective $g_A = 0.904$ derived from observed $2\nu\beta\beta$-decay half-lives, exhibit a significant reduction in χ^2/N compared to earlier pn-QRPA calculations presented in [243]. The latter employed β-decay observables to fine-tune nucleon-nucleon interactions and single-particle energies for each $\beta\beta$-decay system, yet yielded larger deviations from experimental data.

We further assess the $2\nu\beta\beta$-SEF by comparing it with earlier empirical models and evaluating its design, stability, and predictive capabilities. Table 8.3 displays NMEs obtained from this work alongside those derived from previous phenomenological models [295, 296, 297] and the corresponding experimental values. To evaluate the quality of the fits, we calculated the reduced chi-squared values, $\chi^2_\nu = \chi^2/\nu$, where ν denotes the number of degrees of freedom (DOF). The results reveal that previous models yield significantly larger χ^2_ν values compared to the $2\nu\beta\beta$-SEF proposed in this study. This highlights the better performance of the SEF in capturing experimental trends. It is also worth noting that the model proposed in [296] may suffer from overfitting, as it has only two DOF, making it less robust given the limited size of the experimental dataset analyzed.

To gain deeper insight into the foundation of the $2\nu\beta\beta$-SEF, the analytical form of $(Z_f/N_f)^{50}T_f^5$ was progressively refined by optimizing fit parameters and enhancing model complexity. The analytical expressions for each iteration are provided in the caption of Table 8.3. Interestingly, Model A achieves a χ^2_ν value comparable to the best prior model from [295]. However, Model B demonstrates that slightly reducing the exponents controlling

Table 8.2: The $2\nu\beta\beta$-decay NMEs obtained with the SEF, the ones from the SSD hypothesis, and the most recent calculations from various nuclear structure models. The row labeled "χ^2/N" displays the chi-squared divided by the number of available data for each set.

	$M^{2\nu-\mathrm{th}}$											$M^{2\nu-\mathrm{ph}}$	
Nucleus	QRPA [243]	QRPA [78]	IBM [288]	IBM [287]	IBM [286]	NSM [284]	NSM [281]	PHFB [289]	FSQP [291]	ET [292]	$M^{2\nu-\mathrm{exp}}$	SEF	SSD [192]
Fitted													
^{48}Ca	–	0.016	0.069	0.024	0.045	–	0.039	–	–	–	0.0314 ± 0.0030	0.022	–
^{76}Ge	–	0.063	0.083	0.018	0.085	–	0.097	–	0.083	0.085	0.0987 ± 0.0010	0.105	–
^{82}Se	–	0.058	0.072	0.024	0.063	0.099	0.105	–	0.103	0.156	0.0828 ± 0.0005	0.081	–
^{96}Zr	–	0.133	0.058	0.054	0.034	–	–	0.092	0.072	–	0.0770 ± 0.0040	0.063	–
^{100}Mo	0.105	0.251	0.197	0.157	0.045	–	–	0.164	0.154	0.179	0.2019 ± 0.0016	0.199	0.174
^{116}Cd	0.112	0.049	0.089	0.069	0.031	–	–	–	0.088	0.137	0.1142 ± 0.0027	0.120	0.148
^{130}Te	0.057	0.053	0.035	0.010	0.038	0.027	0.036	0.059	0.027	0.034	0.0265 ± 0.0003	0.028	–
^{136}Xe	0.036	0.030	0.056	0.022	0.032	0.024	0.021	–	–	–	0.0174 ± 0.0002	0.016	–
^{150}Nd	–	–	0.077	0.054	0.017	0.069	–	0.048	–	–	0.0527 ± 0.0019	0.032	0.023
^{238}U	–	–	–	–	0.023	–	–	–	–	–	0.0550 ± 0.0110	0.026	–
χ^2/N	5170	2100	2845	2828	1773	470	686	3442	480	4774	–	30	233
Predicted													
^{110}Pd	0.167	–	–	0.022	0.041	–	–	–	0.233	0.211	< 2.61	0.147	–
^{124}Sn	0.023	–	–	–	0.034	0.037	–	–	–	–	–	0.029	–
^{128}Te	0.051	0.063	0.022	0.018	0.044	0.013	0.049	0.058	0.030	0.050	0.0366 ± 0.0007	0.047	0.015
^{134}Xe	0.063	–	–	–	–	–	–	–	–	–	< 1.25	0.033	–

Table 8.3: The $2\nu\beta\beta$-decay NMEs obtained with previous phenomenological models [295, 296, 297] compared with those predicted by: (A) $(Z_f/N_f)^{50}T_f^5$, (B) $(Z_f/N_f)^{46.94}T_f^{4.90}$, (C) $(Z_f/N_f)^{46.94}T_f^{4.90}\Delta_{\rm pn}^{0.22}$, (D) $(Z_f/N_f)^{48.44}T_f^{4.95}\,[\Delta_{\rm pn}/(\beta_> - \beta_<)]^{0.21}$ and (SEF) $(Z_f/N_f)^{46.94}T_f^{4.90}\,[\Delta_{\rm pn}/(1-\beta_</\beta_>)]^{0.22}$. The row labeled "$\chi^2_\nu$ (ν)" displays the values of reduced chi-squared and, in parenthesis, the DOF for each model. The last column shows the reduced chi-squared when a specific nucleus is involved in the LOOCV for SEF and, in parenthesis, the NME prediction of the excluded case.

	$M^{2\nu-\rm ph}$									
	Previous models			Present models						LOOCV for SEF
Nucleus	[295]	[296]	[297]	A	B	C	D	SEF	$M^{2\nu-\rm exp}$	χ^2_ν (prediction)
Fitted										
^{48}Ca	0.030	0.035	0.037	0.008	0.012	0.020	0.023	0.022	0.0314 ± 0.0030	48 (0.022)
^{78}Ge	0.198	0.123	0.410	0.026	0.044	0.068	0.108	0.105	0.0987 ± 0.0010	41 (0.107)
^{82}Se	0.095	0.096	0.163	0.015	0.027	0.040	0.080	0.081	0.0828 ± 0.0005	35 (0.073)
^{96}Zr	0.060	0.063	0.008	0.027	0.049	0.058	0.068	0.063	0.0770 ± 0.0040	48 (0.063)
^{100}Mo	0.073	0.091	0.220	0.045	0.079	0.110	0.197	0.199	0.2019 ± 0.0016	47 (0.183)
^{116}Cd	0.071	0.093	0.121	0.031	0.058	0.081	0.129	0.120	0.1142 ± 0.0027	49 (0.121)
^{130}Te	0.077	0.068	0.032	0.006	0.014	0.016	0.029	0.028	0.0265 ± 0.0003	32 (0.030)
^{136}Xe	0.030	0.055	0.017	0.004	0.010	0.012	0.016	0.016	0.0174 ± 0.0002	40 (0.015)
^{150}Nd	0.030	0.061	0.203	0.009	0.021	0.025	0.027	0.032	0.0527 ± 0.0019	29 (0.031)
^{238}U	0.024	–	0.046	0.005	0.014	0.010	0.020	0.026	0.0550 ± 0.0110	48 (0.026)
χ^2_ν (ν)	5651 (9)	24981 (2)	17632 (7)	5450 (8)	3171 (8)	2017 (7)	67 (7)	43 (7)		
Predicted										
^{110}Pd	0.135	0.160	0.270	0.047	0.084	0.115	0.143	0.147	< 2.61	
^{124}Sn	0.098	–	0.019	0.009	0.018	0.025	0.029	0.029	–	
^{128}Te	0.067	–	0.042	0.014	0.030	0.037	0.045	0.047	0.0366 ± 0.0007	
^{134}Xe	–	–	0.086	0.010	0.022	0.025	0.033	0.033	< 1.25	

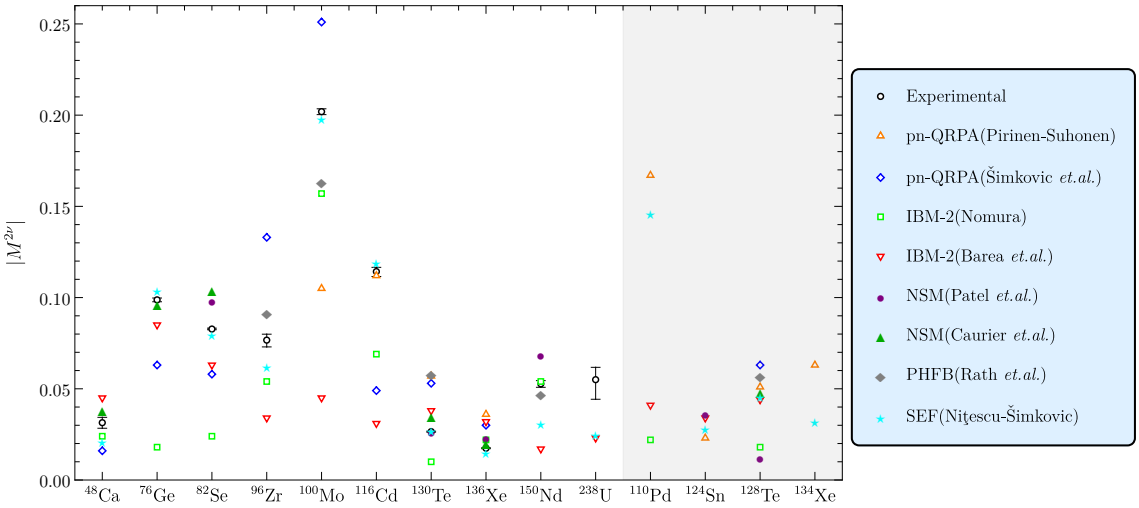

Figure 8.2: The $2\nu\beta\beta$-decay NMEs obtained with the SEF in comparison with the experimental data and the most recent calculations from various nuclear structure models: pn-QRPA [243, 78], IBM [288, 287, 286], NSM [284, 281], PHFB [289]. The gray box included cases with no experimental values of the half-lives.

Z_f/N_f and T_f yields a substantial improvement in alignment with experimental NMEs. Further refinements, including pairing parameters and quadrupole deformation, highlight that incorporating deformation overlap represents the most impactful enhancement to the initial form, which only relied on Z_f/N_f and T_f. Additionally, we observe that modeling the deformation overlap as $(1 - \beta_</\beta_>)$ is preferable to $(\beta_> - \beta_<)$, based on the current experimental dataset.

We employed leave-one-out cross-validation (LOOCV) to evaluate the robustness of the $2\nu\beta\beta$-SEF in fitting experimental data and generating predictions. This method systematically omits one data point at a time during the fitting process and assesses the performance of the $2\nu\beta\beta$-SEF using the remaining data. The χ^2_ν values obtained for each exclusion are provided in the last column of Table 8.3, with the predicted NME for the omitted case displayed in parentheses. The results demonstrate that removing any single case has a negligible impact on the predictions. Additionally, the minimal fluctuations in χ^2_ν values validate the SEF's stability and its predictive reliability.

At first glance, the predicted $2\nu\beta\beta$-decay NME for ^{128}Te appears to deviate from the experimental value. However, it is essential to emphasize that the experimental NME for ^{128}Te is based on geochemical measurements of ancient tellurium ores [50]. Such measurements warrant careful scrutiny, as unknown processes during ore formation may have influenced the production of daughter isotopes. For instance, it has been proposed in [308, 249] that these results could be affected by potential time variations in the weak interaction strength. Similar concerns may also apply to measurements involving ^{130}Ba and ^{132}Ba. Given these uncertainties, we have excluded all geochemical data from the fit. By contrast, the radiochemical measurement of ^{238}U was retained, as its larger uncertainty reduces the likelihood of distorting the fit parameters. This choice is supported by the LOOCV of ^{238}U presented in Table 8.3.

The $2\nu\beta\beta$-SEF predicts notably different NMEs for isotope pairs differing by two neutrons, a feature also reflected in modern nuclear structure models presented in Table 8.2. For example, the SEF estimates NME ratios close to 2 for the isotope pairs ^{128,130}Te and ^{134,136}Xe. This result contrasts with Pontecorvo's earlier assumption that such pairs should exhibit nearly equal NMEs [309]. Other pairs showing similar trends include ^{98,100}Mo,

^{114,116}Cd, and ^{94,96}Zr, although the small Q-values of the neutron-deficient isotopes may limit near-future measurements for these cases. Fortunately, the $2\nu\beta\beta$-decay of ^{134}Xe could soon be detected, as it constitutes an unavoidable background in Dark Matter searches [81, 82, 84, 310]. The SEF also provides optimistic half-life predictions, in the range of 10^{20}–10^{21} years, for the $2\nu\beta\beta$-decay of ^{110}Pd and ^{124}Sn, as well as for the 2νECEC of ^{106}Cd. These nuclei, with relatively large Q-values, are already being investigated as candidates for upcoming measurements [219, 311, 312, 35, 36]. Future direct counter experiments could further test and validate the SEF, which, despite its simplicity and reliance on just a few parameters, has successfully reproduced the wide spread of experimentally measured $2\nu\beta\beta$-decay NMEs.

8.5 Conclusions

In this Chapter, we introduced a semi-empirical formula to describe the NMEs for two-neutrino double beta decay. Drawing insights from nuclear many-body methods and patterns observed in experimental data, the proposed $2\nu\beta\beta$-SEF incorporates dependencies on proton and neutron numbers, pairing effects, isospin, and deformation properties of the initial and final nuclei. Additionally, we identified indications of multilevel modeling applicability for both $2\nu\beta\beta$-decay and the 2νECEC process. However, further measurements involving proton-rich nuclei are necessary to confirm this hypothesis.

A detailed comparison with prior phenomenological and nuclear models demonstrated that the SEF achieves the closest agreement with experimental data, effectively capturing the wide variations observed in measured $2\nu\beta\beta$-decay NMEs. The model's robustness was validated through LOOCV, and we also provided justifications for excluding geochemical measurements as inputs. Finally, we highlighted that the SEF predicts significantly different NMEs, by approximately a factor of 2, for nuclear systems differing by two neutrons, challenging earlier assumptions of near equality. Future measurements of additional $2\nu\beta\beta$ transitions will be instrumental in verifying the accuracy of these predictions.

9 Summary and outlook

This thesis is dedicated to refining theoretical predictions for nuclear β-decay and $\beta\beta$-decay in atomic nuclei, which act as crucial probes for exploring the fundamental properties and interactions of neutrinos. Using quantum field theory and advanced many-body methods, the thesis addresses several key topics: the atomic exchange correction for allowed β-decay, with a particular focus on the unique first forbidden β-decay of ^{187}Re; an improved formalism for predicting observables in $2\nu\beta\beta$-decay and 2νECEC processes; the influence of electron phase shifts on the angular correlation between emitted electrons in $2\nu\beta\beta$-decay and $0\nu\beta\beta$-decay; and a semi-empirical formula for predicting NMEs in $2\nu\beta\beta$-decay. The key findings of this dissertation thesis are summarized below.

- We reexamined the atomic exchange correction for allowed β transitions, accounting for contributions from all occupied $s_{1/2}$ and $p_{1/2}$ orbitals. The electron wave functions were calculated using a modified DHFS self-consistent method. To ensure orthogonality between the continuum and bound electron states in the potential of the final atom, we modified the final iteration of the self-consistent procedure. Our findings demonstrate that orthogonality plays a crucial role in the computation the exchange correction. Failure to enforce orthogonality between the continuum and bound states in the final atom introduces errors in the overlaps between the initial atom's bound states and the final atom's continuum states, resulting in a downturn in the total exchange correction. After enforcing orthogonality, we observed significant differences in both magnitude and energy dependence compared to prior studies. We tested the present model with the experimental electron spectra of the β-decay of ^{67}Ni, ^{151}Sm and ^{210}Pb. We found a very good agreement, especially in the low-energy region of the spectra where the previous models fail to describe the increasing behavior of the experimental data.

  In addition, motivated by the agreement with the experimental data, an analytical parametrization for the exchange correction was developed for a broad range of β-decaying nuclei, with atomic numbers spanning from $Z = 1$ to $Z = 102$. From the systematic study, we found that, apart from the low-energy region, the total exchange correction exhibits a progressive increase with nuclear charge. At ultra-low energies, such as 5 eV, the Z dependence of the total exchange effect is influenced by the closure of $s_{1/2}$ and $p_{1/2}$ orbitals. At higher energies, however, the exchange correction shows a smooth dependence on nuclear charge—a behavior that differs markedly from earlier studies. We attribute this discrepancy to the enforcement of orthogonality between the continuum and bound states in our approach. Additionally, we demonstrated that contributions from orbitals beyond the $2s_{1/2}$ orbital are crucial for accurately determining the total effect, especially at low energies. Finally, the analytical parametrization of the total exchange correction was tabulated for each atomic number, for a straightforward implementation in future experimental analyses.

- We investigated one relevant candidate for neutrino mass scale measurement, the ground-state to ground-state unique first forbidden β-decay of $^{187}\mathrm{Re}(5/2^+)$ to $^{187}\mathrm{Os}(1/2^-)$. In the β-decay model for rhenium, we have included the corrections for finite nuclear size, diffuse nuclear surface, screening, and atomic exchange effects. The latter two effects were calculated using a self-consistent DHFS description for the atomic bound electrons of the final atom. Given that rhenium β emission involves

a mixture of $s_{1/2}$-state and $p_{3/2}$-state electrons, our exchange correction accounts for all possible contributions from exchanges with $s_{1/2}$, $p_{3/2}$, $p_{1/2}$, and $d_{3/2}$ bound orbitals. Our results reveal significant modifications to the partial decay rates of both $s_{1/2}$- and $p_{3/2}$-state emission channels due to screening and exchange effects, while preserving the experimentally established dominance of $p_{3/2}$-state emission.

A key outcome is that, beyond altering the partial decay rates, the atomic exchange correction introduces substantial modifications in the shape of the total electron spectrum for rhenium β-decay. By analyzing deviations from an allowed spectrum, we found that calculations with and without the exchange effect produce entirely different shape factors, changing from an increasing linear behavior to a decreasing quadratic one. We provided best-fit parameters for both cases. The shape modification was found to be significant enough to incorporate the exchange correction into the definition of the Kurie plot to preserve its linearity in scenarios with zero effective neutrino mass. Furthermore, we showed how varying effective neutrino masses influence the Kurie plots near the endpoint of ^{187}Re β-decay. In conclusion, our findings highlight the critical role of atomic effects, particularly the exchange correction, in current and future investigations of the neutrino mass scale using β-decay.

- The $2\nu\beta\beta$-decay model was enhanced by incorporating radiative and atomic exchange corrections. As these corrections are introduced on top of our previous Taylor expansion formalism, we presented a connection between this approach and the SSD and HSD hypotheses. Additionally, we demonstrated that while the SSD hypothesis is an approximation for separating the decay rate, it remains useful in testing the truncation order of the Taylor series. We found that the exchange effect for one electron emitted in $\beta\beta$-decay is larger than in β-decay, as the atomic system's charge changes by two units in the former case.

  For the $2\nu\beta\beta$-decay of ^{100}Mo, we found a steep increase in the number of event in the low-energy region of the single electron distribution due to the atomic exchange correction, which is in accordance with the previous studies on β-decay. Although the radiative correction leave the shape of the single electron spectrum unchanged, it is responsible for an overall increase in the decay rate of about 5%. We also found that the both correction contribute constructively to a leftward shift of the maximum in the summed electron spectrum, amounting to about 10 keV for the $2\nu\beta\beta$-decay of ^{100}Mo. Since similar shifts are predicted by new physics scenarios in $2\nu\beta\beta$-decay, our finding might influence the experimental constrains of the BSM parameters. Additionally, this corrections might affect the future ξ_{31} and ξ_{51} measurements. We also provided the corrected single and summed electron spectra for the $2\nu\beta\beta$-decay of ^{100}Mo under the assumptions of the SSD and HSD hypotheses, as well as for experimentally measured values of the ξ_{31} and ξ_{51} parameters.

  The Taylor expansion formalism including radiative and exchange corrections was also extended for the $2\nu\beta\beta$-decay to final 2^+ excited states. The new model was for tested the $2\nu\beta\beta$-decay of ^{150}Nd and ^{148}Nd. Measurements of various transitions of these isotopes to different excited states were conducted over a period of 5.845 years using a four-crystal low-background HPGe γ spectrometry system at the STELLA underground low-background laboratory of LNGS-INFN. We found that the half-life predictions, based on the Taylor expansion formalism and pn-QRPA NMEs calculations, are in good agreement with the experimental half-lives and limits.

- The Taylor expansion formalism was also extended to the angular correlations between the emitted electrons in $2\nu\beta\beta$-decay. With the new model, we investigated the impact

of electron phase shifts on the kinematics of $\beta\beta$-decay in ^{100}Mo. For completeness, we have considered both $0\nu\beta\beta$-decay and $2\nu\beta\beta$-decay. For $0\nu\beta\beta$-decay only the light-neutrino exchange mechanism was considered and the others are reserved for future studies. Our analysis of the angular correlation distributions, α and κ, revealed a striking feature: when electron phase shifts are included, electrons are most likely emitted in the same direction if one has an energy below 2 keV.

From a systematic review of the previously reported angular correlation coefficients $K^{2\nu}$, we demonstrated that incorporating phase shifts influences the results, irrespective of the approximations employed in factorizing the $2\nu\beta\beta$-decay rate or accounting for atomic screening effects. Specifically, we found that properly accounting for phase shifts increases the angular correlation coefficient, K, by 7% in the $2\nu\beta\beta$-decay and 2% in the $0\nu\beta\beta$-decay.

- We have performed a systematic study of the all atoms undergoing 2νECEC processes. The theoretical model was enhanced with two improvements. First, we employed the DHFS self-consistent framework to refine the description of bound wave function and to improve the accuracy of binding energy estimates for captured electrons. Second, we extended our analysis to include captures from outer orbitals, beyond the K and L_1 shells considered in previous studies.

  Using this enhanced model, we updated the PSFs for all atoms undergoing the 2νECEC process. For lighter atoms, we observed minimal differences relative to earlier models that assumed simplified atomic screening and restricted captures to the K and L_1 orbitals. This similarity arises from a cancellation effect, where the decay rate reduction caused by more precise screening is balanced by the increase resulting from higher-orbital captures. However, for medium and heavy atoms, our model predicted a nearly linear increase in the decay rate with atomic number, reaching enhancements of approximately 10% in the decay rates for the heaviest cases.

  For the recently measured 2νECEC process of ^{124}Xe, special attention was addressed. For this case, we provided the atomic relaxation energies and the updated PSFs including also the Pauli blocking effects. Moreover, the NMEs of the process were computed within the NSM and pn-QRPA models. The NSM result falls within the 2σ uncertainty range of the experimental measurement. Compared to earlier pn-QRPA calculations, our results yielded significantly smaller values for $M^{2\nu\mathrm{ECEC}}_{GT-1}$. We found that NMEs for 2νECEC in ^{124}Xe are comparable to those for $2\nu\beta\beta$ in ^{128,130}Te.

- A novel semi-empirical formula to describe the NMEs for $2\nu\beta\beta$-decay was introduced. Drawing insights from nuclear many-body methods and patterns observed in experimental data, the proposed $2\nu\beta\beta$-SEF incorporates dependencies on the ratio of proton and neutron numbers, pairing effects, isospin, and deformation properties of the initial and final nuclei. Additionally, we identified indications of multilevel modeling applicability for both $2\nu\beta\beta$-decay and the 2νECEC process. However, further measurements involving proton-rich nuclei are necessary to confirm this hypothesis.

  A detailed comparison with prior phenomenological and nuclear models demonstrated that the SEF achieves the best agreement with experimental data, effectively capturing the wide variations of the measured $2\nu\beta\beta$-decay NMEs. The model's robustness was validated through LOOCV. Finally, we highlighted that the SEF predicts significantly different NMEs, by approximately a factor of 2, for nuclear systems differing by two neutrons, challenging earlier assumptions of near equality. Future measurements of additional $2\nu\beta\beta$ transitions will be instrumental in verifying the accuracy of these predictions.

The results presented in this dissertation represent a significant step forward in understanding nuclear β-decay and $\beta\beta$-decay. The proposed approaches, refined calculations, and theoretical insights provide a strong foundation for ongoing and future experimental studies of electron spectra and angular correlations in β-decay and $\beta\beta$-decay. Additionally, some of these findings may prove valuable for dark matter search experiments, where the studied cases in this thesis constitute unavoidable sources of background. The achievements presented here open new avenues for research and lay the groundwork for further advancements.

A Wave functions for relativistic spin-1/2 particles

A.1 Dirac equation

The stationary states of a relativistic particle with spin 1/2 and mass M, under the influence of a potential $V(\boldsymbol{r})$, are described by the Dirac equation,

$$\mathcal{H}_D\psi(\boldsymbol{r}) = E\psi(\boldsymbol{r}) \tag{A.1}$$

with the Dirac Hamiltonian,

$$\mathcal{H}_D = -i\vec{\alpha}\cdot\vec{\nabla} + \beta M + V(\boldsymbol{r}), \tag{A.2}$$

where $\vec{\alpha} = (\alpha_1, \alpha_2, \alpha_3)$ and β are matrices of size 4×4. In the spinorial representation they can be written as

$$\vec{\alpha} = \begin{pmatrix} 0 & \vec{\sigma} \\ \vec{\sigma} & 0 \end{pmatrix}, \beta = \begin{pmatrix} I_2 & 0 \\ 0 & -I_2 \end{pmatrix}. \tag{A.3}$$

In the above expression, the vector $\vec{\sigma} = (\sigma_1, \sigma_2, \sigma_3)$ is determined by the Pauli matrices of size 2×2 defined by,

$$\sigma_1 = \begin{pmatrix} 0 & 1 \\ 1 & 0 \end{pmatrix}, \sigma_2 = \begin{pmatrix} 0 & -i \\ i & 0 \end{pmatrix}, \sigma_3 = \begin{pmatrix} 1 & 0 \\ 0 & -1 \end{pmatrix}, \tag{A.4}$$

and I_2 is the unit matrix of size 2×2. It is important to note that E in Equation (A.1) is the total energy of the relativistic particle, including its rest energy M. In this chapter, we adopt the system of units where $\hbar = c = 1$.

As for the operators associated with the observables of the relativistic particle, the orbital angular momentum operator $\boldsymbol{L}$ no longer commutes with the Hamiltonian of the system, as it did in the case of a non-relativistic particle, described by the Scrödinger equation. In order to construct the total angular moment operator, it is necessary to define the relativistic spin operator [155, 313],

$$\boldsymbol{\Sigma} = \frac{1}{2}\begin{pmatrix} \vec{\alpha} & 0 \\ 0 & \vec{\alpha} \end{pmatrix}. \tag{A.5}$$

In the relativistic case, the total kinetic moment operator, defined as

$$\boldsymbol{J} = \boldsymbol{L} + \boldsymbol{\Sigma}, \tag{A.6}$$

commutes with the Dirac Hamiltonian from Equation (A.2). In addition to this, the following operator can be defined,

$$K \equiv -\beta(2\boldsymbol{\Sigma}\cdot\boldsymbol{L} + 1) = \begin{pmatrix} -(J^2 - L^2 + \frac{1}{4})I_2 & 0 \\ 0 & (J^2 - L^2 + \frac{1}{4})I_2 \end{pmatrix}, \tag{A.7}$$

which commutes with the operators $\mathcal{H}_D$, J^2 and J_z. Thus, one can simultaneously construct eigenfunctions for the operators $\mathcal{H}_D$, J^2, J_z and K, having the eigenvalues E, $j(j+1)$, m and κ respectively. The new quantum number, κ, also called the relativistic quantum number, can take both negative and positive integer values, and for a fixed value, one can identify both the quantum number corresponding to the total angular momentum, j, and

the quantum number corresponding to the orbital angular momentum, ℓ. The values of κ, ℓ, and j are connected by the following relations,

$$j = |\kappa| - 1/2, \quad \ell = \begin{cases} \kappa & \text{if } \kappa > 0, \\ |\kappa| - 1 & \text{if } \kappa < 0, \end{cases} \tag{A.8}$$

or,

$$\kappa = \begin{cases} -\left(j + \frac{1}{2}\right) & \text{if } j = \ell + \frac{1}{2}, \\ j + \frac{1}{2} & \text{if } j = \ell - \frac{1}{2}, \end{cases} \quad \kappa = \begin{cases} -\ell - 1 & \text{if } j = \ell + \frac{1}{2}, \\ \ell & \text{if } j = \ell - \frac{1}{2}. \end{cases} \tag{A.9}$$

For an electron with the rest energy $M = m_e = 511$ keV, the construction of the atomic potential, $V(\boldsymbol{r})$, is crucial in determining the electronic wave functions. In what follows, we consider only spherical symmetric potentials and we separate the discussion for the bound and continuum states.

A.2 Bound states

For bound states ($E_e < m_e$), each discrete energy level is characterized by its relativistic quantum number κ, its principle quantum number n and its total energy $e_{n\kappa} = m_e - |t_{n\kappa}|$. Here, $t_{n\kappa}$ is the binding energy of the electron in the (n, κ) state. The wave function can be written as [33]

$$\psi_{n,\kappa,m}(\boldsymbol{r}) = \begin{pmatrix} g_{n,\kappa}(r)\Omega_{\kappa,m}(\hat{\boldsymbol{r}}) \\ i f_{n,\kappa}(r)\Omega_{-\kappa,m}(\hat{\boldsymbol{r}}) \end{pmatrix}. \tag{A.10}$$

The spherical spinors, $\Omega_{\kappa,m}(\hat{\boldsymbol{r}})$, are defined by [314, 315]

$$\Omega_{\kappa,m}(\hat{\boldsymbol{r}}) \equiv \Omega^{\ell}_{j,m}(\hat{\boldsymbol{r}}) = \sum_{\mu=\pm 1/2} \left\langle \ell, \frac{1}{2}, m-\mu, \mu \middle| j, m \right\rangle Y_{\ell,m-\mu}(\hat{\boldsymbol{r}})\chi_{\mu} \tag{A.11}$$

where $\langle j_1, j_2, m_1, m_2 | j, m\rangle$ are the Clebsch-Gordan coefficients and $Y_{\ell,m}(\hat{\boldsymbol{r}})$ are the spherical harmonic functions. If the operator is defined,

$$\boldsymbol{S} = \frac{1}{2}\vec{\sigma}, \tag{A.12}$$

then, the spinors χ_{μ} are eigenvectors for the operators S^2 and S_z with eigenvalues $3/4$ and $\mu = \pm 1/2$ respectively, with

$$\chi_{+1/2} = \begin{pmatrix} 1 \\ 0 \end{pmatrix}, \qquad \chi_{-1/2} = \begin{pmatrix} 0 \\ 1 \end{pmatrix}. \tag{A.13}$$

In the case of $1/2$ spin particles, the Clebsch-Gordan coefficients in Equation (A.11) have a simple analytic form [316], so the spherical spinors can be written in the following compact form,

$$\Omega^{\ell}_{\ell\pm 1/2,m}(\hat{\boldsymbol{r}}) = \frac{1}{\sqrt{2\ell+1}} \begin{pmatrix} \pm\sqrt{\ell \pm m + \frac{1}{2}}\, Y_{\ell,m-1/2}(\hat{\boldsymbol{r}}) \\ \sqrt{\ell \mp m + \frac{1}{2}}\, Y_{\ell,m+1/2}(\hat{\boldsymbol{r}}) \end{pmatrix}. \tag{A.14}$$

The radial components of the bound orbitals satisfy the normalization condition,

$$\int_0^{\infty} r^2 \left[g^2_{n,\kappa}(r) + f^2_{n,\kappa}(r)\right] dr = 1. \tag{A.15}$$

A.2.1 DHFS self-consistent method

For the calculation of the bound orbitals, we employed the RADIAL subroutine package [207]. The program DHFS.f, included in the package, solves the Dirac-Hartree-Fock-Slater (DHFS) equations for the ground-state configuration of neutral atoms and positive ions with N_e bound electrons and Z_p protons in the nucleus. Although the DHFS equations are obtained by replacing the non-local exchange potential with a local exchange approximation [317] the results are reliable and the procedure is efficient. There are evidences [318] that the local exchange approximation can lead to accurate electron binding energies without need for the extensive numerical calculations of the non-local exchange potential entailed by the full Hartree-Fock approach.

Following the DHFS approach, the large- and small-component radial functions for bound orbitals satisfy the radial Dirac equation,

$$\begin{aligned}\left(\frac{d}{dr}+\frac{\kappa+1}{r}\right)g_{n,\kappa}(r)-(e_{n\kappa}-V_{\mathrm{DHFS}}(r)+m_e)f_{n,\kappa}(r)=0,\\ \left(\frac{d}{dr}-\frac{\kappa-1}{r}\right)f_{n,\kappa}(r)+(e_{n\kappa}-V_{\mathrm{DHFS}}(r)-m_e)g_{n,\kappa}(r)=0,\end{aligned} \tag{A.16}$$

where the DHFS potential,

$$V_{\mathrm{DHFS}}(r)=V_{\mathrm{nuc}}(r)+V_{\mathrm{el}}(r)+V_{\mathrm{ex}}(r), \tag{A.17}$$

is a sum of the nuclear, electronic and exchange potentials.

For the nuclear potential, $V_{\mathrm{nuc}}(r)$, it is considered the electrostatic interaction of an electron at r with a spherical nucleus filled with protons following a Fermi distribution [319]

$$\rho_p(r)=\frac{\rho_0}{1+e^{(r-R_n)/z}}, \tag{A.18}$$

where $R_n=1.07A^{1/3}$ fm, $z=0.546$ fm, and ρ_0 must be determined from normalization. Thus, the nuclear potential is

$$V_{\mathrm{nuc}}(r)=-\alpha\int\frac{\rho_p(r')}{|\boldsymbol{r}-\boldsymbol{r'}|}d\boldsymbol{r'}. \tag{A.19}$$

The electronic potential describes the interaction energy of an electron at r with the atomic cloud, and it is found from integrating over the volume of the electron density, $\rho(r)$,

$$V_{\mathrm{el}}(r)=\alpha\int\frac{\rho(r')}{|\boldsymbol{r}-\boldsymbol{r'}|}d\boldsymbol{r'}. \tag{A.20}$$

Due to Slater's approximation [317], the exchange potential can be expressed in terms of the electron density in the following way

$$V_{\mathrm{ex}}^{\mathrm{Slater}}(r)=-\frac{3}{2}\alpha\left(\frac{3}{\pi}\right)^{1/3}[\rho(r)]^{1/3}. \tag{A.21}$$

With the exchange potential, $V_{\mathrm{ex}}^{\mathrm{Slater}}(r)$, the obtained self-consistent potential does respect the correct asymptotic behavior,

$$\lim_{r\to\infty}rV_{\mathrm{DHFS}}(r)=-\alpha(Z_p-N_e+1), \tag{A.22}$$

because the exchange term cannot cancel the self-interaction term from the electronic potential. The drawback is solved with the introduction of the Latter's tail correction [320] for the exchange potential,

$$V_{\mathrm{ex}}(r) = \begin{cases} V_{\mathrm{ex}}^{\mathrm{Slater}}(r) & r < r_{\mathrm{Latter}}, \\ -\frac{\alpha(Z-N+1)}{r} - V_{\mathrm{nuc}}(r) - V_{\mathrm{el}}(r) & r \geq r_{\mathrm{Latter}}. \end{cases} \tag{A.23}$$

The cutoff radius, r_{Latter}, is determined by solving the equation

$$V_{\mathrm{nuc}}(r) + V_{\mathrm{el}}(r) + V_{\mathrm{ex}}^{\mathrm{Slater}}(r) = -\frac{\alpha(Z_p - N_e + 1)}{r}. \tag{A.24}$$

The only unknown in determining the potential, $V_{\mathrm{DHFS}}(r)$, is the charge density of the atomic cloud, $\rho_e(r)$. This is determined iteratively until stabilization, hence the self-consistency of the Dirac-Hartree-Fock-Slater method [321, 322]. For the first electron density it is obtained analytically from the Moliere parametrization of the Thomas-Fermi potential [323],

$$\rho_e^{(1)}(r) = \frac{N_e}{4\pi r b^2}\left[3.60e^{-6r/b} + 0.792e^{-1.2r/b} + 0.0315e^{-0.3r/b}\right], \tag{A.25}$$

where $b = 0.88534 Z_p^{-1/3} a_0$ is the Thomas-Fermi radius, with a_0 the Bohr radius, and N_e is the number of bound electrons of the neutral atom or positive ion. Through this, the first exchange and electronic potentials are determined, and finally the first DHFS potential, $V_{\mathrm{DHFS}}^{(1)}(r)$, by Equation (A.17). With this potential the system of coupled differential equations (A.16) is solved, and the first single-particle wave functions and the first binding energies are obtained. Having the single-particle wave functions, the electronic charge density can be renewed with the following relation,

$$\rho_e^{(2)}(r) = \sum \psi_{n,\kappa,m}^{\dagger}(r)\psi_{n,\kappa,m}(r) \tag{A.26}$$

where the summation is done after all shells occupied with electrons. In the case of electronic configurations in which all shells (indexed by a and determined by the quantum numbers n_a and κ_a) are completely occupied by electrons, the total charge density has spherical symmetry (Unsöld theorem) [324] and is given by,

$$\rho_e^{(2)}(r) = \frac{1}{4\pi}\sum_a q_a \left[g_{n_a,\kappa_a}^2(r) + f_{n_a,\kappa_a}^2(r)\right]. \tag{A.27}$$

Here $q_a = 2j_a + 1 = 2|\kappa_a|$ is the number of bound electrons in the a shell. In the case of configurations with incompletely occupied shells, with $q_a < 2j_a + 1 = 2|\kappa_a|$, spherical symmetry of the charge density is imposed by considering a fractional occupation number of the incompletely occupied shell equal to $q_a/(2j_a + 1)$. Having electron charge density, $\rho_e^{(2)}(r)$, one can determine the potential, $V_{\mathrm{DHFS}}^{(2)}(r)$.

The next iteration will use the combined potential,

$$V_{\mathrm{DHFS}}^{(3)}(r) = (1-w)V_{\mathrm{DHFS}}^{(1)}(r) + wV_{\mathrm{DHFS}}^{(2)}(r), \tag{A.28}$$

where the weight parameter, w, has a starting value 0.05. During the iterative stabilization of the electronic charge density, the weight parameter gradually increases up to a maximum value of 0.5. The self-consistent procedure stops when neither the single-particle wave functions nor the binding energies anymore vary within a user-imposed numerical tolerance.

At this moment the electronic charge density, and implicitly the Dirac-Hartree-Fock-Slater type potential, reach convergence.

The implementation of the self-consistent procedure described above can be found in the DHFS.F program included in the RADIAL package. This is available in the supplementary materials of [207], where a comprehensive package manual is also presented.

A.2.2 The DHFS bound states of ^{124}Xe

In the context of the ground state 2νECEC process in the neutral atom ^{124}Xe, the reaction can be described as follows:

$$^{124}\text{Xe} + 2e^- \rightarrow ^{124}\text{Te}^* + 2\nu_e, \tag{A.29}$$

During this process, two atomic electrons are captured by the ^{124}Xe nucleus. Consequently, the resulting ^{124}Te atom is left with two vacancies in its electronic configuration, corresponding to the captured electrons. Importantly, despite the electron capture, the overall charge of the ^{124}Te atom remains neutral. Hence, in the context of 2νECEC (and EC) processes, it becomes necessary to consider the description of atomic excited states. This particular aspect will be discussed in the subsequent Section, focusing on the topic of atomic relaxation energy.

Table A.1: *Binding energies for bound electrons in the neutral ^{124}Xe atom. The results are obtained with the self-consistent DHFS method presented and used in this work (second column). The last column presents the experimental measurements [325].*

Shell $(n\ell_j)$	$t_{n\kappa}$ (DHFS) [eV]	$t_{n\kappa}$(EXP) [325] [eV]
$1s_{1/2}$	-34556.5	-34564.4 ± 2
$2s_{1/2}$	-5417.3	-5452.8 ± 2
$2p_{1/2}$	-5104.3	-5103.7 ± 2
$2p_{3/2}$	-4774.6	-4782.2 ± 2
$3s_{1/2}$	-1122.2	-1148.7 ± 2
$3p_{1/2}$	-989.7	-1002.1 ± 2
$3p_{3/2}$	-926.5	-940.6 ± 2
$3d_{3/2}$	-690.9	-689.4 ± 2
$3d_{5/2}$	-677.4	-676.7 ± 2
$4s_{1/2}$	-208.5	-213.3 ± 2
$4p_{1/2}$	-160.8	-145.5 ± 2
$4p_{3/2}$	-147.9	-145.5 ± 2
$4d_{3/2}$	-69.8	-69.5 ± 2
$4d_{5/2}$	-67.7	-67.5 ± 2
$5s_{1/2}$	-23.6	-23.4 ± 2
$5p_{1/2}$	-12.4	-13.4 ± 2
$5p_{3/2}$	-11.0	-12.1 ± 2

Table A.1 presents the binding energies for all orbitals of the neutral atom ^{124}Xe. Consistent with the findings in ^{150}Nd, a remarkable agreement is observed between the DHFS binding energies and the corresponding experimental data. This agreement is particularly notable for inner shells with $\kappa = -1$ form, which corresponds to the orbital where the electron is most likely to be captured.

A.2.3 Total electron binding energy

In Chapter 7, we have shown that the detection of double electron capture (2νECEC) events depends on the atomic relaxation of the final system, which results in the emission

of X-rays and Auger electrons. The theoretical determination of the position of the experimental peak in the detector relies on the atomic relaxation energy. As the final atom remains with holes in the shells x and y and relaxes to its atomic ground state configuration, the atomic relaxation energy can be expressed in terms of the total electron binding energies of those configurations, as shown in Eq. (7.4),

$$R_{\mathrm{xy}} = B_{\mathrm{gs}}(Z) - B_{\mathrm{xy}}(Z) \qquad \text{for } 2\nu\text{ECEC from shells x and y.} \tag{A.30}$$

The following section presents the primary components involved in calculating the total electron binding energy, B, for a given atomic configuration using the DHFS self-consistent approach. It is important to note that the total electron binding energy is defined as negative, and is therefore included in the atomic mass as a subtraction,

$$\mathcal{M}(A,Z) = M(A,Z) + Zm_e - B(Z). \tag{A.31}$$

The total electron binding energy for a ground state atomic configuration can be obtained from the evaluation of the following matrix elements,

$$B_{\mathrm{gs}}[\Psi_{\mathrm{gs}}] = \langle \Psi_{\mathrm{gs}} \left| \mathcal{H} \right| \Psi_{\mathrm{gs}} \rangle, \tag{A.32}$$

where $\mathcal{H}$ is the atomic Hamiltonian defined as,

$$\mathcal{H} = \sum_{i=1}^{Z} \left[\boldsymbol{\alpha}_i \cdot \boldsymbol{p}_i + (\beta - 1)\, m_e \right] + \sum_{i=1}^{Z} V_{\mathrm{nuc}}(\boldsymbol{r}_i) + \sum_{i<j=1}^{Z} \frac{\alpha}{|\boldsymbol{r}_i - \boldsymbol{r}_j|}, \tag{A.33}$$

where the matrices $\boldsymbol{\alpha}$ and β are defined in Eq. A.3. Here, $\boldsymbol{r}_i$ and $\boldsymbol{p}_i$ are respectively the position and momentum operators of the i-th electron.

The ground state atomic wave function, Ψ_{gs}, is constructed as a Slater determinant from the individual electron wave functions,

$$\Psi_{\mathrm{gs}} = \frac{1}{\sqrt{Z!}} \begin{vmatrix} \psi_1(\boldsymbol{r}_1) & \dots & \psi_1(\boldsymbol{r}_Z) \\ \vdots & \ddots & \vdots \\ \psi_Z(\boldsymbol{r}_1) & \dots & \psi_Z(\boldsymbol{r}_Z) \end{vmatrix} \tag{A.34}$$

Here, the orthonormality of the bound electron wave functions holds,

$$\begin{aligned} \langle \psi_i | \psi_j \rangle &= \int \psi_i^{\dagger}(\boldsymbol{r}) \psi_j(\boldsymbol{r}) d\boldsymbol{r} \\ &= \int_0^{\infty} r^2 \left[g_i(r) g_j(r) + f_i(r) f_j(r) \right] dr \\ &= \delta_{ij} \end{aligned} \tag{A.35}$$

It is worth noting that when the atom is in an excited state after undergoing the EC process with a hole in shell x, the construction of the atomic wave function Ψ_{x} involves a different set of individual electron wave functions. For ease of notation, we generally denote these sets as $\psi_1, \psi_2, \dots, \psi_Z$. There may be slight differences in the individual wave functions due to changes in the electronic configuration.

Using the Slater-Condon rules [326, 327], the total electron binding energy can be separated as,

$$B[\Psi] = B_{\mathrm{kin}} + B_{\mathrm{nuc}} + B_{\mathrm{el}} + B_{\mathrm{ex}}, \tag{A.36}$$

where the individual terms are given by,

$$B_{\text{kin}} = \sum_i \int \psi_i^\dagger(\boldsymbol{r}) \left[\boldsymbol{\alpha} \cdot \boldsymbol{p} + (\beta - 1) m_e\right] \psi(\boldsymbol{r}) d\boldsymbol{r}, \tag{A.37}$$

$$B_{\text{nuc}} = \sum_i \int \psi_i^\dagger(\boldsymbol{r}) V_{\text{nuc}}(r) \psi(\boldsymbol{r}) d\boldsymbol{r}, \tag{A.38}$$

$$B_{\text{el}} = \frac{\alpha}{2} \sum_{i,j} \int \int \left[\psi_i^\dagger(\boldsymbol{r}) \psi_i(\boldsymbol{r}')\right] \left[\psi_j^\dagger(\boldsymbol{r}) \psi_j(\boldsymbol{r}')\right] \frac{1}{|\boldsymbol{r} - \boldsymbol{r}'|} d\boldsymbol{r} d\boldsymbol{r}' \tag{A.39}$$

and

$$B_{\text{ex}} = -\frac{\alpha}{2} \sum_{i,j} \int \int \left[\psi_i^\dagger(\boldsymbol{r}) \psi_j(\boldsymbol{r}')\right] \left[\psi_j^\dagger(\boldsymbol{r}) \psi_i(\boldsymbol{r}')\right] \frac{1}{|\boldsymbol{r} - \boldsymbol{r}'|} d\boldsymbol{r} d\boldsymbol{r}'. \tag{A.40}$$

The first two terms are the kinetic and respectively the nuclear total energies. In the last two expressions the unrestricted sums create terms with $i = j$, called self-interacting terms. Those are not contributing in the expression of total binding energy because the mutual cancellations in $B_{\text{el}} + B_{\text{ex}}$. If one needs to extract the actual total exchange energy and total electron-electron interaction energy, one need to exclude the self-interaction terms from the expressions of B_{el} and B_{ex}.

Depending on whether the atomic configuration is closed or not, the calculation of the total electron binding energy is different. For configurations with completely filled shells the Eq. A.32 holds. For opened-shell configurations the total binding electron energy is obtained as an average energy,

$$B_{\text{av}} = \frac{1}{\mathcal{D}} \sum_{\Psi} \langle \Psi \left| \mathcal{H} \right| \Psi \rangle, \tag{A.41}$$

where the sum runs over all states corresponding to all combinations of filled orbitals in the open shells. Here, $\mathcal{D}$ is the number of states in the summation. If we denote with,

$$B_{\text{pot}} = B_{\text{nuc}} + B_{\text{el}} + B_{\text{ex}}, \tag{A.42}$$

then the total electronic binding energy for opened-shell configurations is given by,

$$B_{\text{av}} = B_{\text{av,kin}} + B_{\text{av,pot}}. \tag{A.43}$$

In terms of radial integrals the average kinetic term is given by [328]

$$\begin{aligned} B_{\text{av,kin}} = \sum_a q_a \int \Bigg\{ & g_{n_a\kappa_a} \left(\frac{\kappa_a}{r} f_{n_a\kappa_a} - \frac{df_{n_a\kappa_a}}{dr} \right) \\ & + f_{n_a\kappa_a} \left[\left(\frac{\kappa_a}{r} g_{n_a\kappa_a} + \frac{dg_{n_a\kappa_a}}{dr} \right) - 2m_e f_{n_a\kappa_a} \right] \Bigg\} dr \end{aligned} \tag{A.44}$$

where as previous $q_a = 2j_a + 1 = 2\left|\kappa_a\right|$ is the number of bound electrons in the a shell and for opened-shells, with $q_a < 2j_a + 1 = 2\left|\kappa_a\right|$, a fractional occupation number $q_a/(2j_a + 1)$ is considered. The average potential energy is given by [328],

$$
\begin{aligned}
B_{\mathrm{av,pot}} = \sum_a q_a \Bigg\{ & \int \left(g^2_{n_a\kappa_a} + f^2_{n_a\kappa_a}\right) V_{\mathrm{nuc}} dr \\
& + \frac{\alpha}{2}\left(q_a - 1\right)\left[F^0(a,a) - \sum_{L=1}^{\infty} \frac{d^L(\kappa_a,\kappa_a)}{2j_a} F^L(a,a)\right] \\
& + \frac{\alpha}{2}\sum_{b\neq a} q_b \left[F^0(a,b) - \sum_{L=0}^{\infty} \frac{d^L(\kappa_a,\kappa_b)}{2j_b+1} G^L(a,b)\right]\Bigg\}.
\end{aligned}
\tag{A.45}
$$

Here the sum runs over all occupied shells a and

$$
\begin{aligned}
F^L(a,b) &= R^L(a\ b, a\ b) \\
G^L(a,b) &= R^L(a\ b, b\ a)
\end{aligned}
\tag{A.46}
$$

are the Slater integrals,

$$
\begin{aligned}
R^L(a\ b, c\ d) = \int_0^\infty \int_0^\infty & \left[g_{n_a\kappa_a}(r_1) g_{n_c\kappa_c}(r_1) + f_{n_a\kappa_a}(r_1) f_{n_c\kappa_c}(r_1)\right] \frac{r_<^L}{r_>^{L+1}} \\
& \times \left[g_{n_b\kappa_b}(r_2) g_{n_d\kappa_d}(r_2) + f_{n_b\kappa_b}(r_2) f_{n_d\kappa_d}(r_2)\right] dr_1 dr_2,
\end{aligned}
\tag{A.47}
$$

with $r_< = \min(r_1, r_2)$ and $r_> = \max(r_1, r_2)$. The coefficients $d^L(\kappa_a, \kappa_b)$ is defined as,

$$
d^L(\kappa_a,\kappa_b) = v^L(\ell_a,\ell_b)\frac{2j_b+1}{2j_a+1}\left\langle Lj_b0\frac{1}{2}\middle| j_a\frac{1}{2}\right\rangle,
\tag{A.48}
$$

where

$$
v^L(\ell_a,\ell_b) = \begin{cases} 1 & \text{if } L+\ell_a+\ell_b \text{ is even,} \\ 0 & \text{otherwise.} \end{cases}
\tag{A.49}
$$

In the definition of $d^L(\kappa_a, \kappa_b)$ coefficients, the Clebsch-Gordan coefficient can be evaluated with the useful relation [316],

$$
\begin{aligned}
\sqrt{2j_a\left(2j_b+1\right)}\left\langle L, j_b, 0, \frac{1}{2}\middle| j_a, \frac{1}{2}\right\rangle = & \sqrt{\left(J-2L\right)\left(J+1\right)}\left\langle L, j_b-\frac{1}{2}, 0, 0\middle| j_a-\frac{1}{2}, 0\right\rangle \\
& \sqrt{\left(J-2j_b\right)\left(J-2j_a+1\right)}\left\langle L, j_b+\frac{1}{2}, 0, 0\middle| j_a-\frac{1}{2}, 0\right\rangle,
\end{aligned}
\tag{A.50}
$$

where $J = L + j_a + j_b$. The Clebsch-Gordan coefficients, $\langle j_1, j_2, 0, 0 | j_3, 0\rangle$, in the right-hand side vanish if $j_1 + j_2 + j_3 = 2K$ is odd. If $j_1 + j_2 + j_3$ is even,

$$
\langle j_1, j_2, 0, 0 | j_3, 0\rangle = (-1)^{K-j_3}\sqrt{\frac{2j_3+1}{2J+1}}\left[\frac{\tau(K)}{\tau(K-j_1)\tau(K-j_2)\tau(K-j_3)}\right]^{1/2}
\tag{A.51}
$$

with

$$
\tau(K) = \frac{2^K (K!)^2}{(2K)!} = \frac{K!}{1\cdot 3\cdot 5\cdot \ldots \cdot (2K-1)}.
\tag{A.52}
$$

The evaluation of Slater integrals is a challenging task that requires careful consideration. A direct evaluation approach is often not sufficiently accurate, and it can also be computationally intensive, making it impractical in many cases. The aforementioned drawbacks can be overcome by employing Hartree's method to solve the Slater integrals. This method provides a more accurate and efficient approach for evaluating the integrals, addressing both the accuracy and computational efficiency issues. For the presentation and implementation of the method we indicate the Supplementary Materials of [207].

A.3 Continuum states

The electrons/positrons emitted in DBD processes are not free particles but interact with the Coulomb field generated by the atomic final systems, which is a positive/negative ion of charge $Z_f = \pm 2$. The scattering wave functions of the outgoing charged particles are essential ingredients that influence the kinematics of the DBD process. For an electron with momentum $\boldsymbol{p}_e$, energy $E_e = \sqrt{\boldsymbol{p}_e^2 + m_e^2}$, and spin projection s, its wave function $\psi_s(E_e, \boldsymbol{r})$ can be expanded in term of Coulomb-distorted spherical waves [155, 63, 181]

$$\psi_s(E_e, \boldsymbol{r}) = \sum_{\kappa,\mu} 4\pi i^\ell \left\langle \ell_\kappa, \frac{1}{2}, \mu - s, s \middle| j, \mu \right\rangle Y^*_{\ell_\kappa, \mu-s}(\hat{\boldsymbol{p}}_e) \begin{pmatrix} \tilde{g}_\kappa(E_e, r)\Omega_{\kappa,m}(\hat{\boldsymbol{r}}) \\ i\tilde{f}_\kappa(E_e, r)\Omega_{-\kappa,m}(\hat{\boldsymbol{r}}) \end{pmatrix}, \tag{A.53}$$

where $\langle j_1, j_2, m_1, m_2 | j, m \rangle$ are the Clebsch-Gordan coefficients, $\boldsymbol{r}$ stands for the position vector of the electron with $\hat{\boldsymbol{r}} = \boldsymbol{r}/r$, κ is the relativistic quantum number and $\Omega_{\kappa,m}(\hat{\boldsymbol{r}})$ are the spherical spinors [314, 315]. The label μ is the projection of the total angular momentum $j = |\kappa| - 1/2$, and the orbital angular momentum is: $\ell_\kappa = \kappa$ if $\kappa > 0$ and $\ell_\kappa = |\kappa| - 1$ if $\kappa < 0$. The large- and small-component radial functions, $\tilde{g}_\kappa(E_e, r)$ and $\tilde{f}_\kappa(E_e, r)$, respectively, satisfy the following spherical Dirac equation,

$$\begin{aligned} \left(\frac{d}{dr} + \frac{\kappa+1}{r}\right)\tilde{g}_\kappa - (E_e - V(r) + m_e)\tilde{f}_\kappa = 0, \\ \left(\frac{d}{dr} - \frac{\kappa-1}{r}\right)\tilde{f}_\kappa + (E_e - V(r) - m_e)\tilde{g}_\kappa = 0. \end{aligned} \tag{A.54}$$

The functions $\tilde{g}_\kappa(E_e, r)$ and $\tilde{f}_\kappa(E_e, r)$ must also satisfy the boundary condition "a plane wave plus incoming spherical waves" and are normalized in such a way that [63, 181]

$$\begin{aligned} \begin{Bmatrix} \tilde{g}_\kappa(E_e, r) \\ \tilde{f}_\kappa(E_e, r) \end{Bmatrix} &= \exp\left(-i\bar{\Delta}_\kappa\right) \begin{Bmatrix} g_\kappa(E_e, r) \\ f_\kappa(E_e, r) \end{Bmatrix} \\ &\xrightarrow[r\to\infty]{} \frac{\exp\left(-i\bar{\Delta}_\kappa\right)}{p_e r} \begin{Bmatrix} \sqrt{\frac{E_e+m_e}{2E_e}} \sin\left(p_e r - \ell_\kappa \frac{\pi}{2} + \eta \ln(2p_e r) + \bar{\Delta}_\kappa\right) \\ \sqrt{\frac{E_e-m_e}{2E_e}} \cos\left(p_e r - \ell_\kappa \frac{\pi}{2} + \eta \ln(2p_e r) + \bar{\Delta}_\kappa\right) \end{Bmatrix}, \end{aligned} \tag{A.55}$$

where $\bar{\Delta}_\kappa$ is the overall phase shift and $\eta = \alpha Z_f E_e / p_e$ is the Sommerfeld parameter. The usual approximation in the DBD is that only the leading order from the expansion of the wave function contributes and thus the leptons are emitted in $s_{1/2}$-wave.

It is useful to expand the electron wave function in terms of spherical waves,

$$\psi(E_e, \boldsymbol{r}) = \psi^{(s_{1/2})}(E_e, \boldsymbol{r}) + \psi^{(p_{1/2})}(E_e, \boldsymbol{r}) + \psi^{(p_{3/2})}(E_e, \boldsymbol{r}) + \ldots, \tag{A.56}$$

where the superscript represents the orbital and total angular momentum ($\ell_j = 0_{1/2}, 1_{1/2}, 1_{3/2}, ...$) written in the spectroscopic notation ($\ell_j = s_{1/2}, p_{1/2}, p_{3/2}, ...$). The

first few spherical waves are the following [128]

$$\psi^{(s_{1/2})}(E_e,\boldsymbol{r}) = \begin{pmatrix} g_{-1}(E_e,r)\chi_\mu \\ f_{+1}(E_e,r)(\boldsymbol{\sigma}\cdot\hat{\boldsymbol{p}})\chi_\mu \end{pmatrix}, \tag{A.57}$$

$$\psi^{(p_{1/2})}(E_e,\boldsymbol{r}) = i\begin{pmatrix} g_{1}(E_e,r)(\boldsymbol{\sigma}\cdot\hat{\boldsymbol{r}})(\boldsymbol{\sigma}\cdot\hat{\boldsymbol{p}})\chi_\mu \\ -f_{-1}(E_e,r)(\boldsymbol{\sigma}\cdot\hat{\boldsymbol{r}})\chi_\mu \end{pmatrix}, \tag{A.58}$$

$$\psi^{(p_{3/2})}(E_e,\boldsymbol{r}) = i\begin{pmatrix} g_{-2}(E_e,r)\left[3(\hat{\boldsymbol{r}}\cdot\hat{\boldsymbol{p}}) - (\boldsymbol{\sigma}\cdot\hat{\boldsymbol{r}})(\boldsymbol{\sigma}\cdot\hat{\boldsymbol{p}})\right]\chi_\mu \\ f_{+2}(E_e,r)\left[(\hat{\boldsymbol{r}}\cdot\hat{\boldsymbol{p}})(\boldsymbol{\sigma}\cdot\hat{\boldsymbol{p}}) - (\boldsymbol{\sigma}\cdot\hat{\boldsymbol{r}})\right]\chi_\mu \end{pmatrix}, \tag{A.59}$$

where $\hat{\boldsymbol{p}} = \boldsymbol{p_e}/p_e$ is defined by the momentum of the electron, $p_e = \sqrt{E_e^2 - m_e^2}$.

For continuum states ($E_e > m_e$), the wave functions are not square integrable, so usually the normalization is done on the energy scale, i.e.

$$\left\langle \psi_{E_e\kappa} \middle| \psi_{E'_e\kappa} \right\rangle = \delta(E_e - E'_e). \tag{A.60}$$

In the following sections, we present multiple analytical and numerical continuum wave functions for a given potential $V(r)$. The normalization of large- and small-component radial functions, $g_\kappa(E_e,r)$ and $f_\kappa(E_e,r)$ respectively, is chosen so that they reproduce the following spherical Bessel function in the limit $V(r) \to 0$:

$$g_\kappa(E_e,r) \Rightarrow \sqrt{\frac{E_e+m_e}{2E_e}} j_{l_\kappa}(pr), \qquad f_\kappa(E_e,r) \Rightarrow \sqrt{\frac{E_e-m_e}{2E_e}} \frac{\kappa}{|\kappa|} j_{l_{-\kappa}}(pr). \tag{A.61}$$

In particular cases of the spherical waves expansion, Eq. (A.56), we have

$$\begin{aligned}
g_{-1}(E_e,r) &\to \sqrt{\frac{E_e+m_e}{2E_e}}\, j_0(pr), \quad & f_{-1}(E_e,r) &\to -\sqrt{\frac{E_e-m_e}{2E_e}}\, j_1(pr) \\
g_{+1}(E_e,r) &\to \sqrt{\frac{E_e+m_e}{2E_e}}\, j_1(pr), \quad & f_{+1}(E_e,r) &\to \sqrt{\frac{E_e-m_e}{2E_e}}\, j_0(pr) \\
g_{-2}(E_e,r) &\to \sqrt{\frac{E_e+m_e}{2E_e}}\, j_1(pr), \quad & f_{-2}(E_e,r) &\to -\sqrt{\frac{E_e-m_e}{2E_e}}\, j_2(pr) \\
g_{+2}(E_e,r) &\to \sqrt{\frac{E_e+m_e}{2E_e}}\, j_2(pr), \quad & f_{+2}(E_e,r) &\to \sqrt{\frac{E_e-m_e}{2E_e}}\, j_1(pr).
\end{aligned} \tag{A.62}$$

A.3.1 Charged sphere potential: approximated solutions

We assume the final nucleus as a uniformly charged sphere, generating the following potential,

$$V(r) = \begin{cases} -\frac{\alpha Z}{r} & \text{for } r \geq R, \\ -\frac{\alpha Z}{2R}\left[3 - \left(\frac{r}{R}\right)^2\right] & \text{for } r < R. \end{cases} \tag{A.63}$$

Here, R is the radius of the final nucleus, $R = r_0 A^{1/3}$ with $r_0 = 1.2$ fm. By keeping the lowest power of the expansion of r, the radial wave functions for the $s_{1/2}$ wave and $p_{3/2}$ wave states are given by [63]

$$\begin{pmatrix} g_{-1}(E_e,r) \\ f_{+1}(E_e,r) \end{pmatrix} = \begin{pmatrix} A_{-1} \\ A_{+1} \end{pmatrix}, \tag{A.64}$$

and

$$\begin{pmatrix} g_{-2}(E_e,r) \\ f_{+2}(E_e,r) \end{pmatrix} = \frac{p_e r}{3}\begin{pmatrix} A_{-2} \\ A_{+2} \end{pmatrix}, \tag{A.65}$$

respectively.

The normalization constant can be expressed in a good approximation as

$$A_{\pm k} \simeq \sqrt{F_{k-1}(Z,E_e)}\sqrt{\frac{E_e \mp m_e}{2E_e}} \tag{A.66}$$

where $k = |\kappa|$ and the Fermi function $F_{k-1}(Z,E_e)$ is given by

$$F_{k-1}(Z,E_e) = \left[\frac{\Gamma(2k+1)}{\Gamma(k)\Gamma(2\gamma_k+1)}\right]^2 (2p_eR)^{2(\gamma_k-k)} e^{\pi\eta} \left|\Gamma(\gamma_k+i\eta)\right|^2 . \tag{A.67}$$

The remaining quantity is given by

$$\gamma_k = \sqrt{k^2-(\alpha Z)^2}, \tag{A.68}$$

and $\Gamma(z)$ is the Gamma function.

A.3.2 Point-like potential: analytical solutions

In this approximation scheme, we consider the case, where the final nucleus generates a point-like potential, $V(r) = -\alpha Z/r$. The radial wave functions can be expressed analytically as [214]

$$\begin{aligned} g_\kappa(E_e,r) &= \frac{\kappa}{k}\frac{1}{pr}\sqrt{\frac{E_e+m_e}{2E_e}}\frac{|\Gamma(1+\gamma_k+i\eta)|}{\Gamma(1+2\gamma_k)}(2pr)^{\gamma_k}e^{\pi\eta/2} \\ &\quad \times \mathrm{Im}\{e^{i(pr+\zeta)}{}_1F_1(\gamma_k-i\eta,1+2\gamma_k,-2ipr)\}, \\ f_\kappa(E_e,r) &= \frac{\kappa}{k}\frac{1}{pr}\sqrt{\frac{E_e-m_e}{2E_e}}\frac{|\Gamma(1+\gamma_k+i\eta)|}{\Gamma(1+2\gamma_k)}(2pr)^{\gamma_k}e^{\pi\eta/2} \\ &\quad \times \mathrm{Re}\{e^{i(pr+\zeta)}{}_1F_1(\gamma_k-i\eta,1+2\gamma_k,-2ipr)\}, \end{aligned} \tag{A.69}$$

with

$$e^{i\zeta} = \sqrt{\frac{\kappa - i\eta m_e/E_e}{\gamma_k - i\eta}}. \tag{A.70}$$

Here, ${}_1F_1(a,b,z)$ is the confluent hypergeometric function. We mention that the numerical solutions from the RADIAL package, with the input $rV(r) = -\alpha Z$, are equivalent to the analytical solutions presented in Eq. (A.69), if we fix r on the nuclear surface.

A.3.3 Charged sphere nucleus with Fermi proton distribution: numerical solutions

We consider the final nucleus as a sphere filled with protons following a Fermi distribution [319]

$$\rho_p(r) = \frac{\rho_0}{1+e^{(r-c_{\mathrm{rms}})/a}}, \tag{A.71}$$

where we chose for the half-way radius $c_{\mathrm{rms}} = 1.07A^{1/3} = 6.118$ fm (only for ^{187}Re) and for the surface thickness $a = 0.546$ fm. ρ_0 is determined from the normalization to Z.Thus, the electrostatic interaction of an electron at r with the final nucleus is described by $V_{\mathrm{nuc}}(r)$ from Eq. (A.19).

A.3.4 Charged sphere potential and Thomas-Fermi screening: numerical solutions

In this scheme, we consider the numerical solutions of the radial Dirac equation for a uniform charged distribution of the final nucleus. Using the numerical wave functions as solutions of the radial Dirac equation for the potential described by Eq. (A.63), we consider the finite size effect of the final nucleus. Moreover, the screening effect of atomic electrons is considered by the Thomas-Fermi approximation. The universal screening function used $\phi(r)$ is the solution of the Thomas-Fermi equation

$$\frac{d^2\phi}{dx^2} = \frac{\phi^{3/2}}{\sqrt{x}}, \tag{A.72}$$

with the boundary conditions $\phi(0) = 1$ and $\phi(\infty) = 0$. In Eq. (A.72) $x = r/b$, with $b \approx 0.8853 a_0 Z_f^{-1/3}$ and a_0 is the Bohr radius. For solving the Thomas-Fermi equation we implied the numerical Majorana method described in [329].

A.3.5 Modified and true DHFS potential: numerical solutions

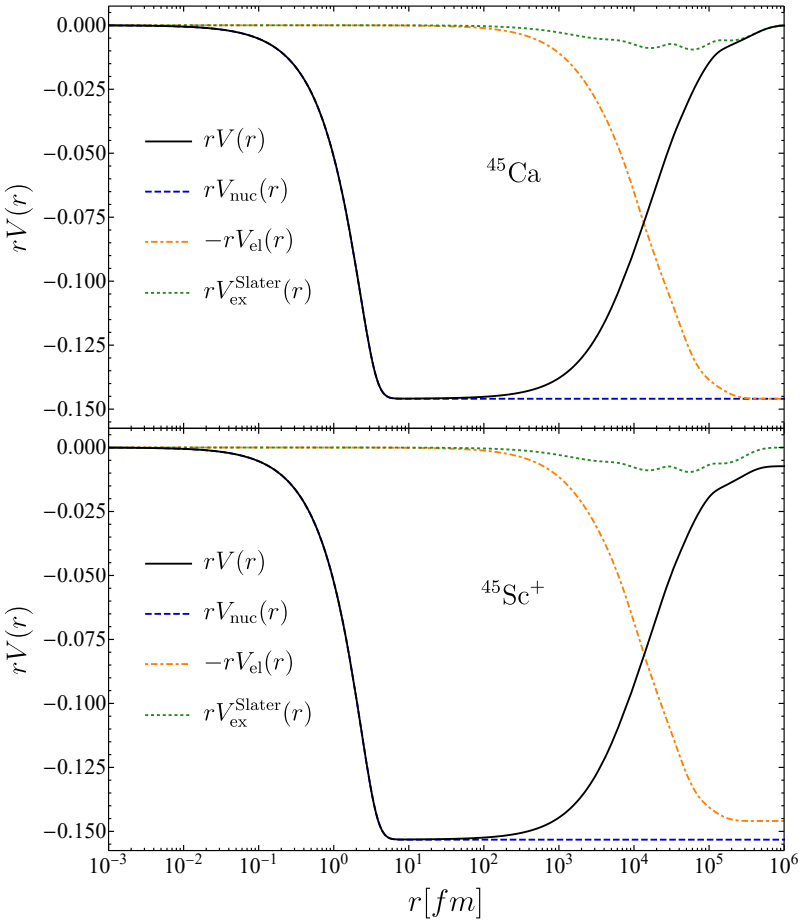

Figure A.1: Modified self-consistent potentials (solid curves) for the initial neutral atom, ^{45}Ca (top), and the final positive ion, $^{45}Sc^{+}$ (bottom). See Eq. (A.73) and text for details. In both cases, we indicate the nuclear potential (dashed curve), the electronic potential (dot-dashed curve) and the Slater's exchange potential (dotted curve). Figure is taken from [165].

Table A.2: Binding energies for neutral atom ^{45}Ca in eV. In the first column, containing the occupied shells, we indicate with $*$ the relevant shells for the calculation of the exchange correction. In the second and third column, we present the true DHFS self-consistent method binding energies and the results obtained with the modified potential, respectively. In the last column, the experimental values taken from [325], are presented.

Orbital $(n\ell_j)$	$t_{n\kappa}$(true)	$t_{n\kappa}$(modified)	$t_{n\kappa}$(exp) [325]
$*1s_{1/2}$	-4015.1	-4015.1	-4041 ± 2
$*2s_{1/2}$	-434.1	-434.1	-441 ± 2
$*2p_{1/2}$	-359.1	-359.1	-353 ± 2
$2p_{3/2}$	-355.2	-355.2	-349 ± 2
$*3s_{1/2}$	-53.2	-53.2	-46 ± 2
$*3p_{1/2}$	-34.0	-34.0	-28 ± 2
$3p_{3/2}$	-33.6	-33.6	-28 ± 2
$*4s_{1/2}$	-5.45	-5.08	-6.113 ± 0.01

Table A.3: Binding energies for neutral atom ^{187}Re in eV. In the first column, we indicate all occupied shells using the spectroscopic notation [207, 330]. In the second and third columns, we present the true DHFS self-consistent method binding energies and the results obtained with the modified DHFS self-consistent method, respectively. In the last column, we present the experimental values taken from [325].

Orbital $(n\ell_j)$	$t_{n\kappa}$ (true)	$t_{n\kappa}$ (modified)	$t_{n\kappa}$(exp) [325]
$1s_{1/2}$	-71857.5	-71857.5	-71681 ± 2
$2s_{1/2}$	-12508.4	-12508.4	-12532 ± 2
$2p_{1/2}$	-11993.7	-11993.7	-11963 ± 2
$2p_{3/2}$	-10537.7	-10537.7	-10540 ± 2
$3s_{1/2}$	-2911.9	-2911.9	-2937 ± 2
$3p_{1/2}$	-2677.7	-2677.7	-2686 ± 2
$3p_{3/2}$	-2360.0	-2360.0	-2371 ± 2
$3d_{3/2}$	-1961.4	-1961.4	-1953 ± 2
$3d_{5/2}$	-1891.9	-1891.9	-1887 ± 2
$4s_{1/2}$	-615.7	-615.7	-629 ± 2
$4p_{1/2}$	-516.7	-516.7	-522 ± 2
$4p_{3/2}$	-442.2	-442.2	-450 ± 2
$4d_{3/2}$	-277.8	-277.8	-278 ± 2
$4d_{5/2}$	-263.9	-263.9	-264 ± 2
$5s_{1/2}$	-91.2	-91.2	-86 ± 2
$5p_{1/2}$	-60.6	-60.6	-56 ± 2
$4f_{5/2}$	-55.0	-55.0	-47 ± 2
$4f_{7/2}$	-52.3	-52.3	-45 ± 2
$5p_{3/2}$	-49.0	-49.0	-45 ± 2
$5d_{3/2}$	-9.28	-9.24	-9.6 ± 1
$5d_{5/2}$	-8.24	-8.20	-9.6 ± 1
$6s_{1/2}$	-7.98	-7.67	-7.9 ± 1

The easiest way to ensure the orthogonality between continuum and bound states, e.g., $\langle \psi'_{E_e s} | \psi'_{ns} \rangle = 0$, is to use the same potential in the calculation of the continuum and bound wave functions for the final positive ion atom. The procedure we used is that when obtaining the bound states, in the last iteration of the DHFS self-consistent method, we do not impose the Latter's tail correction for the exchange potential, Eq. A.23. In this way the potential for both continuum and bound states is written as,

$$V(r) = V_{\rm nuc}(r) + V_{\rm el}(r) + V_{\rm ex}^{\rm Slater}(r), \tag{A.73}$$

where the electronic and exchange components are obtained from the last iterated electron density. In this way, we respect the correct asymptotic condition for a scattering potential, $\lim_{r\to\infty} rV(r) = -\alpha(Z_p - N_e)$. In Fig. A.1, we present the modified potentials for the initial neutral atom ^{45}Ca, and the final positive ion ^{45}Sc^{+}. In what follows, when we use the potential from Eq. (A.73), for both continuum and bound states, we call the procedure a modified DHFS self-consistent method. Contrary, when the Latter's tail correction is imposed on the exchange potential as in Eq. (A.17), we call the procedure a true DHFS self-consistent method.

We indeed deviate from the true DHFS self-consistent method, but it turns out that the modifications in the binding energies and the bound wave functions are negligible. In Table A.2, we present the binding energies of the occupied states for the neutral atom ^{45}Ca. The difference between the true self-consistent DHFS potential and the modified potential leads to a negligible difference just in the binding energy of the last occupied orbital, $4s_{1/2}$. In Table A.3, we compare the binding energies obtained with the true and modified DHFS methods with the experimental values for the neutral atom ^{187}Re. We can see again that the deviation from the conventional (true) DHFS method subtly influences the binding energies of the last three occupied orbitals.

B List of publications and contributions

B.1 Publications in international journals

1. Angular Distributions of Emitted Electrons in the Two-Neutrino $\beta\beta$ Decay
   O. Nitescu, R. Dvornický, S. Stoica and F. Šimkovic,
   Universe **7** (5), 147 (2021).

2. Exchange correction for allowed β-decay
   O. Nitescu, S. Stoica and F. Šimkovic,
   Physical Review C **107** (2), 025501 (2023).

3. Atomic corrections for the unique first-forbidden β transition of ^{187}Re
   O. Nitescu, R. Dvornický and F. Šimkovic,
   Physical Review C **109** (2), 025501 (2024).

4. A Systematic Study of Two-Neutrino Double Electron Capture
   O. Nitescu, S. Ghinescu, S. Stoica and F. Šimkovic,
   Universe **10** (2), 98 (2024).

5. Addressing the discrepancy between experimental and theoretical spectra of low-energy β transitions
   O. Nitescu, S. Stoica and F. Šimkovic,
   AIP Conference Proceedings **3138**, 020012 (2024).

6. Mixture between the SSD and HSD hypothesis in $2\nu\beta\beta$-decay
   O. Nitescu, R. Dvornický and F. Šimkovic,
   AIP Conference Proceedings **3138**, 020019 (2024).

7. Theoretical analysis and predictions for the two-neutrino double electron capture of ^{124}Xe O. Nitescu, S. Ghinescu,, V. Sevestrean, M. Horoi, F. Šimkovic and S. Stoica
   Journal of Physics G: Nuclear and Particle Physics **51** (12), 125103 (2024).

8. The Impact of Electron Phase Shifts on $\beta\beta$-Decay Kinematics
   O. Nitescu, S. Ghinescu and F. Šimkovic,
   Universe **10** (12), 442 (2024).

9. Double-beta decay of ^{150}Nd to excited levels of ^{150}Sm
   STELLA collaboration + D.-L. Fang, O. Nitescu and F. Šimkovic,
   Accepted in The European Physical Journal C (2024), arxiv:2502.00748

10. Radiative and exchange corrections for two-neutrino double-beta decay
    O. Nitescu and F. Šimkovic,
    Submitted to Physical Review C, arXiv:2411.05405

11. A Semi-Empirical Formula for Two-Neutrino Double-Beta Decay
    O. Nitescu and F. Šimkovic,
    Accepted in Physical Review C, arXiv:2407.10422

B.2 International conferences

1. O. Nitescu [20 minutes talk]
   New Physics scenarios within Two-Neutrino Double-Beta Decay
   EuCAPT Astroneutrino Theory Workshop,
   Prague, 20 September – 1 October 2021.

2. O. Niţescu [30 minutes talk]
   Angular Distributions of Emitted Electrons in the Two-Neutrino Double-Beta Decay
   Matrix Elements for the Double beta decay EXperiments 2022 (MEDEX'22),
   Prague, 13–17 June 2022.

3. O. Niţescu [30 minutes talk]
   Atomic exchange correction for allowed β-decay and $2\nu\beta\beta$-decay
   Matrix Elements for the Double beta decay EXperiments 2023 (MEDEX'23),
   Prague, 04–08 September 2023.

4. O. Niţescu [25 minutes talk]
   Atomic corrections for the β-decay of neutrino mass measurement candidates
   Determination of the absolute electron (anti-)neutrino mass (NuMass 2024),
   Genoa, 26 February–01 March 2024.

5. O. Niţescu [30 minutes invited talk]
   Improved description of double beta-decay
   Theoretical and experimental approaches for nuclear matrix elements of double-beta decay (NME2025),
   Osaka, 20-21 January 2025.

Bibliography

[1] E. Fermi, Zeitschrift für Physik **88**, 161 (1934).

[2] R. L. Workman, V. D. Burkert, V. Crede, E. Klempt, U. Thoma, L. Tiator, K. Agashe, G. Aielli, B. C. Allanach, C. Amsler, *et al.* (Particle Data Group), Progress of Theoretical and Experimental Physics **2022**, 083C01 (2022).

[3] H. Shopper, *Weak interactions and nuclear beta decay* (North-Holland Publishing Company, 1966).

[4] H. Behrens and W. Büring, *Electron Radial Wave Functions and Nuclear Beta Decay* (Clarendon Press, 1982).

[5] Livechart of nuclides (2024).

[6] J. Suhonen, *From Nucleons to Nucleus: Concepts of Microscopic Nuclear Theory* (Springer Science & Business Media, 2007).

[7] S. Weinberg, Journal of Physics: Conference Series **196**, 012002 (2009).

[8] L. Hayen, N. Severijns, K. Bodek, D. Rozpedzik, and X. Mougeot, Rev. Mod. Phys. **90**, 015008 (2018).

[9] K. K. Vos, H. W. Wilschut, and R. G. E. Timmermans, Rev. Mod. Phys. **87**, 1483 (2015).

[10] J. P. Noordmans, H. W. Wilschut, and R. G. E. Timmermans, Phys. Rev. C **87**, 055502 (2013).

[11] N. Severijns, M. Beck, and O. Naviliat-Cuncic, Rev. Mod. Phys. **78**, 991 (2006).

[12] N. Severijns and O. Naviliat-Cuncic, Annual Review of Nuclear and Particle Science **61**, 23 (2011).

[13] N. Severijns, Journal of Physics G: Nuclear and Particle Physics **41**, 114006 (2014).

[14] J. C. Hardy and I. S. Towner, Phys. Rev. C **71**, 055501 (2005).

[15] J. C. Hardy and I. S. Towner, Phys. Rev. C **102**, 045501 (2020).

[16] A. Falkowski, M. González-Alonso, O. Naviliat-Cuncic, and N. Severijns, The European Physical Journal A **59**, 113 (2023).

[17] M. Faverzani *et al.*, Journal of Low Temperature Physics **184**, 10.1007/s10909-016-1540-x (2016).

[18] M. P. Croce *et al.*, Journal of Low Temperature Physics **184**, 10.1007/s10909-015-1451-2 (2016).

[19] L. Gastaldo *et al.*, The European Physical Journal Special Topics **226**, 10.1140/epjst/e2017-70071-y (2017).

[20] K. Langanke, G. Martínez-Pinedo, and R. G. T. Zegers, Reports on Progress in Physics **84**, 066301 (2021).

[21] R. Broda, P. Cassette, and K. Kossert, Metrologia **44**, S36 (2007).

[22] F. Buchegger, F. Perillo-Adamer, Y. M. Dupertuis, and A. Bischof Delaloye, European Journal of Nuclear Medicine and Molecular Imaging **33**, 1352 (2006).

[23] E. Bezak, B. Q. Lee, T. Kibédi, A. E. Stuchbery, and K. A. Robertson, Computational and Mathematical Methods in Medicine **2012**, 651475 (2012).

[24] G. Pirovano, T. C. Wilson, and T. Reiner, Nuclear Medicine and Biology **96-97**, 50 (2021).

[25] A. Ku, V. J. Facca, Z. Cai, and R. M. Reilly, EJNMMI Radiopharmacy and Chemistry **4**, 10.1186/s41181-019-0075-2 (2019).

[26] F. T. Avignone, S. R. Elliott, and J. Engel, Rev. Mod. Phys. **80**, 481 (2008).

[27] H. Ejiri, J. Suhonen, and K. Zuber, Physics Reports **797**, 1 (2019).

[28] F. Šimkovic, Physics-Uspekhi **64**, 1238 (2021).

[29] M. Goeppert-Mayer, Phys. Rev. **48**, 512 (1935).

[30] E. Majorana, Il Nuovo Cimento **14** (1937).

[31] W. H. Furry, Phys. Rev. **56**, 1184 (1939).

[32] G. Racah, Il Nuovo Cimento **14** (1937).

[33] M. Doi and T. Kotani, Progress of Theoretical Physics **87**, 1207 (1992).

[34] M. Doi and T. Kotani, Progress of Theoretical Physics **89**, 139 (1993).

[35] N. I. Rukhadze, J. Gascon, K. N. Gusev, A. A. Klimenko, M. Fürst, S. V. Rozov, E. Rukhadze, A. V. Salamatin, F. Šimkovic, Y. A. Shitov, I. Štekl, V. V. Timkin, and E. A. Yakushev, Journal of Physics: Conference Series **2156**, 012134 (2021).

[36] P. Belli, R. Bernabei, and V. Caracciolo, Particles **4**, 241 (2021).

[37] R. Saakyan, Annual Review of Nuclear and Particle Science **63**, 503 (2013).

[38] S. R. Elliott, A. A. Hahn, and M. K. Moe, Phys. Rev. Lett. **59**, 2020 (1987).

[39] M. K. Moe, Annual Review of Nuclear and Particle Science **64**, 247 (2014).

[40] A. Barabash, Universe **6**, 10.3390/universe6100159 (2020).

[41] A. S. Barabash and R. R. Saakyan, Physics of Atomic Nuclei **59**, 179 (1996).

[42] A. P. Meshik, C. M. Hohenberg, O. V. Pravdivtseva, and Y. S. Kapusta, Phys. Rev. C **64**, 035205 (2001).

[43] M. Pujol, B. Marty, P. Burnard, and P. Philippot, Geochimica et Cosmochimica Acta **73**, 6834 (2009).

[44] Y. M. Gavrilyuk, A. M. Gangapshev, V. V. Kazalov, V. V. Kuzminov, S. I. Panasenko, and S. S. Ratkevich, Phys. Rev. C **87**, 035501 (2013).

[45] S. S. Ratkevich, A. M. Gangapshev, Y. M. Gavrilyuk, F. F. Karpeshin, V. V. Kazalov, V. V. Kuzminov, S. I. Panasenko, M. B. Trzhaskovskaya, and S. P. Yakimenko, Phys. Rev. C **96**, 065502 (2017).

[46] E. Aprile, J. Aalbers, F. Agostini, M. Alfonsi, L. Althueser, F. D. Amaro, *et al.* (XENON Collaboration), Nature **568**, 532 (2019).

[47] E. Aprile, K. Abe, F. Agostini, S. Ahmed Maouloud, M. Alfonsi, L. Althueser, *et al.* (XENON Collaboration), Phys. Rev. C **106**, 024328 (2022).

[48] J. Aalbers, D. S. Akerib, A. K. A. Musalhi, F. Alder, C. S. Amarasinghe, A. Ames, T. J. Anderson, N. Angelides, H. M. Araújo, J. E. Armstrong, *et al.* (The LZ collaboration), Journal of Physics G: Nuclear and Particle Physics **52**, 015103 (2024).

[49] Z. Bo, W. Chen, X. Chen, Y. Chen, Z. Cheng, X. Cui, Y. Fan, D. Fang, Z. Gao, L. Geng, K. Giboni, X. Guo, *et al.* (PandaX Collaboration), Measurement of two-neutrino double electron capture half-life of ^{124}xe with pandax-4t (2024), arXiv:2411.14355 [nucl-ex] .

[50] T. Bernatowicz, J. Brannon, R. Brazzle, R. Cowsik, C. Hohenberg, and F. Podosek, Phys. Rev. C **47**, 806 (1993).

[51] R. Arnold, C. Augier, A. M. Bakalyarov, J. D. Baker, A. S. Barabash, A. Basharina-Freshville, S. Blondel, S. Blot, M. Bongrand, V. Brudanin, *et al.* (NEMO-3 Collaboration), Phys. Rev. D **93**, 112008 (2016).

[52] M. Agostini, A. Alexander, G. R. Araujo, A. M. Bakalyarov, M. Balata, I. Barabanov, L. Baudis, C. Bauer, S. Belogurov, A. Bettini, *et al.* (GERDA Collaboration), Phys. Rev. Lett. **131**, 142501 (2023).

[53] O. Azzolini, J. W. Beeman, F. Bellini, M. Beretta, M. Biassoni, C. Brofferio, C. Bucci, S. Capelli, V. Caracciolo, L. Cardani, *et al.*, Phys. Rev. Lett. **131**, 222501 (2023).

[54] J. Argyriades, R. Arnold, C. Augier, J. Baker, A. Barabash, A. Basharina-Freshville, M. Bongrand, G. Broudin-Bay, V. Brudanin, A. Caffrey, *et al.*, Nuclear Physics A **847**, 168 (2010).

[55] C. Augier, A. S. Barabash, F. Bellini, G. Benato, M. Beretta, L. Bergé, *et al.* (CUPID-Mo Collaboration), Phys. Rev. Lett. **131**, 162501 (2023).

[56] A. S. Barabash, P. Belli, R. Bernabei, F. Cappella, V. Caracciolo, R. Cerulli, D. M. Chernyak, F. A. Danevich, S. d'Angelo, A. Incicchitti, D. V. Kasperovych, V. V. Kobychev, S. I. Konovalov, M. Laubenstein, D. V. Poda, O. G. Polischuk, V. N. Shlegel, V. I. Tretyak, V. I. Umatov, and Y. V. Vasiliev, Phys. Rev. D **98**, 092007 (2018).

[57] D. Q. Adams, C. Alduino, K. Alfonso, F. T. Avignone, O. Azzolini, G. Bari, F. Bellini, G. Benato, M. Biassoni, A. Branca, *et al.*, Phys. Rev. Lett. **126**, 171801 (2021).

[58] D. Q. Adams, C. Alduino, K. Alfonso, F. T. Avignone, O. Azzolini, G. Bari, F. Bellini, G. Benato, M. Biassoni, A. Branca, *et al.*, Phys. Rev. Lett. **131**, 249902 (2023).

[59] J. B. Albert, M. Auger, D. J. Auty, P. S. Barbeau, E. Beauchamp, D. Beck, V. Belov, C. Benitez-Medina, J. Bonatt, M. Breidenbach, *et al.* (EXO Collaboration), Phys. Rev. C **89**, 015502 (2014).

[60] R. Arnold, C. Augier, J. D. Baker, A. S. Barabash, A. Basharina-Freshville, S. Blondel, S. Blot, M. Bongrand, V. Brudanin, J. Busto, *et al.* (NEMO-3 Collaboration), Phys. Rev. D **94**, 072003 (2016).

[61] A. L. Turkevich, T. E. Economou, and G. A. Cowan, Phys. Rev. Lett. **67**, 3211 (1991).

[62] J. H. Thies *et al.*, Phys. Rev. C **86**, 044309 (2012).

[63] M. Doi, T. Kotani, and E. Takasugi, Progress of Theoretical Physics Supplement **83**, 1 (1985).

[64] W. Haxton and G. Stephenson, Progress in Particle and Nuclear Physics **12**, 409 (1984).

[65] J. Suhonen and O. Civitarese, Physics Reports **300**, 123 (1998).

[66] A. Faessler and F. Simkovic, Journal of Physics G: Nuclear and Particle Physics **24**, 2139 (1998).

[67] J. D. Vergados, H. Ejiri, and F. Šimkovic, International Journal of Modern Physics E **25**, 1630007 (2016).

[68] V. Cirigliano, W. Dekens, J. de Vries, M. L. Graesser, and E. Mereghetti, Journal of High Energy Physics **2018**, 97 (2018).

[69] L. Graf, F. F. Deppisch, F. Iachello, and J. Kotila, Phys. Rev. D **98**, 095023 (2018).

[70] F. F. Deppisch, M. Hirsch, and H. Päs, Journal of Physics G: Nuclear and Particle Physics **39**, 124007 (2012).

[71] W. Rodejohann, Journal of Physics G: Nuclear and Particle Physics **39**, 124008 (2012).

[72] D. Štefánik, R. Dvornický, F. Šimkovic, and P. Vogel, Phys. Rev. C **92**, 055502 (2015).

[73] M. Horoi and A. Neacsu, Phys. Rev. D **93**, 113014 (2016).

[74] J. Engel and J. Menéndez, Reports on Progress in Physics **80**, 046301 (2017).

[75] F. Šimkovic, P. Domin, and S. V. Semenov, Journal of Physics G: Nuclear and Particle Physics **27**, 2233 (2001).

[76] P. Domin, S. Kovalenko, F. Šimkovic, and S. Semenov, Nuclear Physics A **753**, 337 (2005).

[77] A. Neacsu and M. Horoi, Advances in High Energy Physics **2016**, 1903767 (2016).

[78] F. Šimkovic, R. Dvornický, D. Štefánik, and A. Faessler, Phys. Rev. C **97**, 034315 (2018).

[79] L. Gráf, M. Lindner, and O. Scholer, Phys. Rev. D **106**, 035022 (2022).

[80] O. Scholer, J. de Vries, and L. Gráf, Journal of High Energy Physics **2023**, 43 (2023).

[81] E. Aprile *et al.*, Journal of Cosmology and Astroparticle Physics **2020** (11), 031.

[82] D. S. Akerib *et al.* (LUX-ZEPLIN Collaboration), Phys. Rev. D **101**, 052002 (2020).

[83] J. Aalbers, F. Agostini, M. Alfonsi, F. Amaro, C. Amsler, E. Aprile, *et al.* (DARWIN Collaboration), Journal of Cosmology and Astroparticle Physics **2016** (11), 017.

[84] J. Aalbers, S. S. AbdusSalam, K. Abe, V. Aerne, F. Agostini, S. A. Maouloud, *et al.* (DARWIN Collaboration), Journal of Physics G: Nuclear and Particle Physics **50**, 013001 (2022).

[85] C. Adams *et al.*, Neutrinoless double beta decay, https://arxiv.org/pdf/2212.11099.pdf (2022).

[86] E. Bossio and M. Agostini, Journal of Physics G: Nuclear and Particle Physics **51**, 023001 (2023).

[87] F. F. Deppisch, L. Graf, and F. Šimkovic, Phys. Rev. Lett. **125**, 171801 (2020).

[88] F. F. Deppisch, L. Graf, W. Rodejohann, and X.-J. Xu, Phys. Rev. D **102**, 051701 (2020).

[89] A. Barabash, A. Dolgov, R. Dvornický, F. Šimkovic, and A. Smirnov, Nuclear Physics B **783**, 90 (2007).

[90] J. S. Díaz, Phys. Rev. D **89**, 036002 (2014).

[91] O. Nitescu, S. Ghinescu, and S. Stoica, Journal of Physics G: Nuclear and Particle Physics **47**, 055112 (2020).

[92] O. V. Nitescu, S. A. Ghinescu, M. Mirea, and S. Stoica, Phys. Rev. D **103**, L031701 (2021).

[93] S. A. Ghinescu, O. Nitescu, and S. Stoica, Phys. Rev. D **105**, 055032 (2022).

[94] P. D. Bolton, F. F. Deppisch, L. Gráf, and F. Šimkovic, Phys. Rev. D **103**, 055019 (2021).

[95] M. Agostini, E. Bossio, A. Ibarra, and X. Marcano, Physics Letters B **815**, 136127 (2021).

[96] R. Mohapatra and E. Takasugi, Physics Letters B **211**, 192 (1988).

[97] Z. Berezhiani, A. Smirnov, and J. Valle, Physics Letters B **291**, 99 (1992).

[98] C. Burgess and J. Cline, Physics Letters B **298**, 141 (1993).

[99] C. D. Carone, Physics Letters B **308**, 85 (1993).

[100] C. P. Burgess and J. M. Cline, Phys. Rev. D **49**, 5925 (1994).

[101] P. Bamert, C. Burgess, and R. Mohapatra, Nuclear Physics B **449**, 25 (1995).

[102] M. Hirsch, H. Klapdor-Kleingrothaus, S. Kovalenko, and H. Päs, Physics Letters B **372**, 8 (1996).

[103] R. Mohapatra, A. Pérez-Lorenzana, and C. de S. Pires, Physics Letters B **491**, 143 (2000).

[104] J. Kotila, J. Barea, and F. Iachello, Phys. Rev. C **91**, 064310 (2015).

[105] R. Cepedello, F. F. Deppisch, L. González, C. Hati, and M. Hirsch, Phys. Rev. Lett. **122**, 181801 (2019).

[106] J. Kotila and F. Iachello, Phys. Rev. C **103**, 044302 (2021).

[107] R. Arnold, C. Augier, A. S. Barabash, A. Basharina-Freshville, S. Blondel, S. Blot, M. Bongrand, D. Boursette, V. Brudanin, J. Busto, *et al.* (NEMO-3 Collaboration), Phys. Rev. Lett. **119**, 041801 (2017).

[108] R. Arnold *et al.*, The European Physical Journal C **79**, 440 (2019).

[109] R. Arnold, C. Augier, J. Baker, A. S. Barabash, A. Basharina-Freshville, M. Bongrand, V. Brudanin, A. J. Caffrey, S. Cebrián, A. Chapon, *et al.*, The European Physical Journal C **70**, 927 (2010).

[110] P. Ferrario, A. Laing, N. López-March, J. J. Gómez-Cadenas, V. Álvarez, C. D. R. Azevedo, F. I. G. Borges, S. Cárcel, S. Cebrián, A. Cervera, *et al.* (The NEXT collaboration), Journal of High Energy Physics **2016**, 104 (2016).

[111] Y. Fukuda, T. Hayakawa, E. Ichihara, K. Inoue, K. Ishihara, H. Ishino, Y. Itow, T. Kajita, J. Kameda, S. Kasuga, *et al.* (Super-Kamiokande Collaboration), Phys. Rev. Lett. **81**, 1562 (1998).

[112] Y. Fukuda, T. Hayakawa, E. Ichihara, K. Inoue, K. Ishihara, H. Ishino, Y. Itow, T. Kajita, J. Kameda, S. Kasuga, *et al.* (Super-Kamiokande Collaboration), Phys. Rev. Lett. **82**, 1810 (1999).

[113] S. Fukuda, Y. Fukuda, M. Ishitsuka, Y. Itow, T. Kajita, J. Kameda, K. Kaneyuki, K. Kobayashi, Y. Koshio, M. Miura, *et al.* (Super-Kamiokande Collaboration), Phys. Rev. Lett. **85**, 3999 (2000).

[114] S. Fukuda, Y. Fukuda, M. Ishitsuka, Y. Itow, T. Kajita, J. Kameda, K. Kaneyuki, K. Kobayashi, Y. Koshio, M. Miura, *et al.* (Super-Kamiokande Collaboration), Phys. Rev. Lett. **86**, 5651 (2001).

[115] B. T. Cleveland, T. Daily, J. Raymond Davis, J. R. Distel, K. Lande, C. K. Lee, P. S. Wildenhain, and J. Ullman, The Astrophysical Journal **496**, 505 (1998).

[116] W. Hampel, J. Handt, G. Heusser, J. Kiko, T. Kirsten, M. Laubenstein, E. Pernicka, W. Rau, M. Wojcik, Y. Zakharov, *et al.*, Physics Letters B **447**, 127 (1999).

[117] J. N. Abdurashitov, V. N. Gavrin, S. V. Girin, V. V. Gorbachev, T. V. Ibragimova, A. V. Kalikhov, N. G. Khairnasov, T. V. Knodel, I. N. Mirmov, A. A. Shikhin, *et al.* (SAGE Collaboration), Phys. Rev. C **60**, 055801 (1999).

[118] Q. R. Ahmad, R. C. Allen, T. C. Andersen, J. D. Anglin, G. Bühler, J. C. Barton, E. W. Beier, M. Bercovitch, J. Bigu, S. Biller, *et al.* (SNO Collaboration), Phys. Rev. Lett. **87**, 071301 (2001).

[119] Q. R. Ahmad, R. C. Allen, T. C. Andersen, J. D. Anglin, J. C. Barton, E. W. Beier, M. Bercovitch, J. Bigu, S. D. Biller, R. A. Black, *et al.* (SNO Collaboration), Phys. Rev. Lett. **89**, 011302 (2002).

[120] Q. R. Ahmad, R. C. Allen, T. C. Andersen, J. D.Anglin, J. C. Barton, E. W. Beier, M. Bercovitch, J. Bigu, S. D. Biller, R. A. Black, *et al.* (SNO Collaboration), Phys. Rev. Lett. **89**, 011301 (2002).

[121] G. L. Fogli, E. Lisi, A. Marrone, D. Montanino, and A. Palazzo, Phys. Rev. D **66**, 053010 (2002).

[122] K. Eguchi, S. Enomoto, K. Furuno, J. Goldman, H. Hanada, H. Ikeda, K. Ikeda, K. Inoue, K. Ishihara, W. Itoh, *et al.* (KamLAND Collaboration), Phys. Rev. Lett. **90**, 021802 (2003).

[123] F. Capozzi, E. Di Valentino, E. Lisi, A. Marrone, A. Melchiorri, and A. Palazzo, Phys. Rev. D **95**, 096014 (2017).

[124] M. Aker, A. Beglarian, J. Behrens, A. Berlev, U. Besserer, F. Bieringer, B. Block, *et al.* (The KATRIN Collaboration), Nature Physics **18**, 160 (2022).

[125] Aghanim, N. *et al.* (Planck Collaboration), A&A **641**, A6 (2020).

[126] S. Alam, M. Aubert, S. Avila, C. Balland, J. E. Bautista, M. A. Bershady, D. Bizyaev, M. R. Blanton, A. S. Bolton, J. Bovy, *et al.*, Phys. Rev. D **103**, 083533 (2021).

[127] E. Ferri, D. Bagliani, M. Biasotti, G. Ceruti, D. Corsini, M. Faverzani, F. Gatti, A. Giachero, C. Gotti, C. Kilbourne, A. Kling, M. Maino, P. Manfrinetti, A. Nucciotti, G. Pessina, G. Pizzigoni, M. R. Gomes, and M. Sisti, Physics Procedia **61**, 227 (2015), 13th International Conference on Topics in Astroparticle and Underground Physics, TAUP 2013.

[128] R. Dvornický, K. Muto, F. Šimkovic, and A. Faessler, Phys. Rev. C **83**, 045502 (2011).

[129] E. G. Myers, A. Wagner, H. Kracke, and B. A. Wesson, Phys. Rev. Lett. **114**, 013003 (2015).

[130] P. Filianin, C. Lyu, M. Door, K. Blaum, W. J. Huang, M. Haverkort, P. Indelicato, C. H. Keitel, K. Kromer, D. Lange, Y. N. Novikov, A. Rischka, R. X. Schüssler, C. Schweiger, S. Sturm, S. Ulmer, Z. Harman, and S. Eliseev, Phys. Rev. Lett. **127**, 072502 (2021).

[131] S. Eliseev, K. Blaum, M. Block, S. Chenmarev, H. Dorrer, C. E. Düllmann, C. Enss, P. E. Filianin, L. Gastaldo, M. Goncharov, U. Köster, F. Lautenschläger, Y. N. Novikov, A. Rischka, R. X. Schüssler, L. Schweikhard, and A. Türler, Phys. Rev. Lett. **115**, 062501 (2015).

[132] N. D. Gamage, R. Bhandari, M. Horana Gamage, R. Sandler, and M. Redshaw, Hyperfine Interactions **240**, 10.1007/s10751-019-1588-5 (2019).

[133] M. Redshaw, The European Physical Journal A **59**, 18 (2023).

[134] D. K. Keblbeck, R. Bhandari, N. D. Gamage, M. Horana Gamage, K. G. Leach, X. Mougeot, and M. Redshaw, Phys. Rev. C **107**, 015504 (2023).

[135] V. N. Aseev, A. I. Belesev, A. I. Berlev, E. V. Geraskin, A. A. Golubev, N. A. Likhovid, V. M. Lobashev, A. A. Nozik, V. S. Pantuev, V. I. Parfenov, A. K. Skasyrskaya, F. V. Tkachov, and S. V. Zadorozhny, Phys. Rev. D **84**, 112003 (2011).

[136] C. P. Kraus *et al.*, The European Physical Journal C - Particles and Fields **40**, 10.1140/epjc/s2005-02139-7 (2005).

[137] A. Ashtari Esfahani, S. Böser, N. Buzinsky, M. C. Carmona-Benitez, C. Claessens, L. de Viveiros, P. J. Doe, M. Fertl, J. A. Formaggio, J. K. Gaison, L. Gladstone, M. Grando, M. Guigue, J. Hartse, K. M. Heeger, X. Huyan, J. Johnston, A. M. Jones, K. Kazkaz, B. H. LaRoque, M. Li, A. Lindman, E. Machado, A. Marsteller, C. Matthé,

R. Mohiuddin, B. Monreal, R. Mueller, J. A. Nikkel, E. Novitski, N. S. Oblath, J. I. Peña, W. Pettus, R. Reimann, R. G. H. Robertson, D. Rosa De Jesús, G. Rybka, L. Saldaña, M. Schram, P. L. Slocum, J. Stachurska, Y.-H. Sun, P. T. Surukuchi, J. R. Tedeschi, A. B. Telles, F. Thomas, M. Thomas, L. A. Thorne, T. Thümmler, L. Tvrznikova, W. Van De Pontseele, B. A. VanDevender, J. Weintroub, T. E. Weiss, T. Wendler, A. Young, E. Zayas, and A. Ziegler (Project 8 Collaboration), Phys. Rev. Lett. **131**, 102502 (2023).

[138] S. Abe, S. Asami, M. Eizuka, S. Futagi, A. Gando, Y. Gando, *et al.* (KamLAND-Zen Collaboration), Phys. Rev. Lett. **130**, 051801 (2023).

[139] E. Di Valentino, A. Melchiorri, and J. Silk, Phys. Rev. D **92**, 121302 (2015).

[140] A. Boyle and E. Komatsu, Journal of Cosmology and Astroparticle Physics **2018** (03), 035.

[141] M. Agostini, G. R. Araujo, A. M. Bakalyarov, M. Balata, I. Barabanov, L. Baudis, *et al.* (GERDA Collaboration), Phys. Rev. Lett. **125**, 252502 (2020).

[142] D. Q. Adams, C. Alduino, K. Alfonso, F. T. Avignone, O. Azzolini, G. Bari, F. Bellini, G. Benato, M. Beretta, M. Biassoni, *et al.* (The CUORE Collaboration), Nature **604**, 53 (2022).

[143] X. Mougeot, M.-M. Bé, C. Bisch, and M. Loidl, Phys. Rev. A **86**, 042506 (2012).

[144] X. Mougeot and C. Bisch, Phys. Rev. A **90**, 012501 (2014).

[145] S. J. Haselschwardt, J. Kostensalo, X. Mougeot, and J. Suhonen, Phys. Rev. C **102**, 065501 (2020).

[146] A. Nucciotti, Journal of Low Temperature Physics **151**, 597 (2008).

[147] J. A. Formaggio, A. L. C. de Gouvêa, and R. H. Robertson, Physics Reports **914**, 1 (2021), direct measurements of neutrino mass.

[148] D. Wilkinson, Nuclear Physics A **526**, 131 (1991).

[149] M. Kleesiek, J. Behrens, G. Drexlin, K. Eitel, M. Erhard, J. A. Formaggio, F. Glück, S. Groh, M. Hötzel, S. Mertens, A. W. P. Poon, C. Weinheimer, and K. Valerius, The European Physical Journal C **79**, 204 (2019).

[150] M. R. Harston and N. C. Pyper, Phys. Rev. A **45**, 6282 (1992).

[151] N. C. Pyper and M. R. Harston, Proc. R. Soc. Lond. A **420**, 277 (1998).

[152] J. N. Bahcall, Phys. Rev. **129**, 2683 (1963).

[153] W. C. Haxton, Phys. Rev. Lett. **55**, 807 (1985).

[154] H. F. Schopper, *Weak Interactions and Nuclear β Decay* (North-Holland, 1966).

[155] M. E. Rose, *Relativistic electron theory* (John Wiley and Sons, 1961).

[156] E. Aprile *et al.* (XENON Collaboration), Phys. Rev. D **102**, 072004 (2020).

[157] M. Loidl, M. Rodrigues, C. Le-Bret, and X. Mougeot, Applied Radiation and Isotopes **87**, 302 (2014), proceedings of the 19th International Conference on Radionuclide Metrology and its Applications 17–21 June 2013, Antwerp, Belgium.

[158] M. Loidl, J. Beyer, L. Bockhorn, C. Enss, S. Kempf, K. Kossert, R. Mariam, O. Nähle, M. Paulsen, P. Ranitzsch, M. Rodrigues, and M. Schmidt, Applied Radiation and Isotopes **153**, 108830 (2019).

[159] K. Kossert, M. Loidl, X. Mougeot, M. Paulsen, P. Ranitzsch, and M. Rodrigues, Applied Radiation and Isotopes **185**, 110237 (2022).

[160] J. Johansson, H. Sherif, and F. Ghoddoussi, Nuclear Physics A **665**, 403 (2000).

[161] A. Faessler, L. Gastaldo, and F. Šimkovic, Phys. Rev. C **95**, 045502 (2017).

[162] M. Wang, G. Audi, F. G. Kondev, W. Huang, S. Naimi, and X. Xu, Chinese Physics C **41**, 030003 (2017).

[163] F. E. Wietfeldt, E. B. Norman, Y. D. Chan, M. T. F. da Cruz, A. García, E. E. Haller, W. L. Hansen, M. M. Hindi, R.-M. Larimer, K. T. Lesko, P. N. Luke, R. G. Stokstad, B. Sur, and I. Žlimen, Phys. Rev. C **52**, 1028 (1995).

[164] M. Loidl, J. Beyer, L. Bockhorn, *et al.*, Journal of Low Temperature Physics **199**, 451 (2020).

[165] O. Niţescu, S. Stoica, and F. Šimkovic, Exchange correction for allowed β-decay (2022).

[166] L. Hayen, S. Simonucci, and S. Taioli, Detailed β spectrum calculations of ^{214}Pb for new physics searches in liquid xenon (2020).

[167] X. Mougeot, Phys. Rev. C **91**, 055504 (2015).

[168] O. Niţescu, S. Stoica, and F. Šimkovic, Phys. Rev. C **107**, 025501 (2023).

[169] S. Zhang, X. Mougeot, H.-R. Liu, K. Han, T. Sun, W.-T. Wu, R. Cantor, J.-K. Xia, J.-C. Liang, F.-Y. Fan, B.-J. Wu, L. Zhang, M.-Y. Ge, X. Zhou, and Z. Liu, Precise determination of ^{210}pb β decay spectrum at 0 kev and its implication to theoretical calculations (2023), arXiv:2307.16276 [nucl-ex] .

[170] M. Paulsen, P. C.-O. Ranitzsch, M. Loidl, M. Rodrigues, K. Kossert, X. Mougeot, A. Singh, S. Leblond, J. Beyer, L. Bockhorn, C. Enss, M. Wegner, S. Kempf, and O. Nähle, Phys. Rev. C **110**, 055503 (2024).

[171] `https://cea.hal.science/cea-01848119/document`, accessed: 2024-12-30.

[172] O. Niţescu, R. Dvornický, and F. Šimkovic, Phys. Rev. C **109**, 025501 (2024).

[173] O. Niţescu, R. Dvornický, and F. Šimkovic, Atomic corrections for the unique first forbidden β transition of ^{187}re (2023).

[174] P. Mŏller, A. Sierk, T. Ichikawa, and H. Sagawa, Atomic Data and Nuclear Data Tables **109-110**, 1 (2016).

[175] A. Sirlin, Phys. Rev. **164**, 1767 (1967).

[176] A. Sirlin and A. Ferroglia, Rev. Mod. Phys. **85**, 263 (2013).

[177] X. Mougeot, Applied Radiation and Isotopes **201**, 111018 (2023).

[178] M. Basunia, Nuclear Data Sheets **110**, 999 (2009).

[179] O. Nițescu, R. Dvornický, S. Stoica, and F. Šimkovic, Universe **7**, 10.3390/universe7050147 (2021).

[180] P. A. Zyla *et al.* (Particle Data Group), Progress of Theoretical and Experimental Physics **2020**, 10.1093/ptep/ptaa104 (2020).

[181] T. Tomoda, Reports on Progress in Physics **54**, 53 (1991).

[182] J. T. Suhonen, Frontiers in Physics **5**, 10.3389/fphy.2017.00055 (2017).

[183] J. Abad, A. Morales, R. Núñez-Lagos, and A. F. Pacheco, Il Nuovo Cimento A (1965-1970) **75**, 173 (1983).

[184] J. Abad, A. Morales, R. Núñez-Lagos, and A. Pacheco, Journal de Physique Colloques **45**, C3 (1984).

[185] O. Azzolini *et al.*, Phys. Rev. Lett. **123**, 262501 (2019).

[186] A. Gando *et al.* (KamLAND-Zen Collaboration), Phys. Rev. Lett. **122**, 192501 (2019).

[187] O. Nițescu and F. Šimkovic, Radiative and exchange corrections for two-neutrino double-beta decay (2024).

[188] S. Rahaman *et al.*, Physics Letters B **662**, 111 (2008).

[189] B. Singh and J. Chen, Nuclear Data Sheets **172**, 1 (2021).

[190] J. Suhonen, T. Taigel, and A. Faessler, Nuclear Physics A **486**, 91 (1988).

[191] O. Nițescu, R. Dvornický, and F. Šimkovic, AIP Conference Proceedings **3138**, 020019 (2024).

[192] J. Kotila and F. Iachello, Phys. Rev. C **85**, 034316 (2012).

[193] S. Stoica and M. Mirea, Phys. Rev. C **88**, 037303 (2013).

[194] M. Mirea, T. Pahomi, and S. Stoica, Romanian Reports in Physics **67**, 872 (2015).

[195] S. Stoica and M. Mirea, Frontiers in Physics **7**, 10.3389/fphy.2019.00012 (2019).

[196] S. Basu and A. Sonzogni, Nuclear Data Sheets **114**, 435 (2013).

[197] M. Wang, W. Huang, F. Kondev, G. Audi, and S. Naimi, Chinese Physics C **45**, 030003 (2021).

[198] N. Nica, Nuclear Data Sheets **117**, 1 (2014).

[199] F. Šimkovic, V. Rodin, A. Faessler, and P. Vogel, Phys. Rev. C **87**, 045501 (2013).

[200] R. Machleidt, F. Sammarruca, and Y. Song, Phys. Rev. C **53**, R1483 (1996).

[201] M. S. Yousef, V. Rodin, A. Faessler, and F. Šimkovic, Nuclear Physics B - Proceedings Supplements **188**, 56 (2009), proceedings of the Neutrino Oscillation Workshop.

[202] F. Šimkovic, L. Pacearescu, and A. Faessler, Nuclear Physics A **733**, 321 (2004).

[203] J. Schwieger, F. Simkovic, A. Faessler, and W. A. Kaminski, Journal of Physics G: Nuclear and Particle Physics **23**, 1647 (1997).

[204] D.-L. Fang and A. Faessler, Chinese Physics C **44**, 084104 (2020).

[205] F. Šimkovic, M. Nowak, W. A. Kamiński, A. A. Raduta, and A. Faessler, Phys. Rev. C **64**, 035501 (2001).

[206] F. Šimkovic, A. Smetana, and P. Vogel, Phys. Rev. C **98**, 064325 (2018).

[207] F. Salvat and J. M. Fernández-Varea, Computer Physics Communications **240**, 165 (2019).

[208] A. S. Barabash, P. Hubert, A. Nachab, and V. I. Umatov, Phys. Rev. C **79**, 045501 (2009).

[209] B. Märkisch, H. Mest, H. Saul, X. Wang, H. Abele, D. Dubbers, M. Klopf, A. Petoukhov, C. Roick, T. Soldner, and D. Werder, Phys. Rev. Lett. **122**, 242501 (2019).

[210] J. G. Hirsch, O. Castaños, P. O. Hess, and O. Civitarese, Nuclear Physics A **589**, 445 (1995).

[211] C. M. Raduta and A. A. Raduta, Phys. Rev. C **76**, 044306 (2007).

[212] A. A. Raduta, C. M. Raduta, and R. Poenaru, Phys. Rev. C **106**, 044301 (2022).

[213] J. Yao, J. Meng, Y. Niu, and P. Ring, Progress in Particle and Nuclear Physics **126**, 103965 (2022).

[214] V. B. Beresteckij, E. M. Lifshitz, and L. P. Pitaevskij, *Quantum Electrodynamics* (Nauka, 1989).

[215] S. Bustabad, G. Bollen, M. Brodeur, D. L. Lincoln, S. J. Novario, M. Redshaw, R. Ringle, S. Schwarz, and A. A. Valverde, Phys. Rev. C **88**, 022501 (2013).

[216] B. J. Mount, M. Redshaw, and E. G. Myers, Phys. Rev. C **81**, 032501 (2010).

[217] D. L. Lincoln, J. D. Holt, G. Bollen, M. Brodeur, S. Bustabad, J. Engel, S. J. Novario, M. Redshaw, R. Ringle, and S. Schwarz, Phys. Rev. Lett. **110**, 012501 (2013).

[218] M. Alanssari *et al.*, Phys. Rev. Lett. **116**, 072501 (2016).

[219] D. Fink, J. Barea, D. Beck, K. Blaum, C. Böhm, C. Borgmann, M. Breitenfeldt, F. Herfurth, A. Herlert, J. Kotila, M. Kowalska, S. Kreim, D. Lunney, S. Naimi, M. Rosenbusch, S. Schwarz, L. Schweikhard, F. Šimkovic, J. Stanja, and K. Zuber, Phys. Rev. Lett. **108**, 062502 (2012).

[220] S. Rahaman *et al.*, Physics Letters B **703**, 412 (2011).

[221] M. Redshaw, B. J. Mount, E. G. Myers, and F. T. Avignone, Phys. Rev. Lett. **102**, 212502 (2009).

[222] M. Redshaw, E. Wingfield, J. McDaniel, and E. G. Myers, Phys. Rev. Lett. **98**, 053003 (2007).

[223] V. S. Kolhinen, T. Eronen, D. Gorelov, J. Hakala, A. Jokinen, A. Kankainen, I. D. Moore, J. Rissanen, A. Saastamoinen, J. Suhonen, and J. Äystö, Phys. Rev. C **82**, 022501 (2010).

[224] E. G. Drukarev, M. Y. Amusia, and L. V. Chernysheva, Phys. Rev. C **94**, 035504 (2016).

[225] M. I. Krivoruchenko and K. S. Tyrin, The European Physical Journal A **56**, 16 (2020).

[226] M. I. Krivoruchenko, K. S. Tyrin, and F. F. Karpeshin, JETP Letters **117**, 884 (2023).

[227] J. A. Detwiler and R. G. H. Robertson, Phys. Rev. C **107**, L042501 (2023).

[228] G. Parzen, Phys. Rev. **80**, 261 (1950).

[229] O. Niţescu, S. Ghinescu, and F. Šimkovic, Universe **10**, 10.3390/universe10120442 (2024).

[230] H. Primakoff and S. P. Rosen, Reports on Progress in Physics **22**, 121 (1959).

[231] H. Primakoff and S. P. Rosen, Proceedings of the Physical Society **78**, 464 (1961).

[232] J. Vergados, Nuclear Physics B **218**, 109 (1983).

[233] C. W. Kim and K. Kubodera, Phys. Rev. D **27**, 2765 (1983).

[234] F. Boehm and P. Vogel, *Physics of Massive Neutrinos* (Cambridge University Press, 1992).

[235] J. Kotila and F. Iachello, Phys. Rev. C **87**, 024313 (2013).

[236] M. Horoi, S. Stoica, and B. A. Brown, Phys. Rev. C **75**, 034303 (2007).

[237] R. A. Sen'kov, M. Horoi, and B. A. Brown, Phys. Rev. C **89**, 054304 (2014).

[238] R. A. Sen'kov and M. Horoi, Phys. Rev. C **93**, 044334 (2016).

[239] A. Neacsu and M. Horoi, Phys. Rev. C **91**, 024309 (2015).

[240] M. Horoi and A. Neacsu, Phys. Rev. C **93**, 024308 (2016).

[241] M. Horoi, Physics **4**, 1135 (2022).

[242] J. Suhonen, Journal of Physics G: Nuclear and Particle Physics **40**, 075102 (2013).

[243] P. Pirinen and J. Suhonen, Phys. Rev. C **91**, 054309 (2015).

[244] G. Martínez-Lema, M. Martínez-Vara, M. Sorel, C. Adams, V. Álvarez, L. Arazi, *et al.* (The NEXT collaboration), Journal of High Energy Physics **2021**, 1029 (2021).

[245] O. Niţescu, S. Ghinescu, S. Stoica, and F. Šimkovic, Universe **10**, 10.3390/universe10020098 (2024).

[246] E. Coello Pérez, J. Menéndez, and A. Schwenk, Physics Letters B **797**, 134885 (2019).

[247] V. A. Sevestrean, O. Niţescu, S. Ghinescu, and S. Stoica, Phys. Rev. A **108**, 012810 (2023).

[248] W. Lotz, J. Opt. Soc. Am. **60**, 206 (1970).

[249] A. S. Barabash, Journal of Experimental and Theoretical Physics Letters **68**, 1 (1998).

[250] A. S. Barabash, Physics of Atomic Nuclei **63**, 1210 (2000).

[251] A. S. Barabash, Astrophysics and Space Science **283**, 607 (2003).

[252] X. Yan *et al.*, Searching for two-neutrino and neutrinoless double beta decay of ^{134}xe with the pandax-4t experiment (2023), arXiv:2312.15632 [nucl-ex] .

[253] A. Barabash, Universe **6**, 10.3390/universe6100159 (2020).

[254] S. Eliseev, C. Roux, K. Blaum, M. Block, C. Droese, F. Herfurth, H.-J. Kluge, M. I. Krivoruchenko, Y. N. Novikov, E. Minaya Ramirez, L. Schweikhard, V. M. Shabaev, F. Šimkovic, I. I. Tupitsyn, K. Zuber, and N. A. Zubova, Phys. Rev. Lett. **106**, 052504 (2011).

[255] M. Krivoruchenko, F. Šimkovic, D. Frekers, and A. Faessler, Nuclear Physics A **859**, 140 (2011).

[256] K. Blaum, S. Eliseev, F. A. Danevich, V. I. Tretyak, S. Kovalenko, M. I. Krivoruchenko, Y. N. Novikov, and J. Suhonen, Rev. Mod. Phys. **92**, 045007 (2020).

[257] F. Šimkovic, R. Dvornický, and P. Vogel, Phys. Rev. C **102**, 034301 (2020).

[258] I. Angeli and K. Marinova, Atomic Data and Nuclear Data Tables **99**, 69 (2013).

[259] D. A. Nesterenko, K. Blaum, M. Block, C. Droese, S. Eliseev, F. Herfurth, E. Minaya Ramirez, Y. N. Novikov, L. Schweikhard, V. M. Shabaev, M. V. Smirnov, I. I. Tupitsyn, K. Zuber, and N. A. Zubova, Phys. Rev. C **86**, 044313 (2012).

[260] C. Qi and Z. X. Xu, Phys. Rev. C **86**, 044323 (2012).

[261] L. Coraggio, L. De Angelis, T. Fukui, A. Gargano, N. Itaco, and F. Nowacki, Phys. Rev. C **100**, 014316 (2019).

[262] S. R. Stroberg, Particles **4**, 521 (2021).

[263] P. Gysbers, G. Hagen, J. D. Holt, G. R. Jansen, T. D. Morris, P. Navrátil, T. Papenbrock, S. Quaglioni, A. Schwenk, S. R. Stroberg, and K. A. Wendt, Nature Physics **15**, 428 (2019).

[264] A. Faessler, G. L. Fogli, E. Lisi, V. Rodin, A. M. Rotunno, and F. Šimkovic, Journal of Physics G: Nuclear and Particle Physics **35**, 075104 (2008).

[265] National nuclear data center (2024).

[266] O. Niţescu, S. Ghinescu, V. A. Sevestrean, M. Horoi, F. Šimkovic, and S. Stoica, Journal of Physics G: Nuclear and Particle Physics **51**, 125103 (2024).

[267] R. G. Winter, Phys. Rev. **85**, 687 (1952).

[268] X. Yan, Z. Cheng, A. Abdukerim, Z. Bo, W. Chen, X. Chen, C. Cheng, X. Cui, Y. Fan, D. Fang, *et al.* (PandaX Collaboration), Phys. Rev. Lett. **132**, 152502 (2024).

[269] P. Belli, R. Bernabei, V. Brudanin, F. Cappella, V. Caracciolo, R. Cerulli, F. A. Danevich, A. Incicchitti, D. Kasperovych, V. Klavdiienko, V. Kobychev, V. Merlo, O. Polischuk, V. Tretyak, and M. Zarytskyy, Universe **6**, 10.3390/universe6100182 (2020).

[270] P. Vogel and M. R. Zirnbauer, Phys. Rev. Lett. **57**, 3148 (1986).

[271] O. Civitarese, A. Faessler, and T. Tomoda, Physics Letters B **194**, 11 (1987).

[272] M. Aunola and J. Suhonen, Nuclear Physics A **602**, 133 (1996).

[273] M. Aunola, O. Civitarese, J. Kauhanen, and J. Suhonen, Nuclear Physics A **596**, 187 (1996).

[274] S. Stoica and H. Klapdor-Kleingrothaus, Nuclear Physics A **694**, 269 (2001).

[275] S. Stoica and H. Klapdor-Kleingrothaus, The European Physical Journal A - Hadrons and Nuclei **17**, 529 (2003).

[276] R. Álvarez-Rodríguez, P. Sarriguren, E. MoyadeGuerra, L. Pacearescu, A. Faessler, and F. Šimkovic, Phys. Rev. C **70**, 064309 (2004).

[277] V. Rodin, A. Faessler, F. Šimkovic, and P. Vogel, Nuclear Physics A **766**, 107 (2006).

[278] J. Suhonen and O. Civitarese, Journal of Physics G: Nuclear and Particle Physics **39**, 085105 (2012).

[279] E. Caurier, F. Nowacki, A. Poves, and J. Retamosa, Phys. Rev. Lett. **77**, 1954 (1996).

[280] E. Caurier, G. Martínez-Pinedo, F. Nowack, A. Poves, and A. P. Zuker, Rev. Mod. Phys. **77**, 427 (2005).

[281] E. Caurier, F. Nowacki, and A. Poves, Physics Letters B **711**, 62 (2012).

[282] B. A. Brown, D. L. Fang, and M. Horoi, Phys. Rev. C **92**, 041301(R) (2015).

[283] J. Kostensalo and J. Suhonen, Physics Letters B **802**, 135192 (2020).

[284] D. Patel, P. C. Srivastava, V. Kota, and R. Sahu, Nuclear Physics A **1042**, 122808 (2024).

[285] J. Barea, J. Kotila, and F. Iachello, Phys. Rev. C **87**, 014315 (2013).

[286] J. Barea, J. Kotila, and F. Iachello, Phys. Rev. C **91**, 034304 (2015).

[287] K. Nomura, Phys. Rev. C **105**, 044301 (2022).

[288] K. Nomura, Phys. Rev. C **110**, 024304 (2024).

[289] P. K. Rath, R. Chandra, K. Chaturvedi, and P. K. Raina, Frontiers in Physics **7**, 10.3389/fphy.2019.00064 (2019).

[290] H. Ejiri, Journal of the Physical Society of Japan **74**, 2101 (2005).

[291] H. Ejiri, Journal of Physics G: Nuclear and Particle Physics **44**, 115201 (2017).

[292] E. A. Coello Pérez, J. Menéndez, and A. Schwenk, Phys. Rev. C **98**, 045501 (2018).

[293] J. Kotila, J. Suhonen, and D. S. Delion, Journal of Physics G: Nuclear and Particle Physics **37**, 015101 (2009).

[294] N. Popara, A. Ravlić, and N. Paar, Phys. Rev. C **105**, 064315 (2022).

[295] Y. Ren and Z. Ren, Phys. Rev. C **89**, 064603 (2014).

[296] M. K. P. Rajan, R. K. Biju, and K. P. Santhosh, Indian Journal of Physics **92**, 893 (2018).

[297] B. Pritychenko, Nuclear Physics A **1033**, 122628 (2023).

[298] S. Novario, P. Gysbers, J. Engel, G. Hagen, G. R. Jansen, T. D. Morris, P. Navrátil, T. Papenbrock, and S. Quaglioni, Phys. Rev. Lett. **126**, 182502 (2021).

[299] L. Coraggio, N. Itaco, G. De Gregorio, A. Gargano, Z. H. Cheng, Y. Z. Ma, F. R. Xu, and M. Viviani, Phys. Rev. C **109**, 014301 (2024).

[300] D. A. Nesterenko, L. Jokiniemi, J. Kotila, A. Kankainen, Z. Ge, T. Eronen, S. Rinta-Antila, and J. Suhonen, The European Physical Journal A **58**, 44 (2022).

[301] J. Suhonen, Nuclear Physics A **864**, 63 (2011).

[302] V. I. Tretiak and Y. G. Zdesenko, Atomic Data and Nuclear Data Tables **80**, 83 (2002).

[303] O. Niţescu and F. Šimkovic, A semi-empirical formula for two-neutrino double-beta decay (2024).

[304] R. Chandra, J. Singh, P. K. Rath, P. K. Raina, and J. G. Hirsch, The European Physical Journal A - Hadrons and Nuclei **23**, 223 (2005).

[305] K. Chaturvedi, R. Chandra, P. K. Rath, P. K. Raina, and J. G. Hirsch, Phys. Rev. C **78**, 054302 (2008).

[306] J. Menéndez, A. Poves, E. Caurier, and F. Nowacki, Nuclear Physics A **818**, 139 (2009).

[307] F. Šimkovic, C. C. Moustakidis, L. Pacearescu, and A. Faessler, Phys. Rev. C **68**, 054319 (2003).

[308] P. A. M. Dirac, Nature **139**, 323 (1937).

[309] B. Pontecorvo, Physics Letters B **26**, 630 (1968).

[310] Z. Bo, W. Chen, X. Chen, Y. Chen, Z. Cheng, X. Cui, Y. Fan, D. Fang, Z. Gao, L. Geng, *et al.* (PandaX Collaboration), Dark matter search results from 1.54 tonne·year exposure of pandax-4t (2024), arXiv:2408.00664 [hep-ex] .

[311] Nanal, V., EPJ Web of Conferences **66**, 08005 (2014).

[312] O. Chkvorets, C. Kraus, J. Kuettler, V. Lozza, B. von Krosigk, and K. Zuber, A tin-loaded liquid scintillator approach for the 2 neutrino double-beta decay measurement of sn-124 (2017), arXiv:1707.08001 [physics.ins-det] .

[313] J. J. Sakurai, *Advanced Quantum Mechanics* (Addison-Wesley Publ. Co., Reading, 1967).

[314] M. E. Rose, *Elementary Theory of Angular Momentum* (Dover, 1995).

[315] D. A. Varshalovich, A. N. Moskalev, and V. K. Khersonskii, *Quantum Theory of Angular Momentum* (World Scientific, 1995).

[316] A. R. Edmonds, *Angular Momentum in Quantum Mechanics* (Princeton Univ. Press, 1960).

[317] J. C. Slater, Phys. Rev. **81**, 385 (1951).

[318] A. Rosen and I. Lindgren, Phys. Rev. **176**, 114 (1968).

[319] B. Hahn, D. G. Ravenhall, and R. Hofstadter, Phys. Rev. **101**, 1131 (1956).

[320] R. Latter, Phys. Rev. **99**, 510 (1955).

[321] D. Liberman, D. Cromer, and J. Waber, Computer Physics Communications **2**, 107 (1971).

[322] D. Liberman, J. T. Waber, and D. T. Cromer, Phys. Rev. **137**, A27 (1965).

[323] G. Molière, Zeitschrift für Naturforschung A **2**, 133 (1947).

[324] E. Condon and H. Odabaşi, *Atomic Structure* (Cambridge Univ. Press, 1980).

[325] T. A. Carlson, *Photoelectron and Auger Spectroscopy* (Plenum Press, 1975).

[326] J. C. Slater, Phys. Rev. **34**, 1293 (1929).

[327] E. U. Condon, Phys. Rev. **36**, 1121 (1930).

[328] I. Grant, Advances in Physics **19**, 747 (1970).

[329] S. Esposito, American Journal of Physics **70**, 852 (2002).

[330] C. Froese Fischer, G. Gaigalas, P. Jönsson, and J. Bieroń, Computer Physics Communications **237**, 184 (2019).